Coherent Atom-Light Interactions in Rydberg Systems

Thesis

THE OPEN UNIVERSITY

Coherent Atom-Light Interactions in Rydberg Systems

Author:
Ayooluwa Olakunle Odufowora

Supervisor:
Dr. Silvia Bergamini
Dr. Calum Maccormick

A thesis submitted in fulfillment of the requirements for the degree of Doctor of Philosophy

in the

School of Physical Sciences

February 19, 2021

Abstract

This thesis investigates the effects of strong Rydberg-Rydberg interactions in the presence of three-level coherent phenomena such as electromagnetically induced transparency (EIT), Autler-Townes splitting (ATS) and coherent population trapping (CPT). As a result of their remarkable properties, highly excited Rydberg atoms have great potential for applications in diverse areas. The interaction-induced dipole blockade between the Rydberg atoms has been proposed as a fundamental tool in quantum information processing with neutral atoms. Yet, they require an increasing level of understanding and control.

A many-body theory is developed for the Rydberg excitation dynamics in various atomic systems with different densities and velocity distributions such as for atoms in a vapour cell, ultracold atoms in magneto-optical and optical dipole traps, or a system of optical lattices or dipole trap arrays. The systems were investigated by solving the optical Bloch equations numerically for a two-photon ladder excitation scheme, taking into consideration various experimentally relevant conditions for the emergence of the effects of Rydberg-Rydberg interactions. The lineshape properties of the EIT/ATS/CPT spectra are observed and reviewed while the physical arguments for how the lineshape properties change as a function of various parameters are provided. To account for the differing atomic distributions in the atomic systems, a many-body model based on Monte-Carlo simulation is developed to describe the optical response of the multi-atoms systems to two-photon excitation laser lights in the regimes of EIT, ATS and CPT and strong atomic interactions. The study of the lineshape properties allows one to understand possible ways to detect the emergence of interaction-induced excitation suppression, asymmetry, line shift and excitation "antiblockade" enhancement effects. Besides these, the main result of this study is the demonstration that the linewidth properties of the Rydberg EIT/ATS/CPT spectra can reveal collective many-body behaviour associated with the creation of many-body entangled states. The linewidth properties provide compelling evidence of the creation of collective states by confirming the predicted dependence of the generalised Rabi frequency on the square root of the number of atoms in the mesoscopic ensemble. This study could help to quantify and control the conditions necessary for creating many-body entanglement within atomic ensembles.

The thesis also describes the step towards experimentally investigating the response of an atomic system to excitation lasers and studying the excitation dynamics of interacting atoms in such systems. Significant work was done to set up the two-photon excitation system for preparing atoms in high-lying Rydberg states and performing

Rydberg-based vapour cell experiments. Qualitative analysis of the Rydberg states transparency features allows to obtain laser parameters such as the laser linewidths and Rabi frequencies that are used in the theoretical model to create the similarity between the experimental and theoretical parameters.

Further works were carried out towards realising the building blocks for experimentally investigating the interactions between Rydberg atoms in ultracold atom systems. This is by setting-up a trapping system capable of producing a highly dense ultracold atom ensemble within a magneto-optical trap, cold enough to serve as a reservoir from which the optical dipole trap can be loaded efficiently. The optical dipole trap is designed and set up to achieve a micron-size trapping potential capable of producing a sub-micron sized atomic cloud, with a controllable number of atoms, where a full blockade effect can be achieved and exploited to implement a qubit system for quantum gate operations.

Acknowledgements

All glory and honour be to Almighty God for the grace to walk through this journey. My most heartfelt gratitude to Him, the giver of wisdom and strength.

I would like to thank my supervisors, Dr. Silvia Bergamini and Dr. Calum Maccormick, for first giving me the opportunity to do this research. Without your immense help, professional guidance and not the least, your extreme patience, I would not have lasted a day. All my knowledge in the field, I have acquired from you. My experience with you will live with me forever, and I am eternally grateful. I would like to thank my former group members Katarzyna Krzyzanowska, Micheal Copley-May and Rudy Romain, who introduced me to the basics of the lab. I will also like to appreciate my fellow PhD student, Siobhan Patrick. Although we only worked together for a few months, I must say that your resumption into the lab was timely, and it was a real pleasure to work with you.

I feel very grateful to have been blessed with some amazing friends who made my PhD experience memorable. I will like to appreciate Mark Parker for creating the avenue to talk to him any time and for the exciting PhD conversations we had. Special gratitude to Ganiyu D. Adebanjo, with whom I have shared two academic journeys (Italy and UK). I want to say thank you for being more than just a friend at every milestone I reach. I owe a great deal to my friend, Akinwande O. Cole, for his invaluable support since I found myself in Milton Keynes. You practically made me your burden and allowed me to freely inconvenient you every time. It would be impossible to count all the ways that you have helped me in life. Thank you so much for all that you have done, and I only hope I can reciprocate your kind gestures in the nearest future.

I am deeply grateful to my parents and siblings for their prayers and support per time. Thank you so much for nurturing me to the person I am and believing in me in whatever I find myself to do. I also want to appreciate my parents-in-law for their love, support, trust and prayers. Most importantly, I would like to give the most unfeigned gratitude to my lovely wife, Kehinde Mary Taiwo, for her consistent love and countless sacrifices throughout this journey. Walking down the aisle with you was the best thing that happened to me throughout my PhD. You have inspired me to pursue my dreams with dedication. You have always encouraged me to be positive even when I feel like its the end of the road. You have always prayed for me both in secret and in the open. Thank you very much for being my best friend.

Contents

List of Figures

List of Abbreviations

EM	**E**lectro**m**agnetic
OBE	**O**ptical **B**loch **E**quation
EIT	**E**lectomagnetically **I**nduced **T**ransparency
ATS	**A**utler **T**ownes **S**plitting
DSP	**D**ark **S**tate **P**olariton
STIRAP	**Sti**mulated **R**aman **A**diabatic **P**assage
CPT	**C**oherent **P**opulation **T**ransfer
AIC	**A**kaike **I**nformation **C**riterion
DQC1	**D**eterministic **Q**uantum **C**omputation with **one** qubit
TM	**T**uring **M**achine
VNM	**V**on **N**euman **M**achine
CNOT	**C**ontrolled **NOT**
NMR	**N**uclear **M**agnetic **R**esonance
QED	**Q**uantum **E**lectro**d**ynamics
MOT	**M**agneto-**o**ptical **Trap**
ODT	**O**ptical **D**ipole **T**rap
GSDL	**G**rating **S**tabilized **D**iode **L**aser (GSDL)
ECDL	**E**xtended **C**avity **D**iode **L**aser
MTS	**M**odulation **T**ransfer **S**pectroscopy
PZT	**P**iezoelectric **T**ransducer
TEC	**T**hermo**e**lectric **C**ooler
DAVLL	**D**ichroic **A**tomic **V**apour **L**aser **L**ock
SAS	**S**aturated **A**bsorption **S**pectroscopy
EOM	**E**lectro-**o**ptic **M**odulator
FFT	**F**ast **F**ourier **T**ransform
FALC	**F**ast **A**nalog **L**inewidth **C**ontroller
SHG	**S**econd **H**armonic **G**eneration
PID	**P**roportional-**I**ntegral-**D**erivative
FWHM	**F**ull **W**idth at **H**alf **M**aximum
AOM	**A**cousto-**o**ptic **M**odulator
VCO	**V**oltage **C**ontrol **O**scillator
VCA	**V**oltage **C**ontrol **A**ttenuator

CCD	**C**harge-**c**oupled **D**evice
ICCD	**I**ntensified **C**harge-**c**oupled **D**evice
APD	**A**valanche **P**hoto**d**iode
PBS	**P**olarising **B**eam **S**plitter
UHV	**U**ltra**h**igh **V**acuum
AMD	**A**lkali **M**etal **D**ispensers
CMOT	**C**ompressed **M**agneto-**o**ptical **Trap**
ToF	**T**ime **o**f **F**light
RaR	**R**elease **a**nd **R**ecapture

Physical Constants

Reduced Planck constant	$\hbar = 1.054571726 \times 10^{-34}$ J s
Speed of light	$c = 299792458$ m/s
Permeability of free space	$\mu_0 = 1.2566370614 \times 10^{-6}$ N/A^2
Permittivity of free space	$\epsilon_0 = 8.85418781762 \times 10^{-12}$ C^2 N^{-1} m^{-2}
Electronic charge	$e = 1.60217662 \times 10^{-19}$ C
Electron mass	$m_e = 9.10938356 \times 10^{-31}$ kg
Rydberg constant	Ry$= 13.605693122994$ eV
Boltzmann's constant	$k_B = 1.38064852 \times 10^{-23}$ J/K
Atomic mass of Rubidium (Rb) atom	$m_{\text{Rb}} = 1.44316193 \times 10^{-25}$ kg

Introduction

Due to their intriguing properties, Rydberg atoms, which are atoms in highly excited states, have been subject to investigations in various atomic systems for decades. At first, investigations were done for only atoms at room temperature where the thermal energies of the atoms exceed the typical interaction energies. However, with the development of laser cooling and trapping techniques, the investigations of Rydberg atoms extended to the regime of ultracold and frozen Rydberg gases. In this regime, the atomic motion is negligible and the kinetic energies of the atoms are much smaller than the typical interaction energies. Hence, the dynamics of Rydberg atoms in such systems is totally determined by long-range interactions.

The properties of Rydberg states have been found to be practical and distinctive due to the scaling of the properties of Rydberg atoms with the principal quantum number. As a result of their large orbital radius, Rydberg atoms have significantly large transition electric dipole moments. Therefore, they have enhanced electrical polarisabilities and as such extreme sensitivities to external electric fields, even to weak electric fields produced by nearby atoms. Rydberg atoms exhibit strong interactions which give rise to intriguing phenomena with diverse applications. Due to their long radiative lifetimes, Rydberg atoms turn out to be suitable candidates for studying light-matter interactions and interatomic interactions over microseconds timescale. The possibility of tuning their internal states gives room for tuning the properties and interactions. Hence, Rydberg states are ideally suited to the theoretical and experimental study of quantum many-body physics.

A fascinating consequence of the strong long-range interactions between Rydberg atoms is the rise of Rydberg blockade phenomenon which prohibits simultaneous Rydberg excitation of multiple atoms. As a result of the single excitation, there is a possibility of creating shared and highly entangled states within a mesoscopic atomic system. The ability to control the physical mechanism required to create highly entangled atom states combined with the ability to manipulate the states of the atoms indicates that cold Rydberg atoms are ideal as a platform for quantum information processing [1, 2, 3]. The proposed two-qubit gates are operated by exploiting interaction-induced entanglement between Rydberg atoms [4]. Examples are the controlled-not

(C-NOT) logic gates proposed in [5] using Hadamard-C_z and controlled amplitude swap operations. Although the fidelity of controlled gates is still an issue of concern, an impressive breakthrough in scaling up the system has been made. Experimental results on two-qubit Rydberg-blockade quantum gates in a two-dimensional qubit array of traps were used to achieve entanglement [6]. Three-dimensional qubit system produced from an optical lattice has also been used to demonstrate arbitrary single-qubit gates [7].

Although a lot of logic gates rely on Rydberg-blockade effects, some logic gates can also be implemented without exploiting Rydberg blockade [8] while some gates are implemented without substantially populating the Rydberg levels [9, 10, 11]. Basically, these applications require a high degree of control of the Rydberg excitation process to maximise excitation efficiency, create well-defined superpositions of states, and transfer population to Rydberg states [12]. As considered in this thesis, the description of the underlying physical mechanism for controlling the many-body excitation dynamics of the Rydberg gases relies on understanding the coherent processes that are present during Rydberg excitation. In the simple case of a three-level atom where the atoms are coupled to two laser fields, coherent phenomena which have attracted considerable attention in relation to Rydberg atoms are electromagnetically induced transparency (EIT) [13, 14, 15], Autler-Townes splitting (ATS) [14, 15] and coherent population trapping (CPT) [16, 17]. They result from the quantum interference between excitation pathways, which leads to a sharp modification of the optical properties of the atomic medium. In the context of Rydberg-based quantum information applications, these coherent phenomena allow for the effective and non-destructive probing or detection of Rydberg states. For non-interacting atomic gases, they have been found promising not just for manipulating quantum information, but also for optically-controlled slowing, stopping and storage of light [18, 19, 20, 21], as well as precision spectroscopy [22]. Beyond these, it has been realised that the combination of strongly interacting Rydberg atoms coupled to these interference effects opens up new routes to applications such as the generation of non-classical light [23], implementation of photonic phase gates [24] and quantum simulators for many-body systems [25], and most important for the focus of this thesis, the preparation of many-body entangled states [26].

In this thesis, dipole blockade which is induced by van der Waals interactions [27, 28] or dipole-dipole interactions [29, 30] is verified to cause important effects such as spectral broadening of resonance lines, suppression of excitation and changing the probability

distribution of Rydberg atom numbers [31, 32]. Also in this thesis, the interaction-induced many-body effects between atoms were studied by varying the principal quantum number n of the Rydberg excitation level, by varying the density of Rydberg atoms and by varying the intensities of the excitation lasers. Several methods have been proposed for the theoretical description of interacting many-particle systems [33, 34, 35]. Giving that the set of many-body optical Bloch equation (OBE) grows exponentially as 3^N, because of the computational requirement, the number of atoms that are considered for calculations is usually limited which may cause an inaccurate reproduction of observations from physical experiments. However, experimental observations have been shown to be accurately described using a theoretical many-body approach based on either reduced density matrix expansion [36] or Monte Carlo simulations [36, 37]. In the Monte Carlo propagation scheme followed in [36, 37], they resorted to a rate equation treatment of the many-body steady states of the OBEs. The rate equations for atomic populations were obtained upon adiabatic elimination of the coherences in the OBEs obtained from a non-interacting many-body case. In this thesis, however, a many-body approach based on Monte Carlo simulation is also followed but relies on the numerical solutions of the OBEs for a solvable number of atoms. These are then iterated over the whole distribution of the mesoscopic ensemble. Unlike in [36, 37], putting the atom cloud distribution into consideration allows for the description of Rydberg excitation dynamics in different atomic systems.

The observations of the emergence of interaction-induced excitation suppression, asymmetry, line shift and excitation "antiblockade" enhancement effects of resonance spectra are presented in this thesis. Moreover, the major observation in this thesis is the collective effect such as the increase in the coherent many-body Rabi oscillations of atoms between the ground and the Rydberg states. This intriguing effect has been previously observed in [38, 39, 40] where strongly pronounced oscillation is shown to indicate an excitation blockade of an atom ensemble by an excited state. The dependence of this collective Rabi frequency on the square root of the mesoscopic system size is associated with the creation of many-body entangled states containing only one Rydberg excited atom. This collective coherent behaviour is generic for all mesoscopic systems that are capable of carrying only one single excitation. Unlike the approach followed in [38, 39, 40], this study relies on exploring the linewidth properties of the excitation spectra that are obtained from the solution of the many-body OBEs when interaction-induced broadening occurs. The linewidth properties of the excitation spectra reveal the rising collective many-body Rabi oscillation at a frequency $\sqrt{N}\Omega$, involving all $N \gg 1$ interacting atoms. This is a novel and important result, as the oscillations are used to provide compelling evidence for the achievement of collective

coherent behaviour.

This thesis is focused on investigating the creation of many-body entanglement by exploiting long-range Rydberg-Rydberg interactions between Rydberg atoms. This research aims to understand, in details, the effects of strong Rydberg-Rydberg interaction in the regimes of the three-level interference phenomena, i.e. EIT, ATS and CPT. The investigations presented in this thesis cover both atoms in a vapour cell and ultracold atoms in a magneto-optical trap (MOT) and an optical dipole trap (ODT). Understanding the coherent processes present in interacting Rydberg gases constitutes an important step towards understanding how to prepare and manipulate the systems in a controlled way and also how to control the physical mechanism required to create a highly entangled state.

This thesis also presents the steps toward experimentally investigating the interacting Rydberg gases. The design and set up of a two-photon excitation system employed for the excitation of atoms to the Rydberg state is presented. The steps toward achieving an optimised MOT - that is in the regime where it can be regarded as being suitable for Rydberg gas experiments - are also presented. Lastly is the design and setup of the laser and optical systems to achieve a microscopic ODT that fulfils the trapping and size requirements for the implementation of an atomic qubit.

The thesis will be organised as follows:

Chapter 1 gives the full treatment of the semiclassical theory of the interaction of light and atoms. The basic theory of the behaviour of a multilevel atom when its free evolution is perturbed by laser fields under the effects of changing optical parameters is provided. The expression for the linear response of an atomic medium to laser fields will be derived, and the basic knowledge of how it can be used to predict the optical properties of an atomic system will be given. This chapter will end with discussing fundamental differences between the atomic coherent phenomena, i.e. EIT, ATS and CPT, that occur during two-photon excitation processes.

Chapter 2 gives an overview of the physics of alkali Rydberg atoms. The chapter looks into the basic properties of Rydberg atoms, the strong spatially-dependent long-range interactions that occur between them, how they are used to create shared entangled atomic states and implement universal quantum gates from which quantum algorithms can be developed. Then some proposals for quantum gates based on the interactions between Rydberg atoms are reviewed. The chapter ends by describing the cold atoms

implementation of the deterministic quantum computation with a single qubit (DQC1) model, which is the long-term goal of this research.

Chapter 3 gives a detailed description of the experimental realisation of two-photon excitation scheme. The two-photon excitation lasers, the optical setup for the two-photon excitation scheme and the methods for stabilising and locking the lasers to probe highly excited Rydberg states are described.

Chapter 4 begins by introducing the theoretical description of two-photon excitation extended to the case of a large number of non-interacting atoms that is experimentally realistic. The study of the lineshape properties of the optical response of a non-interacting multi-atom system to laser light in the EIT, ATS and CPT regimes is done. The step towards experimentally investigating the response of a homogeneously broadened atomic system to laser fields is also described. Then the quantitative analysis of the linewidth of transparency features that are obtained from a vapour cell experiment is done in comparison with those obtained from the theoretical model. The chapter then gives the theoretical description of the effects of Rydberg-Rydberg interactions in the regimes of three-level interference phenomena such as EIT, ATS and CPT. A Monte-Carlo model of the many-particle system is used to study the effects of interactions for different spatial distributions of atoms covering interacting atoms in a vapour cell, MOT and ODT, with different densities and excitation levels. The focus of this work is on investigating the lineshape and linewidth properties of the resonance spectra. The linewidth properties interestingly prove to be an efficient way to observe collective many-body behaviour associated with the production of an interaction-induced many-body entangled state having single Rydberg excited atom.

Chapter 5 presents the experimental setup towards achieving highly dense ultracold ensemble with a controllable number of atoms created in a MOT and an ODT. The chapter describes the laser systems and experimental setup for obtaining a MOT. The MOT is used to achieve an atom cloud that is dense enough for studying interacting Rydberg gases and cold enough to serve as a reservoir from which the ODT can be loaded efficiently. The chapter then presents the experimental setup for a microscopic ODT. The ODT is set up to produce a small atom ensemble that can be implemented as a qubit system for quantum gate operations.

Finally, chapter 6 gives a summary of the results and the outlook into the future work to be done.

1 Interaction of Multilevel Atoms with Electromagnetic Field

The ability to exploit the effects of light on atoms has brought about the understanding that light intensity gradients could exert forces on atoms [41] and that light can also cool and trap atoms [42]. Absorption of light by atoms can cause photo-excitation, photo-ionisation or atomic transitions, while the emission of light as a result of de-excitation plays an important role in studying the spectroscopic properties of atoms. A two-level atomic system has initially been the basis for describing most of these phenomena. However, since the 1990s, quantum optics developed into understanding more complex systems with three or more levels. This has brought about the development of remarkable new techniques that are now being explored in different physical settings, such as in optical fibres and quantum dots, optomechanical systems and ultracold atomic gases [16, 43, 44, 45, 46, 47]. The developments in the field of quantum gates, optical delay generators, quantum computation and information processing largely depend on the results of the study of multilevel atomic systems [47].

This chapter presents the evolution of a quantum 'atomic' system from being considered a closed or isolated system to an open system. This helps to describe the light-atom interaction and the evolution of the combined light-atom system. The evolution of a reduced system is described by a master equation characterised by noise and dissipation. The evolution of generic multilevel atoms in the presence of perturbations due to interactions with electromagnetic (EM) fields is described. The description is based on a semi-classical argument whereby the atomic system is treated quantum mechanically as ideal dipoles while the EM fields are treated classically by taking them as classical vector fields in the atomic Hamiltonian. The system is then reduced to an ideal three-level atomic system. This helps to fully study the theory of two-photon transition and determine the atomic system's linear optical response to an applied EM field. Then one can study the alteration of the optical response due to the presence of other fields and predict the spectroscopic lineshape properties of the atoms under different conditions such as varying the Rabi frequencies, laser detunings, decay rates and laser linewidths. The last part of the chapter describes the differences between quantum interference phenomena within the two-photon excitation process. Although

the description done in this chapter is for a single atom, it serves as the foundation for studying the case of a many-body non-interacting or interacting system that would be considered later in the thesis.

1.1 Quantum Mechanics of Noiseless and Noisy Systems

A quantum system, such as an atom, can be regarded as a closed or isolated physical system whose states are described by vectors $|\psi\rangle$ in the Hilbert space, $\mathbb{H}$, associated with it. The evolution of the state $|\psi(t)\rangle$ of a closed quantum system at any time t, is governed by the time-dependent Schrödinger equation

$$i\hbar\frac{\partial}{\partial t}|\psi(t)\rangle = \mathcal{H}(t)|\psi(t)\rangle \quad \Longrightarrow \quad |\psi(t)\rangle = U(t)|\psi\rangle \ , \tag{1.1}$$

where $U(t)$ is a unitary time-evolution operator, for which $U^{\dagger}(t) = U^{-1}(t)$. In the case when the Hamiltonian $\mathcal{H}$ is time-independent, one gets the exponential expression

$$U(t) \ = \ \exp\left[-\frac{i}{\hbar}\,\mathcal{H}t\right] \ . \tag{1.2}$$

In the case of incoherent or dissipative processes, it is necessary to switch to a statistical description. The use of the density matrix formalism, instead of deterministic wavefunctions, helps to study the interaction of a single atom or an atomic ensemble with EM field. In the density matrix formalism of quantum mechanics, an atomic system initially prepared, at time t = 0, in a mixed state is described by the weighted sum over projection operators onto possible state vectors,

$$\rho_A = \sum_i p_i \, |\psi_i\rangle\langle\psi_i| \ , \quad 0 \leq p_i \leq 1 \ , \quad \sum_i p_i = 1 \ ,$$

where p_i is the probability that the system is in the state $|\psi_i\rangle$. At any time $t \neq 0$, the unitary operator $U(t)$ causes a time transformation

$$\rho_A \ \xrightarrow{U(t)} \ \rho_A(t) = \sum_i p_i \, U(t) \, |\psi_i\rangle\langle\psi_i| \, U^{\dagger}(t) = U(t) \, \rho_A \, U^{\dagger}(t) \ . \tag{1.3}$$

Taking the time-derivative of $\rho(t)$ gives

$$\frac{\partial \, \rho_A(t)}{\partial t} = -\frac{i}{\hbar}\,[\mathcal{H}, \, \rho_A(t)] \ , \tag{1.4}$$

the *von Neumann-Liouville equation*. This is an evolution in the Schrödinger picture for the states of the system. It is important to emphasize that the density matrix provides the probability distribution over the states of one atom instead of that of the states of the population of many atoms as would be the case of interest. The state distribution of the atoms can be expressed in terms of the single atom density matrix as

$$\varrho(\mathbf{r}, t) = \mathfrak{N}\eta(\mathbf{r})\rho_A(t) \ , \tag{1.5}$$

where $\mathfrak{N}$ is the atom number density and $\eta(\mathbf{r})$ is the spatial distribution profile of the atoms. For most systems, the population operator is generally an operator in the subspace of one atom but not in the Hilbert space of the whole population. However, the idea is that enough information about the entire system is encoded in the probability distribution over the state of a single atom to represent the whole population [48].

Generally, it is impossible to completely isolate any quantum system of interest (say the atom A) from its surroundings (say E), which could be a reservoir, a thermal bath, a measuring device, other systems or atoms of its kind or in this case, an interacting EM field. The Hamiltonian of the composed system $A + E$ is in general given by

$$\mathcal{H} = \mathcal{H}_A \otimes \mathbf{1}_E + \mathbf{1}_A \otimes \mathcal{H}_E + \lambda\mathcal{H}_I \ , \tag{1.6}$$

where $\mathcal{H}_A$ is the free Hamiltonian of A, $\mathcal{H}_E$ is the free Hamiltonian of E, $\mathcal{H}_I$ is the interaction Hamiltonian, λ is a dimensionless coupling constant and $\mathbf{1}_{A,E}$ are identity operators [49, 50].

In the case where the interaction between A and E is weak but not negligible, the reduced density matrix of A can be decoupled from that of the composite system $A + E$. As a result of the interaction with E, the evolution of A is characterised by noise and dissipation, which in the case of an atom may be in the form of spontaneous decay and dephasing processes. Spontaneous decay and depashing rates are influenced by the presence of other atoms via an EM field mediated coupling. Dephasing also occur due to magnetic noise, intensity noise from optical traps or due to motional effects for atoms that are cooled to the vibrational ground state of the trapping potential [51, 52]. These are typical of the time-evolution of *open quantum systems* [49]. To account for these effects, a phenomenological matrix term $\mathfrak{D}$ called the *dissipator* or the *decoherence matrix* is added to equation (1.4), thus becoming

$$\frac{\partial\,\rho_A(t)}{\partial t} = -\frac{i}{\hbar}\left[\mathcal{H}'_A, \rho_A(t)\right] + \mathfrak{D}[\rho_A(t)] \ , \tag{1.7}$$

which is the *quantum master equation*. Meanwhile, $\rho_A(t)$ is now a *reduced density matrix* given by

$$\rho_A(t) = \mathrm{Tr}_E[\rho(t)] = \mathrm{Tr}_E[U(t)(\rho_A \otimes \rho_E)\, U^\dagger(t)] \ .$$

The first term of equation (1.7) describes the free evolution of A by means of a Hamiltonian $\mathcal{H}'_A$. $\mathcal{H}'_A$ is not generally the same as $\mathcal{H}_A$ because it usually contains additional terms due to the coupling of the system to its environment. $\mathcal{H}'_A \approx \mathcal{H}_A$ if the coupling effects are considered to be negligible. On the other hand, the decoherence matrix acts linearly on the state space of A and accounts for the noisy and dissipation effects caused on A as a result of the interaction with E. The form of the decoherence matrix is fixed to satisfy the Gorini-Kossakowski-Sudarshan-Lindblad theorem [53, 54] which states that

$$\mathfrak{D}[\rho_A(t)] \ = \sum_{i,j} \mathcal{C}_{ij} \left(\mathcal{L}_i \rho_A(t) \mathcal{L}_j^\dagger - \frac{1}{2} \left\{ \mathcal{L}_j^\dagger \mathcal{L}_i, \rho_A(t) \right\} \right) \ , \tag{1.8}$$

where the sum is over the atomic energy levels serving as decay channels for atomic relaxation and excitation. $\mathcal{L}$ is the set of Lindblad operators which is given by the atomic projection operator $|i\rangle\langle j|$ for $i, j = 1, 2, \cdots, N$, where N is the number of energy levels considered for an atom. The coefficients $\mathcal{C}_{ij}$ are given by rates of spontaneous decays and dephasing processes.

The state dynamics of the atomic system is obtained by solving the set of equations from (1.7) with each element of the density matrix corresponding to a physical quantity. The diagonal elements are the *population terms*, which denote the atomic population in each atomic level. On the other hand, the off-diagonal elements, the *coherence terms* (also called the *electric dipole terms*), are complex terms and have time-dependent phase factors that describe the evolution of coherent superpositions. Having obtained the master equation from equation (1.7), next is to derive the expression for a generic N-level Hamiltonian. This can then be reduced to a 3-level Hamiltonian to describe two-photon transitions which would be the primary focus of this thesis. The decoherence matrix can also be obtained for a specific configuration of laser transitions.

1.2 Multilevel Atom Model

Consider a generic N-level atom with free Hamiltonian eigenstates, $|1\rangle$, $|2\rangle$, $\cdots$, $|N\rangle$ and eigenenergies $\hbar\omega_1$, $\hbar\omega_2$, $\cdots$, $\hbar\omega_N$, interacting with light-fields with transition

frequencies ω_{ij} where $i, j = 1, 2, \cdots, N$ for $i \neq j$ so that each field is detuned by the frequency $\Delta_{ij} = \Delta\omega_{ij} - \omega_{ij}$ to the corresponding transition frequency. $\Delta\omega_{ij} = \omega_j - \omega_i$ denotes the energy separation between states $|i\rangle$ and $|j\rangle$. Intuitively, the larger the number of levels considered, the more the physical effects that can be observed. In the perturbative regime, the corresponding effective Hamiltonian of a generic N-level atom interacting with a coherent EM light field reads

$$\mathcal{H} = \mathcal{H}_0 + \mathcal{H}_I(t) , \tag{1.9}$$

where $\mathcal{H}_0$ = time-independent free Hamiltonian of a single atom while the perturbation, $\mathcal{H}_I(t)$ is the time-dependent atom-light interaction Hamiltonian. The free Hamiltonian can be written in terms of the basis state $|i\rangle$ of the isolated atom, for $i = 1, 2, \cdots, N$, as

$$\mathcal{H}_0 = \sum_{i=1}^{N} \hbar\omega_i |i\rangle\langle i| , \tag{1.10}$$

assuming that one can form a complete orthonormal basis consisting of these states. $\hbar\omega_i$ are the eigen-energies of the free Hamiltonian.

Consider the presence of perturbing EM fields which drive the electric dipole allowed transitions in the atomic system, the oscillating electric field generally reads

$$\mathbf{E}(\mathbf{r}, t) = \sum_{\substack{\{i,j\} \\ i \neq j}}^{N} \mathbf{E}_{ij} \cos\left(\omega_{ij} t - \mathbf{k}_{ij} \cdot \mathbf{r}\right) \tag{1.11}$$

where $\mathbf{E}_{ij}$ denotes the amplitudes of the oscillating electric fields, $\omega_{ij} = \omega_{ji}$ are the frequencies of the EM fields, $\mathbf{k}_{ij}$ are the wavevectors associated with the these frequencies while $\mathbf{r} = \sum_l \mathbf{r}_l$ gives the position of the electron with respect to the centre of mass of the atom. Since the radius of the atom, which is of the order of Bohr radius, is much less than the typical wavelength ($\approx 10^{-7}$m) of the EM fields so that $\mathbf{k}_{ij} \cdot \mathbf{r} << 1$, one can apply the *dipole approximation* such that spatial dependence of the fields are ignored. The atom-light interaction Hamiltonian as a result of the energy of an electric dipole in an electric field reads

$$\mathcal{H}_I(t) = -\hat{\mu} \cdot \mathbf{E}(t) = -\sum_{i,j} |i\rangle\langle j| \, \mu_{ij} \cdot \mathbf{E}(t) , \qquad \hat{\mu} = -q\hat{\mathbf{r}} \tag{1.12}$$

where μ is the total electric dipole moment of the atom, q is the electronic charge, and $\hat{\mathbf{r}}$ is the position operator which represents the displacement of the charges and acts only in the Hilbert space spanned by $|i\rangle$. $\mu_{ij} = \mu_{ji}^* = \langle i| \hat{\mu} |j\rangle$ is the electric dipole

moment for any dipole-allowed $|i\rangle \leftrightarrow |j\rangle$ transition. $\mu_{ij} \neq 0$ only for $i \neq j$, consistent with the allowed transitions. One can simply re-write (1.12) as,

$$\mathcal{H}_I(t) = -\left[\sum_{\substack{\{i,j\}\\ i<j}} \left(|i\rangle\langle j|\,\mu_{ij}\right) + \mathbf{h.c}\right] \cdot \mathbf{E}(t)\ , \tag{1.13}$$

where the symbol **h.c** represents the Hermitian conjugation. Since the state evolution dynamics of concern is that which involves the interaction between the atom and the EM fields, it is intuitive to transform the dipole interaction Hamiltonian into the interaction picture using the unitary time evolution operator $\mathcal{U}(t) = \mathrm{e}^{\frac{i}{\hbar}\mathcal{H}_0 t}$. Although, the transformation is applied to the total Hamiltonian given by equation (1.9), the free Hamiltonian however remains unaffected. Since the free and dipole interaction Hamiltonian does not commute, only the dipole approximation Hamiltonian is left to be transformed. The transformation on the atom-light interaction Hamiltonian reads

$$\mathcal{H}_{\text{trans}} = \mathcal{U}(t)\,\mathcal{H}_I\,\mathcal{U}^{\dagger}(t) = -\left[\sum_{\substack{\{i,j\}\\ i<j}} \mathrm{e}^{-i\Delta\omega_{ij}t}\,|i\rangle\langle j|\,\mu_{ij}E_{ij}\cos\left(\omega_{ij}t\right) + \mathbf{h.c}\right]\ , \tag{1.14}$$

having considered that the dipole moment aligns with the electric field. One should also keep in mind that $E_{ij} = E_{ji}$ and $\Delta\omega_{ji} = -\Delta\omega_{ij}$. On expanding equation (1.14), one obtains time dependent coefficients that are dependent on $\Delta\omega_{ij} - \omega_{ij}$ and $\Delta\omega_{ij} + \omega_{ij}$. However, since the detuning is very small, terms depending on $\Delta\omega_{ij} + \omega_{ij}$ are rapidly oscillating and can be neglected as these oscillations will quickly average to zero on appreciable observation and interaction time scales. This is the *rotating wave approximation* [55, 56, 48]. Equation (1.14) becomes

$$\mathcal{H}_{\text{trans}} = -\frac{1}{2}\left(\sum_{\substack{\{i,j\}\\ i<j}} \mathrm{e}^{i\left(\omega_{ij}-\Delta\omega_{ij}\right)t}\,|i\rangle\langle j|\,\mu_{ij}E_{ij} + \mathbf{h.c}\right)\ . \tag{1.15}$$

This can be transformed back to the Schödinger picture via the unitary time evolution operator $\mathcal{U}(t) = \mathrm{e}^{\frac{i}{\hbar}\mathcal{H}_0 t}$ as

$$\mathcal{H}'_I = -\mathcal{U}^{\dagger}(t)\,\mathcal{H}_{\text{trans}}\,\mathcal{U}(t) = \frac{1}{2}\left(\sum_{\substack{\{i,j\}\\ i<j}} \mathrm{e}^{i\omega_{ij}t}\,|i\rangle\langle j|\,\mu_{ij}E_{ij} + \mathbf{h.c}\right)\ . \tag{1.16}$$

The transition dipole moment μ_{ij} is a complex quantity and can be written in terms of the magnitude and phase as

$$\mu_{ij} = |\mu_{ij}|\, e^{i\phi_{ij}} \ . \tag{1.17}$$

and define the *Rabi frequency*, $\Omega_{ij} \in \mathbb{R}$, as

$$\hbar\Omega_{ij} = |\mu_{ij}|\, E_{ij} \ . \tag{1.18}$$

One would note that the Rabi frequency has been taken to be time-independent. In the case when a time-dependent Rabi frequency is considered, the time change is gradual so that the atomic system can follow it adiabatically. So the resulting atom-light interaction Hamiltonian reads

$$\mathcal{H}'_I = -\frac{\hbar}{2}\left(\sum_{\substack{\{i,j\}\\ i<j}} \Omega_{ij} e^{i\omega_{ij}t}\, e^{i\phi_{ij}}\, |i\rangle\langle j| + \mathbf{h.c}\right) \ . \tag{1.19}$$

Summing this up with the free Hamiltonian in equation (1.10) gives the effective N-level atom Hamiltonian, $\mathcal{H}_N$. However, in order to make solving equations from (1.7) simple to do, it is convenient to remove the time and phase dependencies of the Hamiltonian. This is done by working in a different basis known as the *rotating basis*. This new basis is related to the old basis via a unitary transformation, namely

$$|\tilde{i}\rangle = \mathcal{U}'(t,\phi)|i\rangle \ . \tag{1.20}$$

The time- and phase-dependent unitary operator must be carefully chosen while the new basis must also satisfy the Schödinger equation [48, 57]

$$i\hbar\frac{\partial|\tilde{i}\rangle}{\partial t} = i\hbar\frac{\partial\left[\mathcal{U}'(t,\phi)|i\rangle\right]}{\partial t} = \mathcal{H}'_N|\tilde{i}\rangle \ . \tag{1.21}$$

This implies that the N-level Hamiltonian is transformed as

$$\mathcal{H}'_N = i\hbar\frac{\partial\mathcal{U}'(t,\phi)}{\partial t}\mathcal{U}'^{\dagger}(t,\phi) + \mathcal{U}'(t,\phi)\,\mathcal{H}_N\,\mathcal{U}'^{\dagger}(t,\phi) \ . \tag{1.22}$$

The appropriate choice of the transformation matrix $\mathcal{U}'(t,\phi)$ is dependent on the EM-field configuration of N-level atom, i.e. for specific configurations of atomic transitions.

Having obtained the Hamiltonian for a generic N-level atomic system (in equation (1.22)), this is applicable in describing the optical properties of an atomic medium

depending on the fields involved and the number of transitions induced by the fields. This thesis will focus on studying optical properties such as the polarisation, linear susceptibility, atomic relaxation processes and quantum interference effects in a three-level atomic system.

1.3 Theory of two-photon transition in a three-level system

Consider the typical three-level systems shown in figure 1.1(a). Mainly, three different configurations can be obtained, namely the cascade (or ladder), the Λ and the V (or Vee) configurations via the interaction of two continuous-wave laser beams with the atomic system. They generally require two dipole-allowed transitions: $|1\rangle \leftrightarrow |2\rangle$ driven by a laser beam which is called the *probe beam* and $|2\rangle \leftrightarrow |3\rangle$ driven by a laser beam which is called the *coupling beam*. Although the $|1\rangle \leftrightarrow |3\rangle$ transition is dipole forbidden, there is a spontaneous decay of atoms from the state $|3\rangle$ to $|1\rangle$ whose rate depends on the choice of state $|3\rangle$. The probe beam is characterised by the frequency ω_p and amplitude E_p, and the coupling beam by frequency ω_c and amplitude E_c. The strengths of both beams are characterised by the Rabi frequencies Ω_P and Ω_C respectively while the detuning of the lasers from the transitions $|1\rangle \leftrightarrow |2\rangle$ and $|2\rangle \leftrightarrow |3\rangle$ are given by Δ_p and Δ_c respectively. γ_2 and γ_3 are the spontaneous decay rates from states $|2\rangle$ and $|3\rangle$ respectively. In the study, Rubidium (Rb) atoms are considered whose energy levels are shown in figure 1.1(b). The probe beam is a 780 nm beam which couples the ground state $|1\rangle = |5S_{1/2}\rangle$ to an intermediate state $|2\rangle = |5P_{3/2}\rangle$. The $|2\rangle = |5P_{3/2}\rangle$ state has a natural linewidth $\gamma_2 = 6.065$ MHz. A 480 nm coupling beam drives the intermediate state to a Rydberg state $|3\rangle = |n\mathrm{D} \text{ or } n\mathrm{S}\rangle$. The description of these laser systems and how they are stabilised to the required transitions are given in chapter 3. This study will consider $|3\rangle = |\,20D_{5/2}\rangle$ Rydberg state which has a natural linewidth of $\gamma_3 \sim 0.003\gamma_2$.

Although derivations will be done for a generic three-level configuration, this thesis will only focus on the ladder-type two-photon excitation scheme (as schematically shown in figure 1.1 (b)) which will be used to study the characteristic properties of hot and ultracold atoms when they are excited to Rydberg states. Generally, the study of two-photon transitions of this kind requires the state $|2\rangle$ to be an unstable state to avoid populating it. The state $|3\rangle$ is a metastable state whose choice, as will be shown later, is paramount for the implementation of quantum computation and quantum information processing with ultracold neutral atoms.

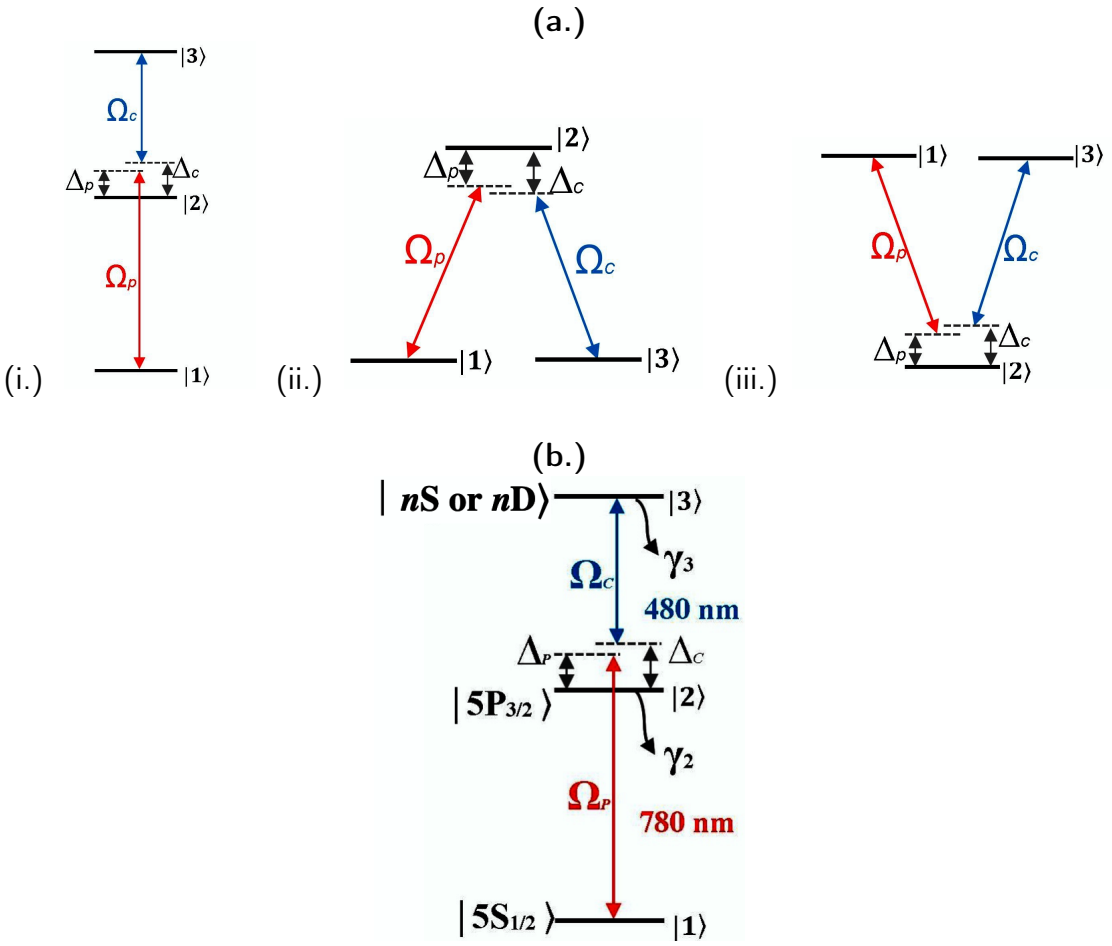

FIGURE 1.1: **(a.)** The different three-level atomic systems configuration: (i.) Cascade or Ladder (ii.) Lambda (iii.) Vee configurations; **(b.)** Three-level ladder-type scheme with the corresponding states shown.

From equations (1.10) and (1.19), the generic effective Hamiltonian for the three-level atom systems [figures 1.1 (i.) - (iii.)] reads

$$\mathcal{H}_3 = \frac{\hbar}{2}\left[\left(\sum_{i=1}^{3}\omega_i\,|i\rangle\langle i|\right) - \left(\Omega_P e^{i\omega_p t}\,e^{i\phi_p}\,|1\rangle\langle 2| + \Omega_C e^{i\omega_c t}\,e^{i\phi_c}\,|2\rangle\langle 3|\right) + \mathbf{h.c}\right]. \tag{1.23}$$

while the unitary transformation matrix from equation (1.20) reads,

$$\mathcal{U}'(t,\phi) = e^{-i\omega_p t}e^{-i\phi_p}\,|1\rangle\langle 1| + |2\rangle\langle 2| + e^{i\omega_c t}e^{i\phi_c}\,|3\rangle\langle 3|\,. \tag{1.24}$$

Substituting equations (1.23) and (1.24) in the time dependent Schrödinger equation results in a time- and phase-independent Hamiltonian

$$\tilde{\mathcal{H}}_3 = \frac{\hbar}{2}\left[\left(\omega_1+\omega_p\right)|1\rangle\langle 1| + \omega_2|2\rangle\langle 2| + \left(\omega_3-\omega_c\right)|3\rangle\langle 3| - \Omega_P|1\rangle\langle 2| - \Omega_C|2\rangle\langle 3| + \mathbf{h.c}\right]. \tag{1.25}$$

Without any loss of generality, this Hamiltonian can further be written in a more interpretable form by adding a multiple of the identity matrix, $-\hbar\left(\omega_1+\omega_p\right)\mathbf{1}_3$. This only changes the eigenvalues by some constant, as the physically relevant terms are the differences between energy level separations and laser transition frequencies [48, 57, 58]. Thus, the generic time-independent Hamiltonian that determines the coherent evolution of the system is given by

$$\tilde{\mathcal{H}}_3 = -\frac{\hbar}{2}\begin{bmatrix} 0 & \Omega_P & 0 \\ \Omega_P & -2\Delta_P & \Omega_C \\ 0 & \Omega_C & -2\left(\Delta_P+\Delta_C\right) \end{bmatrix}. \tag{1.26}$$

The probe and coupling laser detunings are defined as $\Delta_P = \omega_2-\omega_1-\omega_p$ and $\Delta_C = \omega_3-\omega_2-\omega_c$ respectively while $(\Delta_P+\Delta_C)$ stands for the two-photon detuning. Besides using equation (1.26) to study the evolution of a single three-level atom, it is also used as a model for constructing the Hamiltonian of a many-body non-interacting and interacting atomic systems. In that case, the many-body Hamiltonian becomes a sum over all the single atom Hamiltonian (see section 4.1.1).

Besides being collision-induced, the dephasing rates of the off-diagonal coherence terms for the states coupled to the laser fields are also modified by the finite linewidths of the fields (see section 4.2.3). Including the effects of the finite laser linewidth means that one must include the values of the dephasing rates γ_{2d} and γ_{3d} to the natural linewidths of levels $|2\rangle$ and $|3\rangle$ respectively. In an ideal experimental condition, $\gamma_{2d} \ll \gamma_2$, while for a Rydberg level, $\gamma_{3d} \gg \gamma_3$. The decoherence matrix accounting for the decay processes in the atom can be expressed as

$$\mathfrak{D}[\rho_A(t)] = \begin{bmatrix} \gamma_2\rho_{22}(t) & -\gamma_{21}\rho_{12}(t) & -\gamma_{31}\rho_{13}(t) \\ -\gamma_{21}\rho_{21}(t) & -\gamma_2\rho_{22}(t)+\gamma_3\rho_{33}(t) & -\left(\gamma_{21}+\gamma_{31}\right)\rho_{23}(t) \\ -\gamma_{31}\rho_{31}(t) & -\left(\gamma_{21}+\gamma_{31}\right)\rho_{32}(t) & -\gamma_3\rho_{33}(t) \end{bmatrix}, \tag{1.27}$$

where $\gamma_{21} = \frac{1}{2}\left(\gamma_2+\gamma_{2d}\right)$ and $\gamma_{31} = \frac{1}{2}\left(\gamma_3+\gamma_{3d}\right)$.

Inserting the equations (1.26) and (1.27) in (1.7), one obtains the equations of motion for the density matrix $\rho_A(t)$. It is assumed that the state $|1\rangle$ taken as the ground state is stable. So, the decay rate from $|1\rangle$ is zero. The set of *optical Bloch equations* (OBE's) for the populations and coherences reads

$$\begin{aligned}
\dot{\rho}_{11}(t) &= \gamma_2\rho_{22}(t) + \frac{i\Omega_P}{2}\left(\rho_{21}(t) - \rho_{12}(t)\right) \\
\dot{\rho}_{22}(t) &= \frac{i}{2}\left[\Omega_P\left(\rho_{12}(t) - \rho_{21}(t)\right) + \Omega_C\left(\rho_{32}(t) - \rho_{23}(t)\right)\right] - \gamma_2\rho_{22}(t) + \gamma_3\rho_{33}(t) \\
\dot{\rho}_{21}(t) &= \frac{i}{2}\left[\Omega_P\left(\rho_{11}(t) - \rho_{22}(t)\right) + \Omega_C\rho_{31}(t)\right] - \left(i\Delta_P + \gamma_{21}\right)\rho_{21}(t) \\
\dot{\rho}_{23}(t) &= \frac{i}{2}\left[\Omega_P\rho_{13}(t) + \Omega_C\left(\rho_{33}(t) - \rho_{22}(t)\right)\right] - \left(\gamma_{21} + \gamma_{31} + i\Delta_C\right)\rho_{23}(t) \\
\dot{\rho}_{31}(t) &= \frac{i}{2}\left(\Omega_C\rho_{21}(t) - \Omega_P\rho_{32}(t)\right) - \left[i\left(\Delta_P + \Delta_C\right) + \gamma_{31}\right]\rho_{31}(t) \\
\dot{\rho}_{33}(t) &= \frac{i\Omega_C}{2}\left(\rho_{23}(t) - \rho_{32}(t)\right) - \gamma_3\rho_{33}(t)
\end{aligned} \tag{1.28}$$

where $\dot{\rho}_{13}(t) = \dot{\rho}^*_{31}(t)$, $\dot{\rho}_{12}(t) = \dot{\rho}^*_{21}(t)$ and $\dot{\rho}_{32}(t) = \dot{\rho}^*_{23}(t)$. The simple thing to do is to calculate the steady-state solution of the system by setting $\dot{\rho}_{ij} = 0$ $(i, j = 1, 2, 3)$. The normalization condition $\rho_{11}(t) + \rho_{22}(t) + \rho_{33}(t) = 1$ for any time t.

In the case when the coupling laser is turned off, i.e. $\Omega_C = 0$, the system reduces to a typical two-level laser-driven system. As a result of the stimulated absorption and emission of laser light pulses, the atoms oscillate (the *Rabi oscillation*) between the states $|1\rangle$ and $|2\rangle$ with a frequency Ω_P. However, spontaneous decay from the state $|2\rangle$ dampens this oscillation so that the systems reach a steady-state in observational timescales with populations and coherences

$$\begin{aligned}
\rho_{22} &= \frac{\Omega_P^2\gamma_{21}}{2\left[\gamma_2\left(\Delta_P^2 + \gamma_{21}^2\right) + \Omega_P^2\gamma_{21}\right]} \;;\; \rho_{11} = 1 - \rho_{22} \\
\rho_{12} &= \frac{\Omega_P\gamma_2\left(\Delta_P - i\,\gamma_{21}\right)}{2\left[\gamma_2\left(\Delta_P^2 + \gamma_{21}^2\right) + \Omega_P^2\gamma_{21}\right]} \;;\; \rho_{21} = \rho_{12}^* \,.
\end{aligned} \tag{1.29}$$

It is a bit more difficult to analytically solve the steady-state limit of the full set of coupled equations (1.28). However, one can assume the *weak probe limit*, i.e. $\Omega_P \ll \Omega_C,\ \gamma_2$. As such, only terms that are linear in Ω_P are considered so that steady-state equations can be solved analytically or using perturbative calculations [59, 60]. One can further simplify the solutions by assuming that almost all the atom population are in the ground state $|1\rangle$ at all times, hence neglecting the population ρ_{22} and ρ_{33} so

that $\rho_{11} \simeq 1$ and $\rho_{22} \simeq \rho_{33} \simeq 0$. Thus, the probe transition coherence reads

$$\rho_{21} = \frac{2\left(\gamma_{31} + i\left(\Delta_C + \Delta_P\right)\right)\Omega_P}{4\left(\gamma_{21} + i\,\Delta_P\right)\left(\Delta_C + \Delta_P - i\,\gamma_{31}\right) - i\,\Omega_C^2} \tag{1.30}$$

while the two-photon transition coherence reads

$$\rho_{31} = -\frac{\Omega_P \Omega_C}{4\left(\gamma_{21} - i\,\Delta_P\right)\left[\gamma_{31} - i\left(\Delta_C + \Delta_P\right)\right] + \Omega_C^2} \ . \tag{1.31}$$

To determine the optical properties of the EIT medium, as measured by the probe beam, one would require an expression for the linear susceptibility as a function of the probe frequency.

1.4 Linear susceptibility

The optical properties of the atomic system are studied by observing the response of the system to the probe field, given by the field linear susceptibility. To obtain an expression for the linear susceptibility, one recalls that from the classical theory of electromagnetism, the dynamics of the EM field in a dielectric medium is described by the *macroscopic Maxwell's equations*. Without being overly concerned with minute details or formalism (see details in [48, 55, 61, 62]), the standard EM wave equation can be obtained as

$$\nabla^2 \mathbf{E}(\mathbf{r},\, t) - \frac{1}{c^2}\frac{\partial^2 \mathbf{E}(\mathbf{r},\, t)}{\partial t^2} = \mu_0 \frac{\partial^2 \mathbf{P}(\mathbf{r},\, t)}{\partial t^2} \ , \tag{1.32}$$

where $\mathbf{E}(\mathbf{r},\, t)$ is the electric field, c is the speed of light and μ_0 is the permeability of free space respectively. $\mathbf{P}(\mathbf{r},\, t)$ is the polarisation of the atomic medium whose dependence on the properties of the atomic medium enables the description of the EM field as it propagates through. Dipole moments are induced in the medium due to the applied field, thus the polarisation is expressed in terms of the average dipole moment per atom within a small region centred at $\mathbf{r}$ as

$$\mathbf{P}(\mathbf{r},\, t) = \mathfrak{N}\langle \boldsymbol{\mu}(\mathbf{r},\, t)\rangle \ , \tag{1.33}$$

where $\mathfrak{N}$ is the atom number density. Considering the atom population distribution from equation (1.5), the polarisation can be written in terms of the dipole moment operator of an atom in a mixed state $\rho_A(t)$ as

$$\mathbf{P}(\mathbf{r},\, t) = \mathrm{Tr}\left[\hat{\mu}\varrho(\mathbf{r},\, t)\right] = \mathfrak{N}\eta(\mathbf{r})\mathrm{Tr}\left[\hat{\mu}\rho_A(t)\right] \ . \tag{1.34}$$

One can be apply this to the three-level atom systems (figure 1.1) such that when the dipole-allowed transitions are considered, the dipole moment operator reads

$$\hat{\mu} = |1\rangle\langle 2|\,\mu_{12} + |2\rangle\langle 1|\,\mu_{21} + |2\rangle\langle 3|\,\mu_{23} + |3\rangle\langle 2|\,\mu_{32}\ . \tag{1.35}$$

Thus,

$$\mathrm{Tr}\left[\hat{\mu}\rho_A(t)\right] = \mu_{12}\rho_{21} + \mu_{21}\rho_{12} + \mu_{23}\rho_{32} + \mu_{32}\rho_{23}\ . \tag{1.36}$$

To be able to handle the phase-dependence of the transition dipole moments, the density matrix element in the conventional basis can be re-written in terms of the rotating basis density matrix elements by doing an inverse transformation

$$\rho_A = \mathcal{U}'^{\dagger}(t,\phi)\,\tilde{\rho}_A\,\mathcal{U}'(t,\phi)\ . \tag{1.37}$$

Considering equation (1.18) for the transition dipole moment and taking that $|\mu_{ij}| = |\mu_{ji}|$, the polarisation becomes

$$\begin{aligned}\mathbf{P}(\mathbf{r},\,t) = \mathfrak{N}\,\eta(\mathbf{r})\,\Big[&\hat{\mathbf{e}}_p\,|\mu_{21}|\,\left(\mathrm{e}^{i\omega_p t}\tilde{\rho}_{21} + \mathrm{e}^{-i\omega_p t}\tilde{\rho}_{21}\right)\\ &+ \hat{\mathbf{e}}_c\,|\mu_{32}|\,\left(\mathrm{e}^{i\omega_c t}\tilde{\rho}_{32} + \mathrm{e}^{-i\omega_c t}\tilde{\rho}_{23}\right)\Big]\ .\end{aligned} \tag{1.38}$$

where $\hat{\mathbf{e}}_p$ and $\hat{\mathbf{e}}_c$ are unit vectors having written the dipole moments in their full vector forms.

Inserting equation (1.34) into the wave equation implies that the atoms are taken as dipoles in an electric field. In return, the induced dipole affects the EM field as it is driven by the second derivative of the average dipole moment per atom. However, the medium's response to the change in the field is not instantaneous, except for lossless or dispersionless medium which is not the medium of interest but is dependent on the evolution of the field. This implies that the past states of the field must be accounted for to fully obtain the polarisation for any given time. This is done by expressing the polarisation as a power series in the field strength. In doing this, the polarisation can be separated into two parts, with one linear in the electric field and the other non-linear:

$$\mathbf{P}(\mathbf{r},\,t) = \mathbf{P}^{L}(\mathbf{r},\,t) + \mathbf{P}^{NL}(\mathbf{r},\,t)\ , \tag{1.39}$$

where the linear part can be written as

$$\mathbf{P}^{L}(\mathbf{r},\,t) = \mathbf{P}^{(0)}(\mathbf{r},\,t) + \epsilon_0\chi^{(1)}(\omega)\,\mathbf{E}(\mathbf{r},\,t) \tag{1.40}$$

where the coefficient $\chi^{(1)}(\omega)$ is the *linear susceptibility*, a second-rank tensor written for both positive and negative frequencies of the field. Since a dielectric medium is considered, the dipole moment in zero field vanishes because any dipole moment present is induced by the electric field. Hence, the first term vanishes as $\mathbf{P}^{(0)}(\mathbf{r}, t) \neq 0$ indicates permanent dipoles. The nonlinear part can be written as a function

$$\mathbf{P}^{NL}(\mathbf{r}, t) = f\left(\mathbf{E}^2\right) \tag{1.41}$$

which consist of terms that have higher order susceptibilities $\chi^{(j)}(\omega)$ for $j \geq 2$ which are (j+1)-rank tensors. The first-order term in (1.40) and other higher-order terms in (1.41) describe the influence of a time-dependent electric field. Although interesting physics such as the process of second- and high-order harmonic generation rely on this non-linear polarisation, this thesis will only look into studying the linear response in different coherent processes and interference phenomena that occur during two-photon excitations.

A field composed of many quasi-monochromatic frequency components can be written in the form given in equation (1.11). However, assuming that the field is monochromatic, then

$$\mathbf{P}(\mathbf{r}, t) = \epsilon_0 \chi^{(1)}(\omega)\, \hat{\mathbf{e}}\, E(\mathbf{r}, t)\, \cos(\omega t) \ , \tag{1.42}$$

having considered the dipole approximation and having neglected the phase of the field. $E(\mathbf{r}, t))$ is the electric field amplitude. Equation (1.42) can be decomposed into parts with positive and negative frequency components of the fields, so that

$$\begin{aligned} \mathbf{P}(\mathbf{r}, t) = & \frac{\epsilon_0}{2} \hat{\mathbf{e}}_p\, E_p(\mathbf{r}, t) \left(\chi^{(1)}(\omega_p)\, \mathrm{e}^{i\omega_p t} + \chi^{(1)}(-\omega_p)\, \mathrm{e}^{-i\omega_p t}\right) \\ & + \frac{\epsilon_0}{2} \hat{\mathbf{e}}_c\, E_c(\mathbf{r}, t) \left(\chi^{(1)}(\omega_c)\, \mathrm{e}^{i\omega_c t} + \chi^{(1)}(-\omega_c)\, \mathrm{e}^{-i\omega_c t}\right) \end{aligned} \ . \tag{1.43}$$

Comparing equations (1.43) and (1.38) implies that the probe field susceptibility reads

$$\chi^{(1)}(\omega_p) = \frac{2\,\Im\,\eta(\mathbf{r})\,|\mu_{21}|\,\tilde{\rho}_{21}}{\epsilon_0\, E_p(\mathbf{r}, t)} \ . \tag{1.44}$$

By inserting equation (1.30) in this equation and also using the definition of Rabi frequency given in equation (1.18), then

$$\chi^{(1)}(\omega_p) = \beta\, \frac{(\gamma_{31} + i\,(\Delta_C + \Delta_P))}{4\,(\gamma_{21} + i\,\Delta_P)\,(\Delta_C + \Delta_P - i\,\gamma_{31}) - i\,\Omega_C^2} \ , \tag{1.45}$$

where

$$\beta = \frac{4\,\Im\,\eta(\mathbf{r})\,|\mu_{21}|^2}{\epsilon_0\,\hbar}\ .$$

This implies that the system's optical properties in the weak probe limit are independent of the probe field strength but controlled by the coupling beam strength whose effect is seen in the denominator of equation (1.45).

Since the susceptibility is complex, it can be split into the real and imaginary parts, $\chi^{(1)}(\omega_p) = \chi_R^{(1)}(\omega_p) + i\,\chi_I^{(1)}(\omega_p)$, where

$$\begin{aligned}\chi_R^{(1)}(\omega_p) &= \mathrm{Re}\left(\chi^{(1)}(\omega_p)\right) = \beta\,\frac{\left[4\,\mathcal{A}\,\Delta_P - (\Delta_C+\Delta_P)\,\Omega_C^2\right]}{16\,\mathcal{A}\,\mathcal{C} - 8\,\mathcal{B}\,\Omega_C^2 + \Omega_C^4}\\ \chi_I^{(1)}(\omega_p) &= \mathrm{Im}\left(\chi^{(1)}(\omega_p)\right) = -\,\beta\,\frac{\left[4\,\mathcal{A}\,\gamma_{21} + \gamma_{31}\,\Omega_C^2\right]}{16\,\mathcal{A}\,\mathcal{C} - 8\,\mathcal{B}\,\Omega_C^2 + \Omega_C^4}\end{aligned}\ , \tag{1.46}$$

and

$$\begin{aligned}\mathcal{A} &= \gamma_{31}^2 + (\Delta_C+\Delta_P)^2\\ \mathcal{B} &= \Delta_P\,(\Delta_C+\Delta_P) - \gamma_{21}\,\gamma_{31}\\ \mathcal{C} &= \gamma_{21}^2 + \Delta_P^2\end{aligned}$$

These components are related by the *Kramers-Kronig relations* [63].

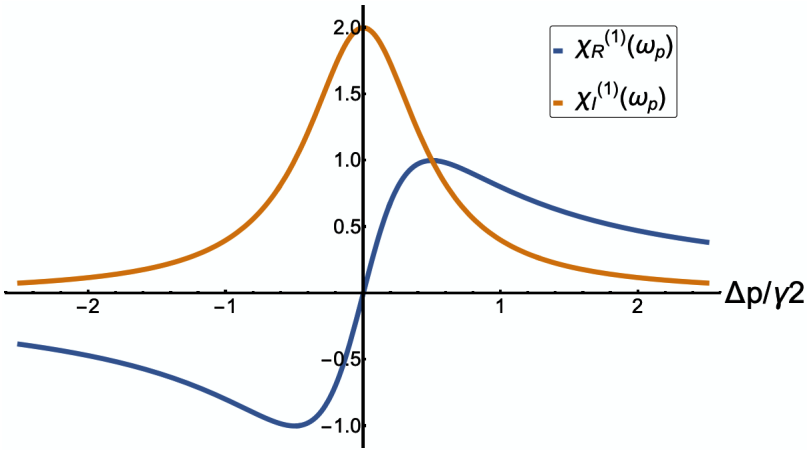

FIGURE 1.2: Plots of the real(blue) and imaginary (orange) parts of the complex linear susceptibility as functions of probe detuning from resonance when the coupling beam is switched off, i.e. $\Omega_C = 0$. In the plots, $\Omega_P = 0.5\gamma_2$. These are equivalent to the absorption and dispersion features of an initial two-level system.

A combined plot of the real and imaginary parts of the susceptibility as a function of the probe laser detuning is given in figure 1.2 for an inactive control laser. The

natural linewidth of the $|2\rangle \rightarrow |1\rangle$ given by the decay rate γ_2 is used as a scaling factor of the probe detuning. The plots show that the real part of this susceptibility corresponds to the dispersive properties of the field, whereas the imaginary part gives the spectroscopic features like the probe absorption as given by the typical Lorentzian absorption peak. Full absorption of the probe beam is seen at resonance where the dispersion crosses zero. Also, the susceptibility has been simplified in such a way that β have been normalised to 1.

In the case when the coupling beam is switched on, the standard thing to do is to consider that one of the laser beams is tuned to resonance while the other is scanned across resonance. Take the case where the coupling beam is tuned to resonance $\Delta_C = 0$ while the probe beam is allowed to scan across resonance[1]. Figure 1.3 shows the components of the susceptibility for increasing coupling beam strength with little or no decoherence in the system. As shown for the imaginary component (upper figure), a drastic reduction in the probe absorption occurs at resonance as soon as the coupling beam is switched on due to the transparency of atoms to the probe beam. The dip causes a splitting of the initial zero-coupling strength probe absorption into two absorption resonance peaks of equal amplitude known as the *Autler-Townes doublets*. The separation between the peaks is equivalent to the Rabi frequency of the coupling laser since these absorption resonances occur at $\Delta_P = \pm\frac{\Omega_C}{2}$. Stronger coupling increases the width of the transparency dip. One would expect the absorption resonance peaks to merge as Ω_C becomes small, however, a sharp and narrow transmission window would remain so long $\Omega_C \neq 0$.

The onset of the transparency dip also has a drastic effect on the dispersion as shown for the real component in figure 1.3 (lower figure), thus confirming the claim of the Kramers-Kronig relations. Firstly, the coupling laser can be seen to switch the dispersion curve slope from positive to negative. Secondly, it causes an initially high dispersion steepness at resonance. The dispersion then becomes gradually less steep as the coupling beam strength increases.

Increasing the decay rate γ_3 of state $|3\rangle$ does not just correspond to lowering the energy level of the state $|3\rangle$ of the atoms, it also corresponds to increasing the decoherence between the states $|3\rangle$ and $|1\rangle$. As shown in figure 1.4, increasing γ_3 causes a gradual overlapping of the resonance absorption peaks till the transparency dip disappears while the probe absorption increases to maximum. Since atoms from $|3\rangle$ decay

[1] The reverse case will be considered in subsequent chapters

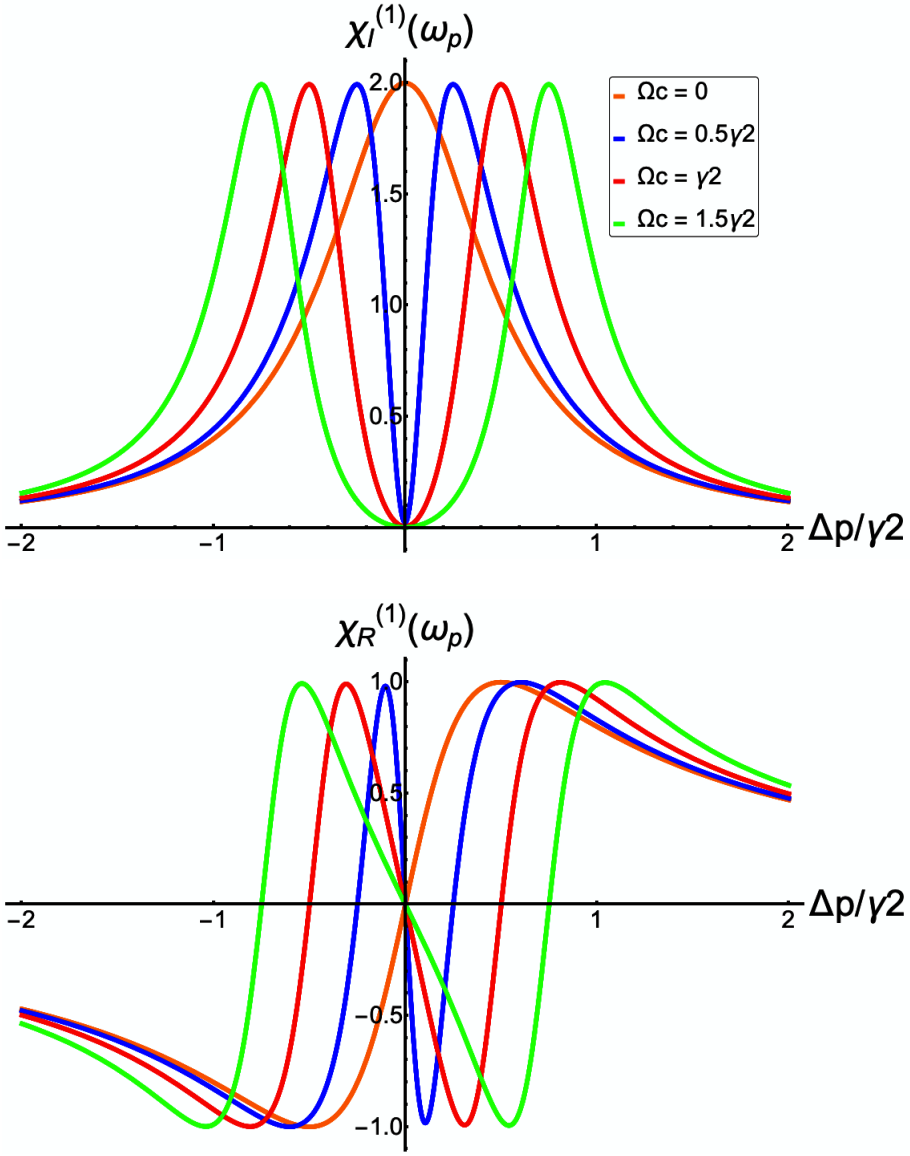

FIGURE 1.3: The imaginary (upper) and real(lower) parts of the complex linear susceptibility as functions of probe detuning from resonance for increasing coupling beam strength. In the plots, $\Omega_P = 0.5\gamma_2$ and $\gamma_3 = 0.003\gamma_2$ while $\Omega_C = 0$ (orange), $0.5\gamma_2$ (blue), γ_2 (red) and $1.5\gamma_2$ (green). Transparency of the probe beam is seen at resonance.

to both states $|1\rangle$ and $|2\rangle$, increasing γ_3 means that the state $|2\rangle$ becomes more populated. As initially stated, the finite linewidths of the lasers modify the dephasing rates of off-diagonal coherence terms of states that are laser-coupled. Taking non-zero laser linewidths further increases the decay rate γ_{31}, thus causing similar laser-induced dephasing effects as shown in figure 1.4. Increasing the probe laser linewidth (as shown in figure 1.5) reduces the probe absorption amplitude while the width of the transparency dip remains the same. However, at high laser linewidths, the probe absorption vanishes. It is important to state that extreme cases $\gamma_{2d} = \gamma_2$, $10\gamma_2$ and $10^3\gamma_2$ are only conceptualised. Ideally, accessing possible and allowable energy levels within the

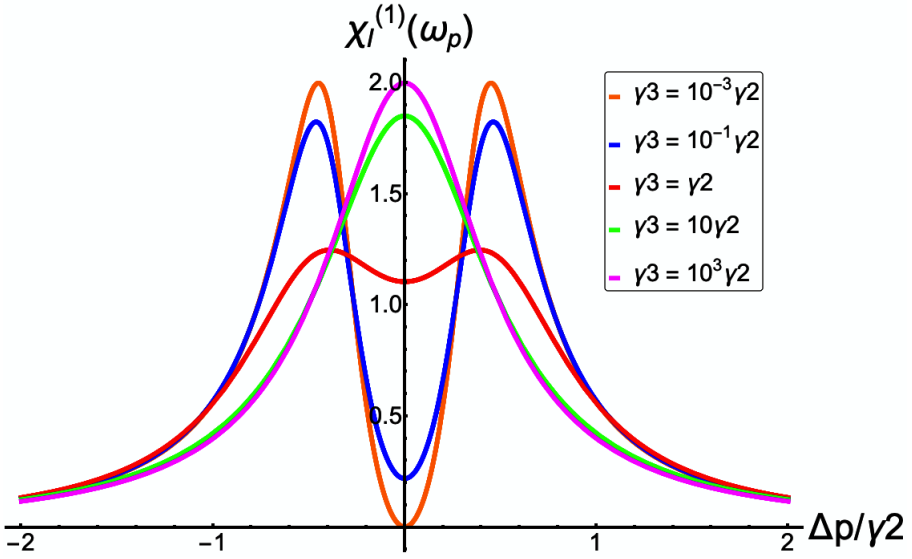

FIGURE 1.4: The imaginary part of the complex linear susceptibility as a function of probe detuning from resonance for increasing upper level decay rate. In the plots, $\Omega_P = 0.5\gamma_2$ and $\Omega_C = 0.9\gamma_2$ while $\gamma_{2d} = 10^{-3}\gamma_2$ (orange), $10^{-1}\gamma_2$ (blue), γ_2 (red), $10\gamma_2$ (green) and $10^3\gamma_2$ (magenta). Transparency of the probe beam at resonance decreases as the decay rates increases.

atom structure requires tunable laser systems that produce very stable and coherent monochromatic narrow-linewidth light such that $\gamma_{2d} \ll \gamma_2$.

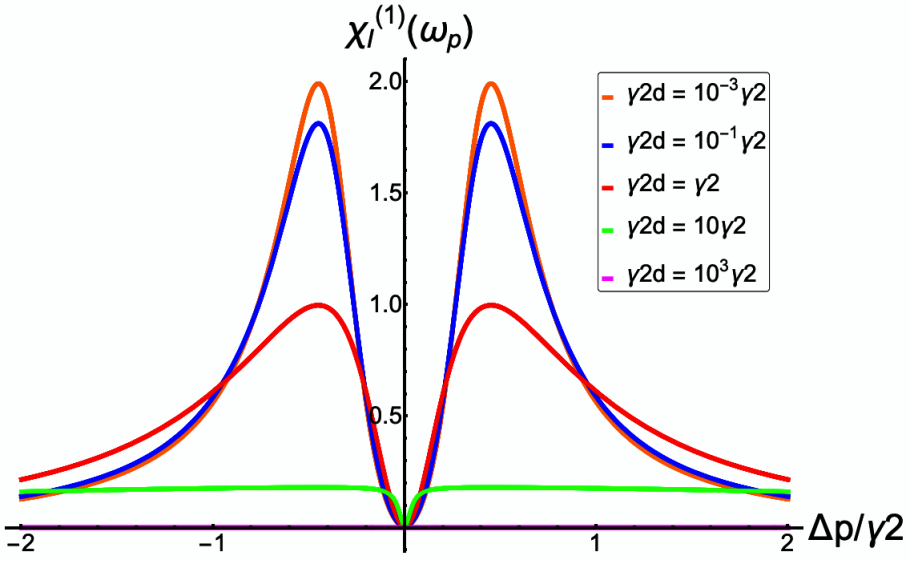

FIGURE 1.5: The imaginary part of the complex linear susceptibility as a function of probe detuning from resonance for increasing probe beam linewidth. In the plots, $\Omega_P = 0.5\gamma_2$ and $\Omega_C = 0.9\gamma_2$ while $\gamma_{2d} = 10^{-3}\gamma_2$ (orange), $10^{-1}\gamma_2$ (blue), γ_2 (red) $10\gamma_2$ (green) and $10^3\gamma_2$ (magenta). The width of the transparency dip at resonance remains as long as there is probe absorption.

The above qualitative predictions were done for the coupling beam tuned to resonance,

$\Delta_C = 0$. As shown in figure 1.6, varying the coupling beam detuning causes the resonance transparency dip to shift within the probe absorption profile. As a result, the resonance moves to a non-zero value of the detuning where the control beam detuning matches that of the probe beam. For non-zero probe detuning, the lineshapes also change drastically causing two different and asymmetric absorption peaks: a secondary absorption around $\Delta_P = \pm\Delta_C$ and a primary absorption around $\Delta_P \simeq 0$ [59]. The amplitudes of these peaks are no longer necessarily equal. Also, the peaks separation becomes larger with increasing magnitude of the detuning. In the weak probe limit, the separation is characterised by the generalised form [64]

$$\Omega_C \longrightarrow \Omega'_C = \sqrt{\Omega_C^2 + \Delta_C^2}\,. \tag{1.47}$$

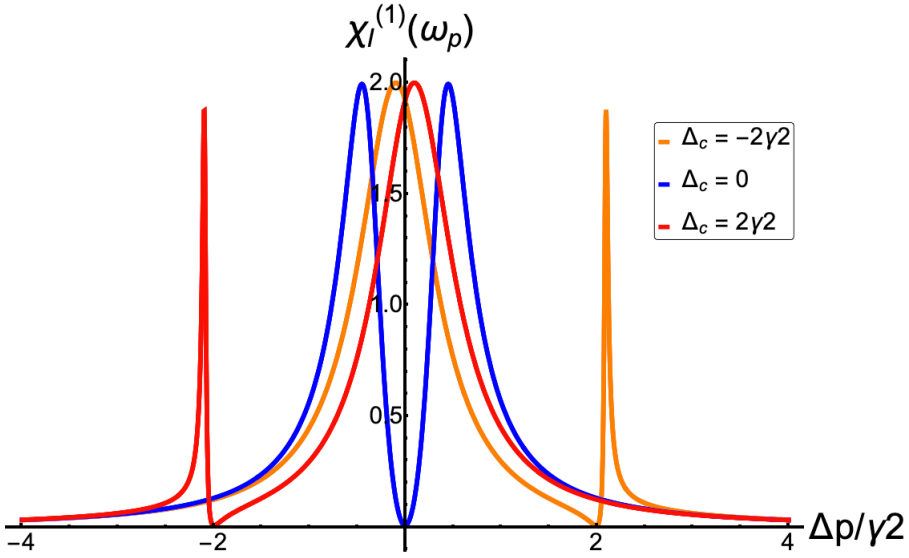

FIGURE 1.6: The imaginary part of the complex linear susceptibility as a function of probe detuning from resonance for varying coupling beam detuning. In the plots, $\Omega_P = 0.5\gamma_2$ and $\Omega_C = 0.9\gamma_2$ while $\Delta_C = -2\gamma_2$ (orange), 0 (blue) and $2\gamma_2$ (red). The transparency dip is shifted to the value of the detuning.

It must be emphasized that all the results discussed above were done for Doppler-free conditions where atoms are assumed to be stationary. Typically in atomic systems, e.g. atoms in a vapour cell, atoms travel at a range of velocities given by the Maxwell-Boltzmann velocity distribution. Thus, they tend to experience Doppler-shifted frequency when irradiated with a light field (see section 4.4.2). There is an exception in trapped atom systems where thermal motions are negligible and Doppler-free conditions suffice. Also, an atomic system is not usually a single-body system as treated in this chapter, but a many-body system. The many-body extension is treated in chapter 4 as the evolution of highly-excited interacting Rydberg atoms is studied. An important

focus in the study of two-photon transitions is the effects of coherent processes that occur as a result of the interaction of the Rydberg excitation lasers with the atoms. The next section highlights the optical coherent phenomena of interest.

1.5 Distinguishing Quantum Interference Phenomena

In the absence of the coupling field, there exist only a single first-order direct $|1\rangle \rightarrow |2\rangle$ excitation pathway (see figure 1.7(a)). However, if the coupling beam is switched on in the weak probe limit, there exist a resulting three-photon $|1\rangle \rightarrow |2\rangle \rightarrow |3\rangle \rightarrow |2\rangle$ excitation pathway which involves a conventional two-excitation process and subsequent remission of the coupling beam (see figure 1.7(b)). Coherent processes that occur during two-photon excitation are due to quantum interference between these alternate $|1\rangle \rightarrow |2\rangle$ excitation pathways. Owing to the relative strengths of the coupling and probe fields, these interferences are classified as either constructive or destructive. The phenomenologically similar but naturally distinct, interference phenomena of interest are electromagnetically induced transparency (EIT) [13, 65, 66], coherent population trapping (CPT) [67, 68, 69], and Autler-Townes splitting (ATS) [70]. EIT is said to be achieved by Fano interference between two atomic transitions or two closely spaced lifetime-broadened resonances that are decaying to the same continuum [71]. In the absence of Fano interference, EIT is simply ATS, equivalent to the linear AC-Stark effect, which corresponds to a doublet structure in atomic-absorption profile requiring strong pumping [70, 72]. CPT is said to occur as the reduction in spontaneous emission as a result of the trapping of the population in non-coupled states [73]. The most popular mechanism for achieving these interference states is via continuous-wave Raman optical pumping. An alternative mechanism is by using stimulated Raman adiabatic passage (STIRAP) pulses [74].

EIT and CPT have been associated with the destructive interference of excitation pathways [15] via the $|1\rangle \leftrightarrow |3\rangle$ atomic coherence established by the coupling field. On the other hand, the investigation done in [73] showed that ATS is associated to the constructive interference of excitation pathways. The contrasts between these three phenomena are described in the following sections using various factors such as the powers of the laser beams, dark and dressed state formalism [65, 75] and the comparison between the transparency linewidth and the relevant natural linewidth [76, 77, 78, 79]. Ultimately, the regimes of the three-level coherent phenomena will be described here, as well as much of the studies done in this thesis, in terms of the

powers of the beams. This is because other factors are resulting consequences of the set powers of the beams.

1.5.1 Powers of the beams

Ultimately, the most consistent way to differentiate the EIT, ATS and CPT regimes is via the strengths of the two-photon transition lasers. EIT occurs in the weak coupling regime, $\Omega_P < \Omega_C \lesssim \gamma_2$ while ATS occurs in the strong-coupling regime, $\Omega_P < \Omega_C > \gamma_2$ [15, 76]. In contrast to EIT and ATS, the probe beam is of high importance in the CPT regime, as it is studied in the strong probe regime, $\Omega_P > \Omega_C$ [36, 77]. In [15], EIT and ATS regimes were distinguished using a threshold factor, $T_v = \frac{\Omega_C}{\gamma_p}$. $\gamma_p \simeq \gamma_2$ being the configuration-dependent threshold polarisation decay rates, obtained by using the results of scattering theory to split the probe absorption coefficient of specific three-level systems into two absorption resonance profiles (see appendix B). The threshold is the value of Ω_C separating the weak and strong coupling regimes.

It is important to state that instead of the widely accepted low probe limit $\Omega_P \ll \Omega_C$ EIT condition, the condition $\Omega_P \lesssim \Omega_C$ is considered because there is a possibility of having a considerably high probe while still in the EIT regime. In this case, an additional but stronger condition of $\Omega \lesssim \gamma_2$ and $\Omega > \gamma_2$ where $\Omega = \sqrt{\Omega_P^2 + \Omega_C^2}$ is the generalised Rabi frequency, is considered for the EIT and ATS regimes respectively.

The transition from the EIT/ATS $\Omega_P \leq \Omega_C$ regime to the CPT $\Omega_C < \Omega_P$ regime implies that one is making a transition from the weak probe limit to the strong probe limit. In the strong probe beam regime, the set of OBEs from equation (1.28) becomes more difficult to solve analytically but instead would be solved numerically. The OBEs were solved numerically in [64] with the simplifying assumption that the system is closed. This requirement is not necessary for the weak probe limit since optical pumping effects are negligible. An iterative solution of the probe absorption obtained in the absence of collisional dephasing for resonant strong probe and coupling fields reads [64]

$$\rho_{21} = -\frac{i\Omega_P}{2\gamma_{21}}\left[1 - \frac{\Omega_C^2}{4\gamma_{21}\gamma_3} - \frac{\Omega_P^2}{\gamma_2\gamma_{21}} + \frac{\Omega_P^2\Omega_C^2}{2\gamma_2\gamma_{21}^2\gamma_3}\right] . \tag{1.48}$$

This implies that as an extension to the weak probe limit, allowing the probe beam to be stronger opens higher-order multi-photon $|1\rangle \rightarrow |2\rangle$ excitation pathways. This is shown in figure 1.7. The first term in equation (1.48) denotes the linear probe absorption which is described by the single probe $|1\rangle \rightarrow |2\rangle$ transition in figure 1.7(a). The

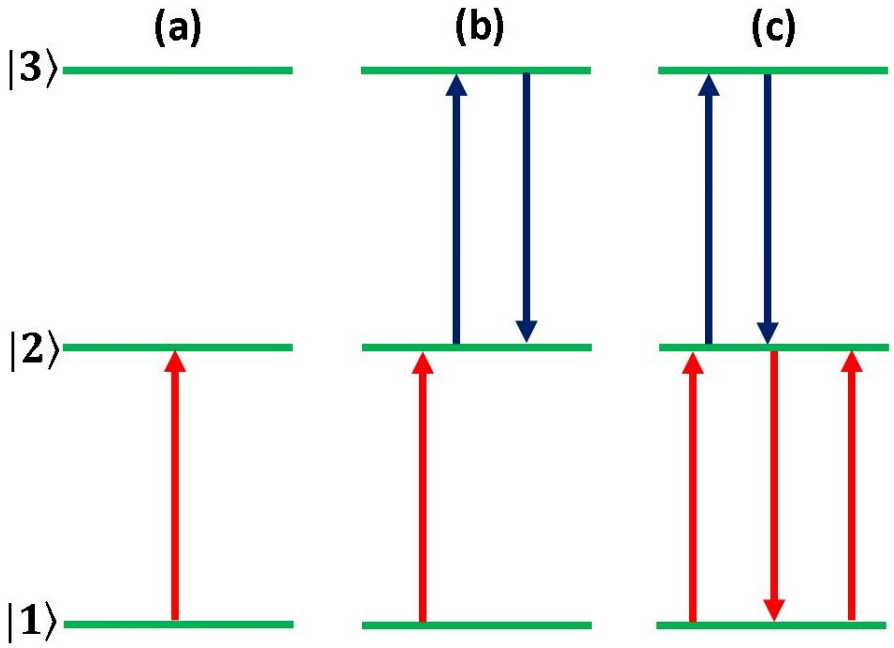

FIGURE 1.7: Various excitation pathways for the $|1\rangle \rightarrow |2\rangle$ transition: **(a)** for $\Omega_C = 0$, there is only a direct $|1\rangle \rightarrow |2\rangle$ excitation pathway; **(b)** for $\Omega_C \neq 0$ and $\Omega_P \ll \Omega_C$, a resulting three-photon $|1\rangle \rightarrow |2\rangle \rightarrow |3\rangle \rightarrow |2\rangle$ excitation pathway opens; **(c)** when $\Omega_C \neq 0$ and $\Omega_P \approx \Omega_C$ or $\Omega_P > \Omega_C$, more multi-photon pathways appears.

second term describes the three-photon pathway in figure 1.7(b). It gives the lowest order term in the coupling field and also the limit of the weak probe regime. The sign shows that it interferes destructively with the linear absorption term. The fourth term describes the five-photon pathway, shown in figure 1.7(c), involving three probe-driven and two coupling-driven transitions. This five-photon pathway and higher-order multi-photon transitions interfere with the single- and three-photon transitions. The third term, independent of the control field, is said to be associated with saturated absorption.

Further observation in [64] is that the increasing importance of higher-order multi-photon pathways result in the deterioration of induced transparency and lead to induced absorption. As it will be verified in this study, it is essential to note that unlike in the weak probe limit, the optical properties of the system gradually become less dependent on the control field strength and more dependent on the probe field strength as it increases and transitions from the EIT to ATS to CPT regimes are made.

As a consequence of the set powers of the beams, various resulting parameters can also be used to illustrate and distinguish the EIT, ATS and CPT regimes. One way is by studying the variation of the dressed or dark state population depending on the

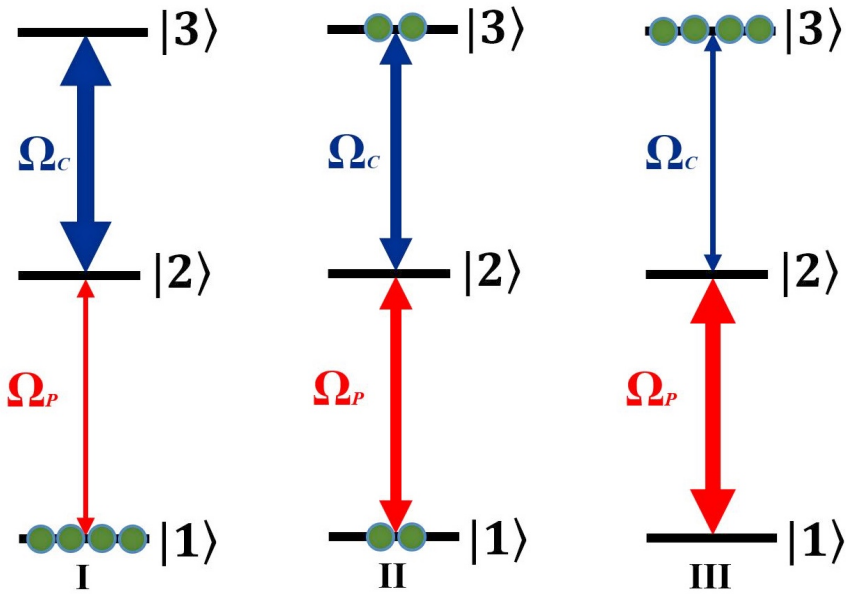

FIGURE 1.8: Variation of the dark state population depending on the probe and coupling beam strengths. (I) Weak probe limit $\Omega_P \ll \Omega_C$ where a majority of the atom population resides in the ground state, (II) Beyond the weak probe limit $\Omega_P = \Omega_C$ where there is atom population transfer into the higher excited state and (III) Very high probe regime $\Omega_P \gg \Omega_C$ where the higher excited state dominates the dark state.

probe and coupling beam strengths. The dressed states are linear superpositions of the unperturbed or bare states $|1\rangle$, $|2\rangle$ and $|3\rangle$, of the atom and are eigenstates of Hamiltonian $\mathcal{H}_3$ [65, 75]. On two-photon resonance, the system evolves into the dark state

$$|D\rangle = -\frac{\Omega_C}{\sqrt{\Omega_P^2 + \Omega_C^2}}|1\rangle + \frac{\Omega_P}{\sqrt{\Omega_P^2 + \Omega_C^2}}|3\rangle \tag{1.49}$$

which does not include any contribution from $|2\rangle$. This implies that any population of atoms prepared in $|D\rangle$ is coherently trapped in states $|1\rangle$ or $|3\rangle$ over time with no probability of excitation into the intermediate state while further spontaneous emission is suppressed. As shown in figure 1.8(I), in the weak probe limit $\Omega_P \ll \Omega_C$, then $|D\rangle \rightarrow |D'\rangle = -|1\rangle$. This implies that most of the population resides in the ground state. This is because the state $|1\rangle$ evolves into a dark state, from which there would be no excitation when the probe beam is slowly turned on, and then it is decoupled from other states [80]. The dark state is maximally coherent when $\Omega_C = \Omega_P$ (shown in figure 1.8(II)) [75]. With a further increment of the probe beam strength, such that $\Omega_P \gg \Omega_C$,

$$|D\rangle \rightarrow |D'\rangle = |3\rangle\ , \tag{1.50}$$

majority of the atoms are coherently transferred into the state $|3\rangle$ (shown in figure 1.8(III). As will be shown in chapter 4 in the study of many-body atomic systems

in highly excited Rydberg states, the effect of Rydberg-Rydberg interactions on the atomic excitation dynamics are significantly visible in the large probe regime.

Another consequence of the set powers of the beams is the effect on transparency linewidth. The comparison of the transparency linewidth to the natural linewidth of the intermediate state, which is $\gamma_2 = 6.065$ MHz for ^{87}Rb D2 narrow line, is considered a means to distinguish the EIT, ATS and CPT regimes. The transparency linewidth is given by the full width at half maximum of the transparency window. Results show that EIT features are *subnatural* (i.e., the linewidth is narrower than $\gamma_2 = 6.065$ MHz). As would be shown in section 4.2.4, since the natural linewidth does not contribute to the broadening of the transparency peak (see equation (1.49)), thus there is a possibility of having either subnatural or non-subnatural transparency linewidths in the ATS/CPT regime depending on the relative strengths of the Rydberg excitation lasers.

Summary

This chapter has given the basic description of light-atom interaction. By finding the solution of the OBEs, a generic understanding of the behaviour of a multilevel atom when laser fields perturb its free evolution is provided. This serves as a basis for understanding the evolution of a large number of interacting or non-interacting atoms within a gas cloud. Also, the description done in this chapter considered only the weak probe limit. As the probe power increases, atoms are not just excited to the Rydberg states, but higher-order excitation pathways are opened. It is therefore necessary to consider the effects of strong Rydberg-Rydberg interactions. This extension will be covered in chapter 4 of this thesis.

As seen in this chapter, the ladder configuration of the two-photon transition helps to probe high lying Rydberg states of the atoms. The Rydberg states appear to have interesting properties and produce phenomena that serve as useful tools in diverse areas such as in the implementation of quantum gates for quantum computation and information processing. Understanding the three-level atomic coherent phenomena during two-photon excitation serves as an essential factor in understanding the preparation of an atomic ensemble to study Rydberg-based phenomena. The next chapter will present the physics of Rydberg atoms and the influence of different Rydberg-Rydberg interactions.

2 Rydberg Atoms and Rydberg interactions

In recent times, the state-dependent properties, dynamics and controllable interactions of Rydberg atoms have been a key subject of research in various scientific disciplines such as quantum computation and information processing as well as cold atoms physics [51, 81, 82], astrophysics [83], quantum chaos [84] and quantum many-body physics [85] to mention but a few. Ultracold Rydberg atoms are exceptionally interesting as a platform for quantum computing, as they offer long coherence times and there are well-established techniques for trapping and cooling atoms.

This chapter gives an overview of the basic physical properties of Rydberg atoms with focus on highly excited alkali atoms. The types of space-dependent interactions between the Rydberg atoms are presented, with the aim of distinguishing the regimes where these interactions are dominant. The chapter then describes the Rydberg blockade effect which is the consequence of the Rydberg-Rydberg interactions and how this effect can be exploited in the creation of entanglement between atoms. Finally, a review of some of the applications of Rydberg atoms and Rydberg interactions is presented, including proposals for quantum gates based on the interaction between a single atoms and an ensemble of atoms.

2.1 Properties of Rydberg Atoms

Rydberg atoms are highly excited atoms having at least one outer electron in an energy level with high principal quantum number, $n \gg 1$, but not ionised. They can be obtained from ground state atoms via charge exchange or electron impact excitation [86, 87], via two-photon or multi-photon excitation processes [88, 89, 90] or a combination of collisional and optical excitation, which can either be state-selective or not [91]. The Rydberg levels have been found to have practical and distinctive properties. The orbital radius ($\propto n^2$) of these atoms are orders of magnitude larger than the orbital (Bohr) radius a_0 of the ground state of Hydrogen atom. Thus, Rydberg atoms have significantly large transition electric dipole moments ($\propto n^2$). As a

result, they have enhanced electrical polarisabilities ($\propto n^7$) and therefore extreme sensitivities to external electric field, even to weak electric field produced by nearby atoms.

Rydberg atoms also have some important properties that depend crucially on the value of the principal quantum number, such as long radiative lifetimes ($\propto n^3$), simple level structures and geometric cross section ($\propto n^4$) [91, 92, 93, 94]. Despite their radiative stability, the lifetimes of Rydberg states are limited by the energy level spacing ($\propto n^{-3}$) between them. This is due to the inter-level transitions that are induced by interaction with blackbody radiation [91, 95].

Considering the case of alkali atoms, similar to Hydrogen atoms, they have a single valence electron orbiting a positively charged core, with the potential at long range described by the $-\frac{1}{r}$ Coulomb law. For an alkali Rydberg atom, the nucleus with Z protons is effectively shielded by $Z-1$ core electrons so that the valence electron, which is further away from the nucleus, experiences $Z_{\text{eff}} = +1$ nuclear charge and an effective Coulomb potential. This is the *shielding effect*. Giving their structure, an alkali Rydberg atom can be treated as a hydrogen atom and hydrogenic approximations tend to suffice. Bohr's model of the atom, or more accurately the Schrödinger equation, can be conveniently used to extract the parameters (some of which have been mentioned earlier) that determine the behaviour of the atom.

For low orbital angular momentum, the orbit of the valence electron is highly elliptical. This creates a possibility for the valence electron to penetrate the closed electron shells. Thus, the valence electron is exposed to an unscreened nuclear charge. The interaction between the valence electron and the inner electrons causes the polarisation of the inner electron shells. As a result of these, the binding energy E_B of a low l-Rydberg state is increased relative to equivalent hydrogenic states. The atomic binding energy E_B and valence electron orbital radius r for a principal quantum number n and orbital angular momentum quantum number l read [93]

$$E_B^{(\text{Hyd})} = -\frac{\text{Ry}}{n^2} \quad \longmapsto \quad E_B^{(\text{Ry})} = -\frac{\text{Ry}}{n^{*2}}\,, \tag{2.1}$$

$$r^{(\text{Hyd})} = \frac{4\pi\epsilon_0\hbar^2 n^2}{Ze^2 m_e} \quad \longmapsto \quad r^{(\text{Ry})} = \frac{4\pi\epsilon_0\hbar^2 n^{*2}}{Ze^2 m_e}, \tag{2.2}$$

where Z, e, m_e and $\hbar$ are the atomic number, electronic charge, electron mass and Planck's constant respectively. $n^* = n - \delta_{nl}$ is the effective principal quantum number, Ry $\approx$ 13.6 eV is the Rydberg constant and δ_{nl} is the quantum defect which is a correction factor and a measure of deviation from the Hydrogen model. δ_{nl} mainly

depends on the angular momentum quantum number such that δ_l decreases as l increases since it corresponds to valence electron orbitals with little overlap with core electron orbitals. In fact, for $l > 3$, $\delta_l \approx 0$ and the core potential is purely Coulombic. These are the *hydrogenic states*, which are degenerate for a given n. However, the quantum defect is slightly dependent on n which allows the values of δ_{nl} to be used for states of same l but different n. This dependence can be obtained by the so-called *Rydberg-Ritz formula* given by

$$\delta_{nl} = \sum_{i=0}^{\infty} \frac{\delta_{(2i)}}{(n-\delta_0)^{2i}} \,, \tag{2.3}$$

where the coefficients $\delta_{(2i)}$ are obtained empirically from spectroscopic measurements [96, 97].

2.2 Rydberg-Rydberg interactions

Contrary to the ideal gas model, atoms interact with one another as a result of the forces arising from the Coulomb interactions between their dipoles, although this is negligible for neutral atoms, even for those that are separated by small interatomic distances. Generally, ground state neutral atoms do not possess permanent dipole moments but they can obtain a temporary dipole moment due to the redistribution of the electrons within the orbitals. These dipoles can interact with neighbouring dipoles or even induce dipole moments in neighbouring atoms. On the other hand, Rydberg atoms have time-varying temporary dipole moments in the absence of an external electric field. Taking advantage of their large polarisabilities and extreme sensitivity to external electric field, they acquire permanent dipole moments in the presence of an extremely weak electric field which may be produced by neighbouring atoms. This enables them to interact strongly via *van der Waals* or *dipole-dipole interactions* [93].

As shown in figure 2.1, when a pair of atoms in a specific Rydberg state interact, they form a molecular state which is dipole coupled to all nearby molecular states with asymptotic energy difference δE. Due to the interaction, one of the atoms gaining energy which excites it to a higher Rydberg excitation level while the other atom losses energy to reside in a lower Rydberg excitation level. Although now in different energy levels, they still interact to form a molecular state whose energy center is δE away from and coupled to the initial molecular state. However, the dominant couplings are the strong ones to the energetically nearby molecular states that are at asymptotic energy difference $\delta\omega$ away, the *Förster defect* [98]. The study will only focus on homonuclear dimers where both atoms are in the same state. Say a pair of Rydberg atoms are in

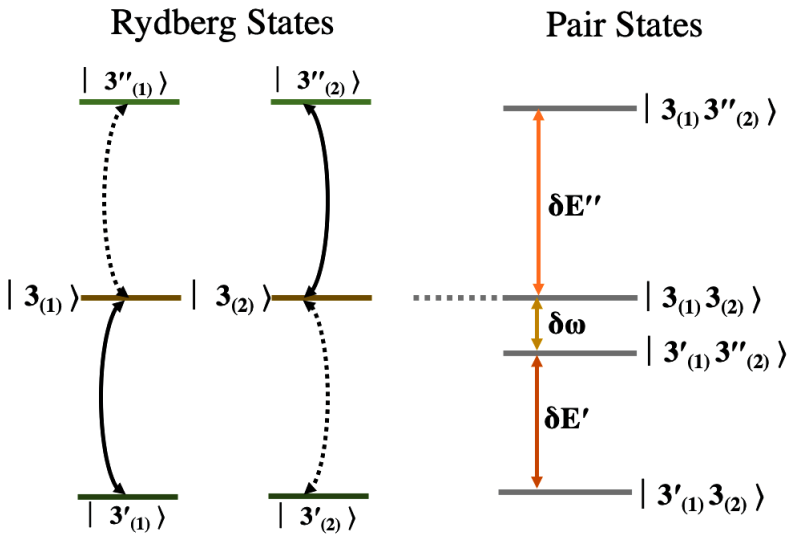

FIGURE 2.1: Single atom states (left) and pair states (right) for the description of interactions between atoms having three Rydberg states $|3\rangle$, $|3'\rangle$ and $|3''\rangle$

states $|3_{(1)}\rangle$ and $|3_{(2)}\rangle$ at distance $R = r_{12}$, the electronic energy shift experienced as a result of an induced dipole coupling $\mathbb{V}_{jk} = \frac{\mu_{3_{(1)}3_{(2)}}\mu_{3'_{(1)}3''_{(2)}}}{r_{12}^3} = \frac{C(n)}{r_{12}^3}$ to energetically nearby pair $|3'_{(1)}\rangle$ and $|3''_{(2)}\rangle$ is given by eigenvalues of the two-state Hamiltonian

$$\mathcal{H}_{RR} = \begin{bmatrix} 0 & \mathbb{V}_{jk} \\ \mathbb{V}_{jk} & \delta\omega \end{bmatrix} \tag{2.4}$$

obtained from the transition between the molecular Rydberg state. $\mu_{3_{(1)}3_{(2)}}$ and $\mu_{3'_{(1)}3''_{(2)}}$ are the dipole matrix elements of the respective transition. $C(n)$ is the state-dependent interaction coefficient and energy defect is given by

$$\delta\omega = \mathcal{E}_{|3'_{(1)}\rangle} + \mathcal{E}_{|3''_{(2)}\rangle} - 2\,\mathcal{E}_{|3_{(1)}\rangle}\ , \tag{2.5}$$

since energy $\mathcal{E}_{|3_{(1)}\rangle} = \mathcal{E}_{|3_{(2)}\rangle}$. The interaction potential produced is given by the eigenvalues of the Hamiltonian in equation (2.4) as

$$\mathbb{V} = \frac{1}{2}\left(\delta\omega \pm \sqrt{\delta\omega^2 + 4\,\mathbb{V}_{jk}^2}\right)\ . \tag{2.6}$$

The values for the $C(n)$ interaction coefficients and energy defects $\delta\omega$ have been calculated for $20 \leq n \leq 60$ using the results from D'yachkov and Pankratov's calculation [99]. The energy defects of some relevant dipole coupling between pair states are shown in figures 2.2(a)-(b) as a function of n. One would see that some states usually appear to have opposite polarity to the ground 5S state, like all the $|n\mathrm{S}\ n\mathrm{S}\rangle$ pair state couplings with $\delta\omega < 0$ in figure 2.2(a) thus resulting in repulsive interactions between

the atoms. As shown in figure 2.2(b), the couplings of the $|n\mathrm{D}\ n\mathrm{D}\rangle$ pair states to the $|(n+2)\mathrm{P}\ (n-2)\mathrm{F}\rangle$ states change sign at some large n, typically $n \geq 44$. Thus, changing from repulsive to attractive interactions. On the other hand, the couplings of the $|n\mathrm{D}\ n\mathrm{D}\rangle$ pair states to the $|(n+1)\mathrm{P}\ (n-1)\mathrm{F}\rangle$ states generally yield attractive interactions. This thesis will consider only nS Rydberg states in order to avoid anisotropic interactions encountered in some of the nD states. The nD states will only be considered for non-interacting cases.

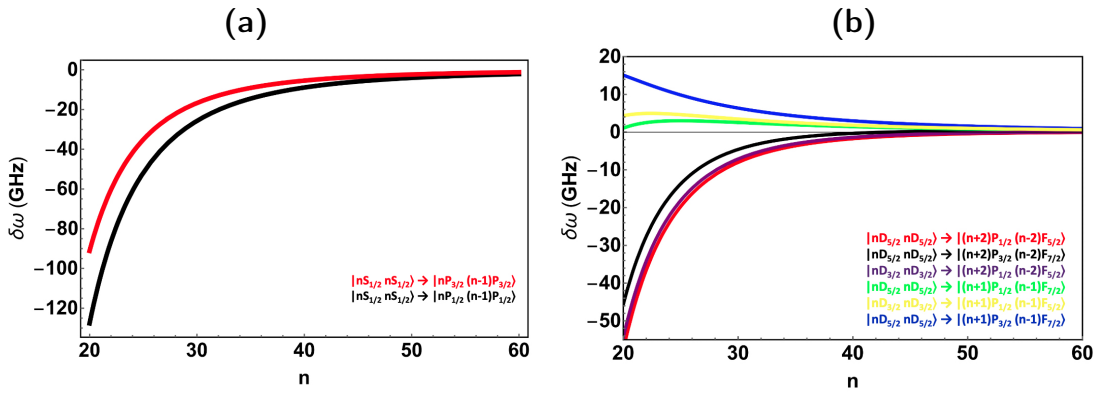

FIGURE 2.2: Energy defect between coupling pair states for Rubidium atoms. **(a)** $|n\mathrm{S}\ n\mathrm{S}\rangle$ pair states have $\delta\omega < 0$ for all possible couplings which result in repulsive interactions; **(b)** Some of the possible couplings for $|n\mathrm{D}\ n\mathrm{D}\rangle$ pair states with couplings to $|(n+2)\mathrm{P}\ (n-2)\mathrm{F}\rangle$ having attractive interactions for high lying Rydberg states

From equation (2.6), the absolute value of the energy defect can be used to distinguish two regimes of Rydberg interaction. First, in the regime where energy difference between coupling molecular states is large, i.e $\delta\omega > \mathbb{V}_{jk}$, so that the interaction potential takes the form

$$\mathbb{V} \approx \pm\frac{1}{\delta\omega}\left(\frac{\mu_{3_{(1)}3_{(2)}}\mu_{3'_{(1)}3''_{(2)}}}{r_{12}^3}\right)^2 = \frac{C_6(n)}{r_{12}^6}\,. \tag{2.7}$$

where $C_6(n) = \pm\frac{C(n)^2}{\delta\omega}$. In this regime, the interaction is a van der Waals interaction scaling as r_{12}^{-6}. From the dominant term in equation (2.7), using $\mu_{3_{(1)}3_{(2)}}\mu_{3'_{(1)}3''_{(2)}} \approx n^4$ and $\delta\omega \approx n^{-3}$, the n^{11} scaling of van der Waals interaction is recovered. The sign of the detuning determines whether the interaction is attractive or repulsive. To put it simply, the van der Waals interaction is only valid for $\frac{C(n)}{r_{12}^3} < \delta\omega$ which results in $r_{12} > r_{\mathrm{CoD}} = \left(\frac{C(n)}{\delta\omega}\right)^{\frac{1}{3}}$. r_{CoD} is the crossover distance which is the interatomic distance threshold when a transition from the van der Waals interaction regime to another interaction regime, i.e. the resonant dipole-dipole interaction, occurs. This is plotted in figure 2.3 as a function of n for $|n\mathrm{S}_{\frac{1}{2}}\ n\mathrm{S}_{\frac{1}{2}}\rangle \rightarrow |(n-1)\mathrm{P}_{\frac{3}{2}}\ n\mathrm{P}_{\frac{3}{2}}\rangle$ coupling.

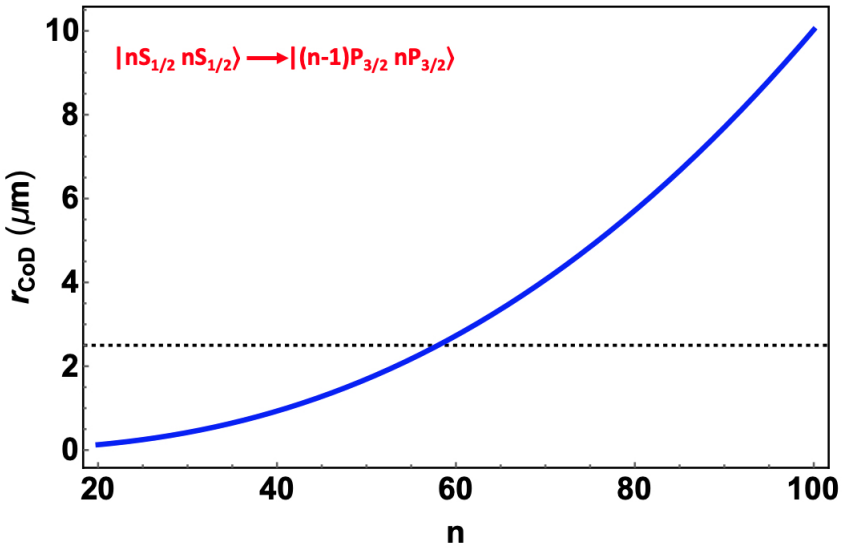

FIGURE 2.3: Plot of crossover distance as a function of r for various n which shows that crossover distance increases with n. Horizontal gridline described the average interatomic distance $\approx 2.5\,\mu$m in low density systems, $\approx 10^{10}$ cm^{-3}.

The dipole-dipole interaction is only valid for states where $\delta\omega$ is small, i.e. $\frac{C(n)}{r_{12}^3} > \delta\omega$, which results in $r_{12} < r_{\text{CoD}}$ while the interaction potential takes the form

$$\mathbb{V} \approx \pm\mathbb{V}_{jk} = \frac{C_3(n)}{r_{12}^3}\,, \tag{2.8}$$

where $C_3(n) = \pm C(n)$. Example of such states are $43\,\text{D}_{5/2}$, $58\,\text{D}_{3/2}$, $59\,\text{D}_{3/2}$ pair states which are almost resonant to the coupling pair states. Equation (2.8) shows that the resonant dipole-dipole interaction scales as n^4.

The log-log plot of the interaction potentials as a function of interatomic distance for $n = 20$, 35, 46, 55, 65 and $80\text{S}_{1/2}$ states plotted in figure 2.4 shows an increase of the interaction strength with n and also the transition from $\frac{1}{r^6}$-dependence to $\frac{1}{r^3}$-dependence at short range. For typical experiments with atom density of $\approx 10^{10}$ cm^{-3}, the average interatomic distance is $\approx 2.5\,\mu$m which corresponds to interactions in the van der Waals regime for $n \leq 60$. Subject to extreme scaling, Rydberg atoms may interact over macroscopic scales which leads to measurable mechanical forces [100].

As a result of different polarisabilities of the pair states, there is a possibility of applying an external electric field to reduce the energy defect between two pair states or bring them into degeneracy to give the *Stark-tuned Förster resonance*. Alternatively, the interaction strength can be increased substantially, without an electric field, by exciting

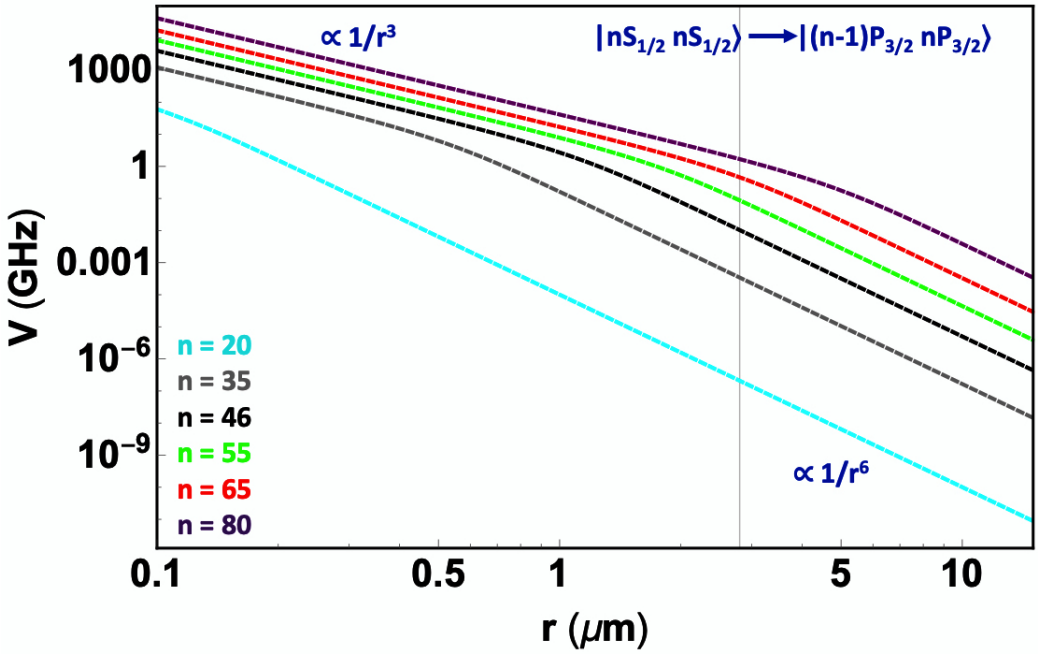

FIGURE 2.4: Plot of interaction strength as a function of r for various n which shows that interaction strength increases with n. It also shows the transition from $\frac{1}{r^6}$-dependence to $\frac{1}{r^3}$-dependence which becomes relevant in high density systems, $\approx 10^{10}$ cm^{-3}, for $n > 60$.

each atom to a different n for which there is a Förster resonance [101]. Around the Förster resonance, various angular momentum states mix while strongly anisotropic interactions can occur. The study done in this thesis will not consider states in the vicinity of Förster resonance.

2.3 Rydberg Blockade

An important consequence of the interactions between Rydberg atoms is the Rydberg blockade phenomenon. To explain this, consider an ensemble of N atoms with each atom having ground state $|g\rangle$ and Rydberg state $|r\rangle$ that can be coupled by laser beams with combined Rabi frequency Ω. Consider the first case of a non-interacting ensemble with atoms that are spatially separated by distance $R > R_b$, where R_b is the *blockade radius* (see figure 2.5). On irradiating these atoms by resonant lasers to a Rydberg level, a collective energy shift occurs such that all the atoms will be excited to the Rydberg state. However, in the regime where the atoms are sufficiently close together within a distance $R < R_b$, such as atoms in a microscopic optical dipole trap, and the interaction between them is sufficiently strong, the collective energy level is shifted from resonance by a value given in equation (2.6), and the simultaneous excitation of more than one Rydberg atom becomes impossible. The presence of a single excited Rydberg atom hinders the resonant excitation of surrounding atoms that

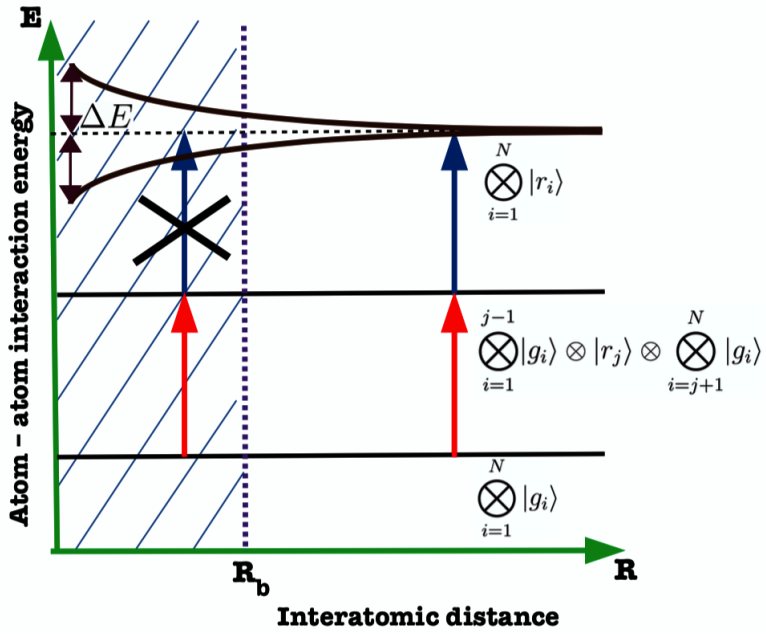

FIGURE 2.5: Dipole blockade within an ensemble of atoms. For interatomic distances $R < R_b$, simultaneous Rydberg excitation of more than one atom is blocked due to the energy level shift ΔE caused by strong Rydberg-Rydberg interactions.

are within its blockade radius R_b [1, 102]. To obtain R_b, one must note that dipole blockade occurs when the interaction shift is larger than the linewidth of the Rydberg state $\bigotimes_{i=1}^{N} |r_i\rangle$

$$\mathbb{V} > \hbar \times \max(\Omega, \gamma_r) \ , \tag{2.9}$$

where the linewidth of $\bigotimes_{i=1}^{N} |r_i\rangle$ state is determined by the larger between the natural linewidth γ_r and the combined Rabi frequency Ω. Typically, $\Omega \gg \gamma_r$ since the Rydberg states are long-lived. Hence, the blockade radius can be obtained from

$$\hbar\Omega = \mathbb{V} = f(R_b) \qquad \Longrightarrow \qquad R_b = f^{-1}(\hbar\Omega) \ . \tag{2.10}$$

This interaction-induced position-dependent blockade effect is reminiscent of the Coulomb blockade in solid-state tunnel junctions, where the charging energy of a quantum dot impedes its population by more than one electron [103]. It provides a generic mechanism for the conditional control of the evolution of quantum states. Such strongly coupled ensembles, taking advantage of the long radiative lifetimes ($\propto n^3$) of the Rydberg states, are ideally suited for the study of quantum many-body physics and quantum information processing. They can be used for implementing (fast) quantum gates [1, 2, 3], measurement and computational protocols [81, 104, 105, 106], collective encoding of multi-qubit registers [10, 102], improving the resolution of atomic

clocks [107, 108, 109], deterministic single-atom state and single photon source preparation [39, 40, 110, 111].

Dipole blockade was experimentally verified in [27, 28] for van der Waals interactions (or second-order dipole-dipole coupling) between ultracold Rydberg atoms to have significant effects of spectral broadening of resonance lines and suppression of excitation. This was done by measuring Rydberg atom density with increasing laser intensity and increasing interaction strength (given by an increasing atomic density or principal quantum number). In [32], blockade effect was confirmed to lead to the quenching of the probability distribution of Rydberg atom numbers.

As a result of the dipole blockade phenomenon, the interacting atoms end up in a shared entangled state containing only one Rydberg excitation which governs the creation of the *superatoms*:

$$|\Psi_0^{(N)}\rangle = |g_1, g_2, \cdots, g_N\rangle \longmapsto |\Psi_1^{(N)}\rangle = \frac{1}{\sqrt{N}} \sum_{i=1}^{N} |g_1, g_2, \cdots, r_i, g_{i+1}, \cdots, g_N\rangle , \tag{2.11}$$

It is important to state that N here is not usually the total number of atoms within the cloud but it is rather the number of atoms within a blockade sphere given by

$$N_b = \varrho_A \frac{4}{3}\pi R_b^3 . \tag{2.12}$$

where ϱ_A is the cloud density. Despite the single excitation constraint, this process of excitation leaves each atom with equal probability of excitation without distinguishing one atom from the other. Such operation is described by the laser excitation operator [4, 112]

$$\mathcal{U}_N = \frac{\hbar\Omega}{N} \sum_{i=1}^{N} \left(|g_1, g_2, \cdots, r_i, g_{i+1}, \cdots, g_N\rangle\langle g_1, g_2, \cdots, g_N| + \text{h.c} \right) . \tag{2.13}$$

In the blockade regime, the ground state atoms are sent into the entangled state via the transformation

$$|\Psi_0^{(N)}\rangle \quad \longmapsto \quad \mathcal{U}_N |\Psi_0^{(N)}\rangle = \frac{\hbar\Omega}{N} \sqrt{N} |\Psi_1^{(N)}\rangle . \tag{2.14}$$

This implies that when the atoms are excited into the shared entangled state, they do so with a probability that oscillates $\sqrt{N}$ times faster than the probability to excite one lone atom. This is an important observation of note from the studies done in this thesis.

Entangled states are fundamental to the field of quantum information specifically to teleportation of quantum states of matter and quantum memory, quantum cryptography, quantum metrology, quantum communication, quantum error correction and quantum coding [114, 115]. The ability to control the physical mechanism required to deterministically create a highly entangled state from the ground state atoms [102, 112] combined with the abilities to manipulate a qubit state stored in the hyperfine state of each atom [116] and also keep and coherently transport or transfer the qubit state without losing the coherence of the qubit [117] provide an excellent resource for implementing fast quantum gates for quantum-information processing with (ultracold) neutral atoms.

2.4 Quantum Gates with Rydberg Atoms

In recent years, there have been numerous proposals and experimental designs of quantum gates that exploit the very large, strong and controllable state-dependent coherent interactions of permanent dipole moments of laser-excited Rydberg atoms as well as the resulting blockade effect which entangles the atoms. The first idea of neutral atom quantum gates mediated by Rydberg interactions was proposed by Jaksch *et al.* [1]. They proposed a controlled-Z gate that shows how the interaction between two qubits that are each encoded in the ground state hyperfine levels of the control and target atoms is turned on or off via Rydberg excitations while the atoms are conditionally phase shifted. So far, Rydberg interactions have been a majorly successful means to demonstrate quantum gates between two neutral atoms even though many alternative two-atom quantum gates have been proposed [118, 119, 120, 121]. The CNOT gate was first experimentally implemented between two individually addressed neutral atoms held in optical traps that are within close proximity to one another in [5], and used to create entanglement between them in [4].

2.4.1 Quantum gate between single qubit and an ensemble qubit

Of importance to the future goal of this research is a two-qubit parallelized C-NOT^N gate based on electromagnetically induced transparency (EIT) and strong long-ranged Rydberg interactions between a single control qubit and a target ensemble qubit proposed by M. Müller *et. al.* [122]. The gate enables entanglement between the mesoscopic ensemble of atoms with the single control atom in a single step. In this gate, the Rydberg blockade effect is used to switch on/off the EIT in the atom ensemble conditional on the state of the control atom. This enables a population transfer of the

ensemble atoms between two logical internal states.

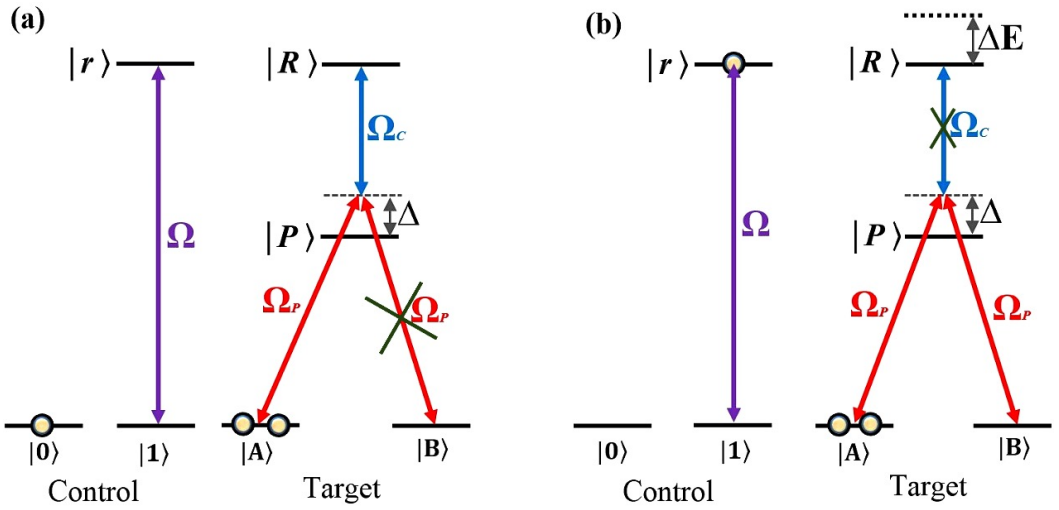

FIGURE 2.6: Schematic representation of a two-qubit gate based on EIT and Rydberg interactions performed between a single control atom and a target ensemble of atoms. (a) The case when the control qubit is initially in $|0\rangle$; (b) The case when the control qubit is initially in $|1\rangle$ so that it is coupled to the Rydberg state $|r\rangle$.

Figure 2.6 shows the control and target atoms having ground state hyperfine structures $\{|0\rangle, |1\rangle\}$ and $\{|A\rangle, |B\rangle\}$ and Rydberg states $|r\rangle$ and $|R\rangle$. In addition, the ensemble atoms have an intermediate state $|P\rangle$ which is off-resonantly coupled to the ground states $|A\rangle$ and $|B\rangle$ by a pair of phase-coherent probe laser beams with Rabi frequency Ω_P and detuning Δ in a Raman configuration. A strong coupling beam with strength Ω_C couples $|P\rangle$ with $|R\rangle$. The ground state $|1\rangle$ is resonantly coupled to $|r\rangle$ by a single beam with strength Ω. Figure 2.6(a) depicts the blocking of population transfer as a result of the control atom being initially in $|0\rangle$. It does not get excited to $|r\rangle$, thus switching on EIT obtained by adiabatically eliminating the far-detuned $|P\rangle$ from the four level system (that is in the limit $\Delta \gg \Omega_P, \Omega_C$). On the other hand, figure 2.6(b) shows the case of population transfer due to the control atom being initially in $|1\rangle$, thus getting excited to $|r\rangle$. The Rydberg-Rydberg interaction creates a shift ΔE in the Rydberg level of the ensemble atoms which lifts the two-photon resonance condition. As a result, EIT is switched off and there is a Raman transfer of atom from $|A\rangle$ to $|B\rangle$.

The possibility of performing quantum gate operations between distant qubits or within ensemble qubits has given room for implementing various quantum processing protocols. However, the future goal of this research is to look towards implementing protocols that are fully controllable and afford the capability to scale to a large number of qubits and are robust to decoherence with little or no entanglement. One of such protocols is the deterministic quantum computation with one qubit (DQC1).

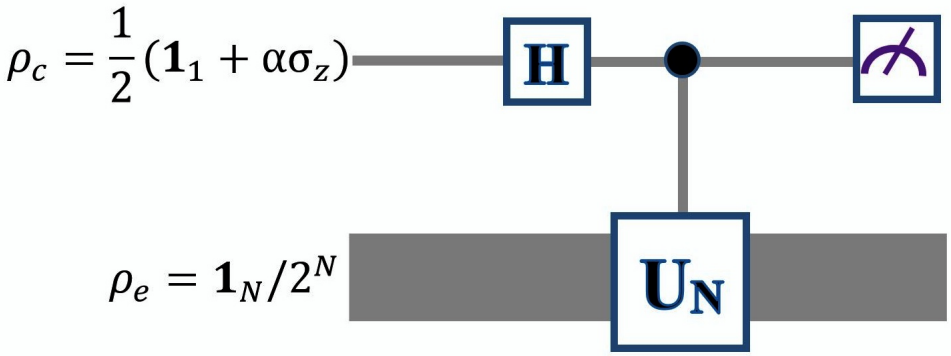

FIGURE 2.7: Quantum circuit diagram for DQC1 computational algorithm.

2.4.2 DQC1

DQC1 is a non-universal computational model that provides speed-up of some computational tasks, such as the calculation of the normalised trace of an arbitrary unitary matrix and phase estimation, for which there are no known efficient classical algorithms [105, 123, 124, 125]. The generic quantum circuit corresponding to the DQC1 protocol is shown in figure (2.7). It relies on the single *special* control qubit prepared in the states whose purity can be varied according to $\rho_c = \frac{1}{2}[\mathbf{1}_1 + \alpha\sigma_z]$ with a sub-unity polarisation $0 \leq \alpha \leq 1$ such that $\alpha = 1$ implies completely pure state, $\rho_c = |0\rangle\langle 0|$ while $\alpha = 0$ implies maximally mixed state. The register of N *unpolarised* ensemble qubits is prepared in a maximally mixed state $\rho_e = \frac{\mathbf{1}_N}{2^N}$. Non-classical correlations, other than entanglement and in this case quantifiable by quantum discord, are created between the control and the register qubits as a result of the unitary operation on ensemble qubits conditional of the control qubit state. The initial combined $N+1$ control-target state reads

$$\rho_0 = \rho_c \otimes \rho_e = \frac{1}{2^{(N+1)}} \begin{bmatrix} (1+\alpha)\,\mathbf{1}_N & 0_N \\ 0_N & (1-\alpha)\,\mathbf{1}_N \end{bmatrix} \quad . \tag{2.15}$$

The action of the Hadamard gate on the control qubit and a controlled unitary operation on the register qubits yield a resulting system state of

$$\rho = \frac{1}{2^{(N+1)}} \begin{bmatrix} \mathbf{1}_N & \alpha\, U_N^\dagger \\ \alpha\, U_N & \mathbf{1}_N \end{bmatrix} \quad . \tag{2.16}$$

Information about the ensemble qubits is obtained by performing measurements on the control qubit thereby bypassing the effect of decoherence. The readout reduced density matrix of the control qubit is obtained by partially tracing out the ensemble

component

$$\rho_c' = \mathrm{Tr}_e\left[\rho\right] = \frac{1}{2}\begin{bmatrix} 1 & \alpha\,\frac{\mathrm{Tr}\left[\mathrm{U_N^\dagger}\right]}{2^N} \\ \alpha\,\frac{\mathrm{Tr}\left[\mathrm{U_N}\right]}{2^N} & 1 \end{bmatrix} . \tag{2.17}$$

It is therefore easy to see that no computation is possible if the control qubit is in a maximally mixed state irrespective of the unitary operation. By measuring the expectation values of the Pauli operators σ_x and σ_y, one obtains the real and imaginary components of the normalised trace

$$\langle\sigma_x\rangle = \mathrm{Tr}\left[\rho_c'\sigma_x\right] = \alpha\,\frac{\mathrm{Re}\left[\mathrm{Tr}\left(\mathrm{U_N}\right)\right]}{2^N}\,; \qquad \langle\sigma_y\rangle = \mathrm{Tr}\left[\rho_c'\sigma_y\right] = -\alpha\,\frac{\mathrm{Im}\left[\mathrm{Tr}\left(\mathrm{U_N}\right)\right]}{2^N}\,. \tag{2.18}$$

This is performed by measuring the populations of the $|0\rangle$ and $|1\rangle$ after X or Y rotation. However it is required, according to central limit theorem, that the measurement process be repeated multiple times to ensure an accurate estimation of the expectation values. Since the measurement is performed only on the control qubit, then the number of repetitions n_{rep} and the accuracy of the measurement $\frac{1}{\sqrt{n_{\mathrm{rep}}}}$ are independent on the number of ensemble qubits. Also, the required computational time for estimating the normalised trace of an arbitrary unitary matrix is independent on its size. This is definitely not the case for classical algorithms in which determining the normalised trace of a $2^N \times 2^N$ unitary matrix scales exponentially with N.

2.4.3 Cold Atoms implementation

Besides the estimation of normalised trace, DQC1 have been found to be efficient in solving problems, for which no efficient classical algorithms are known, in a variety of fields such as in metrology [104], overlap of quantum states [126], thermodynamics [127, 128], chaos and integrability testing [129], also in calculating spectral density [123] and fidelity decay [130] and estimating Jones and HOMFLY polynomials [131]. Experiments based on photonic qubits have been used to evaluate the normalised trace of a 2×2 unitary matrix [132]. A system of four qubits in a liquid state nuclear magnetic resonance (NMR) quantum information processor based on carbon nuclei has been used in the approximation of Jones polynomial [133, 134]. This experimentally demonstrates the principle of mixed state computation. However, there is an unanswered question about what the limit on scaling up the system is before the computational advantage of the protocol is destroyed by the noise and control errors of the system. The future goal of this research is towards the cold-atoms implementation of the protocols.

Appropriate laser cooling and trapping techniques enable the extension of the implementation of the protocol to a large Hilbert space with better detection efficiency [81]. Owing to the microsecond lifetime timescale of cold Rydberg atoms compared to the timescale of interest, under very clean and well-defined conditions, one can study the energy of interactions due to the limited kinetic energy of the atoms. Given the long-range dipole-dipole interaction, the interaction of one Rydberg atom with so many other is possible [135].

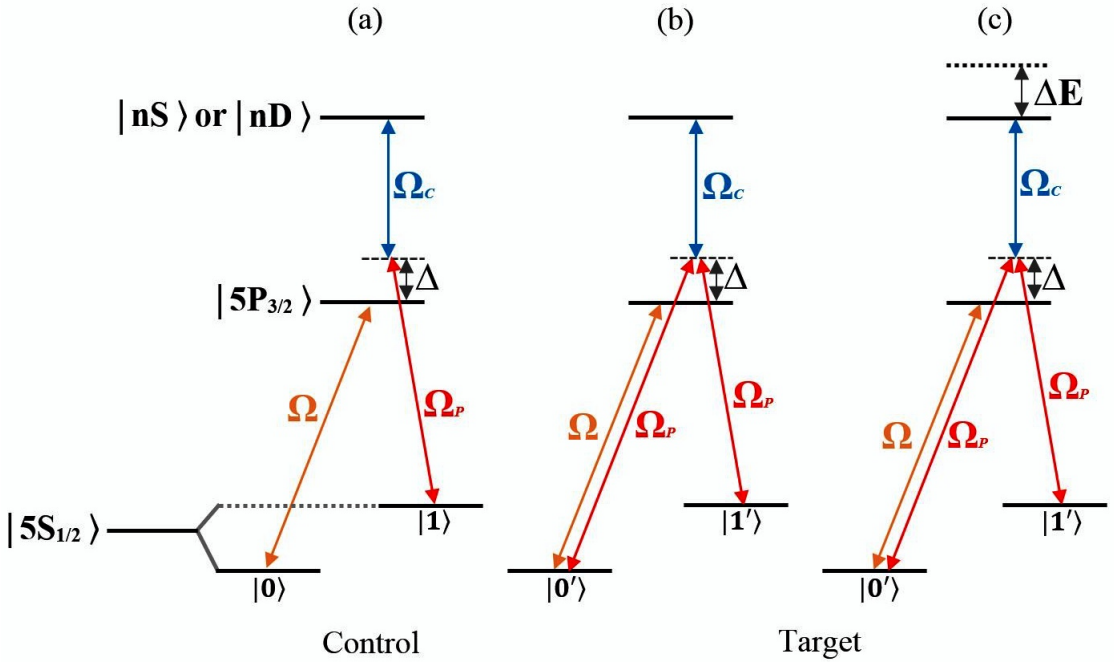

FIGURE 2.8: Schematic representation of the implementation of DQC1 model with Rb atoms. The control and target qubits, represented by $\{|0\rangle, |1\rangle\}$ and $\{|0'\rangle, |1'\rangle\}$ respectively, are encoded in the ground state doublet of ^{87}Rb. They are coupled to the Rydberg state, using 780 nm NIR and 480 nm blue lasers with strengths Ω_P and Ω_C respectively, via the intermediate state. (a) Possible Rydberg excitation when the control atom is in $|1\rangle$. (b) Control atom not initially in $|1\rangle$ thus enabling possible Rydberg excitation of the ensemble. (c) Control atom initially in $|1\rangle$ so that the ensemble atoms are shifted out of resonance by Rydberg-Rydberg interaction.

The optical scheme to implement the DQC1 model is shown in figure 2.8. For this study, Rubidium (Rb) atoms are used (see appendix A). The protocol generally involves the process of atom cooling and trapping, the initialization stage, the processing which involves the application of optical pulse sequence to perform unitary operations and then the probing process. The sequence of operation is summarised in the table below:

	Initialization	Processing		Measure	
Control	$\|+\rangle = \frac{1}{\sqrt{2}}[\|0\rangle + \|1\rangle]$	π-pulse	π-pulse	σ_x (σ_y)	fluorescence
Target	$\frac{\mathbf{1}_N}{2^N}$	U_N			

Rb atoms are first cooled and trapped in a Magneto-Optical trap (MOT). The MOT serves as a reservoir for loading two individually addressable micrometre-sized optical dipole traps (ODTs) placed within very few micrometers of one another, within the range that Rydberg interactions between atoms allow for the possibility of Rydberg blockade effect [122, 136]. One trap holds the single atom control qubit system while the other holds the system of N target ensemble atom qubits as shown in figure 2.9. The control and ensemble qubits are encoded in the ground state hyperfine doublet of ^{87}Rb, $\{|5^2S_{1/2}, F = 1\rangle, |5^2S_{1/2}, F = 2\rangle\}$ represented by $\{|0\rangle, |1\rangle\}$ and $\{|0'\rangle, |1'\rangle\}$ in figure (2.8).

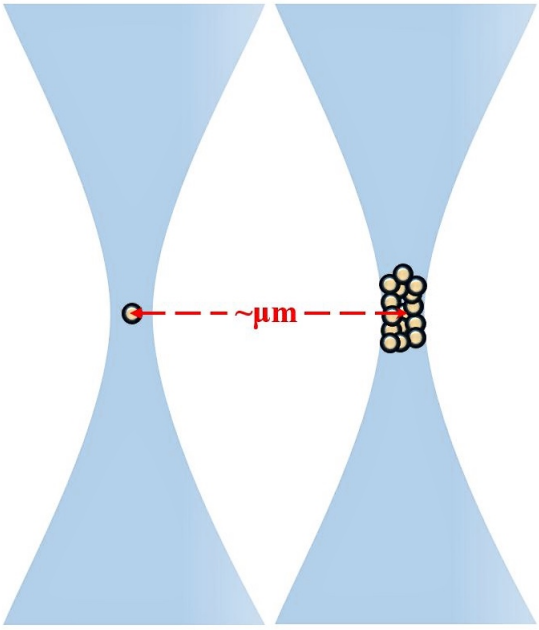

FIGURE 2.9: Diagram showing two individually addressable optical dipole traps with unequal waists (not drawn to scale). The $left$ trap holds the single control atom and while the $right$ trap holds the N target ensemble atoms. The target atoms are placed within the blockade radius of the control atom such that an efficient conditional logic and probing operation can be performed.

In the initialization stage, the control qubit is first prepared by optical pumping to the state $|1\rangle$ using circularly polarised 780 nm NIR laser beam with strength Ω. Then an Hadamard rotation via stimulated Raman transitions is performed with the aid of a π-pulse of strength Ω_P to create a superposition state $|+\rangle = \frac{1}{\sqrt{2}}[|0\rangle + |1\rangle]$. Similar operation is performed on the target atoms to create a pure and phase-coherent superposition state $|+\rangle_N = \frac{1}{\sqrt{2^N}}(|0'\rangle + |1'\rangle)^{\otimes N}$. However, there is an additional optical pumping of one of the two ground state populations to the intermediate state $|5^2P_{3/2}, F = 3\rangle$ so that possible spontaneous decay back into $|+\rangle_N$ destroys the phase coherence. Thus, creating a maximal mixedness of the ensemble qubit state.

One should note that illuminating the control atom simultaneously with both the NIR and blue lasers having Rabi frequencies Ω_P and Ω_C respectively is equivalent to the direct Ω pulse shown in figure 2.6. This results in a π-pulse which excites the control atom to the Rydberg state $|n\mathrm{S}\rangle$ or $|n\mathrm{D}\rangle$. A Rydberg interaction-induced shift ΔE further detunes the Ω_P-Ω_C pulses applied on the target ensemble so that EIT is turned off. As stated in [81, 122, 137], the fidelity of the protocol for any number of target ensemble atoms relies on the conditions that Δ must be must larger than the natural linewidth of $|5^2\mathrm{P}_{3/2}, F = 3\rangle$ to avoid further spontaneous decay, the relative strength of the lasers $\frac{\Omega_C}{\Omega_P} \gg 1$ to satisfy the EIT condition, the lifetime of any chosen $|r\rangle$ must be larger than the gate operation time and that the coupling of the control atom to any laser beam must be avoided when in state $|0\rangle$.

As stated already in equation (4.12), performing repeated measurements on the state of the control qubit helps to obtain information about the ensemble atoms. This is done by statistically obtaining the populations of $|0\rangle$ and $|1\rangle$ after an X or Y rotation. The population of $|0\rangle$ and $|1\rangle$ are obtained via imaging of the emitted fluorescence light from the control atom when a 780 nm laser coupling one of these states to $|5^2\mathrm{P}_{3/2}, F = 3\rangle$ is applied on it.

Summary

This chapter has given a review of the distinctive properties of Rydberg atoms. The strong long-range Rydberg interactions with attention to the van der Waals and resonant dipole-dipole regimes have been described. An important consequence of these interactions, the excitation blockade effect, and the creation of many-body entanglement, which is an essential tool in quantum information processing have also been described. Among many possible physical platforms for implementing quantum gates, the chapter focused on neutral atoms and its possibility of providing scalability. A possible protocol that could be implemented experimentally with neutral atoms and a subject of motivation for the studies done in this thesis is the DQC1 which is described to provide speed-up in performing classically intractable tasks with non-trivial unitary operations. However, it is first necessary to understand how to prepare the atoms in highly excited Rydberg states. The next chapter describes the laser systems and experimental setup used to prepare and detect Rydberg atoms in a vapour cell.

3 Laser Systems for Rydberg State Transition

Quantum computation and information processing require atoms to be in a state where they exhibit enhanced interaction properties. Tunable laser systems provide coherent, monochromatic and narrow-linewidth light that enables one to access different energy levels within the atom structure. This in turn allows one to study transitions between specific energy levels and coherently control and manipulate the quantum states of the atoms. To excite atoms to the desired Rydberg state, the excitation lasers have to be stabilised to the desired frequencies. In the experiment, excitation to Rydberg states can be accomplished via two-photon transition processes, according to the three-level ladder configuration shown in figure 1.1(b). The probe beam is provided by a commercially available 780 nm grating stabilised tunable single-mode diode laser (GSDL), also called the *extended cavity diode laser* (ECDL), frequency stabilised using the modulation transfer spectroscopy (MTS) technique [138]. The coupling beam is provided by a 480 nm commercial high power frequency-doubled tunable diode laser system stabilised and locked in frequency using the technique described in [139].

In this chapter, the technique for probing the Rydberg states of atoms using two-photon excitation scheme is described. The description of the two-photon excitation laser systems is done. The corresponding techniques and setups used for stabilising them are also explained. Finally, the characterisation of the transparency feature and the error signal used for locking the lasers is done.

3.1 Two-Photon Rydberg Excitation System

As stated in section 2.1, Rydberg excitation can be achieved via processes such as electron impact or charge exchange excitation, two-photon or multi-photon excitation processes or a combination of collisional and optical excitation. In this thesis, a ladder-type two-photon excitation scheme is considered (as schematically shown in figure 1.1). The ladder system consist of a probe beam which is given by a near-infrared (NIR) 780 nm single-mode diode laser and is resonant with the ^{87}Rb D2 optical transition between

hyperfine levels $|1\rangle = |5^2S_{\frac{1}{2}}, F = 2\rangle \longrightarrow |2\rangle = |5^2P_{\frac{3}{2}}, F' = 3\rangle$. The second stage is performed by a coupling beam provided by a blue 480 nm high power frequency-doubled tunable diode laser resonant with $|2\rangle = |5^2P_{\frac{3}{2}}, F' = 3\rangle \longrightarrow |3\rangle = |n\mathrm{D}\rangle$ or $|n\mathrm{S}\rangle$ transition. The optical setup for the frequency stabilisation and locking system of the two-photon excitation lasers is shown in figure 3.1, as demonstrated in [139] and [138].

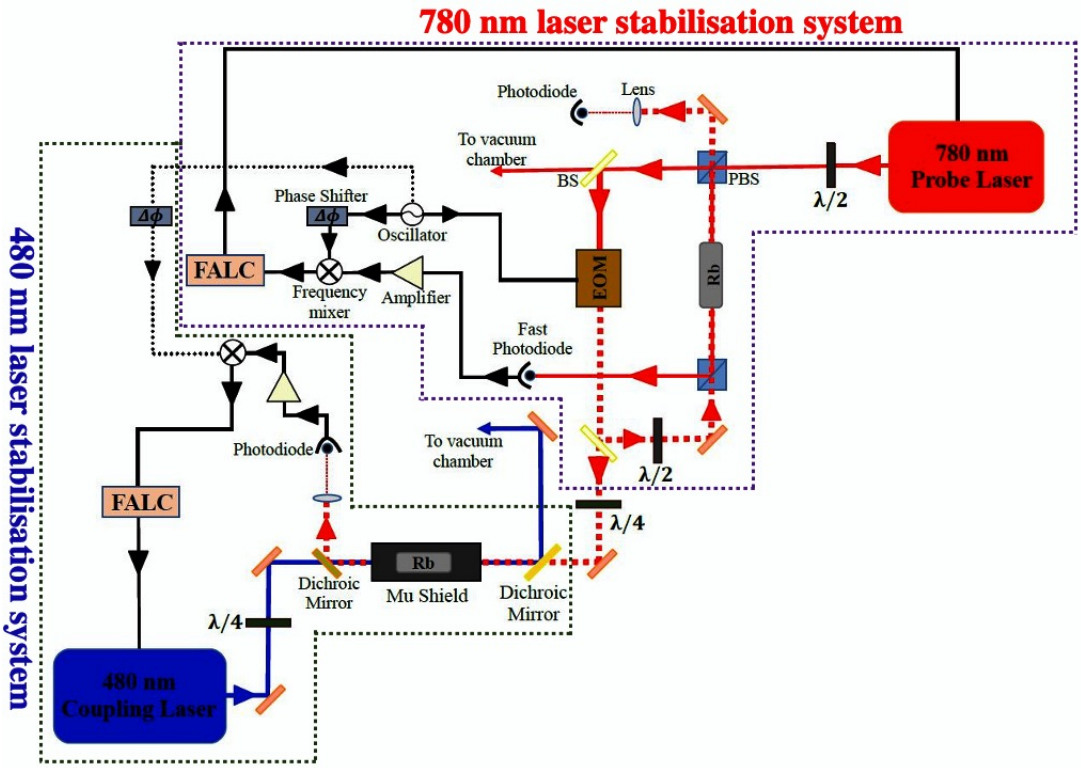

FIGURE 3.1: Schematics of the experimental setup for two-photon excitation system. The 780 nm probe laser is frequency locked using MTS technique while the 480 nm coupling laser is locked by exploiting transparency signal of Rydberg levels.

3.2 Frequency Stabilisation of the 780 nm Probe Laser

3.2.1 Probe Laser System

State selective excitations such as the two-photon Rydberg excitation require coherent and stable laser systems with extremely small laser linewidths. The probe laser is produced by a Toptica DL 100 GSDL system (detailed information about this apparatus can be found in [140]). This contains a well-collimated class 3B laser diode that emits continuous laser radiation of power up to 150 mW and wavelength range 750-980 nm.

Usually, the free-running laser diodes have a linewidth of about 100 MHz. The emitted frequency can be tuned by adjusting the current and temperature of the p-n junction. The laser current is driven by Toptica Current Control DCC 110 plug-in module for the Topita Diode Laser Supply Rack DC 110 which supplies up to about 100 mA to the diode. The laser temperature is controlled by the Toptica Temperature Control DTC 110 plug-in module which allows long-term stability with a drift of < 2 mK. To better control the emission wavelength and linewidth, the diode is set up with an external cavity which forces the laser to a selected frequency mode while other modes are strongly suppressed. Therefore, the laser linewidth is reduced to around 1 MHz. The output beam is linearly polarised and elliptical with beam size ≈ 2.9 mm $\times 2.2$ mm. A radially symmetric beam is obtained by using an anamorphic prism pair. This beam is passed through an in-built high extinction 35 dB optical isolator to prevent spectral disturbances and diode laser damage caused by back-reflections into the diode.

3.2.2 Stabilisation of the probe laser

The performance of the laser systems is affected by random physical factors encountered in the laser oscillator and during the lasing process which tends to broaden the natural frequency linewidth. Factors such as quantum and electronic noise present phase modulation which causes the spreading of emission power among a continuum of frequencies, and thus to the finite emission linewidth of the laser oscillator [141]. Other factors are mechanical instabilities or vibrations, environmental temperature, electronic temperature and current fluctuation which cause drift and instabilities of the emission frequency. To alleviate this problem, a frequency locking system, which provides a means for comparing the laser frequency to the required stable reference frequency, is put in place. The general way of doing this is by using the atomic transition to produce an *error signal*, which is an electronic frequency-dependent signal with zero-crossing at the point of atomic resonance. This error signal helps to check if the laser frequency produced is higher or lower than the transition frequency that the laser is required to be locked to. The error signal is fed back into the laser controlling devices, in *closed servo-loops*, which keeps the laser frequency on transition resonance. Quite a lot of techniques are used to generate the error signal for laser locking. There are the single beam techniques, such as the dichroic atomic vapour laser lock (DAVLL) [142]. They produce Doppler-broadened spectral features and usually exhibit a capture range of several hundreds of MHz. There are also pump-probe techniques such as polarisation spectroscopy [143], frequency modulation saturated absorption spectroscopy [144], to mention but few. These techniques achieve sub-Doppler resolution and as a result, show steeper error signal gradients and enhanced

frequency discrimination. Although they capture a more limited range, typically < 100 MHz. However in this study, the 780 nm probe laser is stabilized and locked to the ^{87}Rb D2 narrow line $|5S_{1/2}, F = 2\rangle \rightarrow |5P_{3/2}, F' = 3\rangle$ transition frequency resonance using the modulation transfer spectroscopy (MTS) technique [138, 145].

The MTS technique whose setup is shown in figure 3.1, similar to the standard frequency modulation *saturated absorption spectroscopy* (SAS), is also a pump-probe technique that minimises Doppler broadening effect on the atomic spectrum and produces sub-Doppler resolution of lineshapes suitable for robust laser locking. Here, the counter-propagating 780 nm laser beams are referred to as the red-pump and red-probe beams to avoid mixing up the specific probe beam that is being referred to. The MTS differs from the standard SAS as the red-pump beam with a carrier frequency ω_{cf} is first phase-modulated with an electro-optic modulator (EOM) so that it acquires sidebands at frequency ω_{mf} before being allowed to counter-propagate the red-probe beam through an atomic vapour cell. Over other techniques, the advantage of using the MTS for laser locking is because it is insensitive to the background absorption and it also produces a flat Doppler-free error signal. This results in the elimination of the fluctuations and background noise, from a typical SAS, that cause a shift of the baseline of the laser locking point. Hence, the zero-crossings of the generated error signals from the MTS technique are usually accurately centred on the corresponding atomic transitions. Also, the MTS error signals are influenced by the contributions from closed atomic transitions. This is of importance in the case where the spectrum contains several closely spaced transitions [138].

The experimental implementation is as follows (see the purple dashed-line segment of figure 3.1). The 780 nm laser is split into the red-pump and red-probe beams using a narrow-band polarizing beam splitter (PBS). The ratio between the red-pump and red-probe powers is controlled using a half-wave $\frac{\lambda}{2}$ plate. The red-pump beam is further split into two parts using an optical glass beam splitter (BS) with one part sent to the vacuum chamber for ultracold Rydberg atoms experiment. The other part is phase-modulated around $\omega_{mf} = 10$ MHz using an EOM, Photonics Technologies EOM-01, which is driven by a low amplitude ~ 5 V_{pp} sinusoidal signal from an Agilent 33250A waveform generator. The fast Fourier transform (FFT) of the signal from the EOM on a fast photodiode is shown in figure 3.2(a). The large peak at about 10 MHz confirms the modulation and the presence of sidebands. As a result, the red-pump beam acquires sidebands at the harmonics of the modulation frequency. The modulated red-pump beam is then aligned to counter-propagate the unmodulated red-probe beam in a 25.4 mm $\times$ 71.8 mm Rubidium Borosilicate vapour cell. As a result

of sufficiently nonlinear interaction of the two beams with the medium, the red-pump modulation sidebands are transferred to the red-probe beam by means of the four-wave mixing phenomenon [145, 146]. That is, when two frequency components of the red-pump beam (for each sideband) interfere with the counterpropagating red-probe beam by means of the non-linearity of the atomic medium, a fourth wave is generated as a sideband for the red-probe beam. This is due to one of the mechanisms responsible for modulation transfer, the *reflection*. As described in [145], when both counterpropagating beams interfere, they create a partial standing-wave field pattern. As a result of saturation, the pattern is induced in the populations of the resonant states of the atomic medium. This in return creates a spatial periodicity in the transparency of the atoms. The spatial periodicity acts as a diffraction grating that Bragg-reflects a part of either of the laser beams back in the opposite direction. As such, the sidebands of the modulated red-pump beam are reflected on the grating, hence, travelling in the direction of the unmodulated red-probe beam, creating a transfer of modulation.

According to the description done in [145], the other mechanism responsible for transferring modulation to the unmodulated beam is the *modulated hole burning*. The modulated beam burns a hole of modulated depth in the velocity distribution of the atom population. In the case when the modulation frequency exceeds the natural (homogeneous) linewidth of the laser transition, several distinct holes that are separated by the modulation frequency and have depths oscillating at the modulation frequency are burned. When the unmodulated beam resonantly interacts with these holes, it senses modulated absorption and dispersion, hence acquiring a modulated amplitude and phase shift.

After the modulation transfer process, the modulated red-probe beam is then sent on a fast photodiode, Electro-Optic Technology (EOT) Amplified Silicon Photodetector ET-2030A, capable of detecting the radio frequency heterodyne beat frequencies between the carrier and the sidebands. The red-pump beam is sent on a pre-amplified photodiode to obtain a saturated absorption signal.

To obtain the error signal for laser locking, the fast photodiode signal is first amplified using a low noise controlled amplifier, Mini-Circuits ZFL-500LN-BNC+ which gives about 30 dB gain at 14 V. It is then mixed (using a Mini-Circuit Mixer ZAD-6+) with a phase-controlled reference sinusoidal signal from the waveform generator. The phase control is done using by Mini-Circuit JSPHS-12+ voltage variable phase shifter. The frequency mixing corresponds to the mathematical product of two signals. This output is a raw and noisy error signal as shown in figure 3.2(b) (blue trace) for ^{85}Rb and ^{87}Rb.

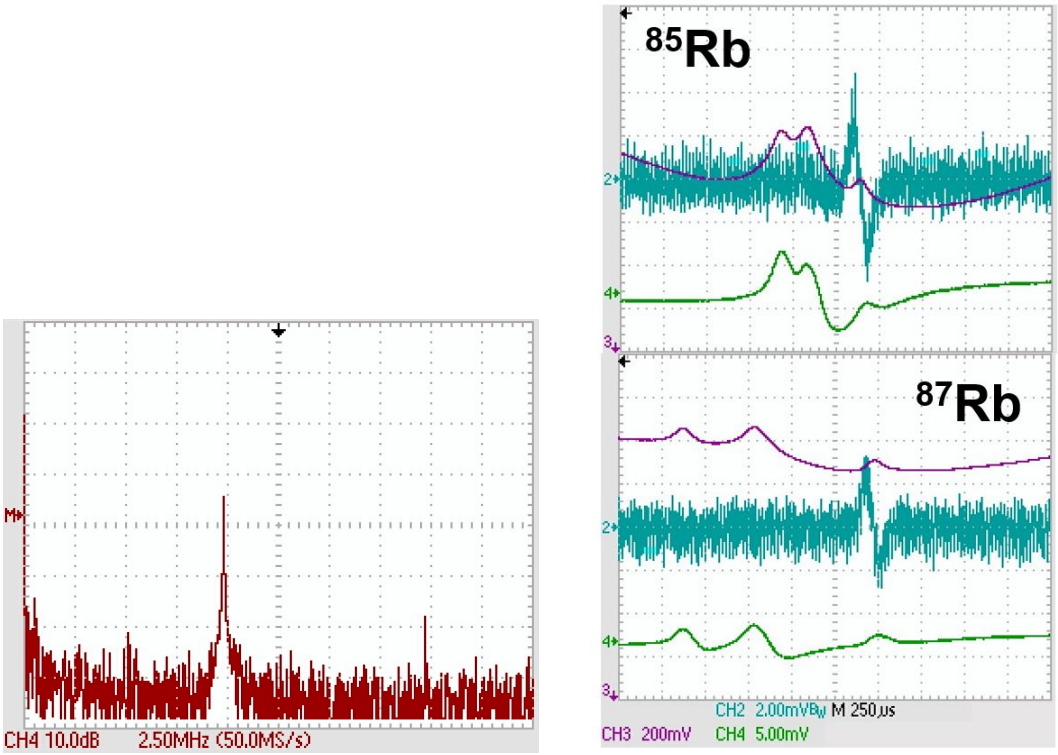

FIGURE 3.2: **(a)** Fast Fourier transform (FFT) of the modulated red-pump beam signal from the EOM detected by a fast photodiode showing a large peak at about 10 MHz. This corresponds to the modulation frequency and presence of generated sidebands; **(b)** (Purple line) Doppler-free saturated absorption (SA) spectrum from the red-pump beam, (blue line) noisy error signal obtained from the frequency mixer output, and (green line) signal from the fast photodiode after detecting the finally modulated red-probe beam; **(c)** (Blue line) Demodulated error signal obtained from the Fast Analog Linewidth Controller (FALC) with clear zero-crossing coinciding with the desired Rb D2 transition and locking point. **N.B** All traces are averaged over four times.

Also shown on figure 3.2(b) is the saturated absorption (SA) spectrum of the red-pump beam as detected by the pre-amplified photodiode (purple line) and the signal from the fast photodiode after detecting the finally modulated red-probe beam (green line). The frequency mixer output signal is passed into a commercial servo amplifier, Toptica Fast Analog Linewidth Controller FALC 110 which is made up of active loop low- and high-pass filters that cover different range of frequencies. The filters within the FALC unit are divided into slow and fast frequency branches. This includes the extra slow limited integrator (XSLI) which covers 0.9-90 Hz frequency range and yields 26 dB gain, the slow limited integrator (SLI) which covers between 11 Hz and 5 kHz with 36 dB gain, the fast limited integrator (FLI) covers between 1.4-650 kHz with 15 dB attenuation and the fast limited differentiator (FLD) which covers between 100 kHz and 4.8 MHz with 15 dB attenuation. The filters were turned on and set to XSLI $= 6$, SLI $= 1$, FLI $= 6$ and FLD $= 1$ to produce a demodulated error signal output (blue line in figure 3.2(c)) with a clear zero-crossing which coincides with the desired Rb D2 transition and locking point. The signal has highest peak-to-peak amplitude for closed transition and cross-over peaks corresponding to ^{85}Rb $|5S_{1/2}, F = 3\rangle \rightarrow |5P_{3/2}, F' = 4\rangle$ and ^{87}Rb $|5S_{1/2}, F = 2\rangle \rightarrow |5P_{3/2}, F' = 3\rangle$ transitions where atoms cannot relax into other ground states. This property is beneficial in the case where many hyperfine transitions are closely-spaced. The peak-to-peak amplitude of the error signal can also be adjusted by adjusting the main gain of the FALC. However, increasing the FALC gain to a level that is considered too high will cause the error signal to jitter. There is a flat, zero background in regions away from the sub-Doppler peaks showing the absence of modulation transfer in such regions. This error signal is fed back into the laser current controlling device DCC 110 via a current servo modulation input BNC.

3.3 Frequency Stabilisation of the 480 nm coupling Laser

3.3.1 Coupling Laser System

As shown in figure 1.1(b), the second wavelength involved in the two-photon Rydberg excitation scheme is a 480 nm blue coupling laser. This is produced using a commercial high power frequency-doubled tunable diode laser system, Toptica TA-SHG 110. Figure 3.3 shows the schematics of the principal components of this system which includes the *fundamental light source* or *master oscillator*, the *tapered amplifier* and the *resonant doubling cavity*. The photograph of the whole TA-SHG 110 system is shown in figure 3.4. A detailed description of the entire system can be found in [147].

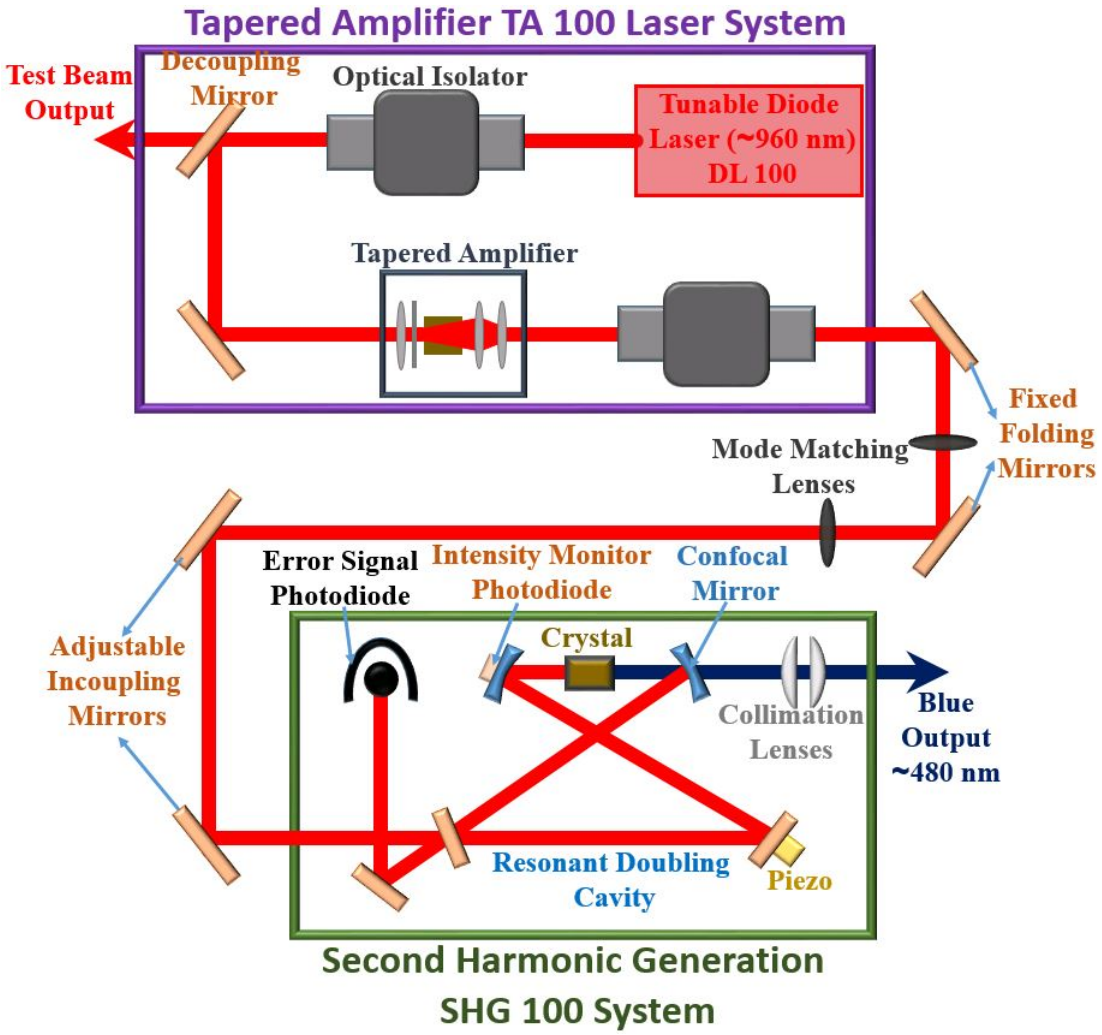

FIGURE 3.3: Schematics of the high power 480 nm coupling laser system which consists of the amplifying and frequency doubling units.

The fundamental light source is provided by a Littrow-mounted ECDL Toptica DL 100 producing continuous laser up to 50 mW and running at a wavelength of about 960 nm that can be tuned over a wide range. This laser system and its controlling electronic devices have been explained in section 3.2.1. The beam passes through an optical isolator, then to a decoupling mirror which divides the beam into 1:10 transmission-reflection ratio. The transmitted part serves as the test beam for wavelength monitoring. The wavelength is measured using a Bristol 521 Wavelength Meter to an accuracy as high as ± 0.005 nm. This measured value is subsequently halved to obtain the wavelength of the output beam. Meanwhile, the reflected beam from the decoupling mirror is coupled to the high power amplifier laser diode with a tapered gain region and a broad gain profile that has about ± 20 nm tuning range. The anti-reflection facet coating of the amplifier prevents laser emission without seeding. This enables the master oscillator to fully control the internal modes of the amplifier so that the resulting beam,

with $\sim$ 500 mW output power for maximum alignment, maintains the single-mode characteristics. High extinction optical isolators ($>$ 60 dB) are employed to secure the master oscillator and tapered amplifier to avoid strong feedback, instability of the laser lock and resulting optical damage.

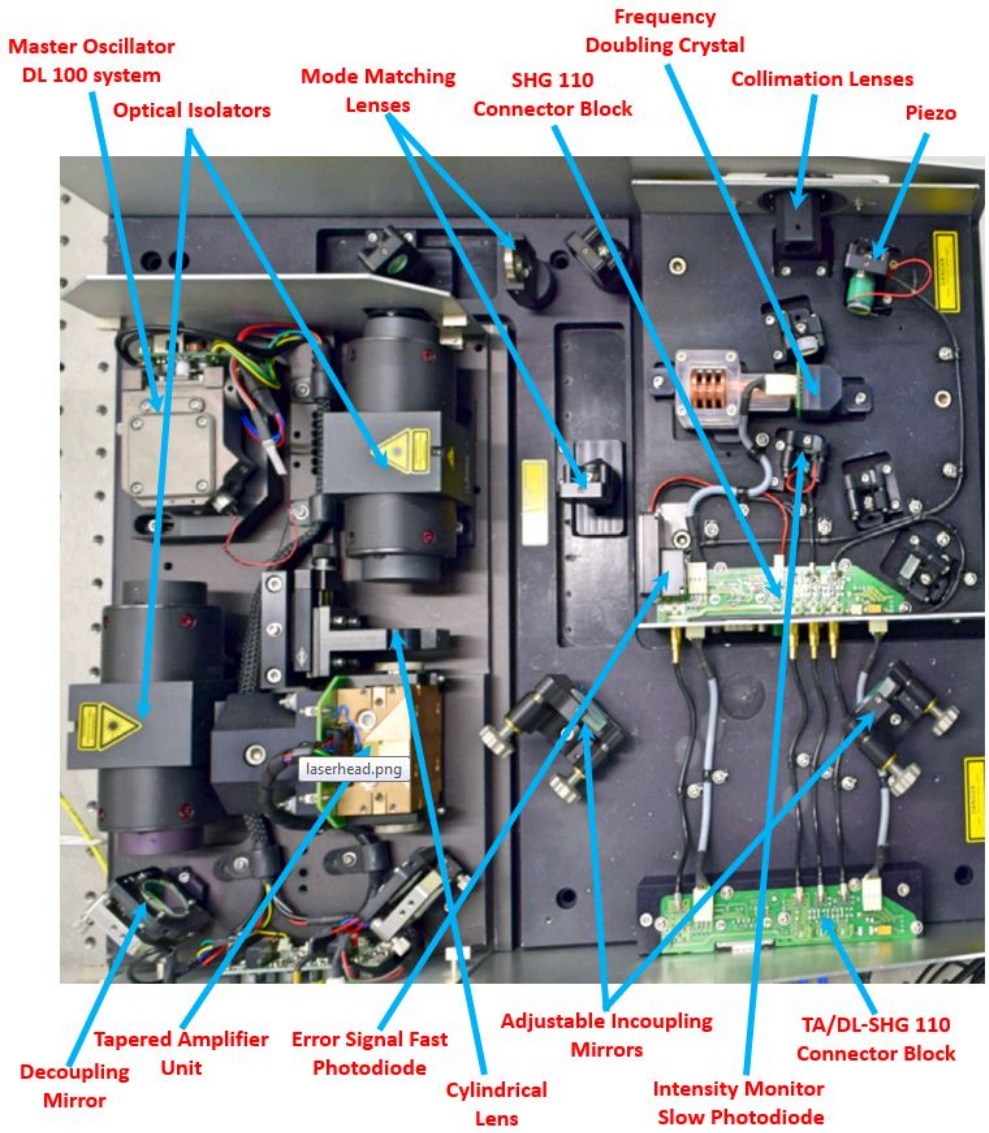

FIGURE 3.4: Picture of TA-SHG 110 system for obtaining the 480 nm coupling beam. The Tunable diode laser produces a fundamental 960 nm NIR laser which is amplified by the tapered amplifier. The output beam is adapted into a resonant doubling cavity where it passes through a frequency doubling crystal to produce a 480 nm blue laser.

The amplified beam is passed to an external resonant doubling folded ring cavity in a *bow-tie geometry* following the design in [148]. The spatial mode of the amplified beam is matched to the mode of the doubling cavity by means of a pair of anti-reflection coated mode-matching lenses. The second harmonic laser is generated by a

potassium niobate ($KNbO_3$) non-linear optics crystal that is placed in the beam waist between two confocal mirrors. The crystal is well suited for wavelengths between 880 nm and 980 nm to achieve the highest conversion efficiency and maximum output power ($\sim$ 280 mW) of the frequency-doubled light. Also, the crystal position is such that unconverted light can pass through multiple times, thus building up the intensity of the fundamental laser and increasing the power of the resulting frequency-doubled laser. As stated in equation (1.39), due to the $\chi^{(2)}$ susceptibility in a non-linear medium, an initial radiation generates a non-linear polarisation wave which oscillates with twice the radiation frequency. Thus, the non-linear polarisation wave emits an electromagnetic field with doubled radiation frequency in the direction of the wave as a result of *phase-matching*. The phase-matching is achieved by tuning the crystal temperature. This is made possible due to the crystal being mounted on a thermoelectric cooler (TEC). Similarly to the master oscillator, the current and temperature of the frequency doubling crystal and tapered amplifier are each stabilised using with Toptica DCC 110 and DTC 100 respectively.

FIGURE 3.5: Cavity PZT error signal fed back into cavity PZT PID controller to lock the cavity to the source laser. The error signals with smaller amplitude corresponds to high order modes of the cavity.

It is required that the cavity length be locked to ensure that the doubling cavity remains resonant with the laser. Thus, one of the cavity mirrors is mounted on a PZT element so that the cavity length is tuned to match the fundamental light frequency. The PZT is driven by the error signal (shown in figure 3.5) generated via the *Pound-Drever-Hall* method on an electronic error signal stabilising unit Toptica PDD 110. The error signal

is fed back to the cavity PZT PID (proportional-integral-derivative) controller (Toptica PID 110) whose feedback is used to lock the cavity to the source laser. However, for spectroscopic reference of specific Rydberg state, the laser is further locked and stabilised using the technique described in [139].

3.3.2 Stabilisation of the coupling laser to Rydberg state transitions

The method for stabilising the 480 nm laser, as described in [139], takes advantage of the transparency feature obtained from an interference phenomenon that arises when both the probe and coupling beams interact with the Rb atoms in the vapour cell. Generally, literature mainly refers to using electromagnetically induced transparency (EIT) due to the probe-coupling Rabi frequency ratio $\frac{\Omega_p}{\Omega_C} \ll 1$. However, the technique does not necessarily depend on the beam powers. As shown in figure 3.1 (see the dark-green dashed-line segment), the modulated beam from the 780 nm laser is split into two by a glass splitter. A part is used for the MTS as described in section 3.2.2 while the other part is aligned to counter-propagate the blue laser in a mu-shielded Rb vapour cell before been passed onto a fast photodiode using a dichroic mirror. The Mu-metal shield, a nickel-iron alloy with high magnetic permeability, is used to reduce stray static or low-frequency background magnetic fields.

The setup for obtaining the error signal to lock the blue laser is similar to that used to lock the probe laser (see section 3.2.2). Figure 3.6 shows the two-photon excitation spectrum (green line) from a fast-photodiode with the SAS spectrum (yellow line) of the probe from the pre-amplified photodiode also shown. First (as shown in figure 3.6(a)), the probe laser is scanned around the ^{85}Rb $|5S_{1/2}, F = 3\rangle \rightarrow |5P_{3/2}, F' = 4\rangle$ and ^{87}Rb $|5S_{1/2}, F = 2\rangle \rightarrow |5P_{3/2}, F' = 3\rangle$ transitions while the coupling beam is turned off. Only Doppler-broadened probe transition peaks appear on the two-photon excitation trace. However, when the coupling beam is turned on and tuned to the 20D Rydberg state, narrow transmission peaks, for fine states $20D_{5/2}$ in figure 3.6(b) and $20D_{3/2}$ in figure 3.6(c), can be observed as a result of an induced transparency. The fast photodiode signal is sent to a home-built EAVS (IFEC) J2948 10 MHz 18 dB Low Noise Preamp and mixed with a phase-shifted oscillator signal to produce a modulated error signal that is sent to the FALC. The error signal obtained from the blue laser FALC is shown in figure 3.6(d). The few hundreds of MHz scan range of the probe transition makes it difficult to view both $20D_{5/2}$ and $20D_{3/2}$ at the same time. Instead, the probe laser is locked to the ^{87}Rb $|5S_{1/2}, F = 2\rangle \rightarrow |5P_{3/2}, F' = 3\rangle$ transition while an approximately 2 GHz scan of the coupling beam across the 20D state makes

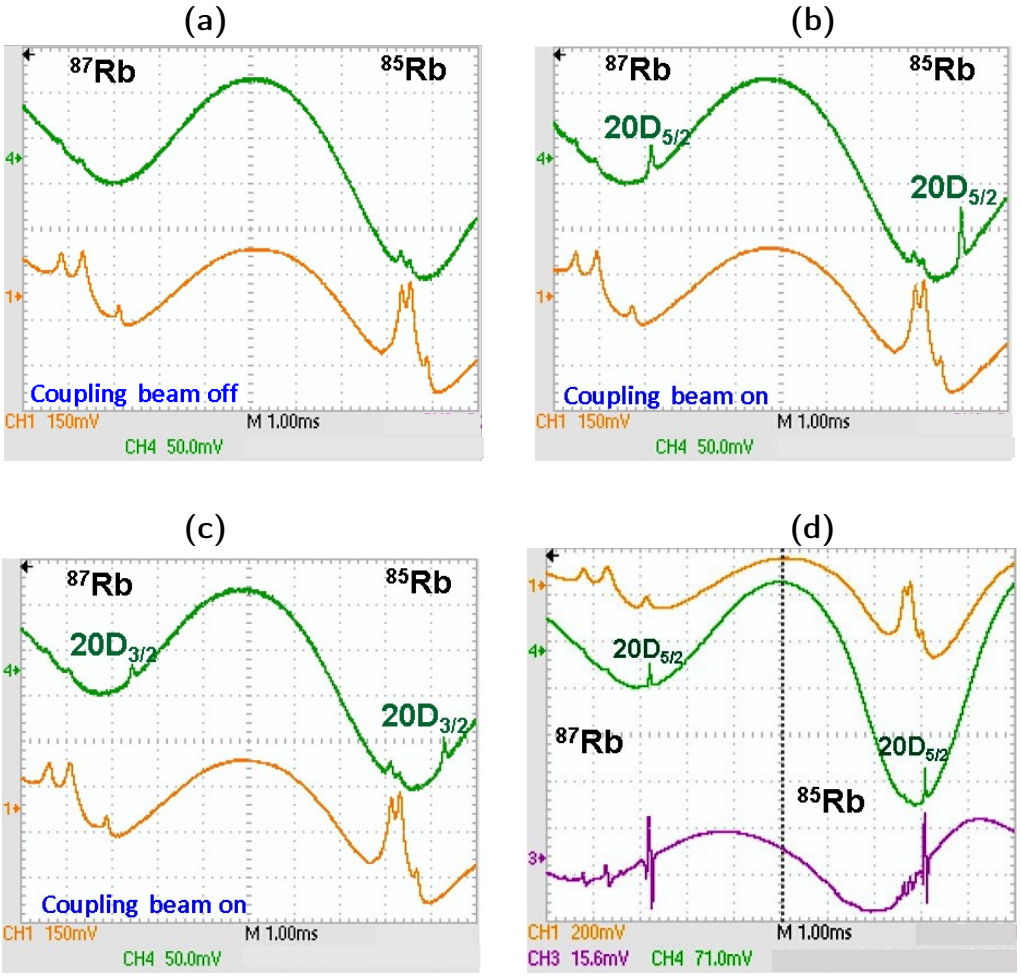

FIGURE 3.6: Images showing the probe saturated absorption spectrum (yellow line), spectrum with two-photon excitation transparency feature (green line) when the probe laser is scanned across the ^{85}Rb $|5S_{1/2}, F = 3\rangle \rightarrow |5P_{3/2}, F' = 4\rangle$ and ^{87}Rb $|5S_{1/2}, F = 2\rangle \rightarrow |5P_{3/2}, F' = 3\rangle$ transitions while the coupling beams is: **(a)** turned off - only the Doppler-broadened probe transition peaks appear on the two-photon excitation line; turned on and scanned around 20D - transparency peak for **(b)** $20D_{5/2}$ and **(c)** $20D_{3/2}$ is shown; **(d)** Error signal (purple line) obtained from the blue laser FALC. For these features coupling beam power $= 15.94 \pm 0.72$ mW and probe beam power $= 476.9 \pm 3.9\,\mu$W. The uncertainties in the beam powers are obtained from the standard deviation of a range of values for the beam powers as measured on the power meter.

it possible to view both the $20D_{3/2}$ and $20D_{5/2}$ fine states which are about 1.7 GHz apart. This can be seen in the plots of the amplitudes of the transparency features and error signal with respect to the coupling beam scan frequency shown in figures 3.7(c)-(d). The error signal shown in figure 3.6(d) contains the Doppler-broadened background from the probe laser, which makes difficult to determine a definite zero-crossing for locking. This shows an expected property that the offset of the error signal changes with changing probe frequency. As shown in figures 3.7(a)-(d), locking the probe laser while scanning the coupling laser allows one to obtain an error signal with

good signal to noise ratio and a clear and definite zero-crossing for locking the blue laser. The performance of the lock generally depends on the noise of the error signal, which has been reduced by the FALC, and the phase of the error signal. The phase of the error signal can be changed by either inverting the signal sent into the FALC or by changing the oscillator signal phase-shifter voltage drive. Figure 3.7(a) shows the case when the probe beam is modulated by the EOM while figures 3.7(b)-(d) show when there is no probe EOM modulation. One would notice that the transparency feature (green line) in figure 3.7(a) has a wavy and noisy nature when compared to the transparency feature (purple line) in figure 3.7(b). This is due to the 10 MHz modulation sideband signal beating with the unmodulated transparency signal.

Figure 3.8 gives a deeper look into the transparency peaks when increasing probe beam power. As a result of the probe modulation, the sidebands beat with the probe beam to produce a detector signal at the modulation frequency. This can be noticed in the transparency peak in figure 3.8(a) with sidebands at about 10 MHz. Increasing the probe field strength increases the carrier-sidebands power ratio (see figure 3.8(b)-(d)). The modulation frequency and amplitude $\sim 2.2\,V_{\text{pp}}$ are carefully chosen to obtain only first order sidebands. Figure 3.8(d) shows the transparency peaks for modulation frequency ~ 10 MHz and amplitude ~ 10 V_{pp} with higher-order sidebands occurring at the harmonics of the modulation frequency. This in fact is one of the factors that hinder the accurate measurement of the linewidth of the transparency peak (see section 4.2.4).

Figure 3.9(a) shows the error signals obtained for varying probe beam power while figure 3.9(c) for varying coupling beam power. The amplitude and steepness of the error signal increase with decreasing probe-coupling power ratio as shown in figures 3.9(c)-(d). This result is true for generic interference phenomena (see section 1.5.1) that occur during two-photon excitation process. In [91] and [139], they only focused on EIT for stabilising the coupling beam and the properties of the error signal is attributed to the coupling beam only. In figure 3.9(c), the coupling beam was fixed at around 68 mW while varying the probe beam power. On the other hand in figure 3.9(d), the coupling beam power is varied with the probe beam fixed at around $150\,\mu$W. Both result in an average rate of error signal slope change of (4.5 ± 0.3) mV/MHz. This result shows that the properties of the error signal is actually dependent on both beams. So, one can set the beam powers to any desired value provided an error signal whose amplitude is visible and large enough to lock the coupling laser is produced.

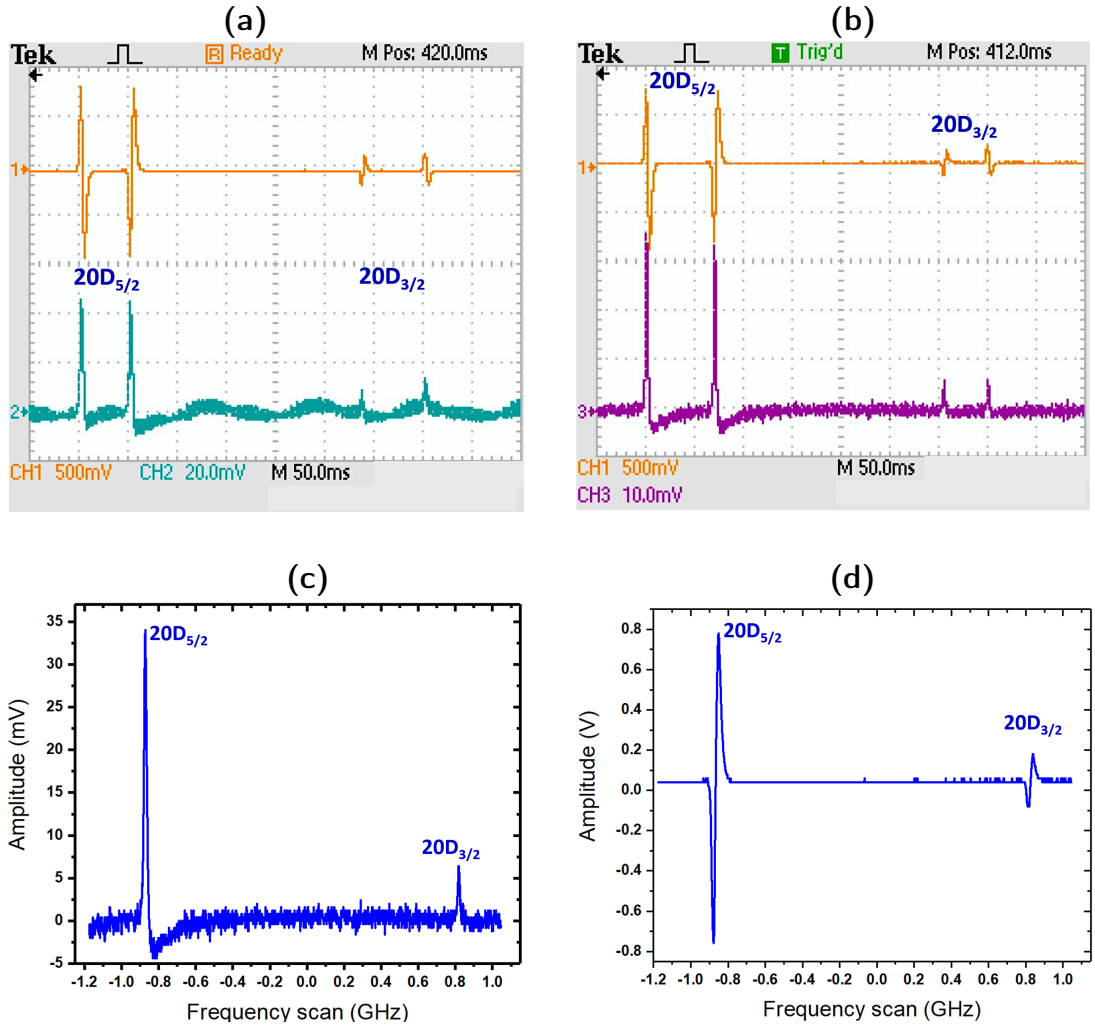

FIGURE 3.7: Transparency peaks and the corresponding error signals for $20D_{3/2}$ and $20D_{5/2}$ Rydberg states for ^{87}Rb for the case: **(a)** when the probe beam is modulated by the EOM; **(b)**, **(c)**, **(d)** when the probe beam is not modulated by the EOM. The probe laser is locked to $|5S_{1/2}, F = 2\rangle \rightarrow |5P_{3/2}, F' = 3\rangle$ transition while a 2 GHz scan of the coupling laser across the 20D state makes it possible to view the both simultaneously since they are about 1.7 GHz apart. **(c)** and **(d)** show the plot of the amplitudes of the transparency feature and error signal with coupling beam scan frequency. The noisy nature of the transparency peaks in **(a)** is as a result of the 10 MHz modulation sideband signal beating with the transparency signal. For these features, **(a)** coupling beam power $= 15.94 \pm 0.72$ mW and probe beam power $= 476.9 \pm 3.9\,\mu$W; **(b)**, **(c)**, **(d)** coupling beam power $= 16.86 \pm 1.21$ mW and probe beam power $= 1.48 \pm 0.01$ mW.

Summary

This chapter gave a detailed description of the experimental realisation of two-photon excitation scheme. This includes the laser systems and their effective locking systems. The stabilisation of the 780 nm lasers using a scheme based on frequency modulation

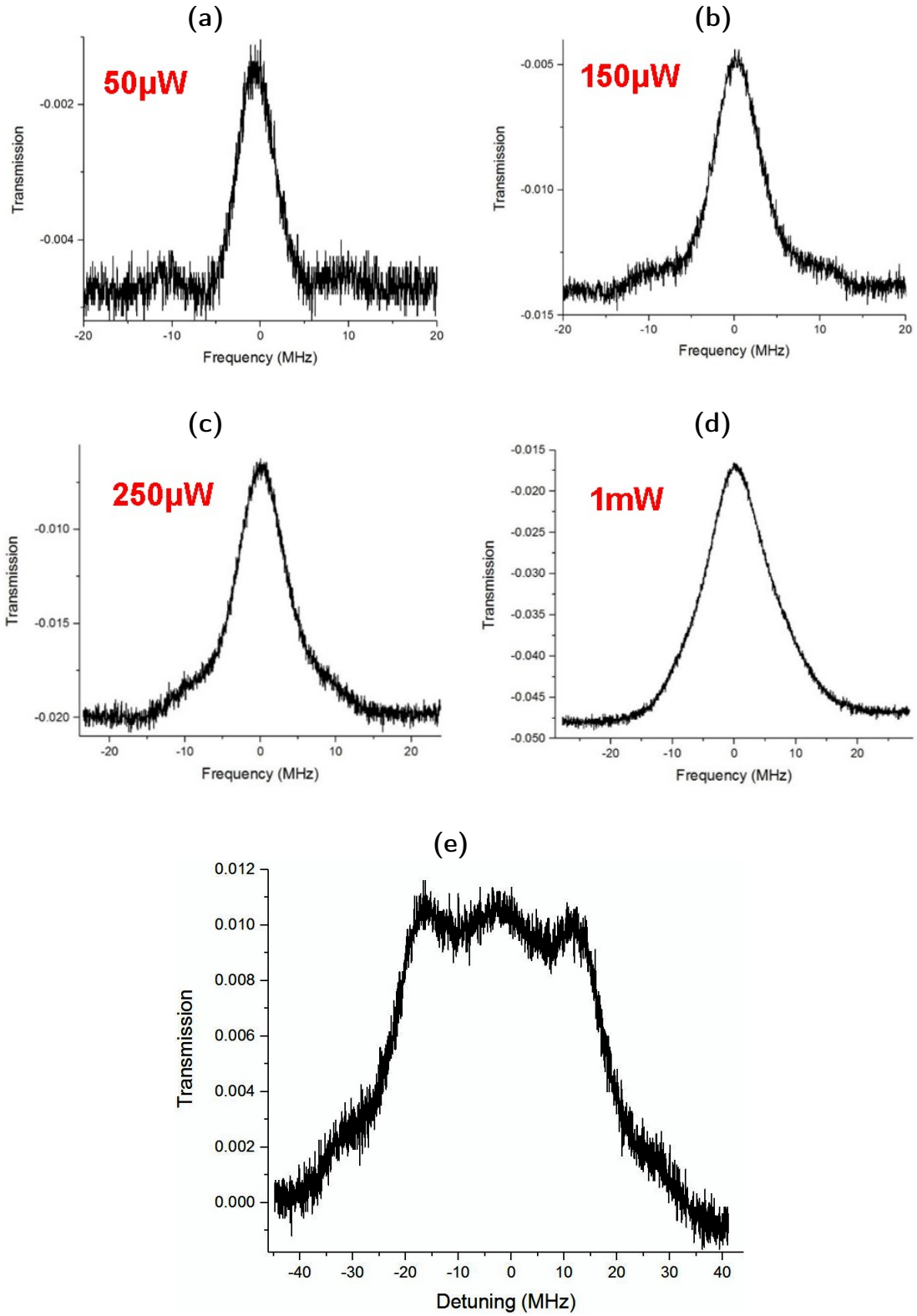

FIGURE 3.8: Transparency peaks showing both the carrier and the sidebands at the probe modulation frequency ($\sim$ 10 MHz). The sidebands fade away as the probe power increases. For the plots, coupling laser power = 100 mW, probe laser power **(a)** 50 μW, **(b)** 150 μW, **(c)** 250 μW, **(d)** 1 mW; **(e)** for modulation frequency $\sim$ 10MHz and amplitude $\sim$ 10 V_{pp} with higher order sidebands.

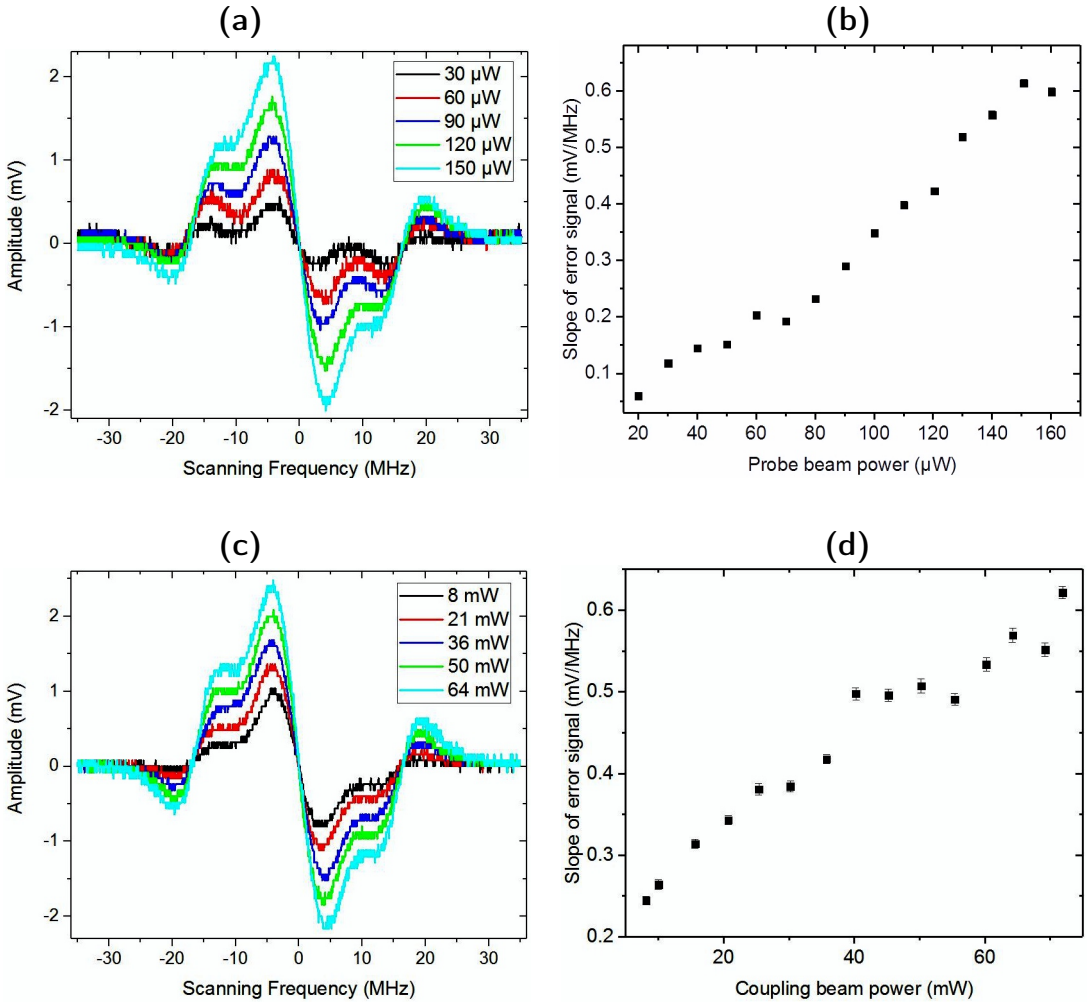

FIGURE 3.9: Error signals for varying **(a)** probe beam power, **(b)** coupling beam power; Slope of the error signal for **(c)** varying probe beam power while the coupling beam power is fixed at 68 mW, **(d)** varying coupling beam power while the probe beam power is fixed at $150\,\mu$W.

in relation to modulation transfer spectroscopy to produce a steep-gradient flat background error signal with clear zero-crossing at the top of the reference peak suitable for locking was described as the first step of the excitation system. The second step of the excitation scheme was described by stabilisation of the 480 nm by exploiting the transparency features obtained from Rydberg spectroscopy. Implementing this two-photon excitation scheme and performing experiments in the level of thermal atoms in a vapour cell is the bedrock for demonstrating dipole blockade effect and controlling the mechanism required for creating many-body entangled state from ground state hot and, most importantly, ultracold atoms. The effects of long-range Rydberg interactions are studied in the next chapter by exploiting the influence of quantum interference phenomena that occur during two-photon transition processes.

4 Quantum Interference Phenomena in Three-Level Rydberg Gases

As discussed in section 1.5, in the study of two-photon excitation, attention is drawn towards coherent processes that occur due to the quantum interference between different $|1\rangle \rightarrow |2\rangle$ excitation pathways that are opened as a result of the presence of the coupling field. Depending on the relative strengths of the coupling and probe fields, phenomena such as electromagnetically induced transparency (EIT), Autler-Townes splitting (ATS) and coherent population trapping (CPT), are associated to either constructive (ATS) or destructive interference (EIT and CPT) of the excitation pathways. In section 3.3.2, these phenomena were used to identify Rydberg transitions, as they are all observed as transparency features in the absorption profile when two resonant laser fields interact with the atomic vapour. For non-interacting atomic systems, these phenomena have been studied extensively and have practical application in precision spectroscopy [22], slowing and storing of light [20, 21], storing and manipulating quantum information [149, 150] to mention but few. However, novel application viewpoints are opened within interacting atomic systems, such as in the implementation of quantum gates and simulators as well as in the generation of many-body entanglement.

This chapter is divided into two parts. In part A, the theoretical and experimental study of the coherent atom-light interaction in a non-interacting atomic system is done. The theoretical description of two-photon excitation is extended to the case of several non-interacting atoms. The optical Bloch equations are solved to study the optical response of the multi-atom system to laser light in EIT, ATS, and CPT regimes. Furthermore, having obtained the transparency peaks for $20\mathrm{D}_{3/2}$ and $20\mathrm{D}_{5/2}$ Rydberg states for ^{87}Rb as described in section 3.3.2, the quantitative analysis of the transparency features is done. However, the setup described in figure 3.1 imposes some broadening effects on the transparency features which make the analysis of the transparency features difficult and the system inappropriate for Rydberg interaction experiments. Hence, this chapter describes a modified setup which is a more sophisticated extension of the setup described in figure 3.1. As a result, the transparency features are

analysed with a focus on studying the linewidths of the excitation transparency features in comparison to an experimentally realistic theoretical model. Numerous efforts that have dealt with differentiating interference phenomena in three-level atomic systems have majorly considered Λ-type systems, considering ideal conditions such as Doppler-free cold $|1\rangle \rightarrow |2\rangle \rightarrow |3\rangle \rightarrow |2\rangle$ atomic systems, vanishing laser linewidths or limited by the weak probe-field limit. This work explores the transition between interference phenomena in a Doppler-broadened three-level ladder system, i.e. atoms in a vapour cell, for the case where ideal conditions are not necessarily satisfied. This allows for laser parameters such as laser linewidths, beams sizes and Rabi frequencies to be obtained from fitting the experimental data to the theoretical model.

Posing additional challenges is the simultaneous treatment of quantum interference phenomena and long-range interactions. Typically, for atomic gas in a magneto-optical trap (MOT) or vapour cell whose densities are considered dilute, the atomic interaction in the ground state is very weak. However, due to the large polarisability of Rydberg atoms which is $\propto n^7$ (where n is the principal quantum number), the Rydberg atoms can still strongly interact with each other. As discussed in section 2.2, a fascinating consequence of strong Rydberg-Rydberg interaction is the dipole blockade effect which occurs when the energy shift, given by equation (2.6) and described in figure 2.5, is large enough (larger than the excitation linewidth) to push resonant frequencies outside the laser bandwidth thereby causing inhibition of multiple excitations in an ensemble of atoms. So in part B of this chapter, the theoretical model is extended to investigate the effects of strong Rydberg-Rydberg interactions in the presence of different coherent phenomena. The study is done for different atomic densities and interaction strengths for atoms in a vapour cell and ultracold atoms in magneto-optical and optical dipole traps. An efficient Monte-Carlo approach is developed to describe the optical response of a multi-atom system to laser light in the regimes of EIT, ATS and CPT and strong atomic interactions. Similar to the study done in part A, the focus will be on studying the lineshape and linewidths properties of the excitation transparency features. The main result of this study confirms that the linewidths properties interestingly show the dependence of the collective Rabi frequency on the square root of the mesoscopic size on the interacting atoms. This is a compelling evidence for observing collective many-body behaviour associated with the production of many-body entangled state between ground and Rydberg levels. This study could help to quantify and control the conditions necessary for the creation of many-body entanglement in atomic ensembles.

PART A

4.1 Many-body theory of the excitation dynamics of non-interacting system

In section 1.3, the solution for the optical Bloch equations was obtained for a single three-level atom. The physical atomic system considered does not generally contain one atom but an ensemble. Thus, it is required to solve a laser-driven interacting many-particle problem whose theoretical description is more challenging. The quantum many-body wavefunction was simulated by direct numerical solution of the Schrödinger equation in [35]. This enabled the investigation of the fraction of excited atoms and the correlation of excited atoms in an atomic ensemble for different types of excitation and in the case where the blockade region is small compared to the sample size. In the study, the blockade phenomenon, which limits the number of excitations in an ensemble, allowed for a substantial reduction in the number of states that were considered for the calculations. However, there was still limit to the number of atoms that could be simulated. As such, appropriate boundary conditions were employed to establish contact with the experiments. Taking a similar approach to [35], this study follows a direct numerical solution of the OBEs, as done in section 1.3, for N-atom system.

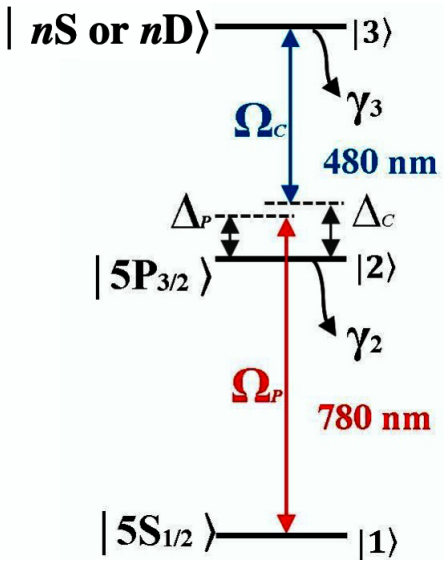

FIGURE 4.1: Three-level ladder-type scheme with the corresponding states shown.

The three-level ladder atomic system considered in this study and the corresponding laser parameters as shown in figure 4.1 have been described in section 1.3. The conditions for differentiating the EIT/ATS/CPT regimes based on the relative strengths

of the probe and coupling beams have been described in section 1.5.1. This model considers generic values of the Rabi frequencies and does not indicate the specific polarisation of the beams, thus not specifying the transitions between hyperfine levels of the atoms as seen in experiments. Furthermore, this study assumes a closed transition between the three atomic levels so that Rydberg atoms only decay back to the intermediate state. Practically, there is a possibility for Rydberg atoms to decay into other ground states. This opens way for the study of atom excitations beyond three-level systems. In such cases, branching factors that account for the weights or probability of every possible decay branch are included in the model.

4.1.1 Many-body excitation dynamics in a non-interacting system

Extending the single-atom discussion done in section 1.3, a system composed of N three level atoms is now considered. The quantum master equation for N-particle density matrix

$$\rho_A(t) \equiv \rho^{(N)} = \rho_1 \otimes \cdots \otimes \rho_N \tag{4.1}$$

is of the type stated in equation (1.7), now written as

$$\frac{\partial \rho^{(N)}}{\partial t} = -\frac{i}{\hbar}\left[{\mathcal{H}_A}^{(N)}, \rho^{(N)}\right] + \mathfrak{D}[\rho^{(N)}] \,, \tag{4.2}$$

where the N-particle Hamiltonian describing the interaction of the levels of each ith atom with the radiation field is given by

$${\mathcal{H}_A}^{(N)} = \sum_{i=1}^{N} \bigotimes_{j=1}^{i-1} \mathbf{1}_3 \otimes {\tilde{\mathcal{H}}_3}^{(i)} \otimes \bigotimes_{j=i+1}^{N} \mathbf{1}_3 \,, \tag{4.3}$$

where ${\tilde{\mathcal{H}}_3}^{(i)}$ is the generic single-particle time-independent three-level Hamiltonian, given in equation (1.26), describing the coherent evolution of the ith atom.

The phenomenological decoherence matrix $\mathfrak{D}\left[\rho_A(t)\right] = \mathfrak{D}\left[\rho^{(N)}\right]$ given in equation (1.8) to account for decay and dephasing processes in the system is obtained from the set of Lindblad operators $\mathcal{L}$ which are given by atomic projection operators $|\alpha\rangle\langle\beta|$, where $\alpha, \beta = 1, 2, 3$ are atomic energy levels. So for the kth atom in a N-atom system, the set of Lindblad operators is a sum of terms for each atoms such that

$$\mathcal{L}_k = \sqrt{\gamma} \bigotimes_{j=1}^{k-1} \mathbf{1}_3 \otimes |\alpha\rangle\langle\beta|^{(k)} \otimes \bigotimes_{j=k+1}^{N} \mathbf{1}_3 \,, \tag{4.4}$$

γ denotes either the non-energy conserving spontaneous decay rate or the energy conserving dephasing of a state. $\gamma = \gamma_2, \gamma_3$ are the rates of spontaneous decay from the intermediate and Rydberg states respectively. $\gamma = \gamma_{2d}, \gamma_{3d}$ are the dephasing rates of the off-diagonal coherence terms for the states coupled to the laser fields. γ_{2d}, γ_{3d} are determined by the finite linewidths of the probe and coupling beams respectively. The linewidths of the laser beams are obtained later in section 4.2.3. For ^{87}Rb atoms considered in this study, $\gamma_2 = 6.065$ MHz, $\gamma_{2d} = 0.38$ MHz and $\gamma_{3d} = 0.19$ MHz. The value of γ_3 depends on the Rydberg level (n) considered but it is usually $\lesssim 0.019$ MHz for $n \geq 20$.

Substituting equations (4.1), (4.3) and (1.8) in equation (4.2) result in the set of optical Bloch equations (OBEs) for the N-atom populations and coherences. The numerical solutions of the OBEs are obtained with a code written in Mathematica. Using the average population $\tilde{\rho}_{22}$ of intermediate state, one can determine the probe scattering rate

$$R_{\text{sc}} = \gamma_2 \tilde{\rho}_{22} \ , \tag{4.5}$$

which yields the absorption of the probe beam as a function of the scanned laser across resonance. In the many-atom picture, the N-body intermediate state population $\tilde{\rho}_{22}$ is obtained by the weighted sum of the probabilities of having N' atoms, for $1 \leq N' \leq N$, in the intermediate state. To be consistent with experimental procedure described in section 3.3.2, the probe laser is locked to the resonance of $|1\rangle \rightarrow |2\rangle$ transition frequency, thus $\Delta_P = 0$, while the coupling laser is scanned across the resonance of the upper $|2\rangle \rightarrow |3\rangle$ transition. Hence, the theoretical probe absorption spectrum mimics the experimental transparency peak shown in figure 3.7(c). First, this makes it easy to fit the experimental data using the theoretical model in order to obtain laser parameters. Secondly, the approach produces a spectrum that can easily be visualised as and approximated by a Lorentzian function. The fit of this spectrum can easily be done to produce the linewidth of the transparency feature. The linewidth of the spectrum can be used as a means to differentiate the EIT, ATS and CPT regimes.

To properly simulate the experimental procedure described in section 3.3.2, the coupling laser is scanned across resonance as slow as possible in time. This is achieved by inserting

$$\Delta_C = \frac{t - t_c}{\delta_r} \tag{4.6}$$

in the calculation. t_c is a parameter that determines the scan time while δ_r denote scan rate. This scan time ranges within $0 \leq t \leq 2t_c$ so that the coupling beam detuning ranges within $-\frac{t_c}{\delta_r} \leq \Delta_C \leq \frac{t_c}{\delta_r}$. Thus, the laser scan range can be adjusted by simply

changing the ratio $\frac{t_c}{\delta_r}$.

One would recall from section 1.3 that the single-atom OBEs in equation (1.28) were solved analytically by assuming a system in steady-state, i.e. the time derivatives of the density matrix is set to zero. Due to computational requirement of the numerical model, δ_r is chosen to ensure that the solution of the density matrix elements produce spectra similar to the steady-state solution. Also, it should be noted that there is a spatial variation of the Rabi frequencies due to the Gaussian intensity distribution of the laser beam. Giving that the dark state is populated at resonance, there is a region around the peak value of the Rabi frequency such that the system is not relaxed into the dark state after the short duration of the laser pulse due to smaller Rabi frequencies [36]. The scan rate must be slow enough for a large percentage of dark state relaxation to occur. On the other hand, the choice of δ_r also determines the computation time. Hence, the choice of δ_r is a compromise between obtaining the right results and minimising computing resources. So, for the calculation, the scan rate of $5\,\mu$s/Hz is considered. Choosing $\delta_r < 5\,\mu$s/Hz would cause the probe absorption spectrum to have spurious spikes or causes a shift effect on the spectrum.

For N non-interacting atoms, the N-atom density matrix factorises completely and the evolution of the atoms is decoupled. Thus the problem is equivalent to the evolution of an independent three-level single atom as described in section 1.3. Figures 4.2(a)-(c) show the plot of the probe photon scattering rate as a function of coupling beam detuning scanned across resonance. The probe scattering rate provides a way to accurately determine the population of a Rydberg-state since the information about the Rydberg state transition is transferred to the probe transition. Figures 4.2(a) shows the comparison between the exact and numerical solutions of the single atom case while figures 4.2(b)-(c) show the comparison of the 2- and 3-atom case to the single-atom exact solution. The result shows that there is no difference between the exact solution of the OBEs for a single atom (dashed black line) and the numerical solution for the OBEs for 1, 2 and 3 non-interacting atoms in the $20\mathrm{D}_{\frac{5}{2}}$ state in the ATS/CPT regime. Although not shown graphically, the similarity of the single-atom solution and N non-interacting atoms solution occurs for any value of Ω_P, be it low or high. Changing the probe beam Rabi frequency only changes the amplitudes of the traces.

Giving the result shown in figures 4.2(a)-(c), distinguishing between the EIT, ATS and CPT regimes is not easily visualised from the transparency lineshape properties. Hence, it is intuitive to turn to the transparency linewidth properties. This can be done by

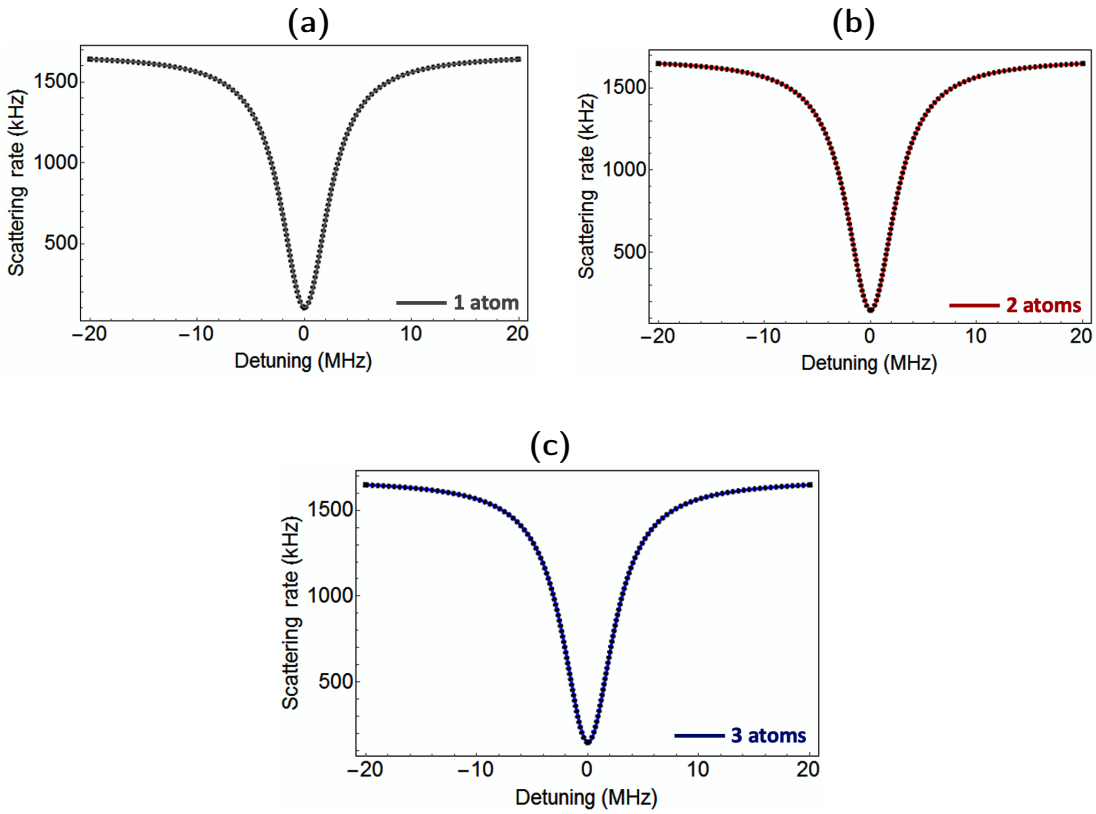

FIGURE 4.2: Comparison between the exact solution of the OBEs for a single atom (black dashed line) and the numerical solution of the OBEs for the case of **(a)** 1 atom (grey line), **(b)** 2 (red line) and **(c)** 3 (blue line) non-interacting atoms. In the plots, $\Omega_C = 5$ MHz, $\Omega_P = 5$ MHz, $\gamma_2 = 6.065$ MHz, $\gamma_3 = 0.019$ MHz, $\gamma_{2d} = 0.38$ MHz and $\gamma_{3d} = 0.19$ MHz.

fitting the probe absorption spectrum to a Lorentzian function and obtaining the full width at half maximum (FWHM) from the fit. This is also done to the transparency features obtained from experimental measurements. As such comparison can be done between theoretical and experimental results. However, there is a need to obtain laser parameters such as laser linewidths, beams sizes and Rabi frequencies. Obtaining the beam Rabi frequencies would require fitting the experimental data to the theoretical model. The next section describes the experimental setup and procedures for obtaining and analysing the transparency features from two-photon excitation.

4.2 Quantitative Analysis of Transparency Features: Vapour Cell Experiment

To study the behaviour of interacting and non-interacting atoms in a vapour cell, experiments are performed using the setup in figure 3.1. The Rydberg excitation

is as a result of a two-photon excitation process in a three-level ladder atomic system, as shown in figure 4.1. The probe beam, which is produced by a 780 nm laser beam, is stabilised to be resonant with the ^{87}Rb D2 optical transition between hyperfine levels $|1\rangle = |5S_{1/2}, F = 2\rangle \rightarrow |2\rangle = |5P_{3/2}, F' = 3\rangle$ with a transition strength given by the Rabi frequency Ω_P. Measurements are focused majorly on ^{87}Rb in order to be consistent with the atomic species that will be used in the trapping systems. A 480 nm coupling beam drives the $|2\rangle = |5P_{3/2}\rangle \rightarrow |3\rangle = |n\mathrm{D} \text{ or } n\mathrm{S}\rangle$ Rydberg transition with transition strength given by Rabi frequency Ω_C. To explore the non-interacting regime, the coupling beam, is stabilised on resonance with the $|2\rangle = |5P_{3/2}, F' = 3\rangle \rightarrow |3\rangle = |20D_{5/2}\rangle$ transition. Locking the probe beam and allowing the coupling probe beam and scanning the coupling beam across resonance produces transparency features similar to the one in figure 3.7(c).

The quantitative analysis of the transparency features is done for varying relative strengths of the probe and coupling fields. As a result, one is able to make transitions between the EIT, ATS and CPT regimes. In the experiment, the dependence of the transparency lineshape on the detunings of the beams is neglected because a two-photon resonance condition is assumed. In a Doppler-broadened system such as atoms in a vapour-cell, the transparency lineshape is well approximated by a Lorentzian function which is used to fit the transparency features to obtain the FWHM. Fitting the spectrum to the theoretical scattering rate for one atom (or for many non-interacting atoms which is considered unnecessary) allows experimental parameters such as the laser Rabi frequencies and the laser linewidths to be determined. The values of experimental parameters obtained from this scattering rate fit are then used in the calculations to obtain spectrum in order to check the agreement between the theoretical and experimental values for the transparency linewidths and in further study, the lineshape properties of interacting atoms.

Obtaining the values for the laser Rabi frequencies have been found to be useful in obtaining other experimental parameters. The relationship between the laser power and the electric field amplitude given by the peak laser intensity, for a Gaussian beam, reads

$$I = \frac{n_0\, c\, \epsilon_0\, E^2}{2} = \frac{2\, P}{\pi\, \omega_0^2}\,, \tag{4.7}$$

where P is the laser power, c is the speed of light, ϵ_0 is the permittivity of free space, n_0 is the refractive index of the medium and ω_0 is the waist of the beam. Using equation (1.18) for the Rabi frequency of the beam coupling two atomic states $|i\rangle \rightarrow |j\rangle$, it

implies that

$$\Omega_{ij} = \frac{2\,|\mu_{ij}|}{\hbar}\sqrt{\frac{P_{ij}}{\pi\, n_0\, c\, \epsilon_0\, \omega_0^2}}\ . \tag{4.8}$$

This shows that for a specific transition, the Rabi frequency Ω_{ij} is directly linked to the square root of the power P_{ij} of the laser driving the transition, with the dipole moment $|\mu_{ij}| = \mu_n$ as the linear coefficient. From the experimental measurements performed in [151], the value for the transition dipole moment was extracted for each n by exploiting the Autler-Townes effect for different values of the laser power. With the value of Ω_{ij}, one can easily to estimate the size of the laser beams. It should be noted that peak value of the laser intensity (from equation (4.7)) is used experimental measurements due to an assumption that the beam intensity is homogeneous across the profile. In actual fact, the intensity of the beam is inhomogeneous across the profile as a result of the Gaussian spatial distribution of its intensity profile.

4.2.1 The effect of beam polarisation

Preparing the atoms in appropriate and known states offer two advantages. First, it gives room to maximise the transition strength and more importantly, to make analysis of experimental results as easy as possible. Being able to vary the polarisation and frequency of the beams makes it possible to control not just the state selection rules for transitions between hyperfine levels, but also the coupling strengths to specific fine states. From the $5P_{3/2}$ intermediate state, one is able to select between the $nS_{1/2}$, $nD_{3/2}$ or $nD_{5/2}$ fine states. As shown in figure 3.7, the $nD_{3/2}$ and $nD_{5/2}$ states are separated by few GHz which makes it possible to view both states within the coupling laser frequency scan range. However, the transition strength for $D_{5/2}$ states are stronger than for $D_{3/2}$ states, while $S_{1/2}$ states have the weakest. Thus, this study will only focus on $D_{5/2}$ states because of their tendencies to produce larger signal-to-noise ratio in the low-probe limit.

The polarisation of the beams determines the F and m_F states to be addressed. From the selection rules, it follows that only transitions with $\Delta F = -1,\, 0,\, +1$ and $\Delta m_F = -1,\, 0,\, +1$ are allowed, and they are induced by the absorption of left-circularly (σ_-), linearly(π) and right-circularly (σ_+) polarised beam respectively. This implies that if both the coupling and probe beams are both in σ_+-σ_+ via appropriate setting of the $\lambda/4$-waveplates, then the transitions $|5S_{1/2},\, F = 2,\, m_F = 2\rangle \rightarrow |5P_{3/2},\, F = 3,\, m_F = 3\rangle \rightarrow |nD_{5/2},\, F = 4,\, m_F = 4\rangle$ are maximised.

The transition strengths between two coupled hyperfine sublevels $|F\, m_F\rangle \rightarrow |F'\, m_{F'}\rangle$

are characterised by the dipole matrix elements given by

$$\mu_q = \langle \mathsf{F}\, m_{\mathsf{F}} |\, e\, r_q \,| \mathsf{F}'\, m_{\mathsf{F}'} \rangle \ , \tag{4.9}$$

where $q = 0, \pm 1$ is the index denoting the spherical components of $\mathbf{r}$. Since the operator $e\mathbf{r}$ does not act on the subspace of quantum number I, it is intuitive to decouple μ_q into the fine structure basis (i.e. J, m_{J}). Using the Wigner-Eckart theorem [152, 153], μ_q can be expressed as a product of an angular-dependent factor using the Wigner 3-j symbol, which is equivalent to the Clebsch-Gordan (C-G) coefficients, and a reduced matrix element

$$\mu_q = (-1)^{\mathsf{F}'+m_{\mathsf{F}}-1} \sqrt{2\mathsf{F}+1} \begin{pmatrix} \mathsf{F}' & 1 & \mathsf{F} \\ m_{\mathsf{F}'} & q & -m_{\mathsf{F}} \end{pmatrix} \langle \mathsf{F} \,||\, e\,\mathbf{r} \,||\, \mathsf{F}' \rangle \ . \tag{4.10}$$

The 3-j symbol is non-zero only for $m_{\mathsf{F}'} + q = m_{\mathsf{F}}$. Due to the fact that the electric dipole Hamiltonian only couples to the J angular momentum, the F-F$'$ dependent reduced matrix element can be further simplified into J-J$'$ dependence by using the Wigner 6-j symbol

$$\langle \mathsf{F} \,||\, e\,\mathbf{r} \,||\, \mathsf{F}' \rangle = (-1)^{\mathsf{F}'+\mathsf{J}+\mathsf{I}+1} \sqrt{(2\mathsf{F}'+1)\,(2\mathsf{J}+1)} \begin{Bmatrix} \mathsf{J} & \mathsf{J}' & 1 \\ \mathsf{F}' & \mathsf{F} & \mathsf{I} \end{Bmatrix} \langle \mathsf{J} \,||\, e\,\mathbf{r} \,||\, \mathsf{J}' \rangle \ . \tag{4.11}$$

The operator acts on the subspace spanned by quantum number L. So, one can still further reduce the J-dependent matrix element to L-dependent matrix element using the 6-j symbol while the matrix element is further calculated using the Numerov algorithm [154]. However, this is a bit complicated and equation (4.11) should suffice. Thus, for every polarisation configuration of the beams, in order to fit experimental data correctly, the measured Rabi frequencies from equation (4.8) are scaled by the overall C-G factors given in appendix C.

Considering four different polarisation configurations for the probe-coupling setup: σ_+-σ_+, σ_+-π, π-σ_+ and π-π configurations which results in C-G coefficients of $\sqrt{\frac{1}{2}}$ - $\sqrt{\frac{2}{3}}$, $\sqrt{\frac{1}{2}}$ - $\left(-\sqrt{\frac{1}{6}}\right)$, $\left(-\sqrt{\frac{1}{6}}\right)$ - $\sqrt{\frac{1}{2}}$ and $\left(-\sqrt{\frac{1}{6}}\right)$ - $\left(-\sqrt{\frac{2}{7}}\right)$ respectively for the probing-coupling transitions. If the generalised Rabi frequency is written as

$$\Omega = \Omega_C \sqrt{\zeta_C^2 + \zeta_P^2 \left(\frac{\Omega_P}{\Omega_C}\right)^2} \ , \tag{4.12}$$

where ζ_P and ζ_C are the C-G coefficients for the probe and coupling transitions respectively. Intuitively, equation (4.12) implies that the σ_+-σ_+ configuration has the

highest two-photon transition strength irrespective of the value of the ratio $\frac{\Omega_P}{\Omega_C}$. On the other hand, the transition strengths of the σ_+-π, π-σ_+ and π-π configurations are largely dependent the ratio $\frac{\Omega_P}{\Omega_C}$.

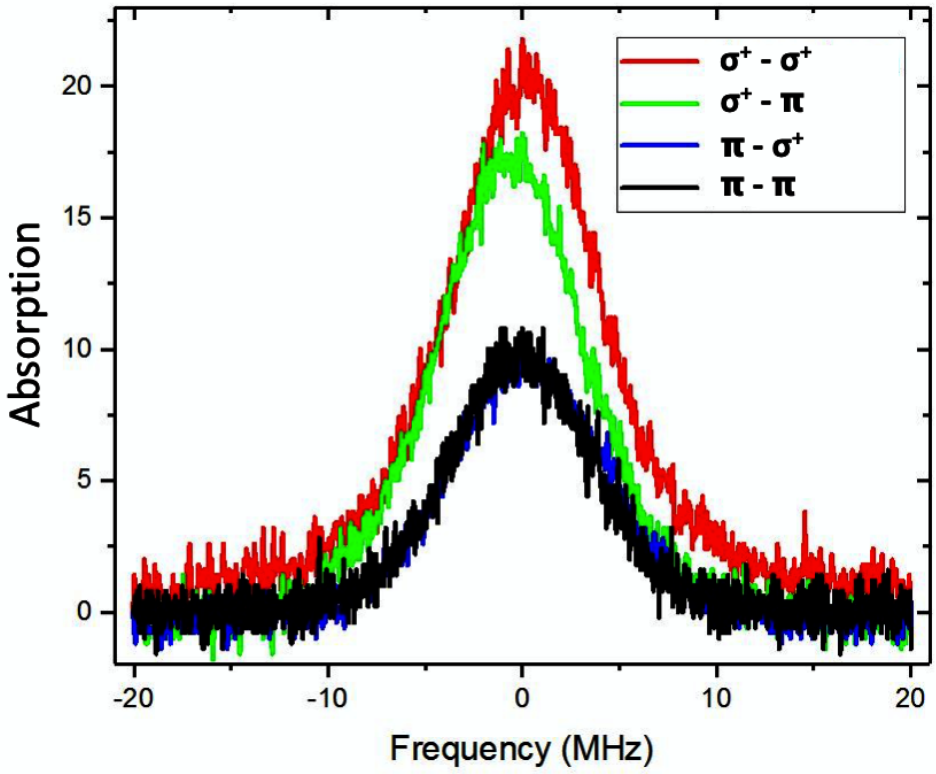

FIGURE 4.3: Plot of the absorption spectra for different configurations for the polarisation of the Rydberg excitation laser beams. For these plots, probe beam power = 100 μW and coupling beam power = 16 mW

A typical set of transparency features for different polarisation configurations for a 100 μW locked probe beam and a 16 mW coupling beam which is unlocked and allowed to freely scan across resonance is shown in figure 4.3. It can be confirmed that the σ_+-σ_+ configuration has the highest two-photon transition strength. The difference between the configurations is from the fact that σ_+-polarised probe beam allows for more probe absorption while σ_+-polarised coupling beam increases the Rydberg coupling strength. One would rather be required to obtain the sizes of the beams and obtain their resulting Rabi frequencies (see equation (4.8)) to confirm the ratio $\frac{\Omega_P}{\Omega_C}$. As will be described later, one way to achieve this is by further investigating the transparency features by fitting the experimental spectrum with the theoretical single-atom model.

To investigate the transparency features using the setup shown in figure 3.1, the σ_+- σ_+ polarisation configuration of the beams is adopted so that the probe beam

is locked to the $|5S_{1/2}, F = 2, m_F = 2\rangle \rightarrow |5P_{3/2}, F = 3, m_F = 3\rangle$ transition while the coupling beam is allowed to scan freely across the $|5P_{3/2}, F = 3, m_F = 3\rangle \rightarrow |20D_{5/2}, F = 4, m_F = 4\rangle$ resonance. The beam polarisations are set by simply tuning the $\frac{\lambda}{4}$-waveplates, the ones closest to the Mu-shielded vapour cell Rb(3), so that the amplitude of the transparency feature is maximised for specific choices of beam strengths. The coupling beam scan is done with the Toptica Piezo Scan Control SC 110 module and it is allowed to scan at a frequency of about 10 Hz over a range of 2 GHz across the $20D_{5/2}$ and $20D_{3/2}$. However, experimental procedures are limited by the photodiode bandwidth. Allowing a 2 GHz coupling beam scan for about 10 times per second is considerably too fast as the photodiode response is not fast enough follow such fast scan. Thus, creating a different limitation for the experiment as compared to the numerical model.

Leaving the blue laser unlocked increases the blue laser jitter. Thus, estimates for the laser parameters such as the laser linewidth or Rabi frequency would be considered too crude. Also, the probe modulation frequency and driving amplitude used for driving the electro-optic modulator (EOM) are carefully chosen to obtain only first order sidebands. This is done to avoid the contributions of the higher harmonics of the sidebands to the spectrum broadening. However, in the low probe regime, the carrier-sideband power ratio is low and it is difficult to resolve the carrier from the sidebands, thus contributing to the broadening of the transparency feature. One way to avoid this is to reduce the drive amplitude of the probe modulating signal obtained from the oscillator. On one hand, it will not be a problem since the blue laser was not locked. On the other hand, this reduces the amplitude of the error signal, thus resulting in a failing of the probe locking system and thereby causing probe laser frequency fluctuation. It is therefore necessary to modify the experimental setup shown in figure 3.1 to accommodate a section for properly locking the lasers and a separate section that can be used to perform two-photon transition experiments in a vapour cell in order to investigate Rydberg-based phenomena.

4.2.2 The experimental setup

The new setup for the frequency stabilisation and locking system of the two-photon excitation lasers is shown in figure 4.4. Similar to the description given in section 3.2.2, the 780 nm probe laser is locked using the modulation transfer spectroscopy (MTS) technique. This is done by using the Rb saturated absorption spectrum produced as a result of the four-wave mixing phenomenon that occurs when the EOM-modulated part of the probe beam and the unmodulated part interact with the Rb atoms in the vapour cell Rb(1). Also, as described in section 3.3.2, the coupling laser is stabilised by

taking advantage of the transparency feature produced as a result of the interference phenomenon that arises when both the coupling and probe beams interact with the Rb atoms in the vapour cell Rb(2).

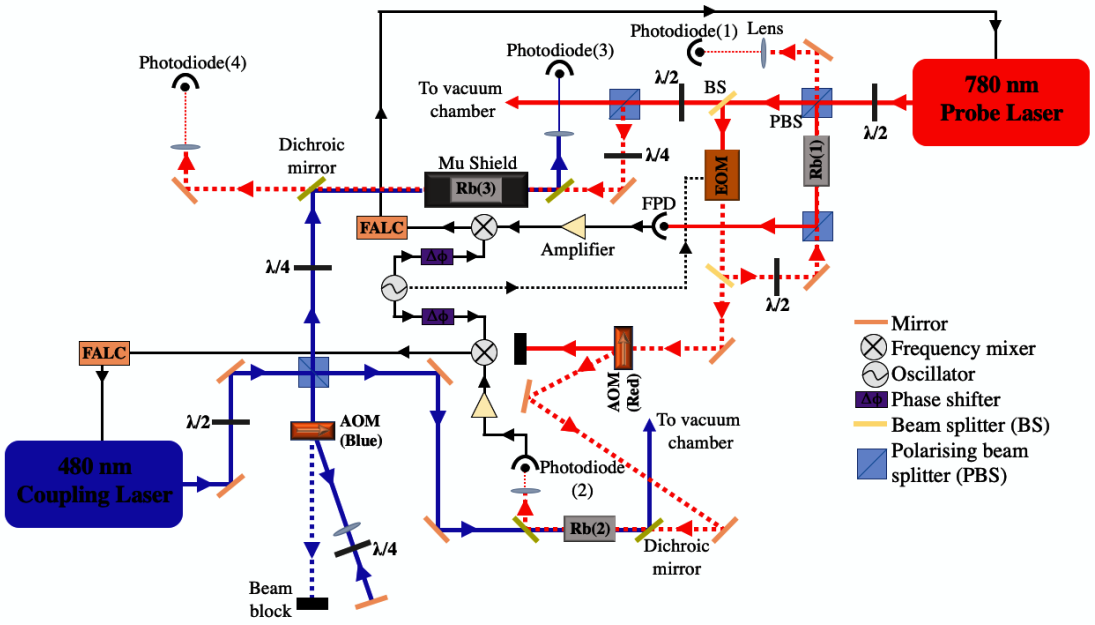

FIGURE 4.4: New schematics of the experimental setup for two-photon excitation. The 780 nm probe laser is frequency locked using MTS technique while the 480 nm coupling laser is locked by exploiting transparency signal.

In this setup, the blue beam is first split into two parts using a polarising beam splitter (PBS). One part is sent through the vapour cell Rb(3) to obtain the locking spectrum. Unlike in the previous setup, the coupling laser locking system is implemented with a shift, $-\delta f_p$, in the EOM-modulated probe beam frequency using an Isomet 1206C acousto-optic modulator (AOM) in a single pass configuration, resulting in a frequency shift of the probe saturated absorption detected by the photodiode(2) by $-\delta f_p$. The AOM, whose central frequency is 110 MHz and bandwidth 50 MHz, is driven by Isomet 630C-100 AO driver at the calibrated rate of 6.06 ± 0.08 MHz/V (shown in figure 4.5(a), the plot of the drive voltage versus the corresponding frequency shift produced by the AOM).

The other part of the coupling beam is shifted in frequency by a Gooch and Housego (G&H) M110-2B/F-GH1 AOM in a double pass configuration before it is guided through a Mu-shielded vapour cell Rb(3) where it is aligned to overlap with a counterpropagating unmodulated probe beam. This blue laser AOM also has a central frequency of 110 MHz and bandwidth of 50 MHz, and is driven at the calibrated rate of 5.82 ± 0.05 MHz/V (as shown in figure 4.5(b)). The double pass allows the

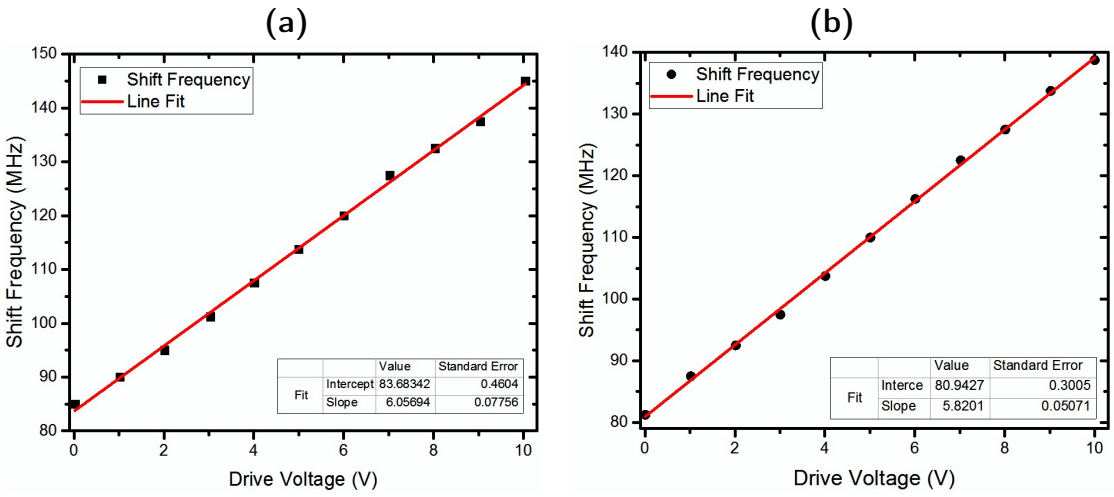

FIGURE 4.5: Plot of shift frequency as a function of the AO drive voltage in order to obtain the calibrated frequency shift per unit voltage for the AO driver driving the **(a)** Isomet AOM used for modulating the probe beam; **(b)** Gooch and Housego AOM used for modulating the coupling beam.

frequency-tuning range of the coupling beam to be widened, as it doubles the AOM bandwidth. The transparency feature obtained on photodiode(4), which is a Thorlabs DET100A Si Detector, are void of the EOM modulation sidebands and their contribution to the transparency linewidth broadening. The mirror and the lens downstream from the blue AOM combine to form the *cat's eye retro-reflector* [155]. The lens is placed at an equal spacing, the lens focal length, between the AOM and the mirror for optimum performance. This removes an expected large angular drift of the beam. This is because since the beam alignment is optimised for a single drive RF frequency, the mirror angle would normally have to change as the angle of first-order beam changes due to changing drive frequency. The lens turns the swing into a position movement. As such, the retro-reflected beam has a small translational offset, rather than an angular change, as well as being collimated. The setup ensures that the coupling beam remains aligned with the unmodulated probe beam all through the scan range. The $\frac{\lambda}{4}$-waveplate is used to convert a vertically-polarised blue laser into a horizontally-polarised beam on the second pass through the AOM.

Due to the motion of the atoms, Doppler effect causes the atoms to see the counter-propagating probe and coupling beams shifted by $\pm\vec{k}_{\mathrm{p}} \cdot \vec{v}$ and $\mp\vec{k}_{\mathrm{c}} \cdot \vec{v}$. Both shifts can be easily related by

$$\vec{k}_{\mathrm{p}} \cdot \vec{v} = \left(\frac{\lambda_{\mathrm{c}}}{\lambda_{\mathrm{p}}}\right) \vec{k}_{\mathrm{c}} \cdot \vec{v}\ , \tag{4.13}$$

where $\vec{k}_p$ and $\vec{k}_c$ are the wavevectors of the probe and coupling beams respectively. Equation (4.13) implies that the shift of the transparency feature detected on photodiode (4), which would normally be $+2\delta f_c$ away from resonance due to the double pass, would be multiplied by a factor $\frac{\lambda_c}{\lambda_p} = 0.62$ when observed compared to a zero-shifted transparency feature. As shown on the oscilloscope data in figure 4.6(a), the blue laser AOM was optimised at the central frequency, 110 MHz and thus at 220 MHz due to the double pass. This results in 136 MHz shift between the second pass first-order peak b_2 and the directly retro-reflected first pass zeroth-order peak b_1. In order to make the transparency peak b_3 from the locking spectrum (photodiode(2)) overlap with the transparency spectrum b_2 from the photodiode(4), the probe beam AOM shift is set at 136 MHz. This also results in similar sub-Doppler peaks (a_1 and a_2) in both probe absorption spectrum being shifted by 136 MHz. Figure 4.6(b) shows the overlapping of the $20D_{\frac{3}{2}}$ and $20D_{\frac{5}{2}}$ peaks from both photodiode (2) and (4) when the probe beam is locked. The error signal (yellow trace) from the Fast Analog Linewidth Control (FALC) is used to lock the coupling beam to the desired peak frequency.

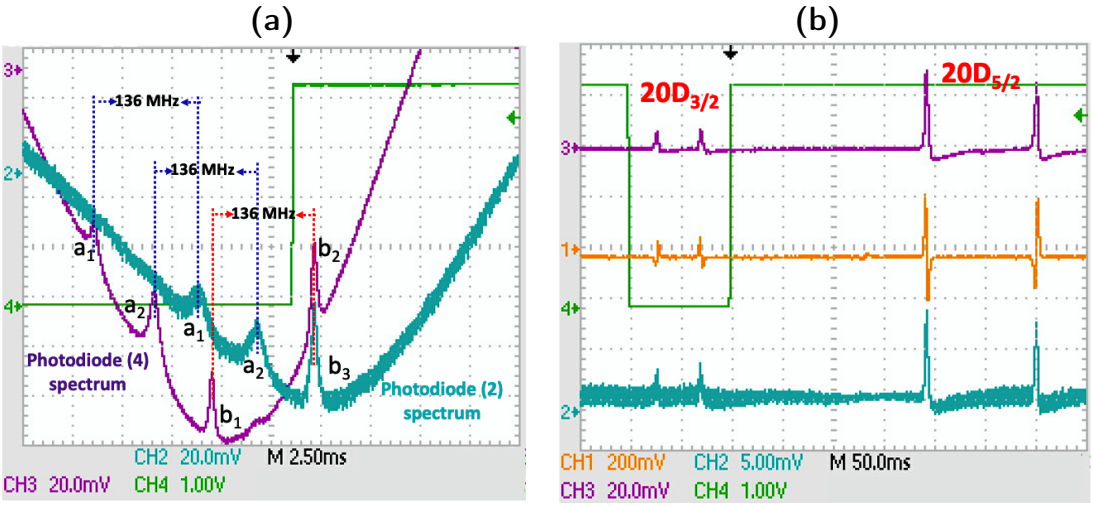

FIGURE 4.6: **(a)** Probe absorption spectra showing the $20D_{\frac{5}{2}}$ transparency peaks when the EOM- modulated probe beam is shifted with single-pass AOM (photodiode (2) cyan line) before being overlapped with an unshifted coupling beam and when an unmodulated probe beam (photodiode (4) purple line) before being overlapped with a coupling beam that was shifted with a double pass AOM. The two transparency peaks on the purple line are obtained when both the directly retro-reflected first pass zeroth-order beam and the second pass first-order beam are overlapped with the unmodulated probe beam; **(b)** Transparency features from the photodiodes (2) (cyan line) and (4) (purple line) when the probe beam is locked and the corresponding error signal (orange line).

With a probe shift of $-\delta f_p$, this implies that the coupling beams are locked at a frequency where the two-photon detuning is $-\delta f_p$ while the coupling beam is scanned

across resonance after being shifted back by the double-pass AOM. The AOMs are externally controlled by LabVIEW software via the voltage control oscillator (VCO) and voltage control attenuator (VCA) that are in-built within the AO drivers to change the scan/shift frequencies and beam intensities respectively. As expected, the power of the coupling beam changes as the frequency scan is done. This can be monitored on the photodiode (3), also a Thorlabs DET100A Si Detector, as shown in figure 4.7(a). Since the coupling beam is required to be roughly constant throughout the scan, it implies that one is only able to scan only few MHz, $\approx \pm 15$ MHz, around the resonance without having a significant change in beam power. In order to increase the scan range, a *piecewise scan approach* is used where the scan range is broken into smaller steps so that the power loss from each step can be compensated for. As such, the coupling beam power can be kept almost constant over a wider scan range, $\approx \pm 30$ MHz around the resonance (as shown in figure 4.7(b)). A typical transparency peak obtained with a $160\,\mu$W probe beam and 9 mW coupling beam is shown in figure 4.8(a) (red line). The plots in figure 4.7 are averaged over 5 scans with each scan taking about 300 seconds.

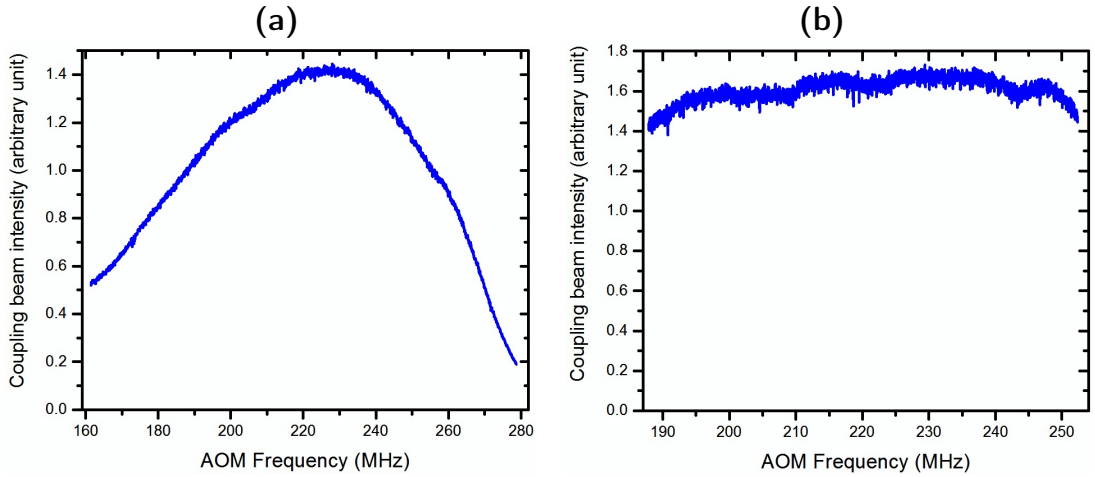

FIGURE 4.7: Coupling beam intensity profile as a function of varying blue AOM frequency. **(a)** when the scan is done in a single step; **(b)** when the piecewise scan approach is used to the break the scan range into smaller steps. The plots are averaged over 5 scans with each scan taking about 300 seconds.

4.2.3 Measuring the laser linewidths

The need to accurately measure and characterise the narrow linewidths of the laser sources arise from the fact that they form an integral part of the analysis of experimental results and modelling physical experiments. The effect of the finite linewidths of laser fields has been said to modify the dephasing rates of the states that are coupled to the fields. The width of the spectrum of a laser beam can be thought of to be

caused by fluctuations in the phase of the optical field which arise from spontaneous emission events that discontinuously alter the phase and intensity of the lasing field [156].

An established method for measuring the linewidth of diode lasers is the *delayed self-homodyne or heterodyne measurement technique* which simply relies on the basic idea of mixing two signals with same or different frequencies while the interference signal is detected with a photodiode[1]. The power spectrum of the photocurrent fluctuations can then be used to obtain the laser linewidth. Similarly, the laser linewidth of the coupling beam can be obtained by overlapping it with the probe beam. Choosing the probe beam as a reference signal is preferable since the photodiode has an extremely higher responsivity for a 780 nm beam compared to a 480 nm beam. To obtain the intensity fluctuation of the coupling beam, the background intensity fluctuation ΔN from the probe laser, when the coupling beam is blocked, is first obtained. This probe intensity fluctuation may be due to the white or flicker frequency noise of the laser, photodiode noise or combination of both [157]. The total intensity fluctuation ΔS is then obtained when the coupling beam is unblocked an allowed to interfere with the probe beam. Hence, it is easy to obtain the pure coupling beam intensity fluctuation ΔV . The intensity fluctuations are obtained by taking the standard deviation of the photocurrent signal. The pure coupling beam intensity fluctuation is calculated by

$$\Delta V = \sqrt{\Delta S^2 - \Delta N^2}\ . \tag{4.14}$$

On an experimental spectrum, the back and forth jitter of the laser is observed in the fluctuation of a voltage signal. This can be observed if the laser is allowed to sit at any point on the transparency peak. It is therefore necessary to obtain the voltage-frequency response produced as a result of the frequency jitter. This can simply be obtained by taking the slope R_{vf} of a line (black line) over the line centre $\frac{V_{max}}{2}$ on a transparency peak as shown in figure 4.8(a). The point on the line centre can definitely be taken from either side of the peak provided the data points that give the steepest slope is chosen. Here, the slope across the line centre is estimated as $\mathrm{R}_{vf} = (23.50 \pm 0.14) \times 10^{-4}$ V/MHz. The noise from the probe beam is obtained by blocking the coupling beam to obtain a flat background photodiode signal of the probe beam (shown in figure 4.8(b)) with estimated fluctuation of $\Delta N = (160 \pm 2) \times 10^{-5}$ V. Then, the AOM is set to about 217 MHz double pass frequency without scanning it so that the coupling laser sits at line centre. This also produces a flat signal with

[1] Detailed studies are done in [157, 158].

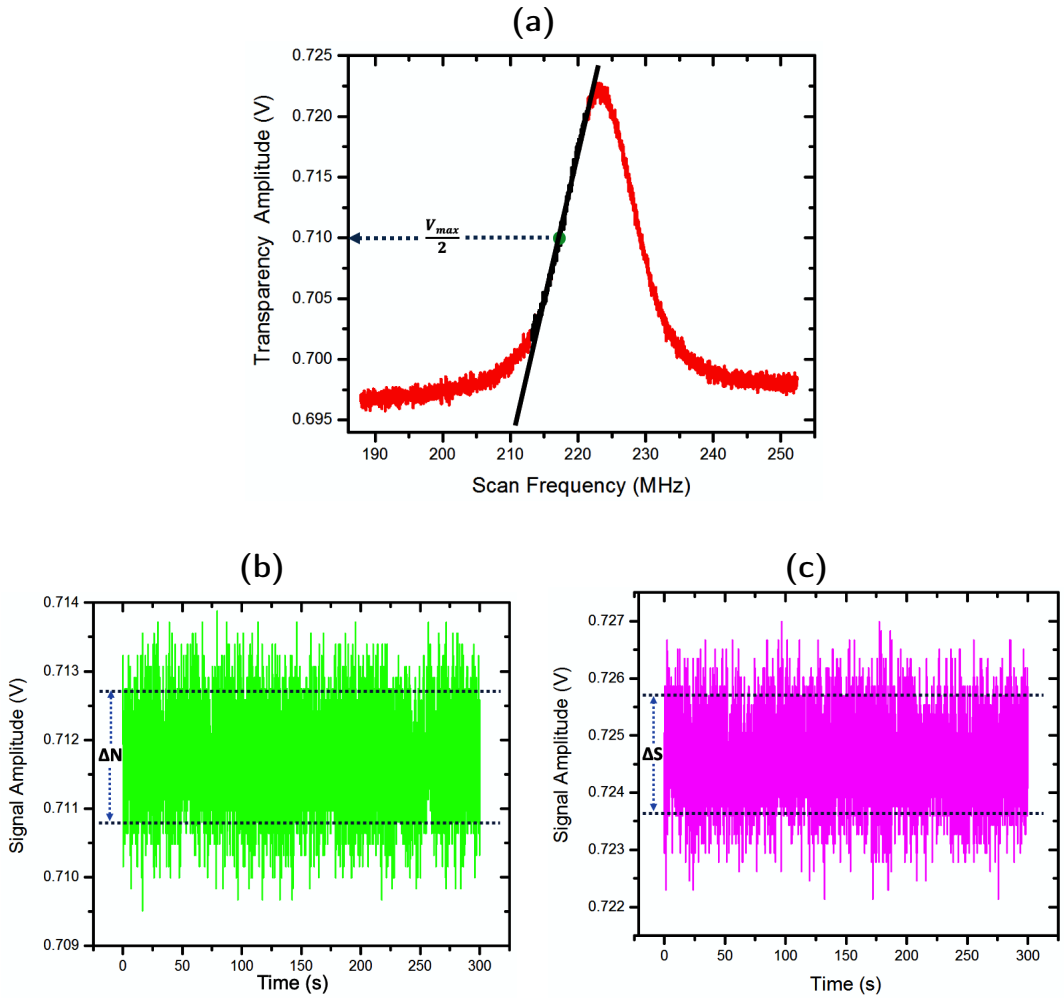

FIGURE 4.8: **(a)** A typical transparency peak (red line) obtained over the scan range with 160 μW probe beam and 13 mW coupling beam. The plot is averaged over 5 scans with each scan taking about 300 seconds. The slope of the line (black line) across the line centre $\frac{V_{max}}{2}$ is used to obtain the frequency-voltage response; **(b)** The flat background signal when the coupling beam is blocked; **(c)** The flat signal when the blue AOM shift is set to 217 MHz so that the coupling beam sits at the line centre.

estimated fluctuation of $\Delta S = (166 \pm 1) \times 10^{-5}$ V shown in figure 4.8(c). Then one would immediately see the increase in the voltage amplitude signal as a result of the probe-coupling interference. The coupling beam frequency jitter can therefore be written as

$$\Delta f_c = \frac{\Delta V}{\mathrm{R}_{vf}} = (186 \pm 42)\,\mathrm{kHz}\ . \tag{4.15}$$

As discussed in section 3.2.1, the linewidth of extended cavity diode lasers is reduced by setting up the diode with an external cavity. The 480 nm coupling laser, as described in section 3.3.1 is setup up with an additional second harmonic generation cavity system. Thus, it is expected that its linewidth is less than that of the probe beam. Although the self-homodyne measurement technique would have been a more accurate technique for obtaining the linewidth of the probe beam, one can intuitively estimate the probe linewidth to be about double that of the coupling beam, i.e. $\Delta f_p \approx (372 \pm 84)$ kHz.

4.2.4 Investigating the transparency features: Non-interacting atoms

In this experiment, the dependence of the transparency lineshape on the detunings of the beams is neglected due to the assumption of a two-photon resonance condition. In a Doppler-broadened system such as the thermal atomic vapour, the transparency lineshape is well approximated by a Lorentzian function which is used to fit the transparency features to obtain the FWHM.

Obtaining the beam Rabi frequencies

To obtain an estimate of the beam Rabi frequencies, waist of the probe beam was measured by shining the beam on a Marlin F033B CCD camera. A neutral density filter attached to the camera in order to prevent over-saturation of and damage to the CCD. A 2-D Gaussian profile fit to the acquired image was done using a code written in MATLAB. This allows the elliptical probe laser waists to be determined as $\omega_{\mathrm{maj}} = 1.14 \pm 0.18$ mm and $\omega_{\mathrm{min}} = 0.85 \pm 0.14$ mm along the major and minor axes of the beam cross-section. However, obtaining an estimate for the coupling beam waist is more demanding as its cross-section cannot be viewed on the CCD camera. A crude way to obtain the beam waist is to place an iris in the path of the beam. The iris is closed till the power is reduced by $1/e^2$ of the maximum value. As such, the coupling beam waist was estimated to be about $\omega_{\mathrm{maj}} = \omega_{\mathrm{min}} = 750 \pm 200\,\mu$m. This method is considered not accurate because it only shows the size around the peak intensity of the Gaussian profile. Thus not producing the full Gaussian intensity profile of the beam. It is also easy to see that this method would not define the actual cross-section of the

beam, it rather assumes that the beam is circular. A more accurate estimate for the beam size can be obtained by fitting the experimental spectrum with the theoretical single-atom model while the previous estimates help to select good starting conditions for the fitting parameters.

To obtain the spectra to be fitted, it is necessary to relate the experimental spectrum obtained from either the oscilloscope or computer-controlled scans to the theoretical spectrum obtained from the solution of the OBEs. Using the two-level model, the 780 nm laser power scattered from a thin slab of Rb vapour with density $\varrho_a \approx 10^{10}\,\mathrm{cm}^{-3}$ is given by

$$P_{\mathrm{sc}} = \frac{\hbar\,\omega_0\,\varrho_a\,\gamma_2^3\,A\,\Delta z}{2\sigma}\frac{s_0}{4\Delta_P^2+\gamma_2^2\,(1+s_0)}\,, \tag{4.16}$$

where Δz is the length of the vapour cell, ω_0 is the transition frequency, A is the beam cross-section and $s_0 = \frac{I}{I_{\mathrm{sat}}}$ is the saturation parameter with $I_{\mathrm{sat}} = 1.67$ mW cm^{-2} being the saturation intensity. Taking the beam to be of uniform intensity, the beam propagating through the absorbing medium attenuates according to the Beer-Lambert law

$$\frac{\mathrm{d}I}{\mathrm{d}z} = -I\,\sigma\varrho_a\,, \quad \Longrightarrow \quad I = I_0\,e^{-\sigma\varrho_a z}\,, \tag{4.17}$$

where σ defines the scattering cross-section

$$\sigma = \frac{\hbar\,\omega_0\,\gamma_2^3}{2I}\frac{s_0}{4\Delta_P^2+\gamma_2^2\,(1+s_0)}\,. \tag{4.18}$$

Equation (4.17) shows two directly measured quantities: I is transmitted probe intensity measured by the photodiode while I_0 is background probe intensity scan measured without the atom absorbing the probe photons. I_0 can either be obtained by removing the vapour cell from the beam path or by detuning the probe beam very far from resonance so that it becomes a see-through to the atoms. The experiment is related to the theory through the scattering cross-section

$$\sigma = \frac{1}{\varrho_a z}\left[\ln(I_0) - \ln(I)\right]\,. \tag{4.19}$$

Using equation (1.29), the scattering cross-section is related to the population of atoms in the $5\mathrm{P}_{3/2}$ state as

$$\sigma = \frac{\hbar\omega_0}{I}\gamma_2\rho_{22}\,. \tag{4.20}$$

where $R_{\mathrm{sc}} = \gamma_2\rho_{22}$ is related to the scattering rate being plotted in figure 4.2 while the factor $A_{\mathrm{sig}} = \frac{\hbar\omega_0}{I}$ is fitted as the amplitude of the signal. Since the background intensity changes with laser intensity, it is necessary to include the intensity-induced

offset, B_{off} in the fit. Thus,

$$\sigma = B_{\text{off}} + A_{\text{sig}}\, R_{\text{sc}} \ . \tag{4.21}$$

The reason for this whole process is based on the fact that I and I_0 are obtained as voltage values of the signals from the oscilloscope. So, fitting the theoretical model directly to the raw transparency feature means fitting two unrelated and different units. Thus, making the fitting extremely difficult.

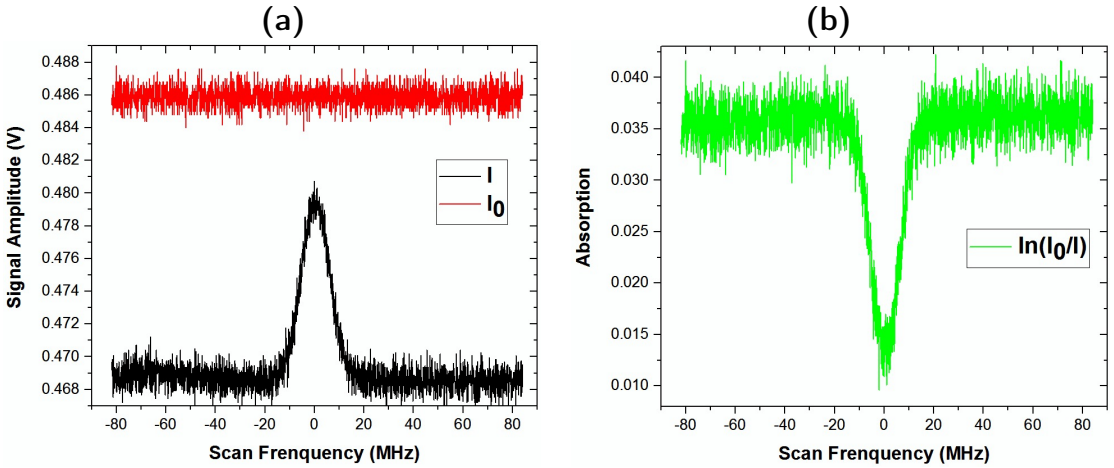

FIGURE 4.9: **(a)**Typical raw I (black trace) and background I_0 (red trace) signals obtained from the oscilloscope data; **(b)** Normalised absorption spectrum obtained as $\ln\left(\frac{I_0}{I}\right)$. For these plots, probe beam power $= 80\,\mu$W and coupling beam power $= 16$ mW.

Typical I and I_0 signals obtained from the oscilloscope data and normalised absorption spectrum are presented in figures 4.9(a-b). In figure 4.9(a), the black trace shows the usual transparency feature from two-photon transition while the red trace shows the variation of the far-detuned probe beam intensity. Using (4.19), the normalised spectrum, similar to the ones shown in figures 4.2(a)-(c), is obtained as $\ln\left(\frac{I_0}{I}\right)$. It should be noted that fitting the model to either $\ln\left(\frac{I_0}{I}\right)$ or $\ln\left(\frac{I}{I_0}\right)$ (which appears as the usual transparency feature such as the black trace in figure 4.9(a)) will yield the same result.

For a $180\,\mu$W probe beam and 13 mW coupling beam inside the vapour cell, the resulting fit of the measured spectrum with the single atom or non-interacting many-body OBEs solution is shown in figure 4.10. The power loss due to the borosilicate glass cell (probe beam inside the cell is $\approx 90\%$ of input while coupling beam inside the cell is $\approx 92\%$ of input beam) have been accounted for. The fit produced probe and coupling Rabi frequencies of (12.39 ± 0.43) MHz and (1.29 ± 0.15) MHz respectively with

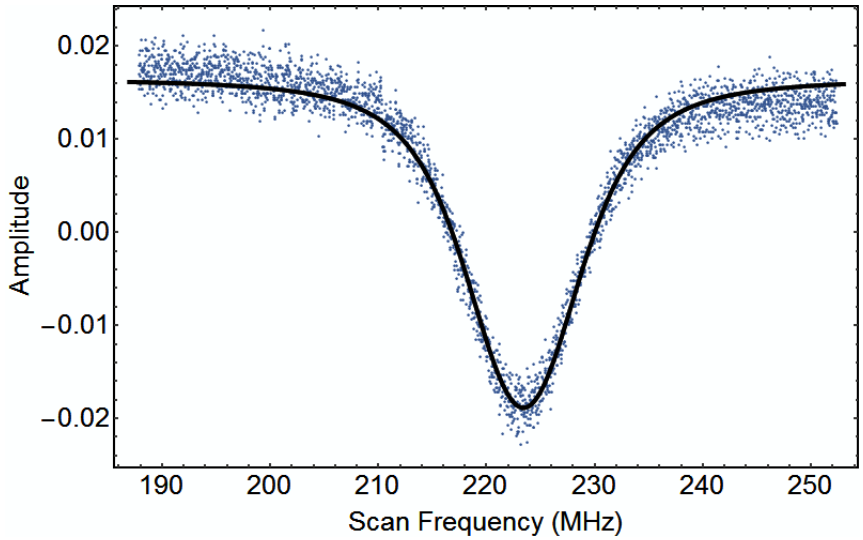

FIGURE 4.10: A typical fit of the single atom or non-interacting many-atom solution (black line) to the transparency feature obtained from experimental measurement. The fit produced probe and coupling Rabi frequencies of (12.39 ± 0.43) MHz and (1.29 ± 0.15) MHz respectively.

p-values less than 0.05 to show statistical significance. Thus, resulting in estimated probe and coupling beam sizes of $907.46 \pm 32.47\,\mu$m and 1.71 ± 0.22 mm respectively. The uncertainties from the Rabi frequencies and beam sizes are the standard deviation on the average over several scans and spectral fits. As already stated, the method used to obtain the measured value of the coupling beam size is too crude. Hence, the wide difference between the estimated and measured values. However, the estimated value of the probe beam size shows an approximate agreement to the measured size $\omega = \frac{\omega_{\text{maj}}+\omega_{\text{min}}}{2} \approx 1$ mm. Ignoring approximations, the little difference between the measured and estimated values can be attributed to the point spread function associated with the optical path.

Accounting for broadening effects

The broadening of the transparency lineshapes is a major factor that determines the accuracy of linewidth measurements. The contribution of the natural linewidth of the $20\text{D}_{5/2}$ state to the broadening is considered negligible since it is just a few kHz. When the intensities of the lasers are increased, this permits light of frequencies farther from atomic resonance to excite transitions. This is called power broadening. Hence, scanning the frequency of an highly intense laser produces a broader resonance spectrum than a weak laser. The power range of the coupling beams is limited to the regime where the power broadening is minimum. However, there is a possibility of power broadening as a result of the very high probe power considered. This can be

accounted for by using [159]

$$\Gamma_{\text{pb}} = \sqrt{\frac{\left(\Omega_C^2 + \Omega_P^2\right)^2}{\gamma_2 + 2\Omega_P^2}} \,. \tag{4.22}$$

Due to the motions of the atoms and the different wavelengths of the excitation lasers, an unavoidable residual Doppler broadening occurs. This can be accounted for using [159]

$$\Gamma_{\text{rDb}} = \gamma_2 \left(\frac{k_c}{k_p} - 1\right) \,, \tag{4.23}$$

where k_p and k_c are the wavenumbers of the probe and coupling beams respectively while Γ_{rDb} is estimated to be about 3.8 MHz for $\lambda_P = 780$ nm and $\lambda_C \approx 480$ nm for the 20D Rydberg state.

Also, there is the transit-time broadening due to the size of the laser beams [159, 160]. This is estimated by the size ω of the smaller laser beam, in this case the red laser, of transition beams by

$$\Gamma_{\text{tt}} = \frac{4v}{\omega}\sqrt{2\ln(2)} \,, \tag{4.24}$$

where $v = \sqrt{\frac{2k_{\text{B}}T}{m_{\text{Rb}}}} = 237$ ms^{-1} is the most probable velocity in the Maxwellian velocity distribution and m_{Rb} is the atomic mass of Rb atoms. Using the probe beam size, the time-transit broadening is estimated to be about 0.2 MHz which implies that it has only a minor contribution to the total transparency linewidth. The contributions of the each broadening mechanism will be deducted from the measured transparency linewidth.

Transparency linewidth measurement

The numerical data obtained from the scans done for varying laser powers are fitted to a Lorentzian function using Origin Pro and the full width at half maximum (FWHM), which gives the value of the transparency linewidth, is obtained from the fit. Also, the corresponding scattering rate lineshape produced from the solution of the single atom or non-interacting many-atom OBEs (a typical example is shown in figure 4.2) are fitted to the Lorentzian function

$$R_{\text{sc}} = R_{\text{sc0}} + \frac{A}{\pi}\frac{\frac{1}{2}\beta}{\left[\left(\frac{1}{2}\beta\right)^2 + (\Delta_C - \Delta_0)^2\right]} \tag{4.25}$$

using Mathematica. R_{sc0} is the baseline offset of the feature, Δ_0 is the center of the peak which determines the shift from resonance, A is the area under the peak and β is the FWHM.

Figure 4.11 shows how the transparency linewidth changes as a function of the probe Rabi frequencies while the coupling Rabi frequency is kept constant at about 2.6 ± 0.3 MHz. The contributions of possible Doppler and transit-time broadening effects have been accounted for while a power broadening of about 1-7 MHz occurs due to the relatively high probe Rabi frequencies of up to 10 MHz. The large error bars at lower probe Rabi frequencies are majorly dependent on the signal-to-noise ratio of the features while the photodiode sensitivity limits how well the low probe regime can be explored. The laser linewidths and the estimated values of the Rabi frequencies are inserted into the single-atom solution of the OBEs to obtain transparency linewidths (red line in figure 4.11) also by Lorentzian fits to the spectra lines. The linear-dependence of the measured linewidths on the probe Rabi frequencies is in agreement with the expected behaviour from theoretical calculation. The linear dependence is basically due to the dependence on the ratio $\frac{\Omega_P}{\Omega_C} \gtrsim 1$. Thus, linewidth at either EIT/ATS or CPT regimes can either be subnatural or not. The natural linewidth does not contribute to the broadening of the transparency peak, thus the subnatural linewidths in the ATS/CPT regimes. One would expect a saturation at some probe Rabi frequency but the power broadening effect quickly kicks in which result in non-subnatural linewidths.

Although the absorption properties are satisfied, the experimental results still showed some discrepancies when compared to the theoretical results. Due to the limited time available for the experiment to be performed and the report to be written, investigation into the cause of the discrepancies was not completed. However, the major cause is reckoned to be due to the sensitivity of the photodiode and also neglecting the velocity distribution in the single atom or non-interacting many-atom solution owing to the computational demand.

Beyond this experimental study, the subnatural linewidths can also be broadened due to Rydberg interaction induced excitation blockade at high atomic densities or excitation level. Rydberg-Rydberg interaction is expected to give rise to nonlinear dependence of the absorption properties on Ω_P and correlated many-body dynamics whose description becomes challenging already for a moderate number of atom. The theoretical description of the effect of strong Rydberg-Rydberg interactions in various atomic systems is described in the next section.

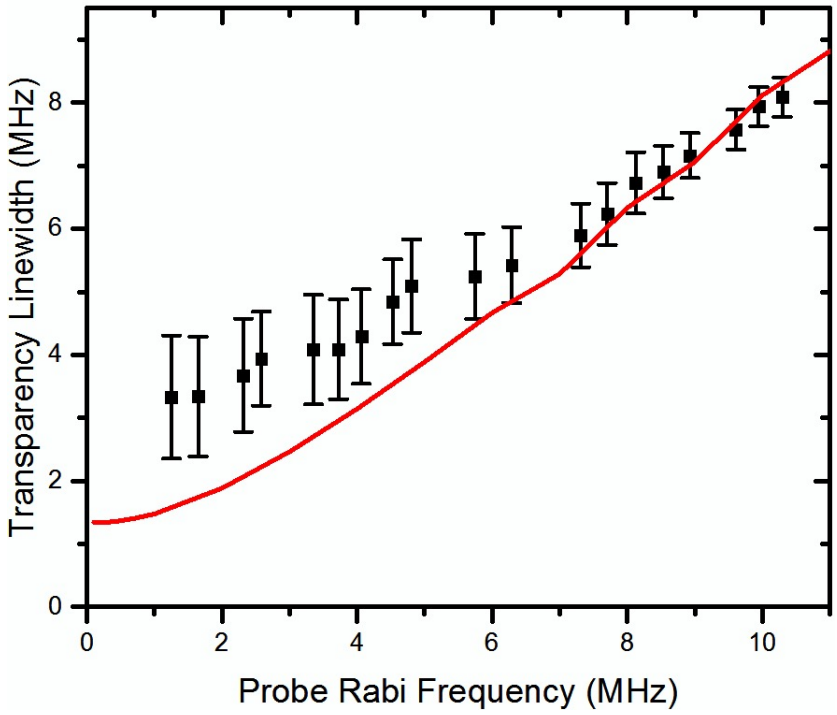

FIGURE 4.11: Transparency linewidths obtained from single atom solution (red line) and experimental measurements (black square) as functions of the probe Rabi frequency. For these plots, coupling Rabi frequency $= 2.6 \pm 0.3$ MHz.

PART B

4.3 Many-body excitation dynamics in an interacting system

As shown in the case of non-interacting particles in section 4.1.1, the rate of excitation to or de-excitation from the Rydberg state depends only on the laser Rabi frequencies and the decay rates. In other words, for non-interacting particles, besides the laser detunings, the excitation rate depends on the state of the atoms only. However in the interacting case, this becomes invalid as the excitation rate depends on the entire many-body configuration. To account for this, a Hamiltonian $\mathcal{H}_{33}$ which describes the Rydberg-Rydberg interaction is added to the initial many-body atom-light interaction Hamiltonian given in equation (4.3). The generic form of the Rydberg-Rydberg interaction Hamiltonian is written as a sum over the interaction energies of Rydberg atom

pairs. This reads

$$\mathcal{H}_{33} = \sum_{j<k}^{N} \mathbb{V}_{jk} \left[\bigotimes_{i=1}^{j-1} \mathbf{1}_3 \otimes |3_j\rangle\langle 3_j| \otimes \bigotimes_{i=j+1}^{k-1} \mathbf{1}_3 \otimes |3_k\rangle\langle 3_k| \otimes \bigotimes_{i=k+1}^{N} \mathbf{1}_3 \right] , \quad (4.26)$$

where $\mathbf{1}_3$ is an identity operator while $\mathbb{V}_{jk}$ is the interaction-induced energy shift, given in equation (2.6), between two Rydberg states.

This study exclusively focus on Rydberg states interacting via van der Waals potential thereby inducing an energy shift given in equation (2.7) between the Rydberg states. In this study, it will be preferred to use the complete expression for the interaction potential as given in equation (2.6) because the transition between the van der Waals regime and resonant dipole-dipole regime can easily be covered. Also, the assumption that the interaction is isotropic for an atomic pair j,k separated by the distance $r_{jk} = |\mathbf{r}_j - \mathbf{r}_k| = r_{kj}$ is considered, so that $\mathbb{V}_{jk} = \mathbb{V}_{kj}$. Hence, the study exclusively focus on nS Rydberg states in order to avoid any anisotropic interaction encountered in some of the nD states which are in the regime of Förster resonances. It is important to note that $\mathcal{H}_{33}$ does not change the structure of the master equation given in equation (4.2), with $\mathcal{H}_A \longrightarrow {\mathcal{H}_A}^{(N)} + \mathcal{H}_{33}$, as it generates no further coherences. Also, solving the commutator in the master equation for a many-body basis reveals that the Rydberg-Rydberg interaction appears as an additional detuning of the atom at $\mathbf{r}_j$ whenever the atom at $\mathbf{r}_k$ is in the Rydberg state [161]. Thus causing an energetic shift of the two-photon detuning

$$\Delta_P + \Delta_C \longrightarrow N(\Delta_P + \Delta_C) + \sum_{j<k=1}^{N} \mathbb{V}_{jk} , \quad (4.27)$$

where N is the number of interacting atoms. In addition, the excitation dynamics of multi-atom systems reveal higher-order processes from simultaneous multi-photon transitions as a result of the transition between states where the atoms are not in the Rydberg state and the state with several Rydberg atoms. The rates of such transitions are slow compared to other single-photon transitions since it requires simultaneous absorption or emission of multiple photons. As will be described in the next section, the multi-photon processes lead to interesting effects of Rydberg-Rydberg interactions.

4.3.1 Spatially ordered interacting atoms

A first study of the impact of Rydberg-Rydberg interaction is done by solving the OBEs for 2 interacting atoms at fixed positions r_1 and r_2 in space, so that the atomic

separation r_{12} is restricted. This can be achieved with a structured potential, such as in systems of optical lattices [162] or dipole trap arrays [136]. A typical dipole trap can hold between 1-100 atoms. An array of micron-sized optical dipole trap (ODT) was generated in [136] whereby individually addressable traps are placed in different geometrical arrangements and relative positions, at close proximities to one another. In such a system, the distances between the traps can be controlled with micrometre precision thereby controlling the interaction mechanisms between the atoms. Such a system has been found to be particularly suitable for studying collective phenomenon [163].

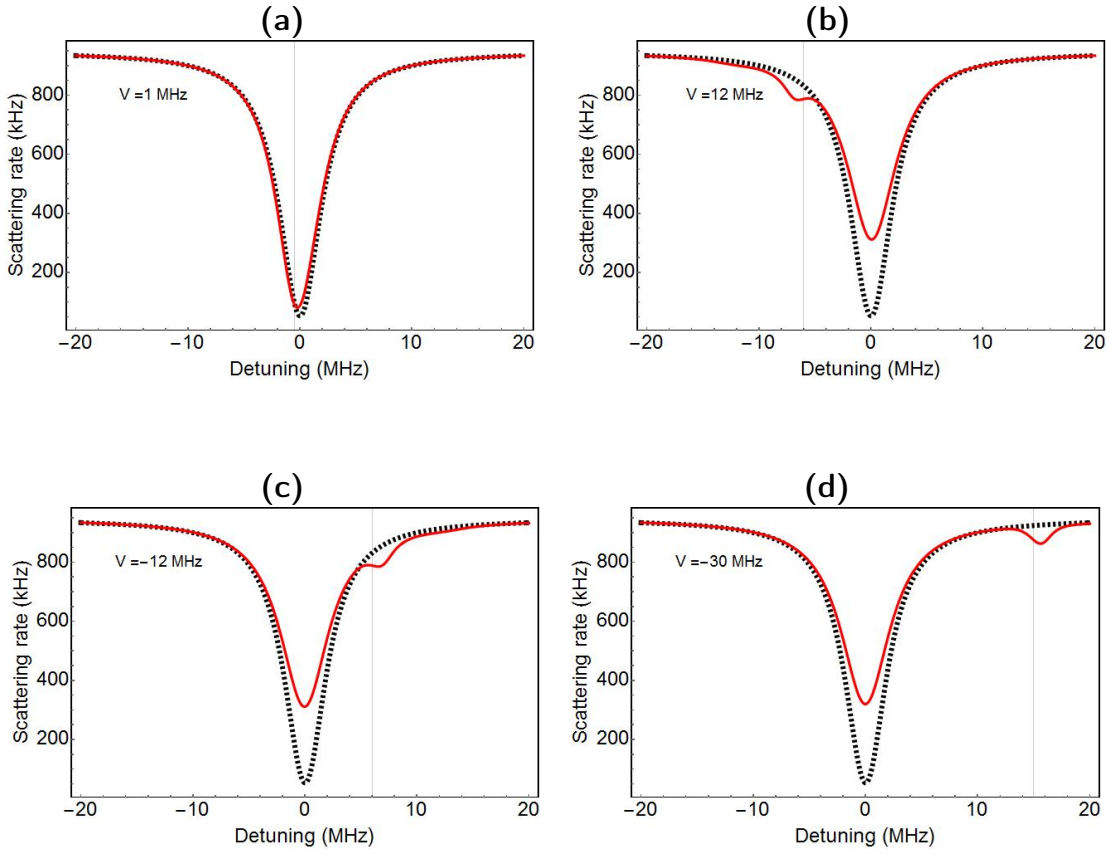

FIGURE 4.12: Plots to show the effect of interaction between two atoms (red line) for interaction strength $\mathbb{V}_{12}$ = **(a)** 1 MHz, **(b)** 12 MHz, **(c)** −12 MHz and **(d)** −30 MHz, as compared to the single atom solution (black dashed line). In the plots, $\Omega_C = 5$ MHz, $\Omega_P = 3$ MHz, $\gamma_2 = 6.065$ MHz, $\gamma_3 = 0.019$ MHz, $\gamma_{2d} = 0.38$ MHz and $\gamma_{3d} = 0.19$ MHz.

On solving the resulting two-atom OBEs from the master equation given in equation (4.2), with $\mathcal{H}_A \longrightarrow \mathcal{H}_A{}^{(N)} + \mathcal{H}_{33}$ and non-zero energy level shift $\mathbb{V}_{12}$, the EIT probe scattering rate (considering $\Omega_C = 5$ MHz and $\Omega_P = 3$ MHz) is shown in figures 4.12(a)-(d) as a function of the coupling detuning for increasing interaction strength,

and it is compared to the single atom solution. One sees that switching on the interaction modifies the transparency feature obtained from a single atom solution. There is a clear suppression of transparency which increases with increasing level shift $\mathbb{V}_{12}$. This is a typical Rydberg excitation blockade effect since increasing the interaction strength reduces the coupling to doubly excited Rydberg state. As such, the suppression effect indicates the decreasing fraction of Rydberg atoms. The suppression increases to roughly 30% at about $\mathbb{V}_{12} = \pm 12$ MHz. However, the solution shows a saturation of the suppression at $\mathbb{V}_{12} = \pm 12$ MHz as further increase in the interaction has little or no effect on the suppression (as shown in figure 4.12(d) for $\mathbb{V}_{12} = -30$ MHz).

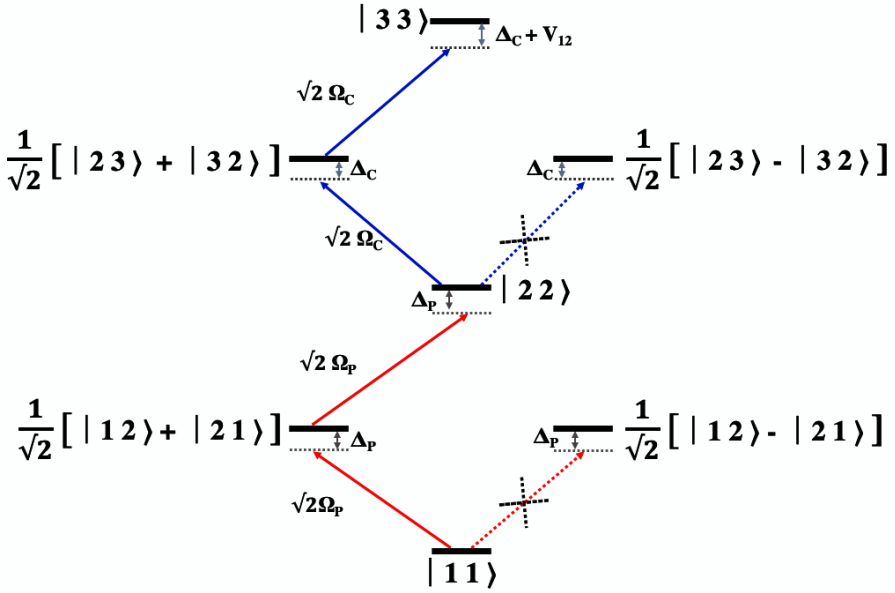

FIGURE 4.13: Multiphoton transitions from two-atom ground state to the level with two Rydberg excitations which cause possible interaction-induced blockade and excitation enhancement effects.

The spectrum in figures 4.12(a)-(d) show an excitation enhancement at $\Delta_C \approx \mp\frac{1}{2}\mathbb{V}_{12}$, i.e. an enhanced fraction of Rydberg atom. This indicates the rise of an antiblockade effect. The excitation enhancement effect is as a result of a multi-photon excitation to the level with two Rydberg excitations. This is illustrated in figure 4.13. When the two interacting atoms interact with the two-photon transition lasers, the two atom spectrum exhibit transitions connecting the states $|1_{(1)}\,1_{(2)}\rangle$ to $\frac{1}{\sqrt{2}}\left[|1_{(1)}\,2_{(2)}\rangle + |2_{(1)}\,1_{(2)}\rangle\right]$ to $|2_{(1)}\,2_{(2)}\rangle$ to $\frac{1}{\sqrt{2}}\left[|2_{(1)}\,3_{(2)}\rangle + |3_{(1)}\,2_{(2)}\rangle\right]$ and then to $|3_{(1)}\,3_{(2)}\rangle$ with total detunings Δ_P, $2\Delta_P$, $2\Delta_P + \Delta_C$ and $2\left(\Delta_P + \Delta_C\right) \pm \mathbb{V}_{12}$ respectively. Considering that the laser excitation is described by the laser excitation operator given in equation (2.13) for applicable coupling states, one would see that the states $\frac{1}{\sqrt{2}}\left[|1_{(1)}\,2_{(2)}\rangle - |2_{(1)}\,1_{(2)}\rangle\right]$ and $\frac{1}{\sqrt{2}}\left[|2_{(1)}\,3_{(2)}\rangle - |3_{(1)}\,2_{(2)}\rangle\right]$ are not coupled by the transition lasers. When the

probe beam is set to resonance, $\Delta_P = 0$, then the detuning of the 4-photon transition to $|3_{(1)}\, 3_{(2)}\rangle$ is $\pm\mathbb{V}_{12}$ for a resonant coupling beam. This causes the blockade effect. However, when the coupling beam is scanned to $\Delta_C \approx \mp\frac{1}{2}\mathbb{V}_{12}$, the laser coupling to $|3_{(1)}\, 3_{(2)}\rangle$ is pushed back to resonance. This creates another transparency dip which indicates an increasing fraction of atoms in the Rydberg state. This is contrary to the dip suppression effect that occurs in the presence of an appreciable interacting strength. Hence, it is called the antiblockade effect.

One would expect the enhanced excitation peak at $\Delta_C \approx \frac{1}{2}\mathbb{V}_{12}$ to have the same depth amplitude as the dip at $\Delta_C = 0$. This is determined by the two-photon coupling strength, given by the effective two-photon Rabi frequency, to the state $|3_{(1)}\, 3_{(2)}\rangle$. Usually, the effective two-photon Rabi frequency is

$$\Omega_{2\text{photon}} = \frac{\sqrt{2\left(\Omega_P^2 + \Omega_C^2\right)}}{2\Delta_C} = \frac{\Omega_{2\text{atoms}}}{2\Delta_C}\ . \tag{4.28}$$

When $\Delta_C = \frac{\mathbb{V}_{12}}{2}$, then $\Omega_{2\text{photon}} = \frac{\Omega_{2\text{atoms}}}{\mathbb{V}_{12}}$ which is highly reduced compared to the infinite coupling strength at $\Delta_C = 0$. Hence, the reduced amplitude of the excitation enhancement peak. One should note that in reality, the coupling strength is always finite. This is because it is experimentally difficult to achieve a precision where $\Delta_C = 0$.

Besides the value of $\mathbb{V}_{12}$, an important contributing factor to the visibility of Rydberg-Rydberg interaction effects is the ratio $\frac{\Omega_P}{\Omega_C}$. Considering a constant Ω_C and an appreciably high interaction strength $\mathbb{V}_{12} = -30$ MHz, figures 4.14(a)-(d) show the probe scattering rate as a function of Δ_C for increasing Ω_P. First, there is no suppression in the low probe regime (as shown in figure 4.14(a)), rather appreciable suppression occurs in the high probe regime (as shown in figures 4.14(b)-(d)). It also appears that the ratio $\frac{\Omega_P}{\Omega_C}$ determines the saturation level of the interaction-induced suppression. Take for example, from figure 4.12(d), the ratio $\frac{\Omega_P}{\Omega_C} = 0.6$ while $\mathbb{V}_{12} = -30$ MHz. The graph shows a saturation at about 28% suppression. Meanwhile from figure 4.14(c), the ratio $\frac{\Omega_P}{\Omega_C} = 2$ while $\mathbb{V}_{12} = -30$ MHz. This results in a saturation at about 50% suppression.

Beyond the excitation enhancement that occur at $\Delta_C = \mp\frac{1}{2}\mathbb{V}_{12}$, a further blockade effect is observed at $\Delta_C = \mp\mathbb{V}_{12}$, as shown in figures 4.14(b)-(c). This occurs because the total detuning of the multi-photon transition to $|3_{(1)}\, 3_{(2)}\rangle$ is now $\mp\mathbb{V}_{12}$. This is similar in magnitude to the value at $\Delta_C = 0$. Also, the coupling strength has now reduced to $\Omega_{2\text{photon}} = \frac{\Omega_{2\text{atoms}}}{2\mathbb{V}_{12}}$, hence the smaller amplitude of the peaks. From

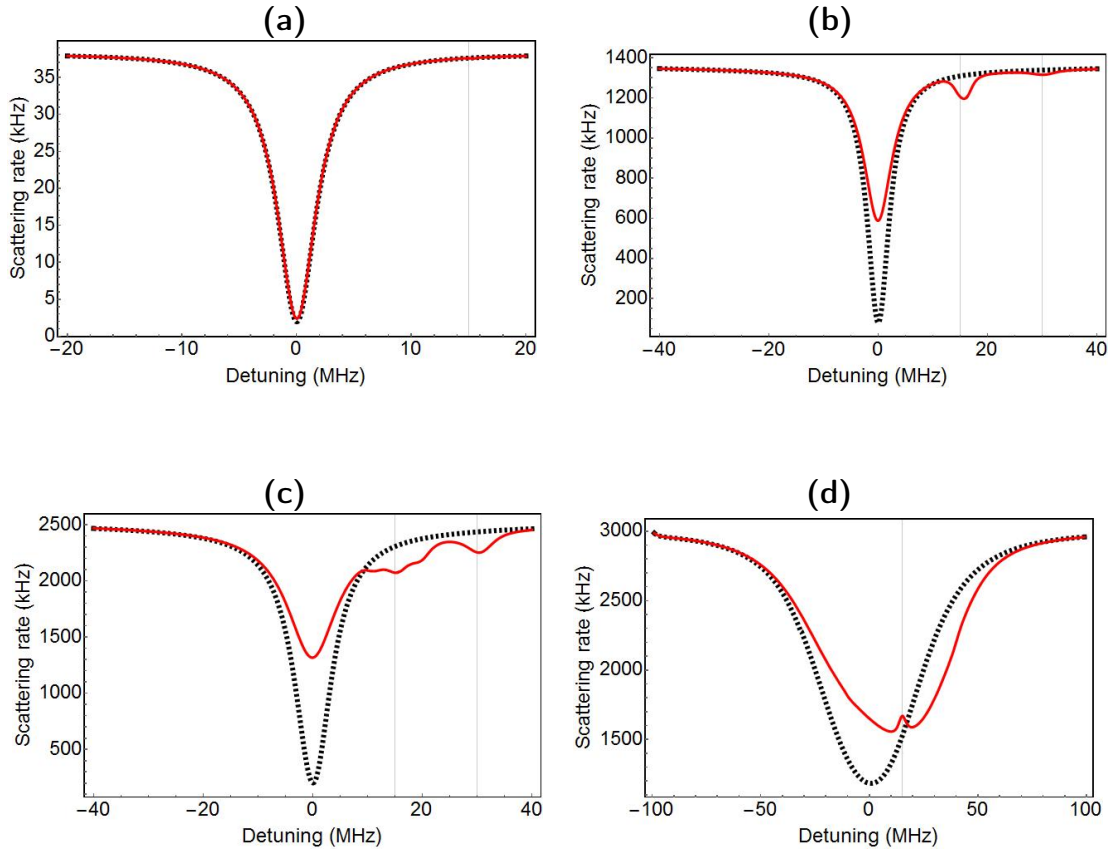

FIGURE 4.14: Plots to show the effect of the ratio $\frac{\Omega_P}{\Omega_C}$ on the excitation suppression and enhancement as transition is made from low probe limit to extremely high probe limit as compared to the single atom solution (black dashed line). For these plots, $\Omega_P =$ **(a)** 0.5 MHz, **(b)** 4 MHz, **(c)** 10 MHz, **(d)** 50 MHz. Also, $\Omega_C = 5$ MHz, $\mathbb{V}_{12} = -30$ MHz, $\gamma_2 = 6.065$ MHz, $\gamma_3 = 0.019$ MHz, $\gamma_{2d} = 0.38$ MHz and $\gamma_{3d} = 0.19$ MHz.

another perspective, one can easily refer to the peak at $\Delta_C = \mathbb{V}_{12}$ in figures 4.14(b)-(c) as an antiblockade peak since its amplitude increases with increasing Ω_P. However, the fact remains that antiblockade effect occurs only when there is zero detuning of the multi-photon transition to $|3_{(1)}\, 3_{(2)}\rangle$. Increasing Ω_P to an extremely high value not only causes a power broadening of the spectrum but it also shifts the two-photon resonance to $\mp\frac{\mathbb{V}_{12}}{2}$ with a cumulative enhanced excitation effect (see figure 4.14(d)). Such high probe Rabi frequency could cause effects such as radiation trapping and hole burning in ultracold gases.

To better appreciate the effect of Rydberg-Rydberg interactions in a spatially ordered atomic system, the OBEs were solved for three interacting atoms (shown in figure 4.15). Usually in experimental setups, $r_{12} \neq r_{23} \neq r_{31}$. Due to the van der Waals interaction, a little difference in the interatomic distance will result in a large change in the interaction strength. Hence, the pairwise Rydberg interactions between atoms

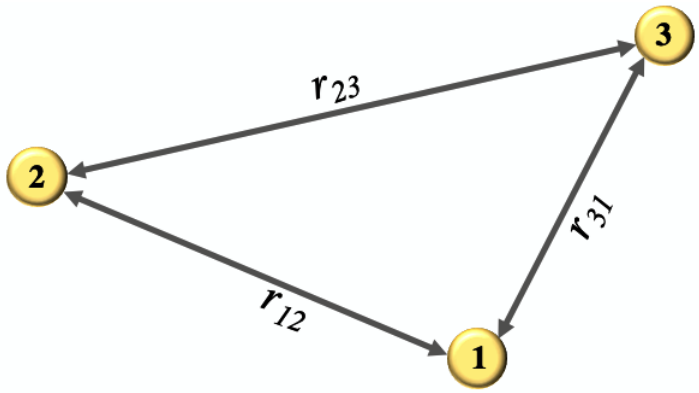

FIGURE 4.15: Three atoms interacting within a spatially ordered atomic system.

would vary. This does not change the structure of the total Hamiltonian. It only rather just affects the total two-photon detuning as more interaction terms are obtained from the sum term in equation (4.27). As shown in figure 4.16(a), taking $\mathbb{V}_{23} = 0.5\mathbb{V}_{12}$, $\mathbb{V}_{31} = 1.5\mathbb{V}_{12}$ and $\mathbb{V}_{12} = -30$ MHz which implies $r_{23} = 2^{\frac{1}{6}} r_{12}$ and $r_{31} = \left(\frac{2}{3}\right)^{\frac{1}{6}} r_{12}$, each interacting pair produces an excitation enhancement at $\mp\frac{\mathbb{V}_{ij}}{2}$. A higher suppression effect is produced when compared to the case of two interacting atoms produced in figure 4.12(d) as a result of the overall contribution from each pairwise interaction, thus causing an increased probability for blockade.

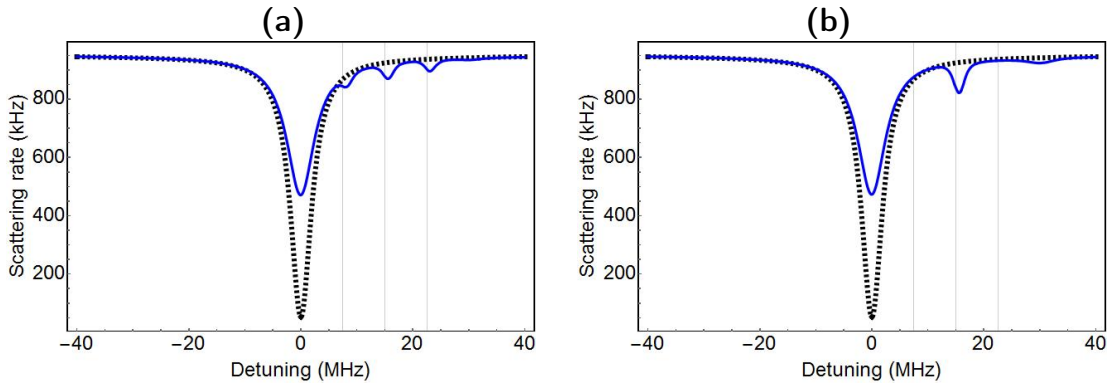

FIGURE 4.16: Plots to show the excitation suppression and enhancement effects for three interacting atoms solution as compared to the single atom solution (black dashed line) for different Rydberg-pair interaction. For these plots, **(a)** $\mathbb{V}_{23} = 0.5\mathbb{V}_{12}$ and $\mathbb{V}_{31} = 1.5\mathbb{V}_{12}$; **(b)** $\mathbb{V}_{12} = \mathbb{V}_{23} = \mathbb{V}_{31}$ where $\mathbb{V}_{12} = -30$ MHz. Also, $\Omega_C = 5$ MHz, $\Omega_P = 3$ MHz, $\gamma_2 = 6.065$ MHz, $\gamma_3 = 0.019$ MHz, $\gamma_{2d} = 0.38$ MHz and $\gamma_{3d} = 0.19$ MHz.

For an idealised case where the atoms are placed at equal distances from one another, that is $r_{12} = r_{13} = r_{23}$, so that $\mathbb{V}_{12} = \mathbb{V}_{31} = \mathbb{V}_{23}$, the EIT spectrum (considering $\Omega_C = 5$ MHz and $\Omega_P = 3$ MHz) produced from the solution of the OBEs is shown in figure 4.16(b). The result shows a similar but higher excitation enhancement effect,

compared to the two-atom case in figure 4.12(d). On one hand, one can say it is due to the weighted sum of the individual Rydberg pair interaction. On the other hand, since there are more energy-level transitions involved within the structure of the three-atom case, there is a higher probability of multi-photon excitation to the level with two Rydberg excitations resonant with $\frac{\mathbb{V}_{ij}}{2}$. There will also be multi-photon transitions to the 3-atom Rydberg state resonant with $\frac{1}{3}\sum_{i<j}\mathbb{V}_{ij}$ but with much lower probability and coupling strength.

A typical optical lattice system or array of dipole traps could have more than three atom sites which could reveal more interesting interaction effects other than the suppression and excitation enhancement effects. It is important to note that so far, the ordered system considered is one in which atoms are assumed not to undergo any appreciable motion inside their respective traps. This is usually not the case as atoms jitter around within a trap. Also, being able to hold the atoms at almost fixed positions depend on the tightness of the traps. As will be shown later in section 4.4.2, appreciable atom motions kill interaction effects. In fact, one finds out that the excitation enhancement, i.e. antiblockade effect, is smeared out [161]. It implies that the effects of multi-photon transitions are reduced. This is consistent with what is usually observed in an experimental spectrum.

4.4 Random Gases: Monte Carlo Sampling

One of the most interesting aspects in many-body theory of excitation is the possibility to find a solution whose validity is not restricted by positions/locations, density and number of atoms. This is possible in this case, as would be considered in this section, when the investigations of Rydberg systems involve a disordered atom ensemble such as in a MOT, a vapour cell and an ODT. The case considered in previous sections either take the separation between pair atoms to be fixed or to be over a certain range. Although it has been shown in figure 4.16 that more suppression effect occurs for three or more interacting atoms as compared to two interacting atoms, this is not generally the case as it will be shown later. This basically depends on how large the interaction is or the contributing factors to the interaction as well as the atom distribution.

When investigating the case where a large number of atoms is taken into account, it is necessary to model the distribution of interatomic distances in the cloud. This helps to understand the contribution of every interacting pair to the total interaction. Giving that the OBEs to be solved grows as 3^N, solving for a large number of atoms can be computationally demanding. An intuitive thing to do would be to consider

solving the OBEs for only a few neighbouring atoms, iterate the solution over all the possible random atom-positions within the ensemble and then obtain the average over all the possible iterations. Hence, to describe the collective behaviour of the atoms, it is interesting to first understand the distribution of the nearest-neighbour interactions and then the average influence of surrounding atoms on the interaction properties of nearest neighbour pairs.

Atomic pair distribution functions

The description of the interatomic distance distribution of nearest neighbour atom is done in [12] and would be followed here within. Consider an atom inside a cloud with density $\varrho_a(\mathbf{r})$. Also consider that the atom is sitting at the centre of the cloud (or origin of the coordinate system). The number of atoms found within the distance interval $[r, r + \mathrm{d}r]$ for a spherically symmetric density distribution around the atom reads

$$\mathrm{d}N = \left[\int_0^{2\pi}\int_0^{\pi} \varrho_a(r,\theta,\phi)\, r^2 \,\sin\theta \,\mathrm{d}\theta \,\mathrm{d}\phi\right] \mathrm{d}r = 4\pi r^2 \varrho_a(r)\,\mathrm{d}r \,. \tag{4.29}$$

As will be shown later to be applicable to real systems, in an atomic system such as in a vapour cell or a MOT, one can assume a homogeneous atomic density distribution and that the atom density is small enough to be considered constant.

Considering an ensemble of N atoms, if the nearest neighbour to the centre atom is at a separation distance r, then it means means the rest $N-2$ particles are at larger distances $r' > r$. The probability to find a particle within the volume of the spherical shell of radius r and width $\mathrm{d}r$ is given by $4\pi r^2 \varrho_a \,\mathrm{d}r$. Since the probability for finding exactly k atoms in a given volume is expressed by the Poisson distribution, $p(k, N_{avg}) = \frac{N_{avg}^k \mathrm{e}^{-N_{avg}}}{k!}$, where $N_{avg} = \frac{4}{3}\pi r^3 \varrho_a$ is the average number of atoms in the sphere of radius r, the probability that no other atom lies inside the sphere is given by $p(0, N_{avg}) = \mathrm{e}^{-\frac{4}{3}\pi r^3 \varrho_a}$. Hence the probability of the nearest neighbour of an atom to be within the spherical shell of radius r and width $\mathrm{d}r$ is given by product

$$P_{NN}(r) = 4\pi r^2 \varrho_a \,\mathrm{e}^{-\frac{4}{3}\pi r^3 \varrho_a} = \left(\frac{3\,r^2}{a^3}\right) \mathrm{e}^{-\left(\frac{r}{a}\right)^3} \,, \tag{4.30}$$

where $a = \left(\frac{3}{4\pi\varrho_a}\right)^{\frac{1}{3}}$ is the *Wigner-Seitz radius* which gives an estimate of the mean interparticle spacing of atoms within a gas cloud. For example, a typical MOT or vapour cell has an atom density of $\approx 10^{-10}\,\mathrm{cm}^{-3}$, as such $a \approx 2.8\,\mu\mathrm{m}$. At about this density, interaction-induced energy level shifts are of the order of MHz occur for

$n \geq 39\mathrm{S}$ or $n \geq 36\mathrm{D}$ states. Giving that $P_{NN}(r)$ is a probability density distribution, then the most probable and average nearest neighbour distance can be easily obtained to be $r_{\mathrm{avg}} = a\Gamma\left(\frac{4}{3}\right) \approx \frac{5}{9}\varrho_a^{-\frac{1}{3}}$, where $\Gamma(x)$ is a gamma function. So, in order to model many-body atomic system, the approach taken in this study is to design a system that would satisfy the probability distribution given in equation (4.30).

Generally in many-body systems, where there are sufficiently strong interactions between the atoms, the pair distribution can be influenced since other atoms contribute to the overall interaction effects. Therefore, it is necessary to estimate the average influence of the surrounding atoms on the properties of the interacting atom pair. This will clarify that for a van der Waal $\frac{1}{r^6}$ interaction, the description in terms of nearest neighbour interaction is sufficient while for a resonant dipole-dipole $\frac{1}{r^3}$ interaction, a larger number of atoms must be taken into account unless when the interparticle distances are finite [12].

Average influence of surrounding atoms

Assuming that the nearest neighbour is at a distance r_{avg} to the centre atom, the nearest neighbour interaction with the atom is $\mathbb{V}_{NN} = \mathbb{V}(r_{\mathrm{avg}})$. Since the surrounding atoms are at distances $> r_{\mathrm{avg}}$, the average interaction energy contributed by all other surrounding atoms in the cloud can be evaluated using

$$\mathbb{V}_{\mathrm{s}} = \int_{r_{\mathrm{avg}}}^{\infty} 4\pi r^2 \varrho\, \mathbb{V}(r)\, \mathrm{d}r \ . \tag{4.31}$$

In the van der Waals regime, $\mathbb{V}(r) \approx \frac{C_6}{r^6}$, then it implies that $\mathbb{V}_{\mathrm{s}} \approx 0.72\, \mathbb{V}_{NN}$. This implies that to simulate interacting Rydberg systems when the van der Waals interaction is dominant, it may be sufficient to consider the nearest neighbour interactions only. However, since $\mathbb{V}_{\mathrm{s}}$ is well appreciable compared to $\mathbb{V}_{NN}$, it is therefore instinctive to consider the interaction energies contributed by all other surrounding atoms. The contribution from every interacting pair in the ensemble is additive. As such, the electronic energy shift induced by the ith atom on the jth atom is written as

$$\mathbb{V}_i = \sum_j \mathbb{V}\left(|\mathbf{r}_i - \mathbf{r}_j|\right) \ , \tag{4.32}$$

where the sum runs over all the surrounding Rydberg atoms. Hence, more interaction effect is expected when the higher-order nearest neighbour distribution is also considered. Since the cloud contains many atoms, then for each atom, it would be

computationally demanding to account for all the contributions from all the surrounding atoms at once. Hence, it is intuitive to consider only a few nearest neighbours to each atom. This is based on the assumption that other atoms outside the consider nearest neighbours are at farther distances to the reference atom such that their contributions are negligible.

In the resonant dipole-dipole interaction regime $\mathbb{V}(r) \approx \frac{C_3}{r^3}$, the integral given in equation (4.31) diverges and can only be evaluated when there is a finite upper limit r_{max}. This implies that the interaction induced by the surrounding atoms is more significant than that of the nearest neighbour. Therefore in the case of an infinite upper limit $r_{\text{max}} \to \infty$, the contributions from all atoms must be accounted for. By using the complete expression for the interaction-induced energy shift as stated in equation (2.6), the response of the atoms to laser field as a transition is made from the van der Waals regime to the resonant dipole-dipole regime can be easily observed. The many-body Hamiltonian and the energy levels of the atoms are the same irrespective of the distance between the atoms or the regime of interaction while the multi-atom basis states are simply the product states of multiple single atom states.

In contrast to the treatment of spatially ordered interacting atoms, in order to investigate the case of a disordered ensemble of Rydberg atoms, one has to account for the fluctuation of the spatial positions of the atoms in the ensemble, the varying density of the interacting atoms and the probability of exciting a specific atom at a given time. To do this, the excitation dynamics must be modelled using Monte-Carlo model. This will be used to model interacting atoms in a MOT, vapour cell and ODT. The difference between these systems lies in the spatial distribution of the atoms or the thermal motions of the atoms.

4.4.1 Atom distribution and interaction-induced excitation dynamics in a magneto-optical trap (MOT)

A typical MOT is obtained by a combination an extremely low pressure (about 10^{-10} Torr) of an ultra-high vacuum medium, a velocity-dependent force from the trapping lasers which slows down atoms and cools the atoms to microKelvin temperature, and a position-dependent force induced by the application of an external non-uniform magnetic field to the atomic system to keep the atoms trapped at a particular position (see section 5.1). This produces a dense atom cloud at a position in space.

It should be noted that the atom cloud in a MOT is approximated by a Gaussian

spatial distribution and could typically hold more than 10^5 atoms with a cloud size of few millimetres. The experimental setup usually involves the coupling and probe beams being tightly focused to waists of only a few tens of micrometres at the centre of the cloud to enhance the beam Rabi frequencies [151]. Hence, only atoms close to the centre of the cloud will have an influence on the interaction mechanism. Also, the MOT cloud can be approximated to a uniform density sphere.

To describe the random spatial arrangement of Rydberg atoms in a MOT and the resulting interaction dynamics from the Monte Carlo model, the following algorithm is used. First, N_p atoms are collected and are uniformly distributed in a box at random positions with a density $\varrho_a = 10^{10}$ cm^{-3} which corresponds to the typical density at the centre of a MOT. Thus, atoms in these positions will form a cloud of size $\varsigma = \left(\frac{N_p}{\varrho_a}\right)^{\frac{1}{3}}$ with centre zero as shown in figure 4.17(a) for 5000 atom-positions. For an atom sitting at the centre/origin of the cloud, for a constant density, the number of pairs would grow with the square of the distance. To obtain a typical spherical cloud of the MOT, the magnitude of the atom-positions are sorted. Then a fraction of the total atom sample is selected. Figure 4.17(b) shows distribution of the closest 2000 atom-positions to the cloud centre atom. In actual fact, this does not only create a spherical cloud, but it also produces an ensemble whose position distribution follow interatomic distance distribution given in equation (4.30). Figure 4.17(c) shows the position distribution (light blue line) of the atoms as a function of the rank of the atom-positions when the magnitude of the positions are sorted. If the average interatomic distance is given by the Wigner-Seitz radius a, then the N_pth atom position will be at $aN_p^{\frac{1}{3}}$ away from the atom at the centre (red line in figure 4.17(c)). The plot shows that atoms that are far away from the centre appear to deviate from the interatomic distance distribution. So, to ensure that any pair separation satisfies the interatomic distance distribution, then only a fraction of the total atom sample positions must be considered.

To account for every interaction that occurs within the atom cloud, the atomic separations between all possible pairs are obtained. It implies that for each atom, all the immediate nearest neighbour distances and higher-order nearest neighbour separations can be obtained. The resulting distribution of nearest neighbour separations is shown in figure 4.18(a) (black trace). This is seen to well approximate the nearest neighbour distance probability distribution function (red line) from equation (4.30). The gridlines show the most probable nearest neighbour distance (red gridline) and average nearest neighbour distance (grey gridline).

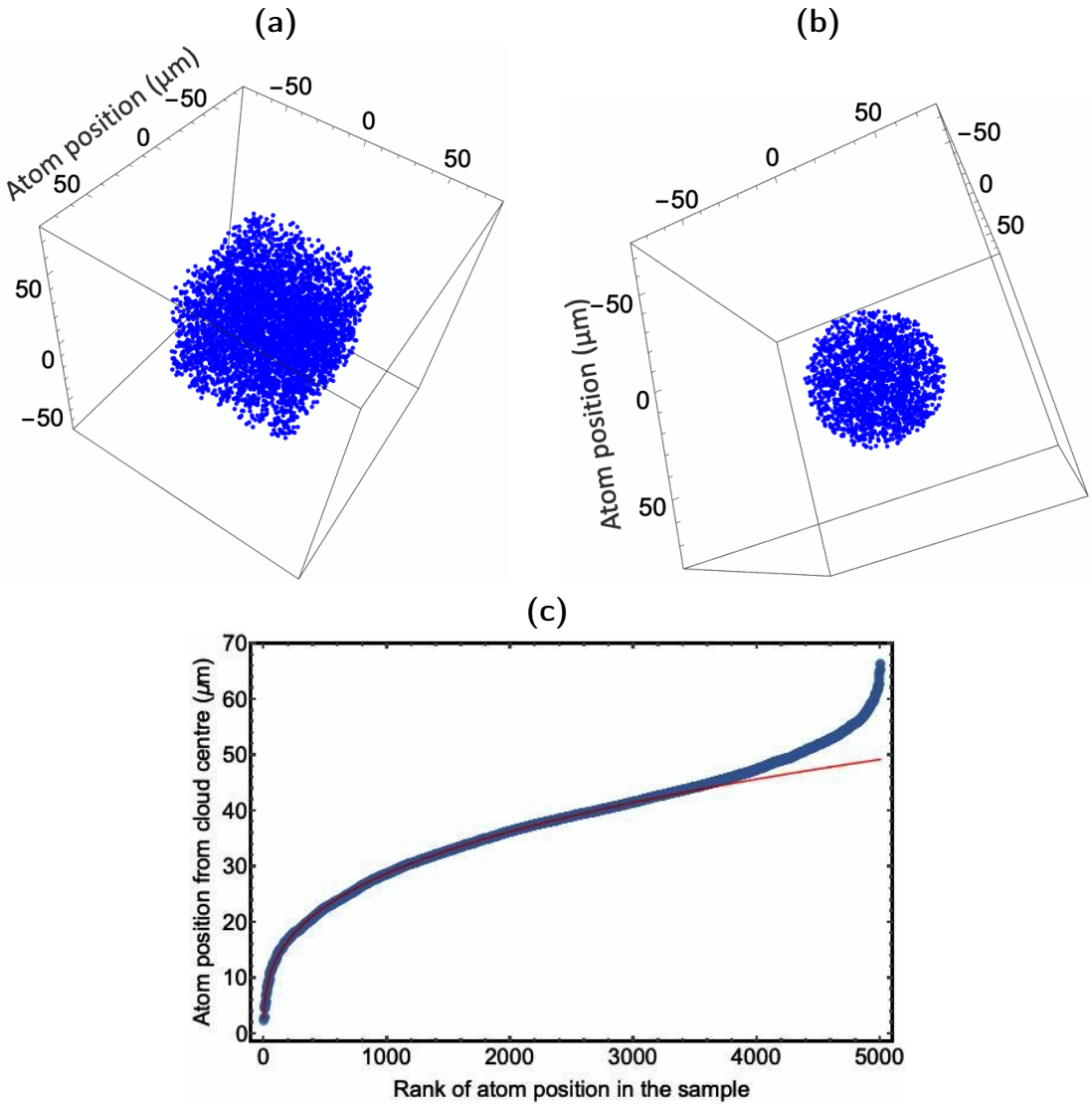

FIGURE 4.17: **(a)** Collection of 5000 atoms randomly placed in space with a density of 10^{10} cm^3; **(b)** Collection of the closest 2000 to the cloud centre which forms a spherical atom cloud; **(c)** (Blue line) Plot of the positions of atoms from the centre of the cloud versus the rank of the atom-positions when the magnitudes of the positions are sorted. (Red line) Plot of the position $aN_p^{\frac{1}{3}}$ of the N_pth atom from the cloud if the average interatomic distance given by the Wigner-Seitz radius a.

Considering atoms in 49S Rydberg state with a density of 10^{10} cm^{-3}, the resulting nearest neighbour interaction potential distribution can be obtained by substituting the nearest neighbour distances in the spatially-dependent interaction-induced shift $\mathbb{V}$ given in equation (2.6). This is shown in figure 4.18(b) (black line). Giving the nearest neighbour distance distribution $P_{NN}(r)$, the resulting interaction potential distribution $P(\mathbb{V})$ for the nearest neighbour atoms can be obtained by first solving for $r = f^{-1}(\mathbb{V})$ from then interaction-induced shift $\mathbb{V} = f(r)$ given in equation (2.6).

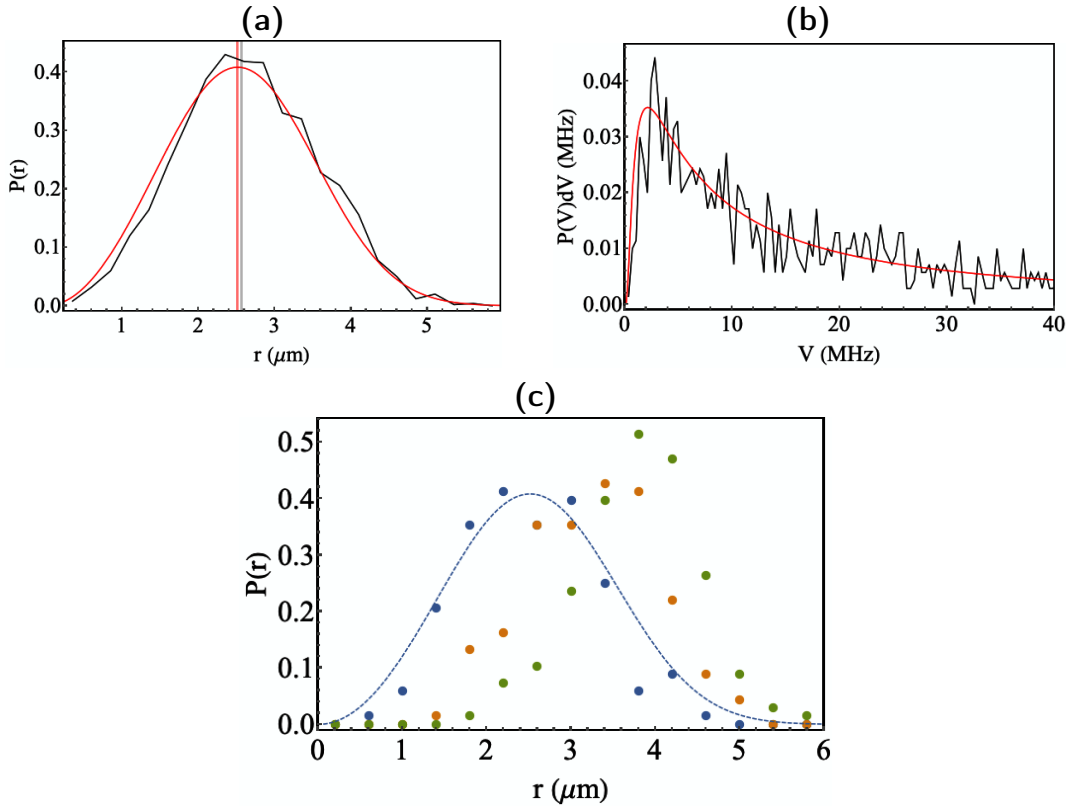

FIGURE 4.18: **(a)** Distribution of nearest neighbour distances of the 2000 sample atoms which is a fraction of a larger 5000 cloud atoms randomly placed in space with a density of 10^{10} cm^3. This distribution well approximates the nearest neighbour atom distance distribution (red line). The gridlines show the most probable nearest neighbour distance (red gridline) and the average nearest neighbour distance (grey gridline); **(b)** Resulting interaction potential distribution from the 2000 sample atoms' positions (red line) which approximates the potential distribution obtained from a transformed nearest neighbour atom distance distribution; **(c)** A typical distribution of three nearest neighbour distances to a sample of 150 atoms showing the closest (blue dots), second (orange dots) and third (green dots) nearest neighbour distance distributions.

Then $r = f^{-1}(\mathbb{V})$ can be substituted into equation (4.30) to obtain

$$P(\mathbb{V}) = \frac{1}{f'(r \longrightarrow f^{-1}(\mathbb{V}))} P_{NN}(r \longrightarrow f^{-1}(\mathbb{V})) \,, \tag{4.33}$$

where f' denotes the derivatives. This is plotted over a possible range of potentials in figure 4.18(b) (red line). The result shows a good agreement between the modelled interaction distribution and the theoretical interaction distribution. The result also shows the most probable interaction potential to be about 4 MHz. This indicates that, giving an atom density of 10^{10} cm^{-3}, the 49S Rydberg atoms are in the regime where interparticle interactions play a significant role.

Having being able to obtain the N_p spherical atom cloud distribution, all the possible relative distances between the cloud atoms and the corresponding interaction potentials, then the OBEs can be solved for all the atoms in the cloud. However, this is almost computationally impossible since N_p is typically large. To ease the task at hand, it is intuitive to consider only OBE solutions for very few N atoms and then iterate over all the possible N_p positions. In this study, only solutions for cases of $N = 2$-4 atoms are considered which are then iterated over all the possible atom-positions. This implies that the iteration is done over all the possible interaction potentials. It should also noted that running the simulation over a large number of atom-positions would be computationally tasking as it would require a large number of iterations. Therefore, one should consider a minimal number of atom-positions provided they can effectively represent the distribution. A typical distribution of nearest neighbour atoms over 150 atom-positions is shown in figure 4.18(c). The nearest neighbours (blue dots) shows good agreement with the nearest neighbour distance distribution (blue dashed-line). This implies that iterating over 150 atom-positions should be sufficient to represent the system. The higher-order nearest neighbour distance distributions (the second (orange dots) and third (green dots) nearest neighbours) are also shown. The higher-order distributions appear as a shift to the nearest neighbour distribution.

Due to the position-dependent force acting on atoms in a MOT that keeps the atoms trapped at a point in space, the thermal motions of atoms become negligible. The dominant atomic motions in such system are the atom motions induced by the strong repulsive van der Waals interactions between the nS Rydberg states. Thus, atoms are made to accelerate away from one another per time. Based on computational requirement, the experimental procedure is simulated by allowing the coupling laser to be scanned across resonance at a rate $\delta_r = 5\,\mu$s/Hz while Δ_C takes the form of the expression given in equation (4.6). One should note that in physical experiments such as in a MOT or an ODT, the continuous beam scan used in the model is not possible. Rather, for each run of the experiment, the coupling beam detuning is fixed at a certain value within the scan range. This is because experimental timescale is limited by the lifetime of the atoms in the trap owing to some major factors such as the collision of trap atoms with the background vapour, collisional dynamics of atoms within the trap, temperature of the trap ensemble, the trap depth, the beam intensity profile and light-induced atom scattering. The duration of the interaction between the atoms and two-photon excitation lasers (which is typically of the order of few μs) is usually part of an experimental sequence that also includes trap loading process, atom cooling process and cloud imaging process. Within this short duration of interaction between the atoms and the two-photon excitation lasers, the atomic motions induced

by the Rydberg-Rydberg interactions are considered negligible.

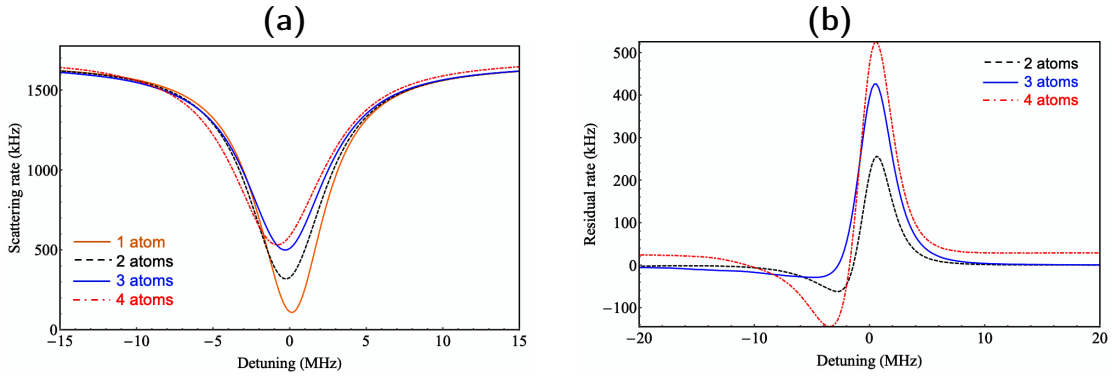

FIGURE 4.19: **(a)** ATS/CPT regime: Theoretical results of the Monte-Carlo simulation for 1, 2, 3 and 4 49S nearest-neighbour atoms averaged over 150 positions with a density of 10^{10} cm^{-3}; **(b)** Corresponding residual plots obtained from the difference in scattering rates between the single atom case and the N-atom case; For these plots $\Omega_C = \Omega_P = 5$ MHz, $\gamma_3 = 0.019$ MHz, $\gamma_{2d} = 0.38$ MHz, $\gamma_{3d} = 0.19$ MHz and $\gamma_2 = 6.065$ MHz.

Figure 4.19 shows the calculated scattering rate resulting from the van der Waals interaction between atoms in 49S Rydberg state using the Monte Carlo approach described above. This is done with 2, 3 and 4 nearest neighbour atoms iterated over 150 positions. Note that on every iteration, the scattering rate is averaged or normalised by the number of atoms. The dependence of the calculated ATS/CPT spectra, considering $\Omega_C = \Omega_P = 5$ MHz, on the number of interacting nearest neighbour atoms considered is shown in figure 4.19(a). The corresponding residual plots, i.e. the difference in scattering rates between the single atom case and the N-atom case, is shown in figure 4.19(b). Besides an increasing suppression effect which is as a result of the additive interaction potentials for all the nearest neighbours and due to increasing van der Waals blockade effect that prohibits simultaneous Rydberg excitation of nearby atoms, the lineshape displays increasing shift from resonance. This increasing shift also causes an increasing asymmetry of the lineshape. On one hand, this can be said to be due to the increasing number of atoms that are shifted out of resonance as a result of the excitation of a single Rydberg atom. On the other hand, the shift and asymmetry effects are a result of multi-photon excitations to doubly Rydberg excited states whose probability increases with increasing number of atoms. To explain this, one would recall that each interacting potential induced from various interacting pairs within the cloud produces a corresponding excitation enhancements that appear as anti-blockade peaks (see figures 4.12, 4.14 and 4.16). Since multiple peaks appear, these peaks overlap and smoothen-out to produce both an asymmetry and a shift of the transparency lineshape. The dependence of these effects on the considered number

of nearest-neighbour atoms is because of the number of antiblockade peaks that are involved in each iteration. Having only observed these interaction effects for a single density and excitation number, it is important to check the generic excitation dynamics of the atoms for different densities and excitation levels.

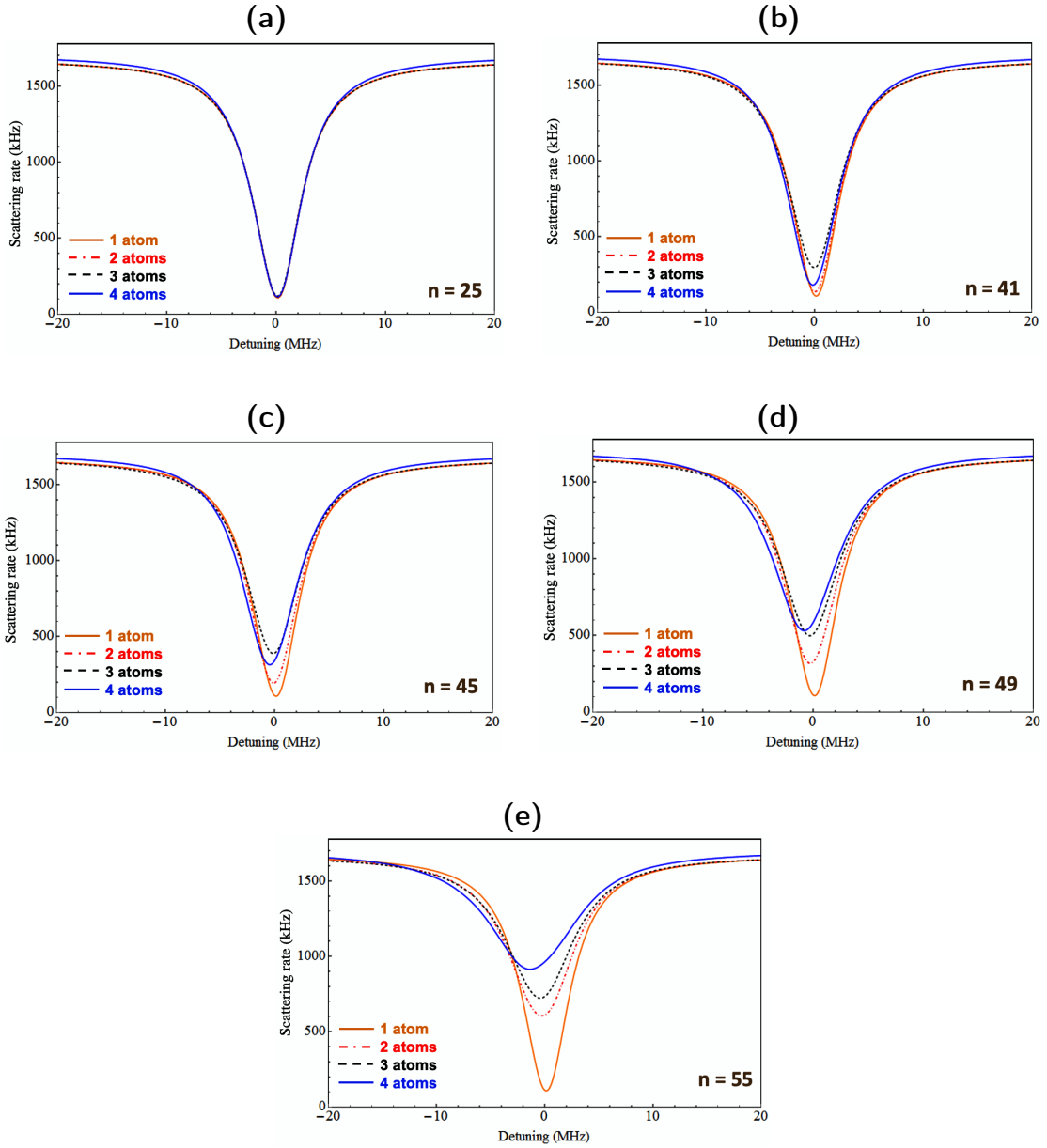

FIGURE 4.20: Plots to show the dependence ATS/CPT spectrum on increasing excitation level n = **(a)** 25, **(b)** 41, **(c)** 45, **(d)** 49 and **(e)** 55, for 2, 3 and 4 nearest neighbours averaged over 150 atoms with a density of 10^{10} cm^{-3} . For these plots, $\Omega_C = \Omega_P = 5$ MHz, $\gamma_3 = 0.019$ MHz, $\gamma_{2d} = 0.38$ MHz, $\gamma_{3d} = 0.19$ MHz and $\gamma_2 = 6.065$ MHz. All Orange lines are single atom solution plotted for the purpose of comparison.

Varying atom densities and excitation levels

The interaction-induced shift and asymmetry in figure 4.20, for 2, 3 and 4 nearest-neighbour solutions averaged over 150 atom-positions with a density of 10^{10} cm^{-3}, are shown to have a high dependence on the Rydberg level due to increasing polarisabilities of the atoms and decreasing fraction of Rydberg atoms. The suppression effect however appears to have a weak dependence on the number of interacting nearest-neighbour atoms for some excitation levels. In figure 4.21, it is also shown to have a weak dependence on the number of interacting nearest-neighbour atoms for low atom densities. The physics behind this behaviour is not clear yet but it is reckoned to be due to the strong influence of the nearest neighbour interaction, which makes the contributions of surrounding atoms unimportant. The compensating duo, i.e. the density and excitation levels, both have to be high enough to make the dependence on the number of nearest-neighbour atoms become clearly distinctive. The atom density dependence of the ATS/CPT regime is shown in figure 4.21 with suppression effect increasing with density as a result of increasing probabilities of blockade.

For an atom density of 10^{10} cm^{-3} considered in figure 4.20, larger n values ($n > 55$) would shift the atoms into the dipole-dipole interaction regime since $r_{CoD} > a$ (see figure 2.3). Similarly in figure 4.21, if the atoms are to remain in the van der Waals regime, then increasing the density would require a reduction in the excitation level considered. The rise of the effect of resonant dipole-dipole interaction is shown in figure 4.21(d) where the spectrum displays a shift back to resonance against the convention of line shifts displayed in the van der Waals regime. The average interparticle distance at $\varrho_a = 5 \times 10^{10}$ cm^{-3} density is $a \approx 1.6\,\mu$m. This is approximately equal to the crossover distance $r_{\mathrm{CoD}} = 1.6\,\mu$m for 49S state. Thus, the interaction is out of the van der Waals regime. However, the interaction-induced suppression and asymmetry remains evident. This result shows that the restriction to the interacting nearest neighbour description when modelling the excitation dynamics of the atomic system remains valid irrespective of the interaction regime, provided the interatomic distances are finite. Although the signature of the dipole-dipole interaction is observed, the model is not completely valid for dipole-dipole interaction since the model has not considered the strongly anisotropic interactions that occur in the dipole-dipole regime. To note in addition, as the excitation levels n and atom density decreases, the ATS/CPT spectrum produced for a different number of atoms would become increasingly less different. As soon as the dependence on the number of nearest-neighbour atoms considered become distinctive, the interaction effect increases with number of atoms until it saturates such that the influence of additional surrounding atoms will be negligible.

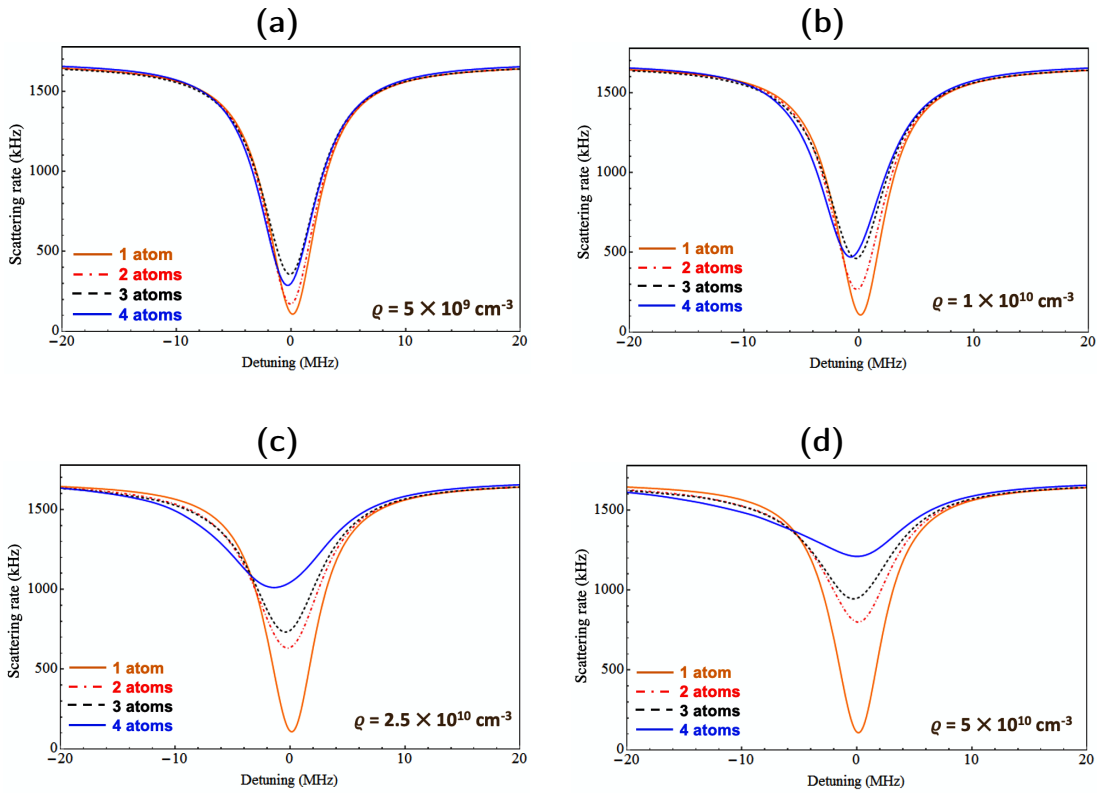

FIGURE 4.21: Plots to show the dependence ATS/CPT spectrum on increasing atoms densities for 2, 3 and 4 nearest neighbours averaged over 150 atom-positions in the 49S state with density ϱ_a = **(a)** 5×10^9 cm^{-3}, **(b)** 10^{10} cm^{-3}, **(c)** 2.5×10^{10} cm^{-3} and **(d)** 5×10^{10} cm^{-3} . For these plots, $\Omega_C = \Omega_P = 5$ MHz, $\gamma_3 = 0.019$ MHz, $\gamma_{2d} = 0.38$ MHz, $\gamma_{3d} = 0.19$ MHz and $\gamma_2 = 6.065$ MHz. All Orange lines are single atom solution plotted for the purpose of comparison.

In the EIT regime (taking $\Omega_C = 5$ MHz and $\Omega_P = 1$ MHz), neither the shift nor asymmetry effect is observed as shown in figure 4.22(a) for three nearest-neighbour atoms solution averaged over 150 atom-positions at different excitation levels. Only the suppression effect is visible in this regime. In actual fact, this is rather an attribute of the low probe limit but not a question of the particular quantum interference regime at play. In figure 4.22(b), similar attribute is shown in ATS regime, $\Omega_C = 7$ MHz and $\Omega_P = 1$ MHz, for 3 atoms solution iterated over 150 positions. One would observe that suppression effect reduces for lower ratio $\frac{\Omega_P}{\Omega_C}$. This indicates that appreciable interaction effects will arise if the probe beam strength is high enough to create an appreciable admixture $\left(\sim \frac{\Omega_P}{\Omega_C}\right)$ of Rydberg states as shown in figure 4.22(c) where the EIT spectrum, $\Omega_C = 2$ MHz and $\Omega_P = 1$ MHz shows dependence on the excitation level.

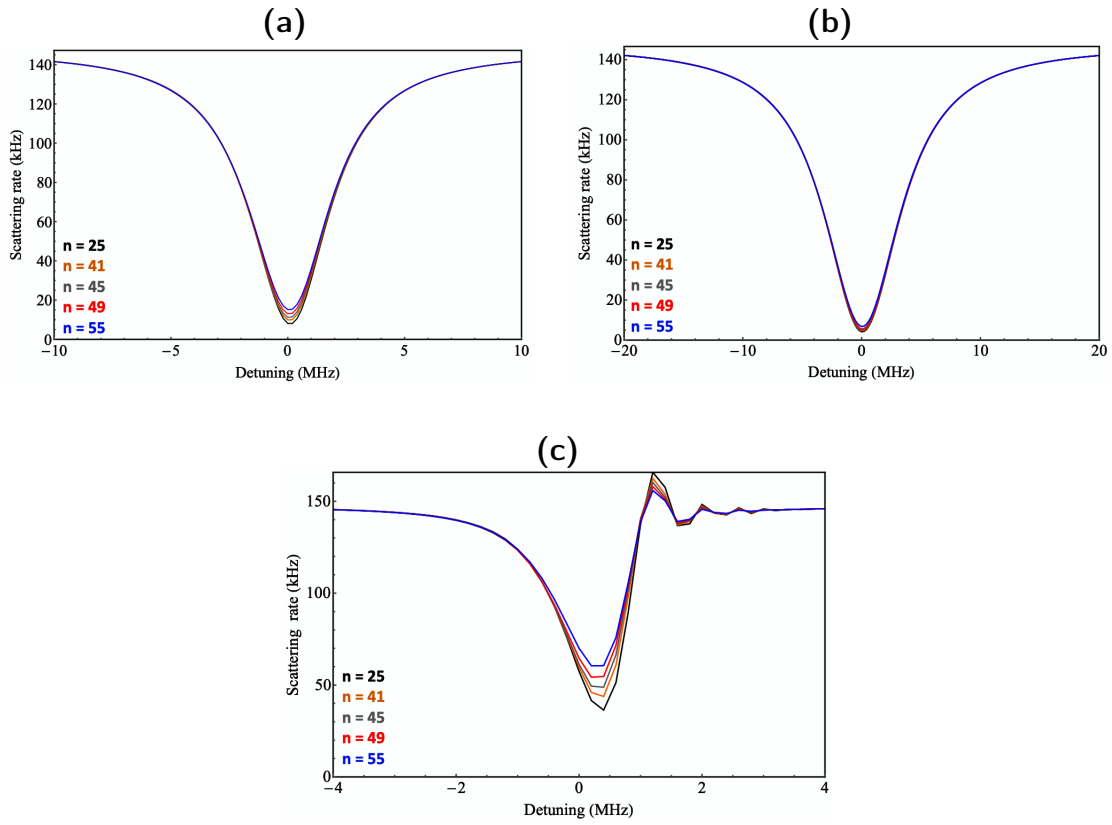

FIGURE 4.22: **(a)** Plots to show the dependence of EIT spectrum on increasing excitation n; **(b)** ATS spectrum dependence on increasing excitation n in the low probe limit; **(c)** EIT spectrum dependence on increasing excitation in the high probe limit. The plots are obtained from 3 nearest neighbours solution averaged over 150 positions with a density of 10^{10} cm^{-3}. For these plots $\gamma_3 = 0.019$ MHz, $\gamma_{2d} = 0.38$ MHz and $\gamma_{3d} = 0.19$ MHz, $\gamma_2 = 6.065$ MHz; **(a)** $\Omega_C = 5$ MHz, $\Omega_P = 1$ MHz; **(b)** $\Omega_C = 7$ MHz, $\Omega_P = 1$ MHz; **(c)** $\Omega_C = 2$ MHz, $\Omega_P = 1$ MHz.

4.4.2 Interacting Rydberg atoms in a vapour cell

A typical borosilicate vapour cell has a pressure of 10^{-6} Torr at about 294 K laboratory temperature. This results in a density $\varrho_a = \frac{\mathrm{p}}{\mathrm{k}_B\, T} \approx 10^{10}\,\mathrm{cm}^{-3}$ of ^{87}Rb atoms in the vapour cell, where k_B is the Boltzmann constant. Hence, significant interaction effects can also be produced therein. It is important to note that the density of ^{87}Rb is $\frac{1}{3}$ of the total atom density due to its 27.8% natural abundance compared to the 72.2% abundance of ^{85}Rb. As such, considering ^{85}Rb atoms is one of the intuitive ways obtaining a higher interaction effects.

In a vapour cell, atoms are distributed uniformly at random positions within the cell with interatomic separation distribution given in equation (4.30). Since the excitation lasers interact with a small fraction of atoms at the centre of the cloud, the description given in section 4.4.1 well represents the distribution of atoms in a vapour cell. In vapour cell experiments, one would expect not to be able to effectively observe the

line shift and asymmetry effects due to the overall thermal motions of the atoms. At room temperature, the thermal motions are dominant such that atoms move within a wide range of velocity distribution. The distribution of the range of atom velocities is given by the Maxwell-Boltzmann velocity distribution

$$f(\mathbf{v}) = \sqrt[3]{\frac{2\,m_{\mathrm{Rb}}}{\pi k_{\mathrm{B}}\,T}}\, e^{-\frac{m_{\mathrm{Rb}}\mathbf{v}^2}{2k_{\mathrm{B}}\,T}}\,, \tag{4.34}$$

where m_{Rb} is the mass of Rb atoms. As a result of the atomic motions, atoms experience Doppler-shifted laser frequencies $\Delta^{(i)} = \frac{\omega_i\, v}{c}$ for $i = C,\, P$. Thus replacing $\Delta_P \rightarrow \Delta_P \mp \Delta^{(P)}$ and $\Delta_C \rightarrow \Delta_C \pm \Delta^{(C)}$ for counterpropagating beams in the OBEs. For each interatomic separation, substituted in the equation (2.6), the solution of OBEs is weighted by the probability given in equation (4.30) to account for the probability of having a specific interaction potential for specific interatomic spacing. The solution is then summed over all possible Doppler shifts. For each value of the Doppler-shift, the solution is also weighted by the Maxwell-Boltzmann velocity distribution to account for the probability to have that Doppler shift.

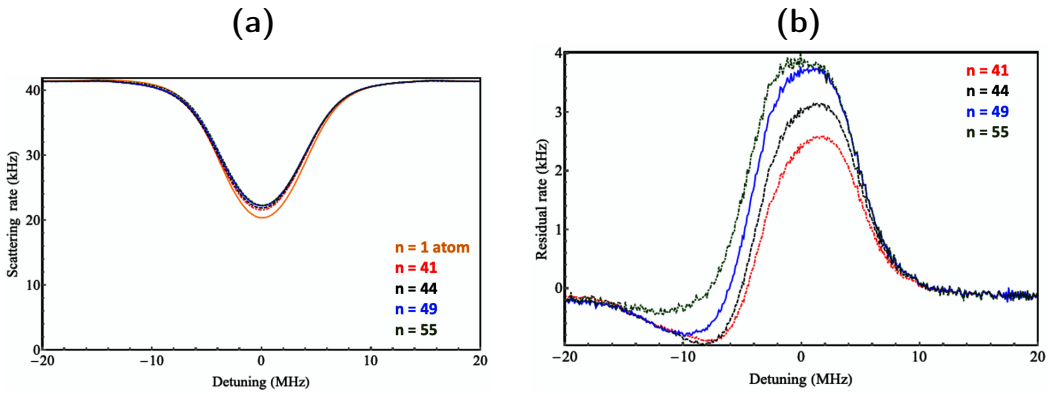

FIGURE 4.23: **(a)** Plots showing the dependence of ATS/CPT spectrum on increasing excitation n; **(b)** corresponding residual plot, when the Maxwell-Boltzmann velocity distribution is included in the Monte-Carlo simulation. The plots are obtained from 2 nearest neighbours solution averaged over 150 positions with a density of 10^{10} cm^{-3}. For these plots $\Omega_C = \Omega_P = 5$ MHz, $\gamma_3 = 0.019$ MHz, $\gamma_{2d} = 0.38$ MHz and $\gamma_{3d} = 0.19$ MHz, $\gamma_2 = 6.065$ MHz.

In the calculation, the probe detuning Δ_P is set to zero, showing that the probe laser is stabilised to the resonance of the probe transition. Thus, the observed probe detunings are only from the probe Doppler shifts $\Delta^{(P)}$. The numerical solution is obtained for the case of 2 nearest neighbour atoms in 49S state with atom-velocities lying within the range $-20 \leq v \leq 20$ m/s. Typically, the range of atom-velocities is wider than the one considered. Take for example, the most probable velocity in

the Maxwellian velocity distribution is $v_p = \sqrt{\frac{2k_B T}{m_{Rb}}} \sim 237$ m/s. Larger velocities imply larger Doppler shifts which also implies larger beam detuning. It appears that large detunings affect the convergence of the numerical solution, hence requiring long computational times. Figure 4.23 shows the resulting ATS/CPT spectrum when the Maxwell-Boltzmann velocity distribution is included in the simulation for 2 nearest neighbours averaged over 150 positions with a density $\varrho_a = 10^{10}$ cm^{-3} in different excitation levels. The result shows that in thermal vapour, suppression effects would be visible only for sufficiently high excitation level. The effect of atomic motions also extends to the reduction of the visibility of the effects of multi-photon processes such as excitation enhancements, which appear in spatially ordered systems such as optical lattices or dipole trap arrays.

4.4.3 Interacting Rydberg atoms in an optical dipole trap (ODT)

Atoms can be collected in an ODT, as will be explained in the next chapter, to fulfil the requirements for controllable qubits based on neutral atoms. These systems are widely used in quantum information for gate operations with Rydberg interactions. A typical ODT is implemented using an intense far off-resonance laser focused at the centre of MOT cloud. Thereby acting as an optical tweezers for trapping only a few atoms from a MOT (see section 5.2). This laser beam is usually Gaussian, thus creating a 3D harmonic potential that is Gaussian in all directions. The spatial distribution of the atomic cloud reads [164]

$$n(\mathbf{r}) = \frac{1}{(2\pi)^{\frac{3}{2}}\,\sigma_x\,\sigma_y\,\sigma_z}\,\mathrm{e}^{-\left(\frac{x^2}{2\sigma_x^2}+\frac{y^2}{2\sigma_y^2}+\frac{z^2}{2\sigma_z^2}\right)}\,, \tag{4.35}$$

where $\sigma_i = \frac{1}{\omega_t^{(i)}}\sqrt{\frac{k_B T}{m_{Rb}}}$ for $i = x, y, z$ is the cloud size on the horizontal axis, vertical axis and along the optical axis respectively, $\omega_t^{(i)}$ are the corresponding trap frequencies, m is the mass of Rb atoms and T is the thermodynamic temperature of the system having considered thermal equilibrium in the whole system. The volume of the trap given by

$$V = (2\pi)^{\frac{3}{2}}\,\sigma_x\,\sigma_y\,\sigma_z\,, \tag{4.36}$$

with a peak density of $\varrho_a = \frac{N}{V}$ for N number of atoms within the trap volume.

Unlike in a MOT, the focused Rydberg transition lasers (with beam sizes of the order of few hundreds of μm) cover the whole ODT cloud whose average size is only a few μm,

assuming a proper alignment of the Rydberg excitation lasers with the ODT. Hence, to simulate the distribution of atoms within the ODT volume, the coordinates of the atom-positions are selected from normal distributions whose standard deviations are given by the cloud sizes. From these, the nearest neighbours can be easily selected. The parameters from the ODT described in section 5.2.1 are considered. A trap with cloud size $\sigma_x = 0.4\,\mu$m, $\sigma_y = 0.5\,\mu$m and $\sigma_z = 5.3\,\mu$m in the horizontal plane, vertical plane and along the optical axis respectively, was obtained with ensemble temperature of about $500\,\mu$K [95]. The trap could hold up to 100 atoms with a density up to about 5×10^{11} cm^{-3}. With such a trap, the interaction between atoms in 49S state would be in the resonant dipole-dipole regime. Hence, the excitation dynamics of the interacting atoms in 35S state is considered instead in order to maintain interaction in van der Waals regimes. For a particular peak density of the MOT, the ODT atom density is usually higher, so one would expect more interaction effect in the ODT. Due to the high degree of control achievable over an ensemble of atoms in the ODTs, the spatial arrangement of the atoms and its effect on the exchange of energy among them can be controlled by controlling the trap geometry. Hence, the trap sizes and cloud densities can be varied.

From figure 4.17, about 70% of the atom-positions offered by uniform distribution satisfy the interatomic distance distribution given in equation (4.30). However, only about 20% of the atom-positions offered by normal distribution satisfy the interatomic distance distribution. Thus, describing the system with the interatomic separation distribution will not be completely accurate. To ensure that the atom distribution follows the interatomic separation distribution, then only about 20% of the possible atoms should be considered. The percentage of the possible ODT atom-positions considered to simulate the Rydberg-Rydberg interactions between atoms within the dipole trap appear to affect the significance of the interaction effects observed. Figures 4.24(a) and (b) show the dependence of the ATS/CPT spectra on the considered fraction of the total ODT atom-positions for 2 and 3 nearest-neighbour solutions with atom density of 5×10^{11} cm^{-3} in the 35S Rydberg state. The results show that more suppression effect is observed with less fraction of total ODT atoms position considered. This implies that restricting the atom-positions to close to the centre of the cloud increases the significance of the Rydberg interaction effect. This is because the larger the ODT sample fraction considered, the larger the volume of the trap considered. Hence, the higher the possibility of having lower interaction strengths between atoms.

Up till this point, the EIT, ATS and CPT regimes have been differentiated based only on the observed interaction effects, i.e. suppression, shift, asymmetry and possibly

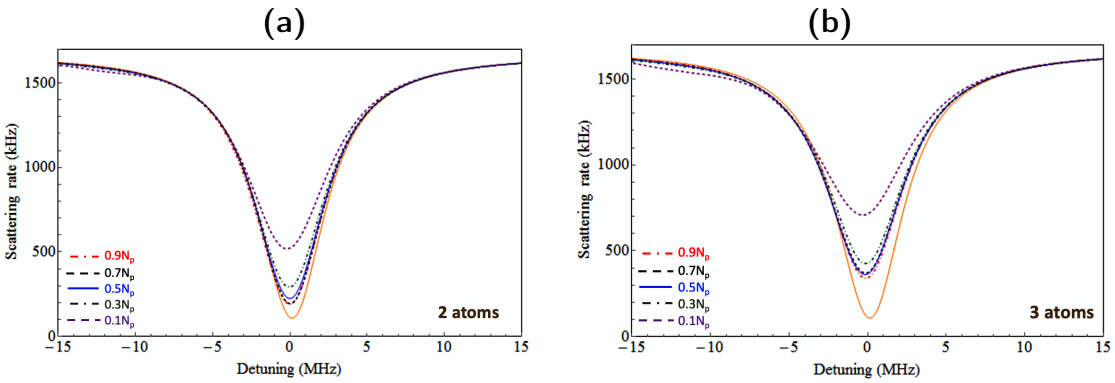

FIGURE 4.24: ATS/CPT dependence on the fraction of the total ODT atom-positions considered for **(a)** 2, **(b)** 3 nearest neighbours in the 35S Rydberg state. For these plots, $\Omega_C = \Omega_P = 5$ MHz, $\gamma_3 = 0.019$ MHz, $\gamma_{2d} = 0.38$ MHz and $\gamma_{3d} = 0.19$ MHz, $\gamma_2 = 6.065$ MHz. All orange lines are single atom solution.

enhanced excitation effects, having focused on the lineshape properties. However, the influence of Rydberg-Rydberg interaction on the transparency linewidth is still left out. The effect of interaction, induced either by increasing the densities or excitation levels, is observed in the broadening of the transparency features. Such effect would not be easily observed when studying lineshape properties. The linewidth properties tend to unravel the interesting effects that are hidden in the lineshape properties.

4.5 Linewidth properties of the excitation dynamics of interacting Rydberg atoms

As shown in the EIT/ATS/CPT spectra obtained in previous sections, stabilising the probe laser to the resonance of the probe transition while the coupling beam is scanned across resonance have produced spectrum that can easily be seen as and approximated by a Lorentzian function. So similarly to what was done in section 4.2.4, the influence of Rydberg-Rydberg interaction on the linewidth of the transparency features is investigated by fitting a Lorentzian function given in equation (4.25) to the scattering rate lineshape produced from the Monte-Carlo solutions. The Full Width at Half Maximum (FWHM) gives the value of the linewidth of the transparency features.

The plot of the linewidth of transparency features as a function probe Rabi frequency for two and three 49S nearest-neighbour atoms solutions averaged over 150 atom-positions is shown in figures 4.25(a) and (b) for varying atom density. This is also similar to considering the case of increasing excitation levels with constant density. In the low probe (EIT) regime, the effect of increasing interactions is negligible because

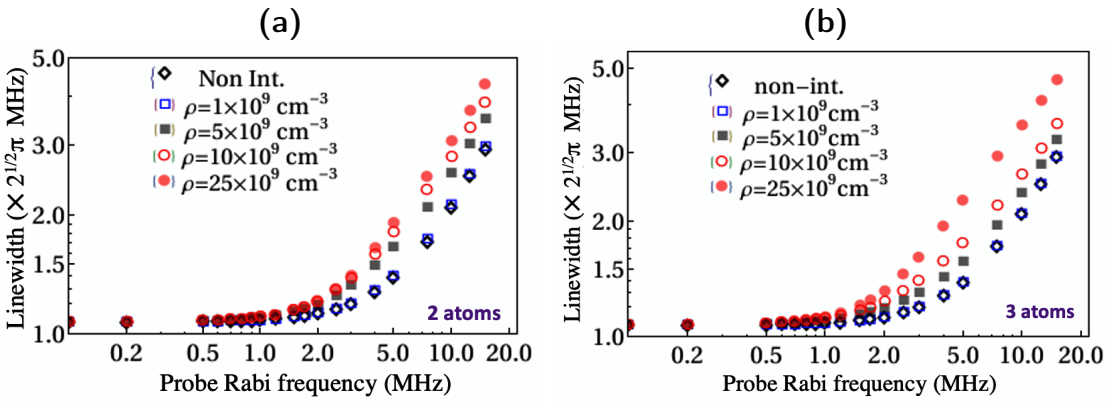

FIGURE 4.25: Linewidth of transparency features as a function probe Rabi frequency for **(a)** 2-atom, **(b)** 3-atom solutions averaged over 150 atom-positions with different atom densities. Interaction-induced broadening effect sets in at high densities. For these plots $\Omega_C = 5$ MHz, $\gamma_{2d} = 0.38$ MHz, $\gamma_{3d} = 0.19$ MHz. **NB:** The $2^{\frac{1}{2}}\pi$ factor on the linewidth axis is different from the 2π factor that usually come with frequency values.

the probe absorption properties are independent of the probe Rabi frequency as expected. On making a transition into the high probe regime, the effect of interaction begins to appear in the broadening of the transparency features for increasing atoms density (or excitation level). In the non-interacting regime which is marked by regimes of low densities or excitation levels (blue unfilled square markers), the solution of the OBEs is equivalent to that of a single atom (black diamond markers) as described in section 4.1.1. Both in the non-interacting and interacting regimes, the size of the transparency linewidth tends to show the same evolution as the transition is made from low to high probe regime. In the low probe regime, the linewidths appear to be subnatural but in the high probe regime, the linewidths appear to be either subnatural or not. This is because the linewidth in the high probe regime depends linearly on Ω_p.

The interaction-induced broadening of the transparency linewidth is shown in figure 4.26 to have a strong dependence on the number of nearest-neighbour atoms considered. Similarly to the lineshape study, this will only occur for an appropriate choice of atom densities and excitation levels for which the dependence on the number of nearest-neighbour atoms considered is distinctive. For example, the solutions in figure 4.26 is done for atoms in 49S state with density $\varrho_a = 2.5 \times 10^{10}$ cm^{-3}. The plot helps to understand the point of transition from the low probe regime to the high probe regime. The high probe regime is the point where the transparency linewidths obtained from each N-atom solution begin to differ. This is similar for figure 4.25, as it is the point where the interaction-induced transparency broadening effects begins to set in for interacting atoms with different densities or in different excitation levels. This implies that the boundaries of high or low probe regimes differ for a different

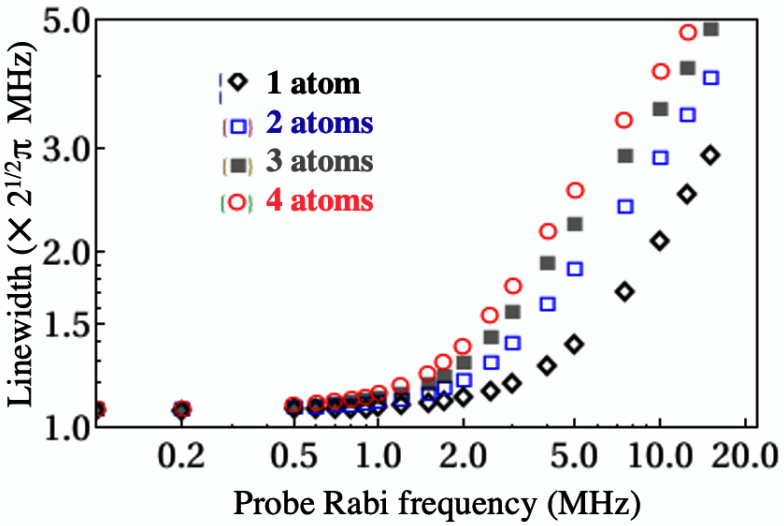

FIGURE 4.26: Plots linewidth of transparency features as a function probe Rabi frequency for singe atom solution and 2-, 3- and 4-atom solutions averaged over 150 atom-positions to show the dependence of the interaction-induced broadening effect on the considered number of nearest neighbours. For these plots $\Omega_C = 5$ MHz, $\gamma_{2d} = 0.38$ MHz, $\gamma_{3d} = 0.19$ MHz and $\varrho_a = 2.5 \times 10^{10}$ cm^{-3}. **NB:** The $2^{\frac{1}{2}}\pi$ factor of the linewidth axis is different from the 2π factor that usual come with frequency values.

choice of atom densities or excitation level.

The broadening is found to increase as $\sqrt{N}$ of the probe Rabi frequency which appears in the excitation of the singly excited Rydberg states as stated in equation (2.14). To confirm this, the linewidth is plotted against a scaled generalised Rabi frequency $\Omega_N^{(P)} = \sqrt{N\Omega_P^2 + \Omega_C^2}$ in figure 4.27(a). In the high probe regime, the 2-, 3- and 4-atom cases line up with the single atom solution due to blockade effect which allows atoms to be excited into an entangled state containing only one Rydberg excited atom with a probability that oscillates $\sqrt{N}$ times faster than the probability to excite a single atom. As shown in figure 4.26, the high probe regime is any point when the interaction-induced broadening effect, i.e. the entanglement effect, sets in depending on the density or excitation level of the system and irrespective of the system being in the EIT, ATS or CPT regime. However, it is important to state that the 2-, 3- and 4-atom cases lining up with the single atom solution in the extremely low probe regime should not be interpreted as the effect of collective excitation. Thus, to deterministically create a highly entangled state from the ground state atoms, one must ensure that the ratio $\frac{\Omega_P}{\Omega_C}$ is high enough with sufficiently large beam intensities.

As shown in figure 4.27(a), plotting the linewidth against $\Omega_N^{(P)}$ does not clearly show how the entire ensemble evolves and where the 2-, 3- and 4-atom cases begin to

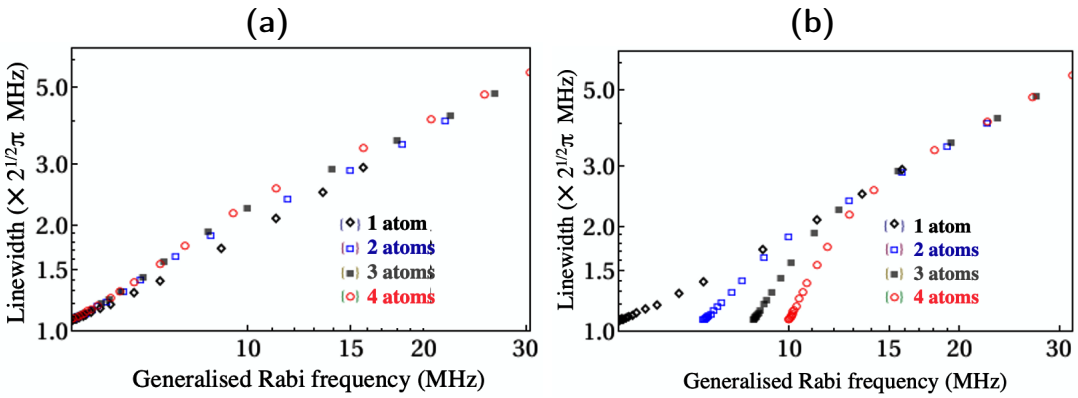

FIGURE 4.27: Linewidth of transparency features plotted against generalised Rabi frequencies **(a)** $\sqrt{N\Omega_P^2 + \Omega_C^2}$ and **(b)** $\sqrt{N\Omega_P^2 + N\Omega_C^2}$, for single atom solution and 2-, 3- and 4-atom solutions averaged over 150 atom-positions to show collective excitation effects. For these plots $\Omega_C = 5$ MHz, $\gamma_{2d} = 0.38$ MHz, $\gamma_{3d} = 0.19$ MHz and $\varrho_a = 2.5 \times 10^{10}\,\mathrm{cm}^{-3}$. **NB:** The $2^{\frac{1}{2}}\pi$ factor of the linewidth axis is different from the 2π factor that usual come with frequency values.

show the effect of collective excitation. This is clearly shown in figure 4.27(b) where the transparency linewidth is plotted against the rescaled generalised Rabi frequency $\Omega_N = \sqrt{N\Omega_P^2 + N\Omega_C^2} = \sqrt{N}\Omega$. The 2-, 3- and 4-atom cases show a total modification from the single atom case. The $\sqrt{N}$ effect is not visible on the left of the plot, i.e. the low probe regime, where there is no collective excitation effect. Meanwhile, on the right of the plot, the high probe regime, the 2-, 3- and 4-atom cases line up perfectly well with the single atom case in indicating an entangled state with single Rydberg atom. Also, the interaction induces a nonlinear dependence of the linewidth on the probe Rabi frequency. The nonlinearity is visible in the 2-, 3- and 4-atom cases. Considering the plot of the transparency linewidth against the scaled generalised Rabi frequency, Ω_N, creates the idea that the collective excitation effect is dependent on the strength of both beams. This is not always true since one of them, in this case Ω_C, is kept constant. In actual fact, it is sufficient to vary the strength of one of the beams to observe the $\sqrt{N}$ effect.

Furthermore, the fit of the transparency spectrum to the Lorentzian function given in equation (4.25) allows one to account for the magnitude of interaction-induced line shift. This is shown in figure 4.28 for single atom, 2- and 3- atom solutions averaged over 150 atom-positions with atoms in 49S state. For the non-interacting case and in the low probe regime, the shift is of kHz, which is less than the laser linewidth and thereby unresolvable. There also appears to be a nonlinear effect on the line shift induced by the van der Waals interaction. The shift could be as large as few MHz for interacting atoms as seen in the high probe regime. For atoms in a vapour cell,

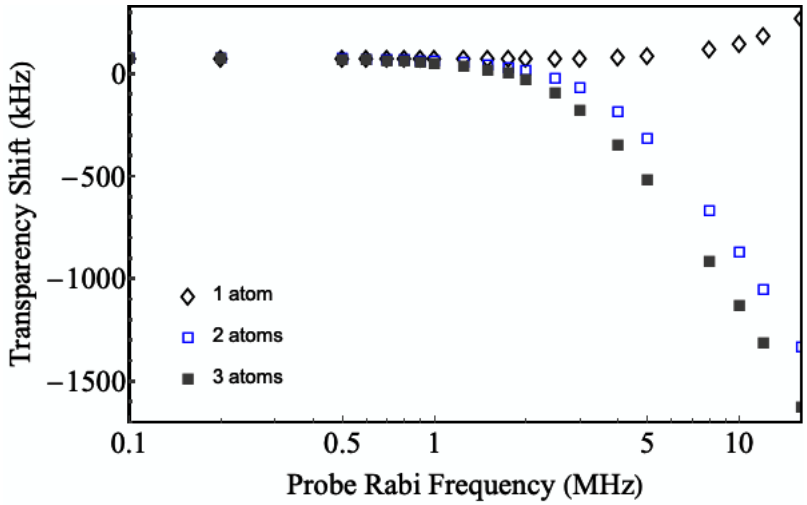

FIGURE 4.28: Plot of interaction-induced transparency line shift as function of probe Rabi frequency for single atom, 2- and 3-atom solutions averaged over 150 atom-positions. For these plot $\Omega_C = 5$ MHz, $\gamma_{2d} = 0.38$ MHz, $\gamma_{3d} = 0.19$ MHz and $\varrho_a = 2.5 \times 10^{10}\,\mathrm{cm}^{-3}$.

it is generally negligible compared to the effect of the thermal motions of the atoms. Hence, it would difficult to observe such shift effects. On the other hand, the effect of the dominant interaction-induced atomic motions in a dense MOT is considered negligible, thus creating the possibility of observing the shift effect. The interaction-induced atomic motions are also negligible in the ODT which usually require a high-resolution imaging system. Hence, besides the effect of the spatial distribution of the atoms, the process of observing the shift effect may also be limited by the resolution of the imaging.

The observation of collective excitation based on methods that rely on blockade mechanism caused by strong interaction between Rydberg atoms is not particularly new [4, 39, 40, 111, 112]. They are majorly based on the observation of coherent many-body Rabi oscillation at frequency Ω_N in an atomic system. The spectral broadening of the resonance lines and suppression of excitation with increasing density or excitation has also been observed in [27, 36, 76]. Also are the observations of the line shift, asymmetry and excitation enhancement effects [32, 33, 37, 161, 162]. In [40], they observed interaction effects between in as few as two atoms by observing coherent population oscillations for single-atom Rydberg excitations. In the presence of two or more Rydberg atom excitations, the van der Waals interactions lead to dephasing of the oscillations. However, this study has successfully investigated the collective excitation effects using the linewidth properties of the resonance spectra which has remained unexplored. This is of fundamental importance when preparing atomic ensembles for quantum information experiments. Also, it gives an understanding of how to control the physical mechanism required to deterministically create a highly entangled quantum

state from the ground state atoms. This is an important step towards demonstration of a neutral atom Rydberg gate [2]. The results also hold promise for studying dynamics and disorder in many-body atomic systems with controllable interactions and for scalable quantum information networks [165].

Summary

In this chapter, the extension of the study of two-photon excitation from a single atom picture to a realistically large number of atoms has been done. First, the theoretical study of the optical response of a non-interacting multi-atom system to laser fields in the EIT, ATS and CPT regimes was done. The step towards experimentally investigating the response of a homogeneously broadened atomic system to strong probe beam was also described. Quantitative analysis of the linewidth of transparency features obtained from a vapour cell experiment was found to agree with an experimentally realistic theoretical model.

The effects of strong Rydberg-Rydberg interactions have been described. This was with regards to the various three-level atomic coherent phenomena (EIT/ATS/CPT) which are described in terms of the transition from low to high probe regime. Using a Monte-Carlo approach, the many-body interaction effects were studied for different spatial distributions of interacting atoms in a vapour cell, MOT and ODT with different densities and excitation levels. The lineshape properties of the resonance spectra have been extremely useful in describing the interaction effects such as suppression effects, excitation enhancement (i.e. antiblockade) effects, line shift and asymmetry. The linewidth properties prove to be an efficient means of observing a collective, many-body generalised Rabi oscillation at a frequency $\sqrt{N}\Omega$ involving all $N \gg 1$ interacting atoms. These oscillations provide a gripping indication of the achievement of a collective Rydberg excitation blockade by a single excited atom which is associated with the production of a many-body entangled state having single Rydberg excited atom. This provides a better understanding of how the physical mechanism required to create many-body entanglement can be controlled.

Future works will involve the experimental investigation of the response of atomic systems to strong probe beam in the presence of Rydberg-Rydberg interactions. This was left unexplored in this thesis due to the Covid19 virus outbreak, which resulted in the total lockdown of the laboratory. However, the experimental setup described in this chapter, which was used to take measurements in a vapour cell in the non-interacting

regime, remains feasible for experimentally studying the excitation dynamics of interacting atoms in a vapour cell. The next chapter describes the ultracold trapping system to implement blockade-induced entanglement and quantum gate operations.

5 Implementation of Trapping Systems

As confirmed in the previous chapter, observing interesting interaction effects is generally difficult in atomic systems where the thermal motions of atoms have a significant effect. Exciting the trapped laser-cooled atoms to specific Rydberg states not only allow one to control the position and spatial structure of the atom sample for a considerable length of time or effectively manipulate the internal state of the atoms, but they can also be made to interact strongly in such a way that the atoms exchange energy quickly enough within an experimental timeframe. Within this timeframe, they move very little so that they can be considered virtually at rest and are thus referred to as a *frozen Rydberg gas*. In such a frozen gas, the atom energy exchange is not dominated by two-body interactions, but rather through simultaneous and collective interactions among atoms in the ensemble [135]. So, for typical cloud temperatures and densities realizable in a magneto-optical trap (MOT) and optical dipole trap (ODT), atoms move only a negligible fraction of the average interatomic spacing.

This chapter describes the techniques, laser systems and experimental setup for cooling and trapping atoms in a MOT. At the early stages of my PhD, I was involved in rebuilding and re-testing the ultrahigh vacuum chamber due to the need to replace previously setup rubidium (Rb) dispensers in the chamber. Thus, a short description of the rebuilding procedure will be done.

The lab had a previously running MOT which has been tested and characterised in [95, 166] and the setup remains mostly unchanged. However, the previous characterisation showed that the trap could not produce a highly dense atomic cloud that can be used to study Rydberg-based phenomenon. So, this chapter describes the effort made to improve the MOT setup so that laser-cooled atomic ensemble optimised to the regime where it is dense enough for the investigation of Rydberg interactions and cold enough to serve as a reservoir from which the ODT is loaded, can be achieved.

Unlike in a MOT where only local blockade is achievable since the size of the Rydberg excitation lasers interacting with the MOT atom cloud size is usually larger than the

typically achievable blockade radius, the size of the ODT atom cloud is usually smaller than the achievable blockade radius, hence making a global blockade achievable. The result of the characterisation of previous ODT running in the lab, done in [166], showed that the cloud produced from the ODT is larger than the required blockade radius. This chapter describes the experimental setup of a high-performance dipole trapping system, capable of producing a system where full blockade effect can be achieved and has the potential of implementing blockade-based quantum gate operations.

5.1 Magneto-optical Trap

The whole operation of trapping relies on the fundamental technique of laser cooling, which is based on the idea that light intensity gradients exert damping forces on atoms to slow the atomic motions [167]. This results in the reduction of the temperature of the atoms since the energy distribution of the atomic ensemble is a Maxwell-Boltzmann distribution, and the velocity of the atoms gives a measure of the temperature. Based on the basic principle of Doppler effect, the Doppler cooling technique allows for producing a velocity-dependent molasses or frictional force that cools atoms to microKelvin temperature when red-detuned counter-propagating beams interact with the atoms.

A typical MOT relies on three orthogonal pairs of red-detuned circularly polarised counter-propagating beams which are used to push the atoms toward the point where all the beams overlap. In the cold-atoms laboratory of the Open University, the cooling of Rb atoms is done with home-built 780 nm extended cavity laser systems. For simplicity, the cooling transition is selected such that the Rb atom is considered to be a two-level system, although it is not so in the general sense. The cooling is performed using the closed D_2 transition line $|5^2S_{\frac{1}{2}}, F = 2\rangle \longrightarrow |5^2P_{\frac{3}{2}}, F' = 3\rangle$ which is resonant to 780.24 nm laser wavelength.

The light absorption follows the general selection rules $\Delta F = 0, \pm 1$ (see appendix A) so that atoms in $|5^2P_{\frac{3}{2}}, F' = 3\rangle$ state can decay spontaneously back to $|5^2S_{\frac{1}{2}}, F = 2\rangle$. The energy level structure is shown in figure A.1. However, there is a probability that atoms in the ground state $|5^2S_{\frac{1}{2}}, F = 2\rangle$ will be excited into $|5^2P_{\frac{3}{2}}, F' = 2\rangle$, at which point, the rule also allows decay of atoms to the state $|5^2S_{\frac{1}{2}}, F = 1\rangle$. Atoms occupying $|5^2S_{\frac{1}{2}}, F = 1\rangle$ are far detuned from the incident cooling laser, hence do not take part in the cooling cycle. This leads to the total loss of atoms from the cooling cycle after many absorption-emission cycles. In other to avoid such a setback, the $|5^2S_{\frac{1}{2}}, F = 1\rangle$ state atoms are restored back to the cooling cycle by means of a *repump laser* which enables $|5^2S_{\frac{1}{2}}, F = 1\rangle \longrightarrow |5^2P_{\frac{3}{2}}, F' = 2\rangle$ transition and therefore ensures a non-zero

probability for decay into the $|5^2S_{\frac{1}{2}}, F = 2\rangle$ state.

Although the optical molasses efficiently slow atoms down with their temperature reduced and their space density increased, they are still not accumulated at a particular position. This is because they diffuse out of the cooling region due to an imbalance in the scattering force and a heating mechanism generated by the counter-propagating cooling beams. Hence, there is a need to extend the cooling system to a trapping system. The radiation force can be made position-dependent by applying a non-uniform magnetic field ($\mathbf{B}$) to the molasses setup. This $\mathbf{B}$-field is produced by two identical coils carrying opposite current, the *anti-Helmholtz* coils. It is zero at the centre of the trap where the three pairs of beams cross and increases linearly radially outwards away from the zero-field point. The $\mathbf{B}$-field also causes the *Zeeman splitting* [168] of atomic excited energy levels into non-degenerate magnetic sub-levels $m_F = -F, \cdots, 0, \cdots, +F$ during atom-field interaction. Since the MOT rely on Zeeman splitting which allows one to take advantage of transitions between hyperfine magnetic sublevels, this enables atoms to be sub-Doppler cooled to temperatures as low as tens of microKelvin [169, 170, 171, 172].

5.1.1 Experimental Setup: Laser Locking and Atom Trapping

The laser systems and layout of the optical components and laser beam paths for achieving the MOT are shown in figure 5.1. This is made up of two segments: the laser locking systems and the trapping system. Similar to the Rydberg excitation probe laser system in section 3.2.1, the cooling and repump lasers are produced by the tunable extended cavity diode lasers (ECDL) using the commercially available Sanyo DL-7140-201 diode laser (775-800 nm) with output powers of few tens of mW. For a stable operation of the diode lasers, the currents and temperatures are controlled using the Thorlabs LDC 202C (200 mA) Laser Diode Controller and TED 200C Temperature Controller or a combined Thorlabs ITC 502 Laser Diode Combi Controller.

The lasers are locked in frequency using the saturated absorption spectroscopy (SAS) technique which produces photodiode-detected Doppler-free locking spectra (similar to the purple trace in figure 3.2 (c)) by passing the lasers through Rb vapour cells. The lasers are then locked to the appropriate cooling and repump transitions, $|5^2S_{\frac{1}{2}}, F = 2\rangle \longrightarrow |5^2P_{\frac{3}{2}}, F' = 1,3\rangle$ and $|5^2S_{\frac{1}{2}}, F = 1\rangle \longrightarrow |5^2P_{\frac{3}{2}}, F' = 1,2\rangle$ *crossover peaks* of ^{87}Rb respectively, by feeding the corresponding electronic frequency-dependent error signals which are produced by external electronics back into the laser

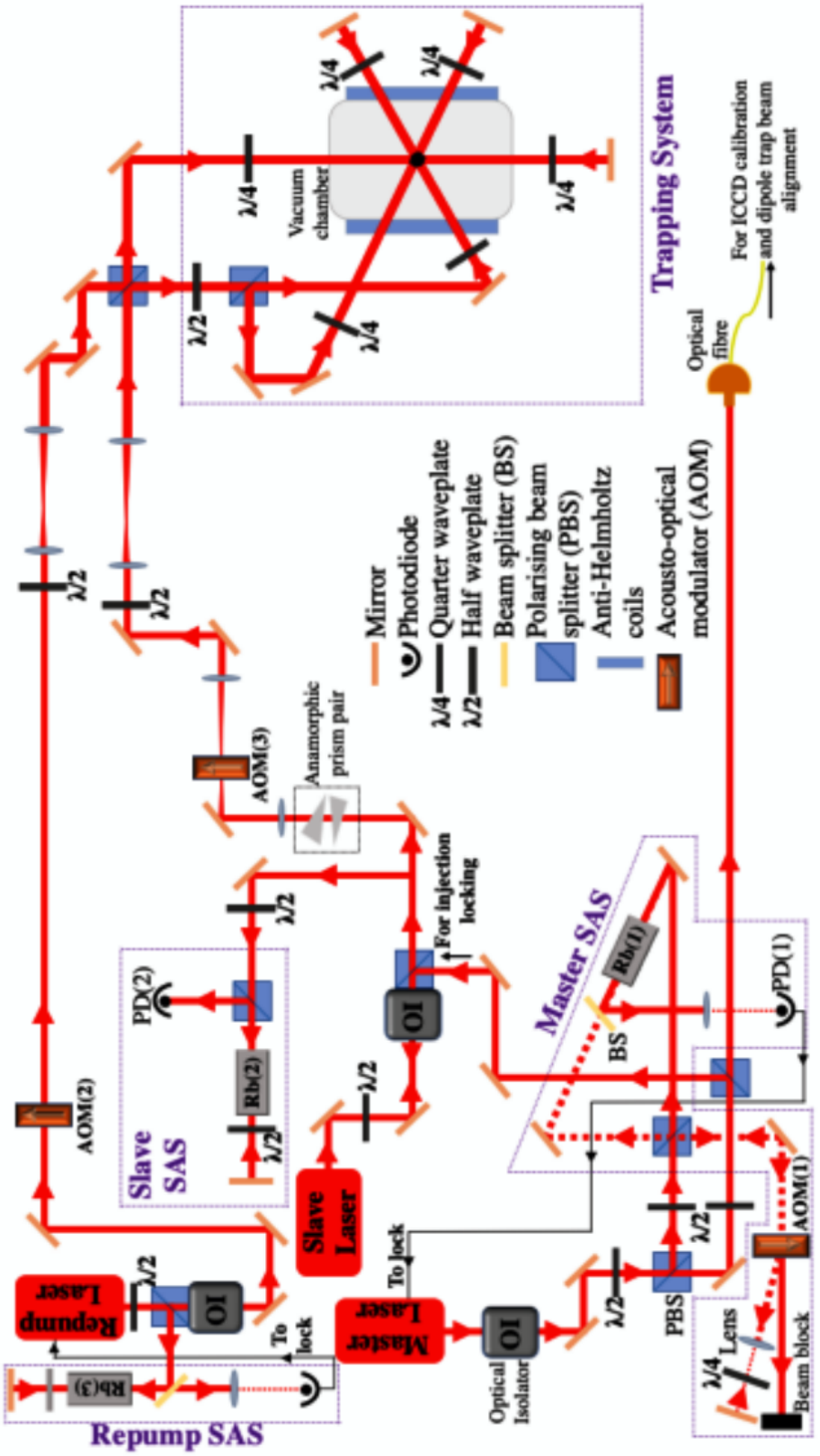

FIGURE 5.1: Schematics of the optical setup of a MOT showing the laser (master and repump) locking setup and the trapping system inside an ultra-high vacuum chamber.

control devices. So much power loss occurs in the SAS process due to coupling of the cooling laser to an acousto-optic modulator AOM(1) in a double-pass configuration. Therefore, to maintain a powerful cooling beam, an *injection locking technique* is used. This is implemented by using a *master-slave* laser configuration where the locked master laser is injected into a more powerful slave laser (with an output power of about 40 mW). So the slave laser is forced to operate at the frequency of the master laser due to their initially close frequencies while the output of the slave laser is now used as the cooling beam for the MOT. This process is unnecessary for the repump beam since a lesser beam power is sufficient for the repump process.

The shape of the cooling beam is initially elliptical. It is corrected by passing the cooling beam through a Thorlabs PS875-B-N-SF11 pre-aligned anamorphic prism pair which converts the initially elliptical beam (see figure 5.2(a)) to nearly circular ((see figure 5.2(b))) by magnifying the beam in one dimension. This helps to improve the intensity profile of trapping beams and produce a more spherical atom cloud. The principle of beam-shape correction is discussed in section 5.2. The images of the beam before and after anamorphic prism is collected on a CCD camera. 2-D Gaussian fits are done on the images to show the beam shape (as shown in figures 5.2(a) and (b)) as well as to extract the sizes from the standard deviations of the fits.

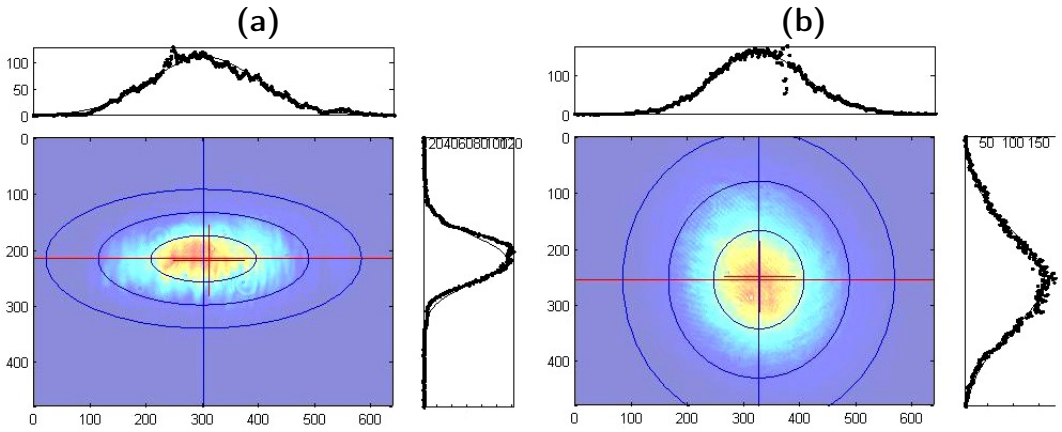

FIGURE 5.2: 2-D Gaussian fit on cooling beam image: **(a)** before beam shape correction; **(b)** after beam shape correction. This shows the beam shape and gives the beam size.

After locking, AOMs are adopted to change the laser detunings and intensities. These AOMs are externally controlled by using an experiment sequence programme written in Labview. The frequency detuning of the cooling beam from resonance is controlled by passing the master laser through an AOM(1) in a double-pass configuration combined with a cat's eye retro-reflector to avoid altering the alignment of the beam. Both the

repump and cooling beams are passed through AOMs 2 and 3 in a single-pass configuration for controlled-switching of the beams in an experiment sequence. Changing the frequencies of the AOMs 2 and 3 causes a change in the deflection angles of the beams. This misaligns the beams and therefore switching them off.

Before finally passing them into the vacuum chamber to obtain the MOT, additional collimation of both the cooling and repump beams is employed using a pair of plano-convex lenses to adjust the sizes of the beams hence, the resulting trapping volume. The collimation is also done to ensure a balance in the intensities of counter-propagating beam pairs when they interact with the atoms. Detailed principle of beam collimation is discussed in section 5.2. For the collimation, the beams are first passed through 5 cm lenses that first converge the beams at focal points after which the beams begin to diverge. As shown in figure 5.3, the divergence of the cooling beam after the first collimating lens is measured by obtaining the images of the beams on a CCD camera at several positions along the path of the beams, and doing 2-D Gaussian fits on the images to extract the beam sizes. By using 15 cm lens as the second collimation lens placed at about 20 cm distance from the first lens, cooling and repump beam diameters of about 2.5 mm were produced after the collimation. However, after travelling about 1 m distance from the second collimating lenses to the centre of the vacuum chamber, the diameters of the beams have diverged to about 3.6 mm [95].

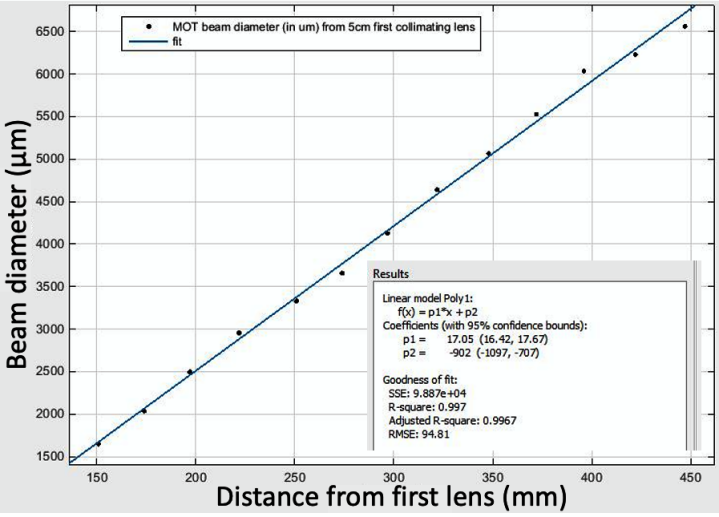

FIGURE 5.3: Cooling beam diameter obtained from 2-D Gaussian fits done on the cooling beam CCD images that are taken at various positions along the beam path after the first collimation lens.

After the collimation stage, both the cooling and repump beams are then sent to the chamber. They are first made to overlap on a set of polarizing beam splitters (PBS)

that split each beam into three equal beams. This typically produced 2 mW beam powers for the three cooling beams and about 0.4 mW each for the three repump beams. The power of each beam is controlled using $\frac{\lambda}{2}$-waveplates that are placed on the paths of the beams. The three beams are then passed orthogonally through the chamber, overlapped at the centre where the atoms are trapped, and then retro-reflected into the chamber to create counter-propagating beam pairs. Each incoming and retro-reflected beam pair are passed through separate $\frac{\lambda}{4}$-waveplates to make them oppositely circularly-polarised. Due to divergence of the beams and coupling to optical components for the retro-reflection process, each beam retro-reflected beam intensity is reduced by a factor of about 1.3 compared to that of the incoming beam [95]. This causes MOT beam imbalance at the trapping centre. Therefore, as described in section 5.1.3, an effort is made to ensure beam balance at the trapping region.

In addition to the pair of anti-Helmholtz coils attached outside the chamber to produce the non-uniform magnetic field gradient necessary for the MOT operation, three pairs of coils in a Helmholtz configuration are also attached provide static uniform **B**-field. The Helmholtz coils produce an offset **B**-field to compensate for any stray field present in the environment. All the coils are driven by currents that are externally controlled using the Labview programme to produce **B**-field gradients, in the range of 10-15 G cm^{-1} for the anti-Helmholtz coils. Turning off the coil current results in just a cooling molasses. The experiment sequence Labview programme is also used to control the camera triggers to obtain the image of emitted fluorescence from trapped atoms.

5.1.2 Ultra High Vacuum Chamber

The whole vacuum system comprises of different parts (some parts are shown in figure 5.4). The main chamber is a commercially available 1.75l volume 8" Multi-CF Spherical Octagon: MCF800-SphOct-G2C8 chamber which is made of stainless steel with anti-reflection coated fused silica viewports for optical access of lasers through the chamber with minimal attenuation. The large side windows of the chamber are sealed with two big 8" Torr Scientific NW150CF6 glass viewports that are covered, on both sides, with anti-reflection coating optimised for 480-780 nm lasers. They provide access for the MOT horizontal beams. The MOT vertical beams access the chamber via two $2\frac{3}{4}$" NW35CF viewports. These can be seen above and below the holders of a system of high numerical aperture (NA = 0.5) dipole trap lenses fixed inside the chamber. Also, the dipole trap beam access the chamber through two small $1\frac{1}{3}$" NW16CF anti-reflection coated viewports optimised for 780-830 nm lasers.

Through a valve and an ion gauge, the main chamber is connected to a Varian VacIon

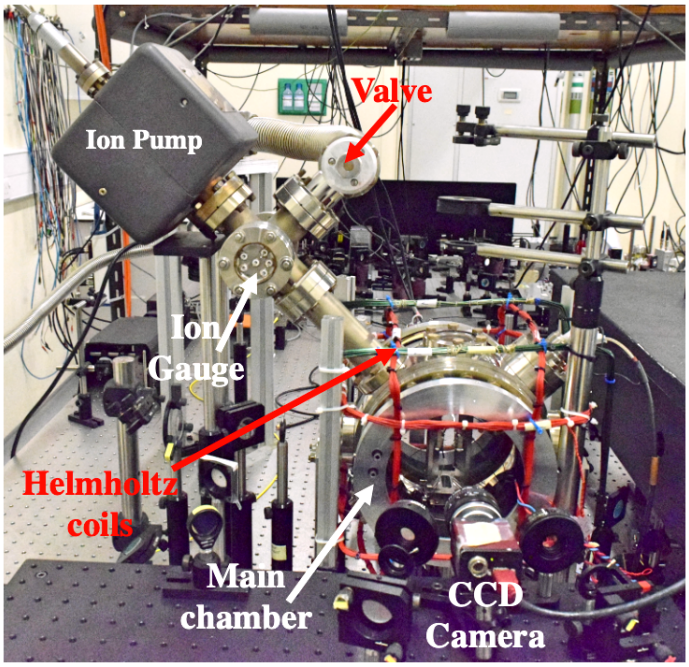

FIGURE 5.4: A partial view of the vacuum system.

Plus 20 StarCell ion pump that maintains the pressure in the system at UHV level. Rb atoms are loaded into the MOT from the background vapour provided from commercially available SAES Getters alkali metal dispensers (AMD) generated from a mixture of rubidium chromate (Rb_2Cr0_4) and a reducing agent, zirconium-aluminium (Zr-Al) alloy. They release Rb vapour, containing both ^{85}Rb and ^{87}Rb isotopes in their natural abundance, via a reduction reaction when the getter material is heated through an externally applied current, typically around 4 A. During the course of this PhD, the Rb dispensers in the chamber were exhausted as the dispensers gradually required higher driving current to dispense atoms. Hence, they are needed to be replaced. This process requires opening the feedthrough channel that holds the electrical pins for mounting the dispensers, as well as rebaking and outgassing the whole chamber.

The loading dynamics, performance and lifetime of any trap depends on the level of background vapour pressure. This should be kept low, about 10^{-10} Torr, to minimise the collisions of trapped atoms with background gas particles. Although pressure as low as 10^{-10} Torr is sufficient to work [173] with a MOT, the ODT would require less to achieve a high trap lifetime. Generally, the major limiting factor in highly dense ODT atom loading and lifetime is the dominant inelastic two-body collisions.

After disassembling the electrical feedthrough, the reassembling process starts by ensuring that all the mechanical components are appropriate for UHV and properly cleaned before being assembled back. The cleaning is done in an ultrasonic bath using a

(a) (b)

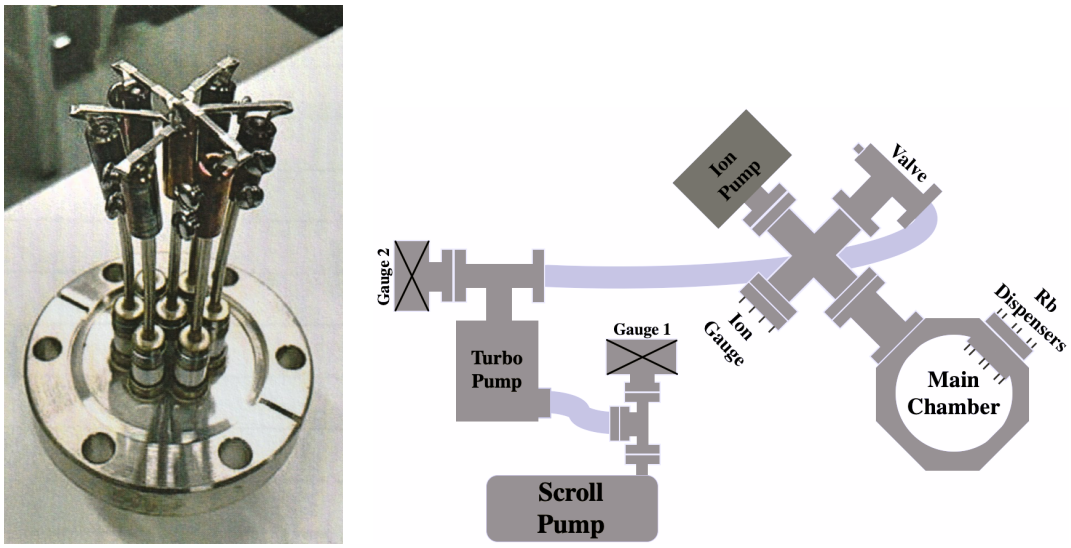

FIGURE 5.5: **(a)** The newly replaced dispensers mounted on the feedthrough pins using Be/Cu inline barrel connectors; **(b)** A overview of the whole vacuum system.

Decon80 detergent while rinsing is done with distilled water. They are then allowed to dry up and wrapped in aluminium foils to avoid being contaminated by dust or other contaminants before the final assembling. All components were held with powder-free disposable nitrile gloves to avoid fingerprint contamination. Using Be/Cu inline barrel connectors, which were also previously cleaned, the new Rb dispensers were fitted on the electric feedthrough pins as shown in figure 5.5(a). When re-assembling the components, one must ensure that flanges are properly connected with well-installed copper gaskets ConFlat seals while they are also tightened down uniformly using a torque wrench.

To achieve the final UHV pressure, the pumping process is done in stages (see figure 5.5(b)). First is an initial pump-down process where the pressure in the chamber was first reduced from atmospheric pressure of ~ 750 Torr down to a range of 10^{-2}-10^{-3} Torr using the Edwards nXDS10i dry scroll pump as shown in figure 5.6(a). A Leybold Vakuum IoniVac pressure gauge (1) is attached to the scroll pump to monitor the pressure fall with time. The turbomolecular pump is then turned on to further complete the initial pump-down to about 10^{-7} Torr as measured with another pressure gauge (2). The turbo pump's initial pump-down curve is shown in figure 5.6(b).

After the initial pump-down process, the pressure is further pumped down by outgassing the chamber surface. This is sped-up by baking the system at a temperature of about $165\,^{\circ}$C. Although the maximum allowable temperature of the main chamber

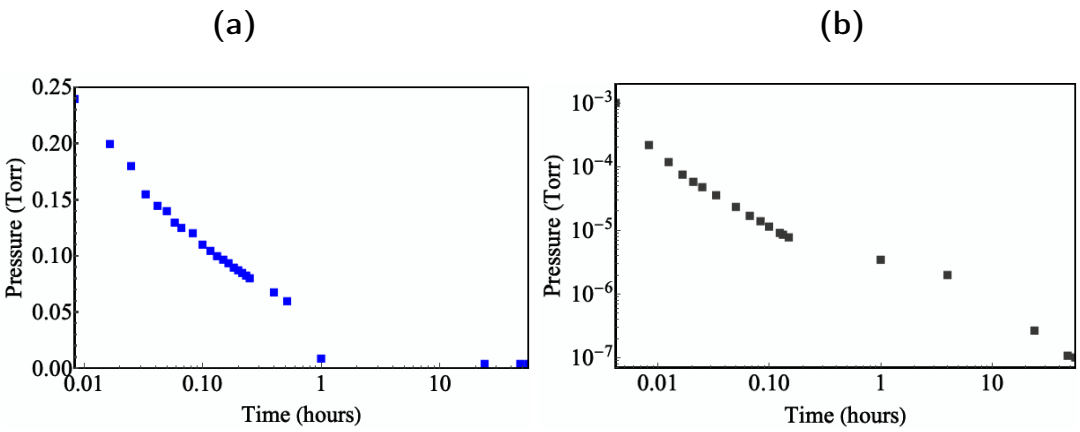

FIGURE 5.6: The curve for the initial vacuum chamber pressure pump-down using the **(a)** scroll pump; **(b)** turbo pump.

viewports is about 220 °C, one must also keep other optical components within the chamber in mind. The baking is done uniformly, to avoid damage caused by thermally-induced stress and uneven expansion of components, by wrapping the chamber and all other components with several layers of conductive foil while a temperature increase is done gradually at a rate of 0.2 °C/min over 10 days. Thermocouples connected to a temperature regulation unit were attached to various parts of the vacuum system, such as the chamber viewports, the 5-way cross above the chamber, the ion pump and the bellows leading to the turbo pump, to monitor and control the temperatures. The evolution of the pressure in the chamber during this period and beyond is shown in figure 5.7. A low outgassing material, such as stainless steel, used to make the chamber provides a great advantage of attaining UHV pressure. The evolution of the varying temperature is shown with blue texts. The baking is done simultaneously with outgassing the Rb dispensers by applying current to release gases without releasing Rb atoms.

After the heating, gradual cooling of the system down to room temperature follows over a few more days. It should be noted that the measured values of the pressure are not totally accurate, they only give insight into the evolution of the pressure inside the chamber. The expected pressure should be a few orders of magnitude lower than the measured pressure. This is typically below 4×10^{10} Torr, which is the lowest value measurable with the gauge. The real pressure inside the chamber is characterised by monitoring the ion pump current. After getting to the room temperature, ion pump is then allowed to continue the pumping till a current of $0.8\,\mu$A is achieved. This indicates a pressure of below 4×10^{10} Torr inside the chamber, thus, making it appropriate for cold atoms experiments.

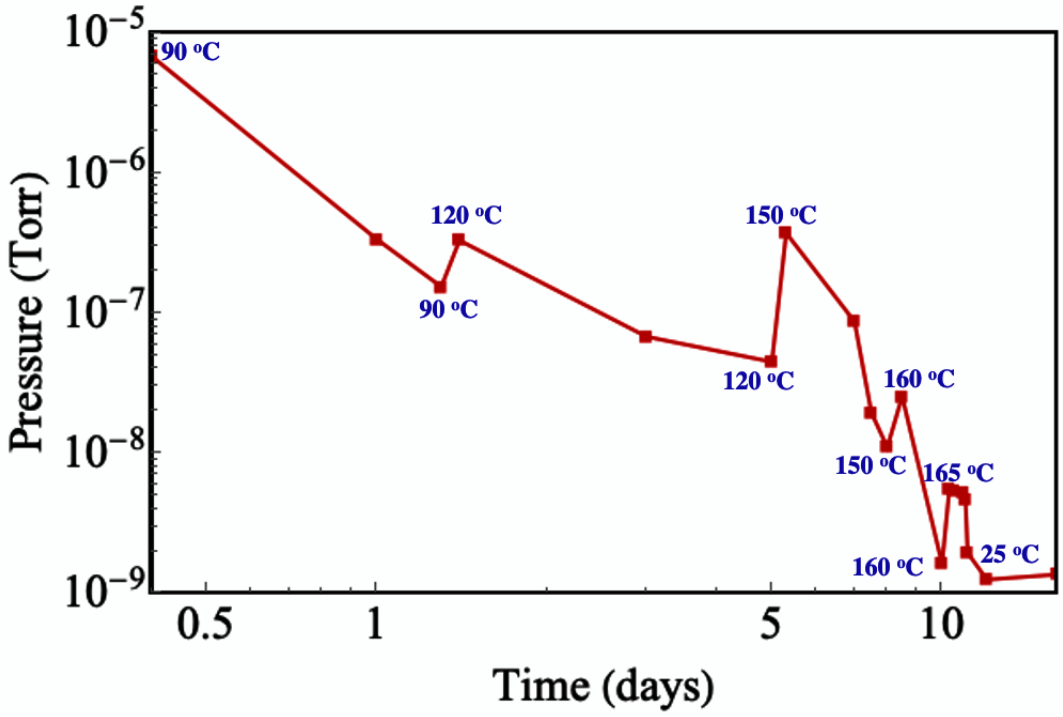

FIGURE 5.7: The evolution of the chamber pressure during baking and cooling down stages. The baking temperature was gradually increased to 165 °C after which cooling is done gradually back to room temperature. The evolution of the varying temperature is also shown with blue texts.

5.1.3 MOT Imaging and Characterisation

Achieving an excellent MOT with a large number of atoms and high spatial density depends significantly on the design of the cooling mechanism. The cooling mechanism itself is determined by several factors such as the alignment, intensities and detunings of the laser beams, temperature and pressure of Rb vapour and background gases inside the chamber or the strength and gradient of the **B**-field. Furthermore, the behaviour of the atoms in the trap will effectively determine the lifetime of the trap.

The MOT is imaged using the fluorescence imaging technique whereby light scattered from the atoms is collected and imaged on the camera or photodiode. This is adopted because, in contrast to the absorption and phase-contrast imaging techniques where it is required to set up an additional probe beam for imaging, the behaviour of cloud atoms can be monitored without extra perturbations. The spatial distribution and position of the cloud, as well as fluorescence of the beam alignment, can be monitored on the CCD camera. Also, the fluorescence and changes in the trapped atom number can be measured using the Thorlabs DET100A/M silicon detector-based photodiode and the Andor iStar CCD 334 intensified charge-coupled device (ICCD) camera. However, the signal from any of the detectors can be digitised for analytic purpose.

The fluorescence from the background Rb atoms in the chamber allows for the alignment of the MOT beams. Beams are made to cross and are optimised at the point where the ODT is to be created. This point is identified by making an intense mimic beam from the optical fibre (see figure 5.1) to pass through and focus at the centre of the chamber by a system of high numerical aperture (NA $= 0.5$) lenses mounted for focusing the dipole trap beams at the centre of the MOT. When tuned to resonance, while the dispenser current is increased to about 4.2A for about a minute to pump a large amount of Rb atoms into the chamber, the MOT beams and the mimic beam then become visible on the CCD camera (as shown in figures 5.8(a) and (b)) as result of sufficient light scattered by the atoms. Hence, the three counter-propagating MOT beams can be aligned to create a cloud of trapped atoms at the trapping region. The angle between the horizontal beams is restricted to $\sim 49^{\circ}$. The acute-intersection angle between the horizontal beams is unavoidable due to the restricted space between the two high-NA dipole trap lenses available as the trapping region. Imaging the MOT cloud also allows for the proper adjustment of the **B**-field offset to be done. Figure 5.8(c) and (d) shows the typical images a typical MOT cloud fluorescence collected on a CCD camera and an ICCD camera respectively.

Once the atoms are trapped in the MOT, it is therefore necessary to characterise the trap to find the optimum parameters for cooling. Parameters such as the trapped atom number and density, the temperature of atoms in the traps, trap depth and trap size are obtained by taking and interpreting fluorescence imaging measurements with the detectors. The MOT was characterised in [95] and was found to trap an average of about 4.9×10^5 atoms with an average lifetime of about 3.2 s. An average cloud radius of ~ 0.4 mm was obtained when 2-D Gaussian function fit was done to the cloud images collected from the CCD camera. The number density was determined to be $\sim 6.2 \times 10^8$ cm^{-3}. The temperature of trapped atoms was measured to be about $500\,\mu$K but this was reduced to about $79\,\mu$K for the molasses, i.e. when the **B**-field is turned off for some few milliseconds before the temperature is measured.

This recorded atom density is relatively low compared to typical MOT experiments where the atom density can reach up to 10^{10} cm^{-3} [174]. It is not sufficient for experimentally studying interacting Rydberg gases as shown in chapter 4 except for choices of very large excitation levels that may not be feasible in the Open University cold atoms laboratory due to the limited available Rydberg excitation laser powers. The first factor limiting the MOT density is the difficulty in aligning the beams due to the small size of the MOT beams. It is possible to achieve a denser MOT cloud with proper beam

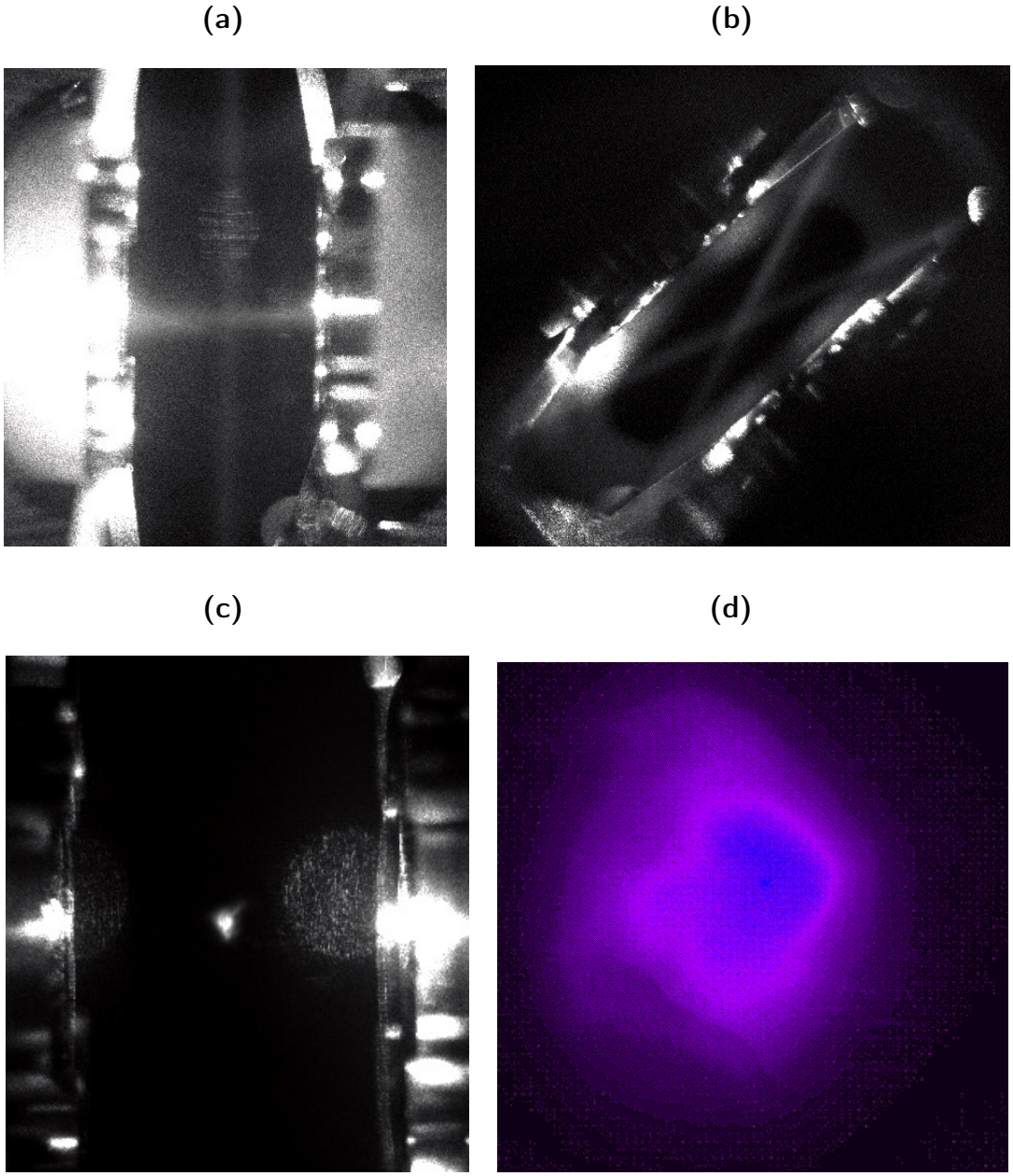

FIGURE 5.8: **(a)** Side view and **(b)** Top view images of the fluorescence trace from the MOT beams; **(c)** A typical CCD image of atoms trapped in the MOT right at the trapping region of the ultra-high vacuum chamber; **(d)** A typical ICCD image of atoms trapped in the MOT.

alignment and the MOT coils setting. However, the trap would not overlap with the dipole trap. Therefore, it is necessary to increase the trapping volume done by increasing the size of the trapping beams to make the alignment of the trapping beams easier.

First, to ensure that high intensities of the trapping beams are maintained with larger beam sizes, the output beams from the single-pass AOMs (2) and (3) are optimised such that the cooling and repump beam powers are optimised to about 4 mW and

2 mW respectively for each counter-propagating beam pair. To create a large MOT [175], the second collimation lenses on the path of the beams were replaced with 30 cm focal length lenses. Thus, resulting in a 4.5 mm cooling beam and a 3.4 mm repump beam from the collimation. As shown in figures 5.9(a)-(b), the collimation is set is to ensure a balance in the intensities of each counter-propagating beam pair when they interact with the atoms. After travelling about 1 m to the chamber, the average cooling and repump beam diameters have converged to about 4.3 mm and 3.3 mm respectively. As a result, each retro-reflected beam's intensity only changes by a factor of about 0.95 and 1.03 for the cooling and repump beams respectively when compared to the incoming beam. This confirms an almost balanced intensity between the incoming and retro-reflected beams as required for the proper functioning of the MOT.

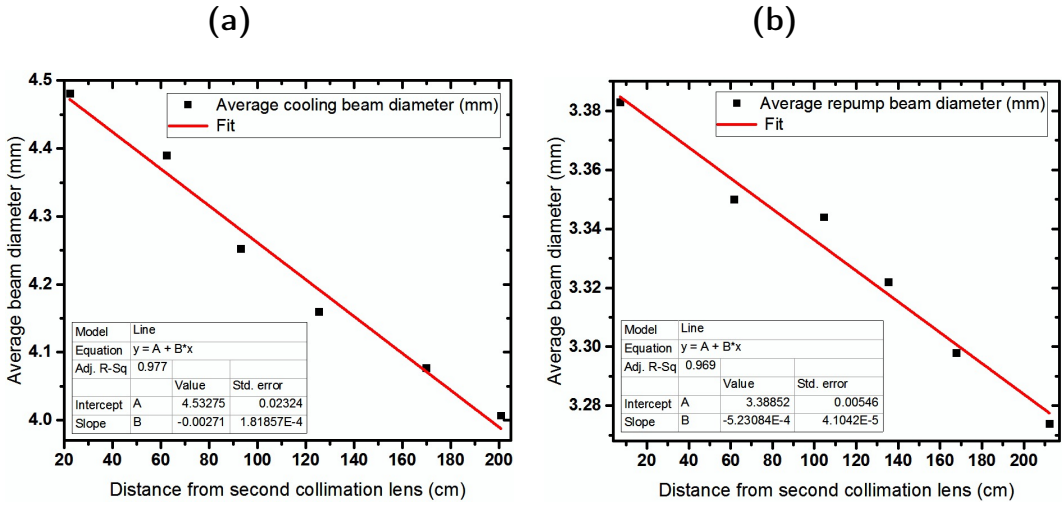

FIGURE 5.9: Average **(a)** cooling and **(b)** repump beam diameters obtained from 2-D Gaussian fits on CCD images of the beams taken at various positions along the path of the beams after the second collimation lens.

As a result of the larger sizes of the MOT beams, the intersection angle between the horizontal beams is reduced to $\sim 40^{\circ}$ due to the space restriction caused by optical components at the trapping region. Although this is necessary for the horizontal beams to pass through without clipping the optical components inside the chamber, such unusual trap geometry would limit the trap's density. Another possible density-limiting factor is the *cold collisions* between atoms such that the internal state of one of the colliding pair changes. Detailed studies of the density-limiting effects are done in [176]. Attempts made to avoid this limitation includes the demonstration of a dark spontaneous-force optical trap, also called *dark SPOT* or *dark MOT*, which involves atoms being predominantly confined in a dark hyperfine level that does not interact

with the trapping light [177]. Another is the demonstration of a compressed magneto-optical trap (CMOT) whereby atoms are first collected from the background vapour using low **B**-field gradients, and then trap compression is done by rapidly increasing the **B**-field gradients. The separation of these collection and compression processes allowed high densities to be achieved for large numbers of atoms [178].

Having stated the efforts made to create a more functional and denser MOT with potential application for investigating Rydberg-Rydberg interactions in ultracold systems, it is still necessary for experimental measurements to re-characterise the MOT properties to be done. Due to the limited time available to see this through, the re-characterisation procedure has been left for future experiments.

5.2 Implementation of Optical Dipole Trap (ODT)

The MOT is obtained to serve two purposes: dense enough to study the dynamics of interacting Rydberg gases and cold enough to serve as a reservoir from which the ODT can be loaded to produce small atom ensemble that can be implemented as a qubit system for quantum gate operations. In MOT systems [27, 28], the cloud size exposed to the Rydberg excitation laser beams is larger than the blockade radius. This creates many collective Rydberg states within the cloud at a time.

The typical density of the ODT is orders of magnitude larger than that of the MOT. Thus, more effective many-body interactions can be produced. However, the strength of many-body interactions does not necessarily translate into a functional fast quantum gate. Usually, large interactions are associated with strong mechanical forces on the trapped atoms, which may cause the internal state of the trapped atoms to be entangled with motional degrees of freedom during the gate operation. Thus, effectively causing additional decoherence [1, 12]. To avoid entanglement with motional states, it is required that extremely tight traps and low temperatures are used in other ensure that gate operation is adiabatic on the timescale of the oscillation period of the trapped atoms [1]. Also, unlike the MOT, the ODT can be so small that they can be used to trap just a single atom or be constructed to achieve a regime where the blockade radius is larger than the cloud size so that a single collective Rydberg state is achieved. This makes the ODT more appropriate for carrying out logic gates [2].

Using the description in [164], when an atom interacts with laser light, the electric field **E** induces an atomic dipole moment **p** that oscillates at the driving frequency ω of the laser light. This induces an interaction potential U_{dip} (also called the *dipole*

potential) so that a trapping force is created from the spatial gradient of the interaction potential or due to the spatial gradient of the intensity of the light. Putting into consideration that ODT relies on far detuned laser light, the general expressions for the dipole trapping potential reads

$$U_{\text{dip}}(\mathbf{r}) = \frac{3\pi c^2}{2\omega_{21}^3}\frac{\gamma_{12}}{\Delta}\, I(\mathbf{r}) \ , \tag{5.1}$$

where ω_{21} is the resonant transition frequency, $I(\mathbf{r})$ is the position-dependent electric field intensity, γ_{12} is the spontaneous decay rate of the excited atomic level, c is the speed of light and $\Delta = \omega - \omega_{12}$ is the detuning of the driving laser from resonance. This is a direct consequence of the dispersive response of the atoms to the field.

Since light is a stream of photons, the absorptive response of the atoms to the laser field can be interpreted in terms of photon scattering in random cycles of absorption and spontaneous emission processes. The corresponding scattering rate reads

$$\Gamma_{\text{sc}}(\mathbf{r}) = \frac{3\pi c^2}{2\hbar\omega_{21}^3}\left(\frac{\gamma_{12}}{\Delta}\right)^2 I(\mathbf{r}) \ . \tag{5.2}$$

The equations (5.1) and (5.2) result in a simple relation between Γ_{sc} and $U_{\text{dip}}(\mathbf{r})$ which reads

$$\Gamma_{\text{sc}} = \frac{\gamma_{12}}{\hbar\Delta}\, U_{\text{dip}} \ . \tag{5.3}$$

If the laser field is red-detuned, i.e. $\Delta < 0$, then $U_{\text{dip}}(\mathbf{r}) < 0$. This implies that a minimum potential lies where $I(\mathbf{r})$ is maximum which is the waist of the beam. The dipole force $\mathbf{F}_{\text{dip}}(\mathbf{r}) = -\nabla U_{\text{dip}}(\mathbf{r})$, thus acts as a restoring force which pushes atoms towards the point of maximum beam intensity in all directions. From equation (5.1), one sees that $U_{\text{dip}}(\mathbf{r}) \propto \frac{I(\mathbf{r})}{\Delta}$ while in equation (5.2), $\Gamma_{\text{sc}}(\mathbf{r}) \propto \frac{I(\mathbf{r})}{\Delta^2}$. Thus, to create an efficient ODT, a highly intense laser beam is needed to produce a large trap depth and a strong dipole force. In addition, large laser detuning is also used to minimise the scattering rate. This results in a reduced heating of the trap atoms.

As shown in figure 5.10, the ODT is obtained with the aid of a highly powerful (maximum output power of 180 mW) home-built Littrow mounted extended cavity diode laser (ECDL) running at a wavelength of about 852 nm. Similar to the MOT beams, the dipole laser beam also has its laser current and temperature controllers, Thorlabs LDC 220C (2A) Laser Diode Controller and TED 200C Temperature Controller respectively, for changing the power and frequency of the beam. Since the dipole trap beam is far-detuned from the 780 nm cooling transition, no locking is required because

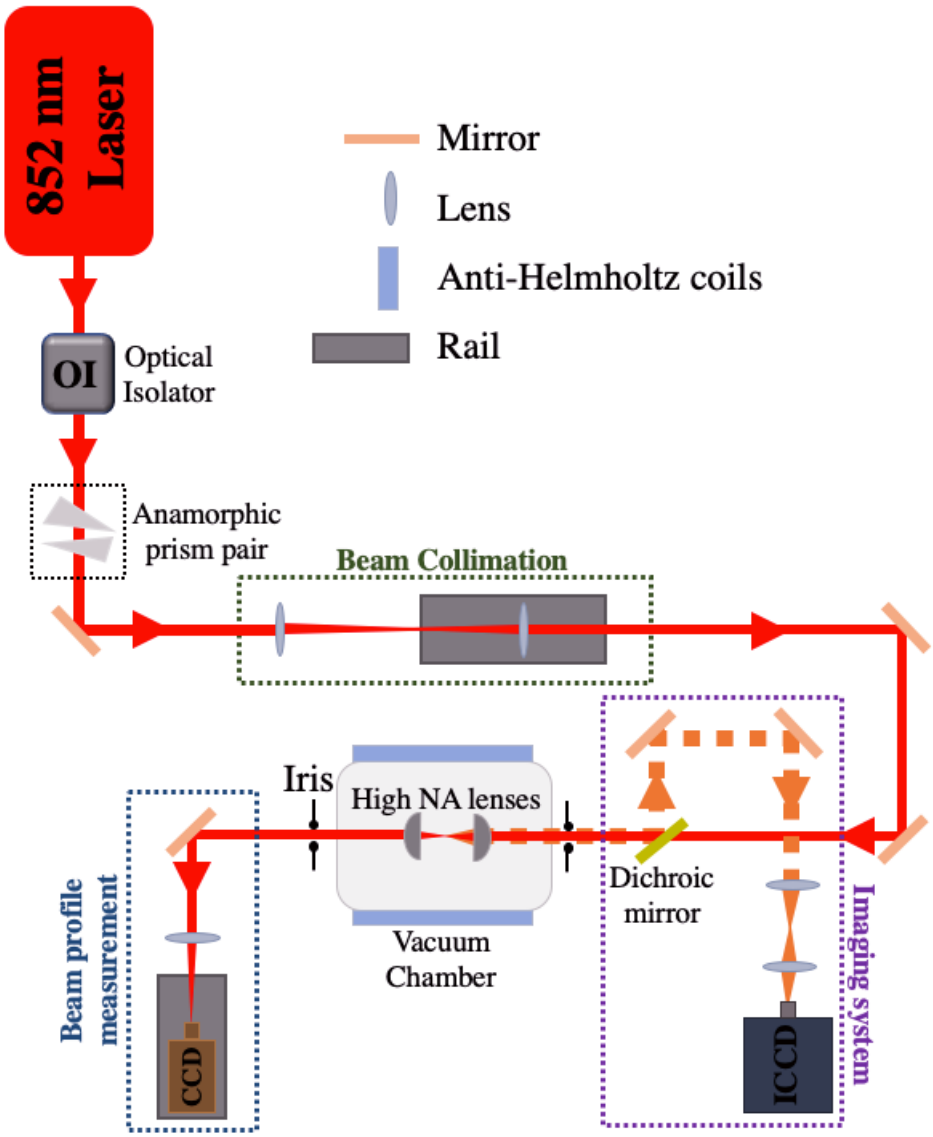

FIGURE 5.10: Experimental setup showing the laser and optical components for obtaining and imaging the ODT.

large frequency drifts are usually non-significant compared to the large detuning.

The ODT beam is passed into the vacuum chamber through an anti-reflection coated glass. After this, it passes through the two identical high numerical aperture (NA = 0.5) lenses that focus the beam, to few μm spot size, at the MOT centre. Each lens, coated with Indium tin oxide (ITO) to ensure electrical conductivity, has an effective focal distance of about 10.03 mm and working focal distance of about 7.03 mm so that the distance between the two front faces of the lenses is about 14.06 mm. Since the Rb atoms are only excited by the 780 nm beams, the 852 nm ODT beams become a see-through to them, but they are attracted to the strongest electric field region, which is the waist of the beam.

Like the MOT, the shape and size of the trapping laser are major determining factors of the beam intensity profile inside the chamber. The position of the ODT is highly sensitive to the collimation of the beam. According to the optical system analysis done in [166] using the software Zemax, a $56\,\mu$rad difference in collimation angle would move the trap by $\sim 1\,\mu$m along the optical axis. Such movement may have a negligible effect on the MOT, but it is large compared to the size of the ODT. The profile of the output beam from the laser head is elliptical. Although the beam is almost collimated on the vertical axis, it diverges significantly on the horizontal. Thus, it is intuitive that a beam-shape correction and beam collimation is done.

Beam-Shape Correction

The beam-shape correction is done using an N-SF11 dense flint glass anamorphic prism pair that reshapes the profile of a laser beam such that an elliptical beam is transformed into a circular beam by expanding/compressing it in only one direction. As shown in figure 5.11(a), the prism pair is set so that the beam is incident on the first prism at an angle called the *Brewster angle*, $\theta_B = \tan^{-1}\left(\frac{n_{\text{prism}}}{n_{\text{air}}}\right)$, to avoid the reflection of any part of the optical power. For an 852 nm laser, $n_{\text{prism}} \sim 1.76$ and $n_{\text{air}} \sim 1$, so that $\theta_B \approx 60.4^\circ$. The orientations angles α_1 and α_2 of the first and second prisms relative to a plane perpendicular to the incident beam are adjusted to set the (de)magnification, $M = \frac{\sigma_{\text{out}}}{\sigma_{\text{in}}}$ of the beam in one axis, where $\sigma_{\text{in}}(\sigma_{\text{out}})$ gives the measure of the input(output) beam size on axis. Actually, the beam size is given in terms of the radius, $\omega = 2\sigma$. Figure 5.11(b) shows the plot of the values α_1 and α_2 must be set for specific magnifications.

The image of the incoming beam is obtained using a CCD camera while a 2D Gaussian fit is done to it using a programme written in MATLAB. Standard deviations of the fit (as shown in figure 5.12(a)) in the horizontal and vertical axes yield $\sigma_h = (0.62 \pm 0.01)$ mm and $\sigma_v = (0.32 \pm 0.01)$ mm respectively, thereby resulting in an aspect ratio $\frac{\sigma_h}{\sigma_v} = 1.94 \pm 0.04$, that confirms the ellipticity of the profile. Also, it implies that the beam needs to be magnified by a factor of 2 on the vertical axis. Thus, the prism pair orientation angles are set to $\alpha_1 = 20.4^\circ$ and $\alpha_2 = 7.3^\circ$ which results in an output beam with horizontal and vertical beam sizes $\sigma_h = (0.61 \pm 0.01)$ mm and $\sigma_v = (0.60 \pm 0.01)$ mm respectively (as shown in figure 5.12(b)). An aspect ratio of $\frac{\sigma_h}{\sigma_v} = 1.02 \pm 0.02$ is obtained and therefore confirms that the beam is roughly circular.

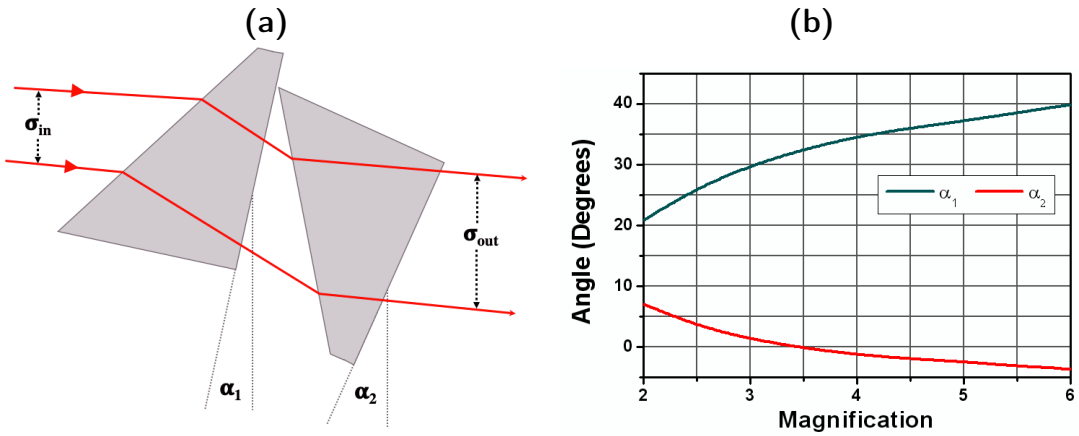

FIGURE 5.11: **(a)** Setup of the anamorphic prism pair for beam-shape correction. The prism angles α_1 and α_2 are adjusted to set the magnification $M = \frac{\sigma_{out}}{\sigma_{in}}$ in one direction; **(b)** Plots showing the values α_1 and α_2 must be set for various magnifications. This figure is obtained from [179].

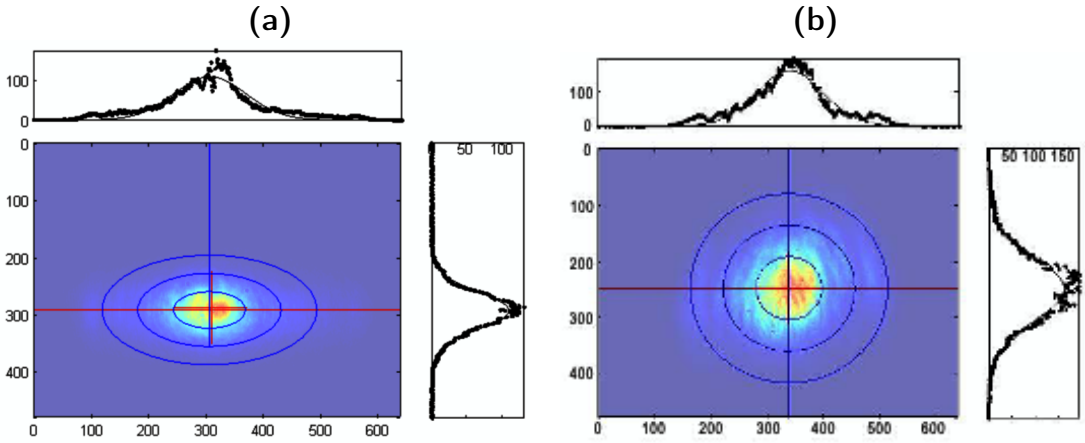

FIGURE 5.12: 2D Gaussian fit of the ODT beam: **(a)** before the anamorphic prism pair; **(b)** after the anamorphic prism pair.

Beam Collimation

After the beam-shape correction, the beam is still diverging but now on both the vertical and horizontal directions. Thus, beam collimation is required. It should be noted that the divergence rate is not the same in both directions. Hence, there is a tendency for the beam to be elliptical over a significant distance. The collimation is done using a pair of plano-convex lenses, as shown in figure 5.13. On passing through the first plano-convex lens with focal length f_1, a diverging beam will focus at point $f_1 + \mathrm{d}f_1$ from the lens. $\mathrm{d}f_1$ is the shift in the focal point due to an incident converging or diverging beam. Images of the beam are collected at different positions from the lens using a Marlin CCD camera to obtain the horizontal, vertical and average standard deviations σ_h, σ_v and $\sigma_{\text{avg}} = \frac{\sigma_h + \sigma_v}{2}$ respectively. The beam's behaviour is shown in figure 5.14(a) for a diverging beam going through a $f_1 = 300$ mm lens. The result

shows that the beam focuses at 306 mm from the lens, so that $\mathrm{d}f_1 = 6$ mm.

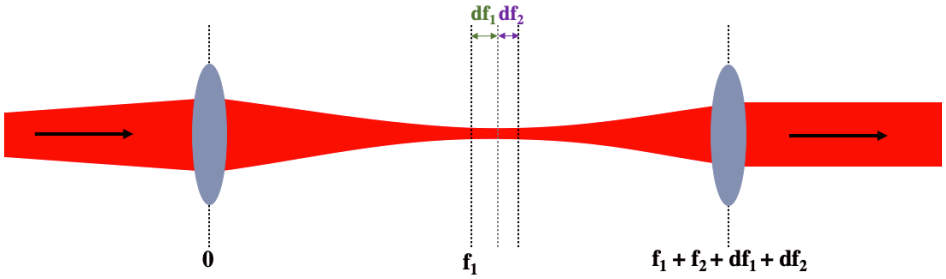

FIGURE 5.13: Schematic of the beam collimation setup.

To complete the collimation process, the second plano-convex lens is placed at the distance $f_1 + f_2 + \mathrm{d}f_1 + \mathrm{d}f_2$ from the first lens (see figure 5.13). The final size of the beam after the lenses depends on the focal length f_2 of the second lens. The dipole trap beam waist inside the chamber depends on the size of the incoming beam into the chamber, which is equivalent to the output beam size from the second collimation lens. To determine the final size of beam going into the chamber, a linear fit is done on the average beam size obtained at various positions after the focal point of the first lens (as shown in figure 5.14(b)). As such, the position corresponding to the desired output beam size can be extrapolated to determine the appropriate focal length for the second lens.

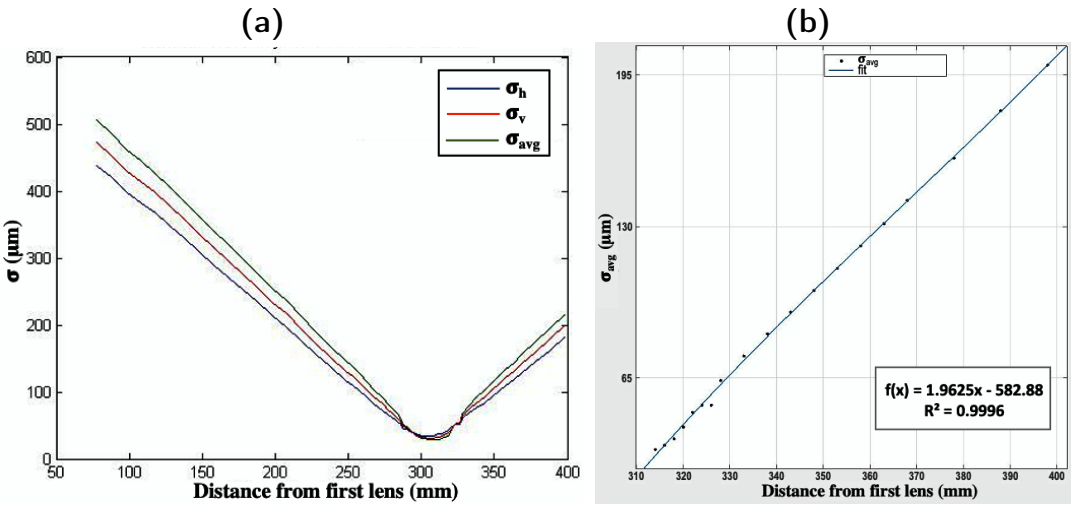

FIGURE 5.14: **(a)** Plots of the horizontal, vertical and average beam sizes at different positions from the first collimation lens. **(b)** Linear fit to the average beam size at various positions after the focal point of the first lens to be able to determine the appropriate focal length of the second collimating lens.

The beam waist ω_0 inside the chamber is defined by [166]

$$\omega_0 = \frac{\lambda f_{NA}}{\pi \omega_{in}}\,, \tag{5.4}$$

where $\lambda = 852$ nm is the wavelength of the dipole trap laser, $f_{NA} = 10.3$ mm is the effective focal length of the high NA lens and $\omega_{\text{in}} = 2\sigma_{\text{in}}$ is the input beam waist. The idea was to focus the ODT beam to a waist $\omega_0 \approx 2\,\mu$m inside the chamber so that a trapped atom cloud with size $\lesssim 1\,\mu$m is obtainable and allows for a global blockade to be achieved. Take for example, for Rydberg level $n = 35$S with interaction coefficient $C = 9108.06$ MHz μm^3 and Förster defect $\delta\omega = 1.23$ GHz and spontaneous decay rate $\gamma_{31} \sim 10$ kHz, the estimated blockade radius is about $R_b = \left(\frac{C_6}{\gamma_{31}}\right)^{\frac{1}{6}} \approx 5.05\,\mu$m. Hence, a single collective Rydberg state can be achieved even for much lower Rydberg levels. To achieve an $\omega_0 \approx 2\,\mu$m trap beam waist inside the chamber, then an input beam size $\sigma_h = \sigma_v = 0.7$ mm is required. This requires a lens with focal length $f_2 = 300$ mm to collimate the ODT beam. Since this is an extrapolation, one should expect that the ODT beam waist at the centre of the chamber should be slightly different from the intended value.

5.2.1 ODT Characterisation: Estimation of Trap size

A direct method for measuring the trap parameters such as the trapped atom cloud size, number of trapped atoms or atom temperature, is by imaging the fluorescence light from the trapped atoms on a camera [95, 166] in conjunction with appropriate experimental procedures for characterisation. To image the dipole trap atoms, the MOT cooling beams are tuned to near resonance so that they can act as probe beams. One of the high NA lenses is used to collimate the fluorescence light emitted from ODT atoms through a dichroic mirror which reflects 780 nm light and transmits 852 nm. Since the emitted fluorescence is in all directions, coupled with the fact that the solid angle of the lens is (0.14 ± 0.01) sr, fluorescence light can only be collected with an efficiency of just 14%. The fluorescence light is then focused using a large 150 mm focal length aspheric lens. This ensures that the light would pass through a pinhole employed to remove stray light from the imaging path. A second 40 mm focal length aspheric lens placed beyond the focal point of the first lens is then used to focus the light onto the ICCD camera. This allows the signal-to-noise ratio to be maximised. To get rid of any residual stray light, a 780 nm narrow band interference filter is placed in front of the ICCD camera. A detailed description of the ICCD calibration, focus, resolution and trigger timing is done in [95]. As imaged on the ICCD camera, a typical fluorescence image of ODT atoms appears as a small dot within the MOT (as shown

in figure 5.15). Unlike for the MOT, the photodiode cannot be used to image the ODT since the fluorescence signal is too small to be resolved from other light sources. However, one can use highly sensitive photon multiplying devices such as an avalanche photodiode (APD) provided one can remove other lights such as the laser or MOT fluorescence light by passing the ODT fluorescence through a pinhole or optic fibre [180].

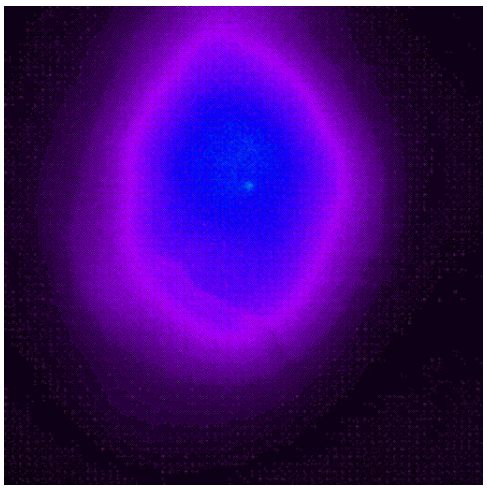

FIGURE 5.15: A typical fluorescence image of the atoms in the ODT as obtained on the ICCD camera. The small dot shows the ODT cloud within the MOT cloud.

Background corrected fluorescence images of the ODT atoms are used when characterising the trap. However, the accuracy of the measurements depends on factors such as the resolution of the optics and camera, and the strength of the fluorescence light from the trapped atoms. One can also estimate some of the trap parameters by relying on the evolution of the trapping beam intensity profile as it travels between the two high NA lenses inside the chamber. Since one cannot physically measure the beam size inside the chamber, it is necessary to set up an external optics after the ODT beam passes through it. The external optics is used to walk back through the propagation history of the beam. As shown in figure 5.10, this is done by focusing the beam on a CCD camera using a 250 mm plano-convex lens after it exits the chamber. A neutral density filter is fitted in front of the CCD camera to reduce the beam power to prevent the camera from being oversaturated. The camera is mounted on a rail to vary the distances between the camera and the lens along the beam's path. A series of images of the beam were acquired at various camera positions away from the lens. The horizontal and vertical beam standard deviations, σ_h and σ_v respectively, at each position were obtained from the 2D Gaussian fit to each image using a programme written in MATLAB. Using simple geometrical optics principles, the acquired beam sizes outside the chamber are used to calculate the beam sizes inside the chamber. These are then

used to estimate the peak intensity of the beam at the trap position.

The evolution of the vertical and horizontal standard deviations obtained from the 2D Gaussian fits of the beam images at different positions along the optical axis inside the chamber is shown in the lower plot of figure 5.16(a). The beam radius at any point can be obtained using $\omega_{h,v} = 2\sigma_{h,v}$. In figure 5.16(a), the upper plot shows the pixel count amplitude at different positions along the optical axis. The half-width at half maximum (HWHM) of a Lorentzian fit to the curve gives the *Rayleigh length*. The horizontal and vertical beam waists of the ODT beam are obtained to be $\omega_{0h} = (2.47 \pm 0.04)\ \mu$m and $\omega_{0v} = (2.07 \pm 0.04)\ \mu$m respectively, where the uncertainties are obtained from the root-mean-square error of the fit. The results are indeed close to the intended $2\,\mu$m beam waist. The slight difference is due to the inaccuracy of the extrapolation used to choose the second collimation lens. The result also shows that the horizontal and vertical beam size does not focus on the same point. This implies that the collimation angles of the beam on both axes are slightly different. Although this causes slightly different beam intensities on both axes, the effect from such difference is deemed negligible. The Lorentzian fit to the pixel count amplitude plot yields a HWHM of $z_R = (17.67 \pm 0.36)\ \mu$m. One would notice that this value is a little different from the theoretical value of the Rayleigh length $z_R = \frac{\pi\,\omega_0^2}{\lambda} = (18.99 \pm 0.12)\ \mu$m, where $\omega_0 = \frac{\omega_{0h}+\omega_{0v}}{2}$. This is expected due to the elliptical shape of the beam waist and the different focus points of the beams on the 2D axes.

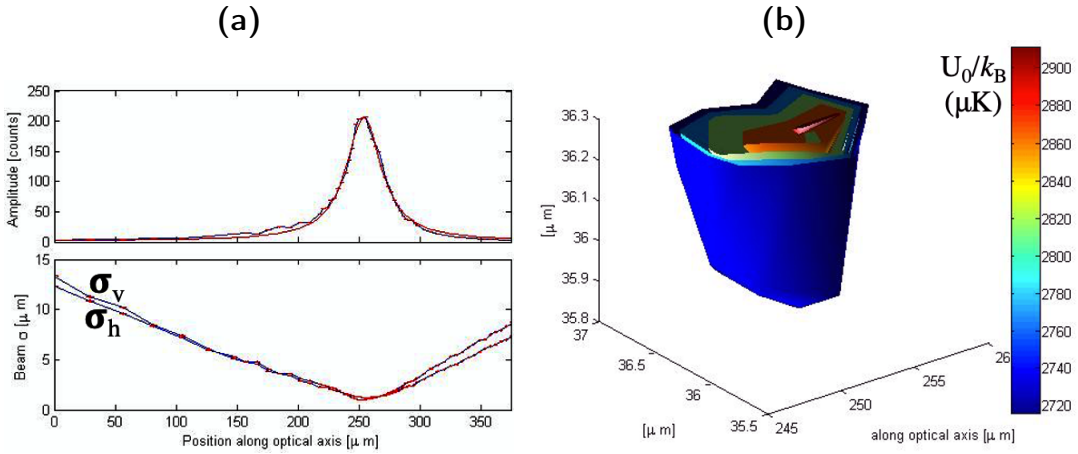

FIGURE 5.16: **(a)** *Upper Plot:* Pixel count amplitude at different positions along the optical axis. The half-width at half maximum of the Lorentzian fit to the curve gives the Rayleigh length; *Lower Plot:* Plot of vertical and horizontal standard deviations obtained from the 2D Gaussian fits of the beam images at different positions along the optical axis, where the beam waist $\omega_{h,v} = 2\sigma_{h,v}$. **(b)** A 3D profile of the trap potential.

Using the ODT beam images acquired above, a 3D profile of the trap can be constructed as shown in figure 5.16(b). With the knowledge of the 3D profile, the ODT beam power and the temperature of the ODT atoms, estimates of trap parameters such as the trapped cloud size, trap depth and the light shift induced by the highly intense ODT beam can be done. The beam has a Gaussian intensity profile whose distribution can be approximated by

$$I(r,z) = \frac{2\,P}{\pi\omega^2(z)} \mathrm{e}^{\left(-\frac{2r^2}{\omega^2(z)}\right)} , \tag{5.5}$$

where z is the distance from the beam's focus along the focal plane, r is the radial distance from the center axis of the beam, P is the beam power, and $\omega(z) = \omega_0\sqrt{1+\left(\frac{z}{z_R}\right)^2}$ is the radius of the beam at distance z from the waist.

At the beam waist $\omega_0 = \omega(0)$, the intensity and potential are given by

$$I(r,0) = I_0\,\mathrm{e}^{\left(-\frac{2r^2}{\omega_0^2}\right)} \qquad \text{and} \qquad U_{\mathrm{dip}}(r,0) = U_0\,\mathrm{e}^{\left(-\frac{2r^2}{\omega_0^2}\right)} \tag{5.6}$$

where

$$I_0 = \frac{2\,P}{\pi\omega_0^2} \qquad \text{and} \qquad U_0 = \frac{\hbar\,\gamma_2^2\,I_0}{8\,I_{\mathrm{sat}}}\left(\frac{1}{3\Delta_{1/2}} + \frac{2}{3\Delta_{3/2}}\right) . \tag{5.7}$$

$\Delta_{1/2}$ and $\Delta_{3/2}$ are the detunings from the 795 nm D_1 $5\,^2S_{1/2} \rightarrow 5\,^2P_{1/2}$ and the 780 nm D_2 $5\,^2S_{1/2} \rightarrow 5\,^2P_{3/2}$ transitions respectively [181]. The trapping potential U_0 is associated to the light shift $U_0 \equiv \Delta_{\mathrm{ls}}$ obtained from the Stark shift in the energy levels of the trapped atoms as a result of the high intensity of the ODT beam [164]. Equation (5.6) implies that the trap profile is Gaussian in the transverse plane and Lorentzian along the propagation axis of the ODT beam. With an 80 mW ODT beam power, the value of the trap depth is estimated as

$$\frac{U_0}{k_B} = (2.98 \pm 0.03)\ \mathrm{mK} \tag{5.8}$$

and the corresponding light shift is estimated as

$$\Delta_{\mathrm{ls}} = (62.13 \pm 0.67)\ \mathrm{MHz}\ . \tag{5.9}$$

Due to the Gaussian profile of the ODT beam, a 3D harmonic potential is created that is Gaussian in all directions. Thus, the spatial distribution of the atomic cloud reads

[164]

$$n(r) = n_0 \, \mathrm{e}^{-\left(\frac{x^2}{2\sigma_{DTx}^2}+\frac{y^2}{2\sigma_{DTy}^2}+\frac{z^2}{2\sigma_{DTz}^2}\right)} , \tag{5.10}$$

where σ_{DTi} for $i = x, y, z$ are the standard deviations of the trapped atom Gaussian density distribution. Also, for atoms trapped within the potential, the thermal density distribution of the atoms is given by the Boltzmann distribution

$$n(r) = n_0 \, \mathrm{e}^{-\left(\frac{U_{\mathrm{dip}}(r)}{k_B T}\right)} . \tag{5.11}$$

For a 3D harmonic potential,

$$U_{\mathrm{dip}}(r) = \frac{1}{2} m_{\mathrm{Rb}} \left(\omega_x^2 x^2 + \omega_y^2 y^2 + \omega_z^2 z^2\right) , \tag{5.12}$$

where ω_i are the trapping frequencies. On equating both the spatial and thermal distributions, using a known ODT beam power of about 80 mW at the centre of the chamber and assuming that the ODT atoms are at a temperature of $(500 \pm 25)\,\mu$K [95], one obtains the radius of the cloud in the vertical and horizontal axes as $\sigma_{DTv} = (0.51 \pm 0.01)\ \mu$m and $\sigma_{DTh} = (0.43 \pm 0.01)\ \mu$m respectively. The Lorentzian HWHM along the optical axis is estimated as $\sigma_{DTz} = (5.34 \pm 0.11)\ \mu$m. As such, the trap volume can be estimated as

$$V = (2\pi)^{\frac{3}{2}} \sigma_{DTh} \sigma_{DTv} \sigma_{DTz} = (18.44 \pm 0.68)\ \mu\mathrm{m}^3 . \tag{5.13}$$

The values for σ_{DTv} and σ_{DTh} imply that the trap meets the required and target cloud diameter of about $1\,\mu$m to ensure that a full blockade is achieved within the trap. Owing to the cylindrical shape of the trap in the axial direction, the value of the cloud diameter along the optical axis is slightly higher than the target blockade radius of $5.05\,\mu$m for at least 35S Rydberg level. This can be further reduced by either adjusting the size of the incoming ODT laser to produce a smaller waist in the chamber or by decreasing the trap depth and temperature of the cloud.

As seen above, the trap parameters that can be estimated using the ODT beam intensity profile in the chamber are limited. Trap parameters such as trap atom number, temperature and lifetime cannot be estimated using this method. Such trap parameters would be measured by imaging the fluorescence light from the cloud atoms on a camera. This would require experimental procedures to be done to characterise the properties behaviour of the trapped atoms. In [95], similar ODT was loaded from a characterised MOT consisting of an average of 5×10^5 atoms with an average peak

density of 6×10^8 cm^{-3}. The average number of atoms measured in [95] for different beam powers is shown in figure 5.17. This result shows that an average of 28-43 atoms can be loaded in the ODT. Thus resulting in an average atom density between (1.25×10^{12}) - (2.33×10^{12}) cm^{-3}. The ODT atoms' temperature of $500\,\mu$K was also obtained from the result of a time of flight measurement [182] done in [95].

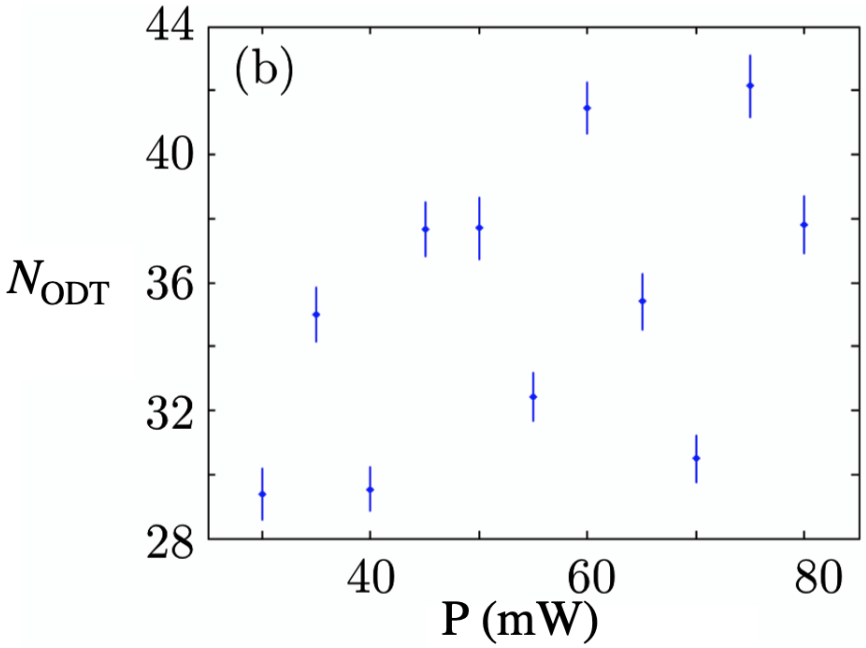

FIGURE 5.17: Average number of ODT atoms measured for different beam powers.
NB: This plot is taken from [95] with permission from the author.

The average number of ODT atoms is expected as a typical ODT is known to trap between 1-100 atoms [3, 180]. The resulting trapped atom density implies that the trap is appropriate for studying the dynamics of interacting atoms.

5.2.2 Multiple dipole traps

As described in section 2.4.3, the cold atoms implementation of protocols such as the DQC1 requires that the control and target atoms be trapped in two individually addressable micrometre-sized ODTs placed within very few micrometres of one another. This allows for a wide variety of Rydberg blockade-induced non-trivial unitary processes to be investigated. It also allows for the preparation of a large number of identical Rydberg pairs which are suitable for investigating long-range binary interactions without the influence of surrounding atoms [12]. As shown in section 4.3.1, interactions between atoms in such spatially ordered systems induce antiblockade effects provided thermal motions of atoms are negligible.

In [136], multiple micron-sized optical dipole traps were generated for neutral atoms using holographic techniques with a programmable liquid crystal spatial light modulator (SLM). The SLM is used to control the optical potential of each ODT and the geometry of the array, thereby creating individually addressable atom sites that are placed in different geometrical arrangements. Micro-optical lens arrays have been successfully used to create arrangements of tight laser foci in [183]. One can also achieve this by focusing different and spatially separated ODT beams with the same high numerical aperture lens through the MOT to create trapping potentials that are close to one another. This can be done by splitting the ODT beam using a polarising beam splitter before allowing both resulting beams to pass through the high-NA lens. Micrometre precision of the initial beam collimation will be required since one of the resulting beams from the beam splitter will travel a longer distance, thereby resulting in traps with different sizes. Relative positions of and the distances between the trapping sites can be fully controlled with micrometre precision. Hence, creating the possibility of controlling the interactions between each atom site. Combined with the ability to control the number of trapped atoms within each trap, such systems are found to be suitable for studying collective phenomena and creating multi-atom entangled states [163].

Summary

In this chapter, the experimental setups toward achieving high density ultracold atomic samples with a controllable number of atoms created in a MOT and an ODT are presented. The atoms created in these traps will be illuminated by two-photon excitation lasers to excite them to high lying Rydberg states. Thus, allowing for the direct observation of the effects on Rydberg-Rydberg interactions.

The setup of the MOT was described and the efforts made to improve the MOT in order to obtain a laser-cooled atomic ensemble optimised to the regime where it is dense enough to study Rydberg interactions and also cold enough to serve as a reservoir of ultracold atoms from which the ODT can be loaded.

The primary goal for setting up the ODT is to achieve an atom cloud with the capability of achieving a full blockade effect. Atoms densities achievable in the ODT are high enough to investigate the effect of Rydberg-Rydberg interactions. However, the setup is considered partially successful for achieving full blockade effect for Rydberg levels with blockade radius $\gtrsim 5\,\mu$m (the ODT cloud size along the optical axis). The trap is also close to fulfilling the size requirements for the implementation of an atomic

qubit. The behaviour of the ODT was described from the measurement of the trap size, the profile of the beam, the trap depth, the line shift induced by the ODT beam, the cloud size and trap volume. All these trap parameters and others such as the number of trapped atoms, trap lifetime and trapped atom temperature can be measured directly by imaging the fluorescence light from the trapped atoms on a camera. Detailed experimental procedures for characterising similar trap have been described in [95].

6 Summary and Outlook

The major focus of this thesis has been on probing Rydberg states, exploring the fascinating properties of Rydberg gases and describing the mechanism for controlling the many-body excitation dynamics of interacting Rydberg gases. The thesis also revealed new interesting features arising due to the effects of strong Rydberg-Rydberg interactions in the presence of different three-level coherent dynamic processes. Electromagnetically induced transparency (EIT), Autler-Townes splitting and coherent population trapping (CPT) are associated with quantum interference excitation pathways when two-photon Rydberg excitation lasers interact with ground state atoms. The results showed that the significance or visibility of the effects of interactions is dependent on the ratio $\frac{\Omega_P}{\Omega_C}$, irrespective of the quantum interference regime.

The study also simultaneously focused on the spatial arrangement and distribution of atoms in a gas. The effect of Rydberg-Rydberg interactions typically appears in the form of suppression of transparency. For spatially ordered interacting atoms at fixed positions such as atoms in an optical lattice system or a system of dipole trap arrays, the effect of interactions also appears as an excitation enhancement (i.e. antiblockade) effect which is as a result of a multi-photon excitation to the level with multiple Rydberg excitations.

Investigations of Rydberg systems usually involve a disordered atom ensemble. To account for fluctuations of the spatial position of the atoms in the ensemble, the Monte-Carlo algorithm is used to model the excitation dynamics. The results show that for ultracold systems (MOT and ODT), the van der Waals interactions induce line shift and asymmetry effects on the atomic spectrum. However, in vapour cell experiments, interaction-induced line shift and asymmetry effects are smeared out as a result of the thermal motion of the atoms. The thermal motion of atoms in a vapour cell also smears out the antiblockade effects, which can be observed in spatially ordered systems.

One other effect induced by Rydberg-Rydberg interactions is the spectral broadening of the resonance lines. Exploring the linewidth properties shows that the broadening increases as $\sqrt{N}$ of the generalised Rabi frequency. This $\sqrt{N}$-behaviour of the collective Rabi frequency indicates the collective behaviour of the many-body system associated

with a many-body entangled state having a single Rydberg excitation. The same $\sqrt{N}$-dependence is also revealed in the direct measurements and calculations of Rabi oscillations as a consequence interaction-induced blockade mechanism [39, 40, 112]. The $\sqrt{N}$-behaviour can also be used to understand the limits of the low and high probe regimes for a particular configuration of the atom density and excitation level. The result shows that the high-probe regime is given by the threshold value of Ω_P for which entanglement effect sets in, irrespective of the system being in EIT, ATS or CPT regime. This study provides an understanding of how to control excitation mechanisms as it is directly applicable to physical experiments, as well as how to control the physical mechanism needed to entangle a macroscopic ensemble of atoms. This is a fundamental requisite for the implementation of quantum information processing schemes with Rydberg atoms.

The study does not include a detailed experimental study of the effects of Rydberg-Rydberg interactions. However, this thesis presented the design and implementation of the necessary building blocks for a future complete experimental study. This includes improving the previously existing optical setup to obtain an optimised MOT [section 5.1] and the development of the laser, optical and imaging systems to develop a microscopic ODT [section 5.2], as well as the development and setup of the laser and optical systems for two-photon excitation.

The setup and practical realisation of the two-photon excitation is based on the techniques described in [138, 139]. The Rydberg states were observed using transparency features from three-level quantum interference phenomena, EIT/ATS/CPT, showing that the excitation levels $n \geq 20$ can be probed successfully. However, the Rydberg level that can be probed is limited by the available coupling beam power. The quantitative analysis of $20\mathrm{D}_{5/2}$ Rydberg state transparency features was done in section 4.2.4 with focus on studying the linewidths of the transparency features in comparison to the features obtained from the solution of the optical Bloch equations for a single atom or a non-interacting many-atom system. Measured laser parameters, such as the laser linewidths and Rabi frequencies, were used in the theoretical model to make it experimentally realistic. Laser linewidths of approximately (186 ± 42) kHz and (372 ± 84) kHz were obtained for the coupling and probe beams respectively. The agreement between the experimental and theoretical transparency linewidth measurements for non-interacting atoms implies that the system is suitable for the experimental study of interacting Rydberg atoms in a vapour cell.

The setup for the preparation of cold atomic samples was presented in this thesis,

as well as the work done to improve the confinement and cooling of the atoms. Efforts were made to improve the MOT setup, as a previous characterisation done in [95] highlighted density-limiting factors such as the unusual trap geometry, the small size of the trapping beams and the imbalance of the intensities of the trapping beams at the trapping region. Further efforts were placed into the design and setup of the ODT, with the target of obtaining a highly dense micro-sized atomic cloud, whose spatial distribution can guarantee full Rydberg blockade across the sample to enable the preparation of a qubit system for quantum gate operations. To achieve full Rydberg blockade for an excitation level $n = 35$, it was necessary to keep the cloud diameter to be about $1\,\mu$m which is possible with the ODT beam focused to a waist of $\omega_0 \sim 2\,\mu$m inside the chamber. The trap design resulted in horizontal and vertical beam waists and Rayleigh length of $\omega_{0h} = (2.47 \pm 0.04)\ \mu$m, $\omega_{0v} = (2.07 \pm 0.04)\ \mu$m and $z_R = (17.67 \pm 0.36)\ \mu$m respectively. The estimated possible cloud radius on the vertical and horizontal axes were obtained as $\sigma_{DTv} = (0.51 \pm 0.01)\ \mu$m and $\sigma_{DTh} = (0.43 \pm 0.01)\ \mu$m respectively showed that this target was met. However, the estimated cloud size along the optical axis acquired as $\sigma_{DTz} = (5.34 \pm 0.11)\ \mu$m shows that the full blockade can only be achieved for excitation levels in the range $n > 35$. This means that the attempt at meeting the target was partially successful. Hence, a further decrease in the trap dimension would be required to achieve full blockade at $n \sim 35$ Rydberg state. The light shift and trap depth for an 80 mW trapping beam were estimated to be $\Delta_{\text{ls}} = (62.13 \pm 0.67)$ MHz and $\frac{U_0}{k_B} = (2.98 \pm 0.03)$ mK respectively. These were obtained under the assumption that the ODT atoms are at a temperature of $(500 \pm 25)\ \mu$K based on the characterisation that was done in [95]. Based on an average of 28-43 atoms loaded in the typical ODT as measured in [95], the average cloud density was estimated to between $\left(1.25 \times 10^{12}\right)$ - $\left(2.33 \times 10^{12}\right)$ cm^{-3}. However, the experimental verification through direct measurements of these atomic ensemble's parameters could not be performed during the time of this thesis and has been left for future work. Nevertheless, the conclusion drawn remains that the trap is suitable for Rydberg gas experiments and could be used for quantum information processing. In addition, the information provided in the thesis would facilitate future study and improvements. As part of future works, one can envisage the addition of more ODTs to create an array of individually addressable and controllable traps with controllable inter-trap interactions.

A natural follow up to this thesis is to complete the experimental work, so future work will focus on the following:

- **Detailed Rydberg gas experiment:** The goal is to observe the collective behaviour of many-body systems through the $\sqrt{N}$-characteristic of the interaction-induced spectral line broadening. This will allow a more thorough comparison between theoretical and experimental results. The first step is to complete the Rydberg gas experiment for atoms in a vapour cell to observe possible interaction-induced suppression effects and line broadening. The probe and coupling lasers will then be used to probe trapped cold atoms in a MOT or an ODT where possible interaction-induced line shift and asymmetry will be more easily observed.

- **Spatially ordered system:** As already mentioned in section 5.2.2, adding a programmable spatial light modulator (SLM) into the ODT setup will allow the arrangement of atoms in individually addressable microtraps and create a fixed pattern for their spatial distribution [136]. If the spacing between the traps is sufficiently small, Rydberg excitation blockade can be achieved between the traps. Therefore, the transparency experiments should be repeated on a spatially ordered system, where more features could be visible, as discussed in chapter 4.

- **The effect of external electric field:** As mentioned in section 2.2, it is possible to apply an external electric field to control the interaction between a pair of atoms. Experiments to demonstrate the sensitivity of a Rydberg system to an external electric field can be performed to study how this changes the transparency spectrum. In the vicinity of Stark-tuned Förster resonance, the interaction is purely in the resonant dipole-dipole regime. There is a mixture of various angular momentum states and the interactions become strongly anisotropic. Appropriate modelling of these conditions can lead to the observation of more interesting effects of Rydberg-Rydberg interactions.

The realization of the above-mentioned tasks will aid in tackling many more interesting applications, such as the implementation of quantum gate operations, creation of Rydberg macrodimers and creation of Rydberg-ground state molecules.

A Rubidium Atoms

Experiments with alkali-atoms have become the very first steps towards implementing quantum information with neutral atoms. They have been used as the basic building blocks of processes such as the loading of high-fidelity quantum register [184] and in the implementation of entangling gates with coherent collisions in optical lattices [185]. Single-electron alkali atoms are also amenable to a detailed treatment of Rydberg state properties and interactions using relatively straightforward theoretical tools [186]. Although, a complete scheme for quantum information processing using the unique features of alkaline earth atoms has also been proposed [187]. The alkali atoms are considered ideal because they have one valence electrons, with ground-state electron configuration s^1, thus can be treated approximately as a hydrogen atom. Hence, taking relativistic effects into account, they can be studied with well-understood and straightforward hydrogenic models. Their ground states consist of two hyperfine levels with large splitting, which makes them appropriate for encoding qubits. One of such alkalis, that will be used in this research, is Rubidium (Rb). The detailed study beyond the scope of this overview can be found in [152].

Rb atom, with electronic configuration $1s^2\,2s^2\,2p^6\,3s^2\,3p^6\,3d^{10}\,4s^2\,4p^6\,5s^1$, is arguably the most popularly used atom in quantum optics experiments because the lasers which produce their electronic transitions are readily available, relatively cheap and quite easy to operate. It has a laser cooling transition corresponding to a near-infrared wavelength of approximately 780.24 nm [152]. Rb has two isotopes: ^{85}Rb and ^{87}Rb with relative natural abundances of 72.17% and 27.83% respectively.

Figure A.1 shows the energy level structure of ^{85}Rb and ^{87}Rb. The fine structure is as a result of the so-called *Rusell-Saunders* L-S coupling. L is the orbital angular momentum given with the values $L = 0, 1, 2, 3, \cdots$ popularly denoted by the spectral terms S, P, D, F, $\cdots$[1]. S is the spin angular momentum with the values $\pm\frac{1}{2}$ which denote the electron intrinsic angular momentum around its axis. This coupling results into the total angular momentum, $J = L + S$ whose value lies within the range $|L - S| \leq J \leq L + S$. As a result, the full spectroscopic notation of the atom state is

[1] Note that S for the spin angular momentum is different from the spectroscopic notation S for orbital angular momentum $L = 0$.

written as $n^{2S+1}L_J$ where n is the principal quantum number. It is straightforward to see that the ground state of the single valence electron is a singlet state $5^2S_{1/2}$ while the first excited state splits into doublet sublevels $5^2P_{1/2}$ and $5^2P_{3/2}$. This "generally" [2] results into two different transitions, that are analogous to the yellow sodium D-lines, between the ground and the first excited state, namely: the D_2 transition for $5^2S_{1/2} \rightarrow 5^2P_{1/2}$ and D_2 transition for $5^2S_{1/2} \rightarrow 5^2P_{3/2}$.

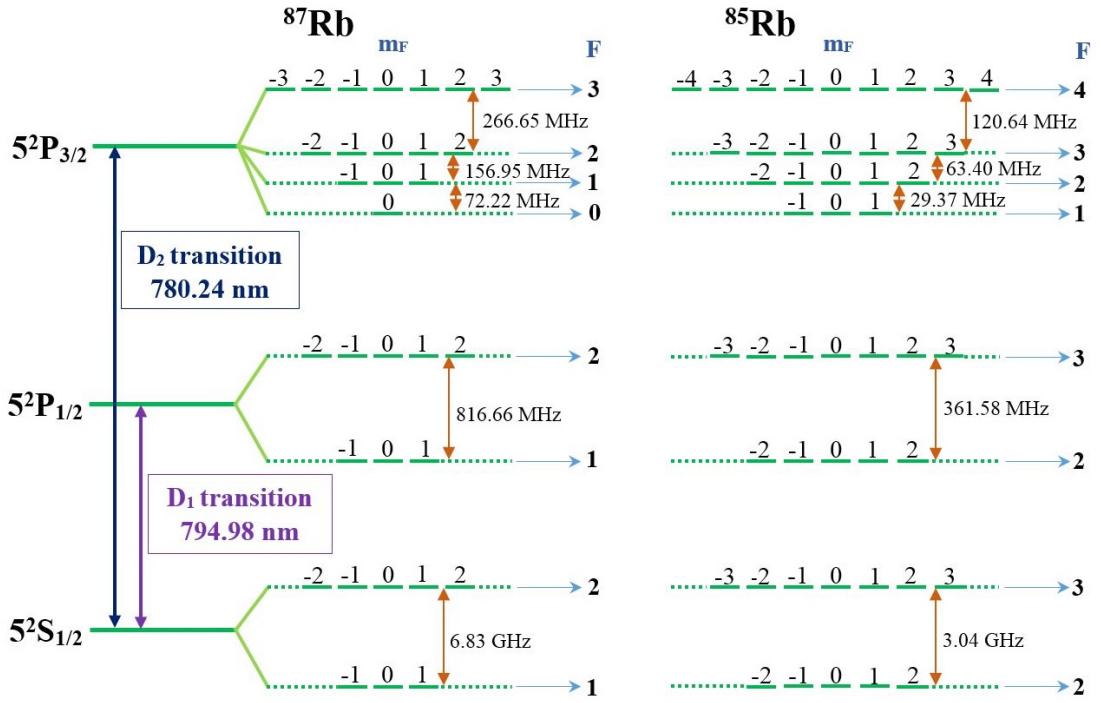

FIGURE A.1: Fine and hyperfine structure of ^{87}Rb and ^{85}Rb showing the difference in frequency between the hyperfine levels and the magnetic sublevels of each hyperfine level. **NB:** Figures are not drawn to scale.

Due to the interaction between the nuclear magnetic moment and the electron magnetic field, the fine structures are further split into hyperfine structures [168]. The hyperfine structure results from the coupling between the nuclear angular momentum I and the total angular momentum J. The results into the atom's total angular momentum which is given by $F = J + I$ whose value lies within the range $|J - I| \leq F \leq J + I$. The nuclear angular momentum has a value $I = 5/2$ for ^{85}Rb and $I = 3/2$ for ^{87}Rb implying different hyperfine level structures for the two Rb isotopes. The ground state further hyperfine split into a doublet with $F = 1$ and 2. These states provide a two-level system for encoding qubits. The excited states

[2] This is not the real transition. Laser systems are generally first locked to transitions between hyperfine levels. As a result of the polarisation of the laser, the transition is further streamlined to occur between specific magnetic sublevels of the hyperfine levels

also further split into their corresponding hyperfine levels. The D_1 and D_2 transitions create a large imbalance in the ground state populations. In the presence of an external magnetic field, the degeneracy in each hyperfine level is removed so that each hyperfine level consists of $2F + 1$ magnetic sublevels given by the quantum number $m_F = -F, -F + 1, \cdots, F - 1, F$. Atom transition between two levels is the transition between the hyperfine levels and sublevels. This is said the follow the so-called *general selection rules* depending on the polarisation of laser light which may be circularly (σ_+ or σ_-) or linearly π polarised. According to quantum mechanics, photons in circularly polarised light carry spin angular momentum $\mathbf{s} = \pm\hbar\frac{\mathbf{k}}{|\mathbf{k}|}$ for σ_+ (in the direction of light propagation) and σ_- (opposite the direction of light propagation) respectively. Where $\mathbf{k}$ is the wavevector of light. Since linearly polarised light is obtained as a superposition of the two circularly polarised ones, photons would carry spin angular momentum $\mathbf{s} = 0$. Thus, atom in an external magnetic field follows transition with $\Delta F = -1, 0, +1$ and $\Delta m_F = -1, 0, +1$ evoked by the absorption of σ_-, π and σ_+ laser respectively. Taking advantage of these distinct energy levels and imposing the general selection rules for light absorption, the internal states of the atoms can be fully controlled. This enables frequency locking, cooling, trapping, transporting, manipulating and unitary operations to be performed. In this study, the NIR laser is locked to a transition from the D_2 line of ^{87}Rb.

B Transition Threshold between EIT and ATS

This section reviews the theory to obtain the transition threshold between EIT and ATS following the reviews given in [15, 14, 188]. Solving the set of optical Bloch equations (1.28) for a generic three-level system (see figure 1.1) result in a probe transition coherence (see section 1.3)

$$\rho_{21} = \frac{2\left(\gamma_{31} + i\left(\Delta_C + \Delta_P\right)\right)\Omega_P}{4\left(\gamma_{21} + i\,\Delta_P\right)\left(\Delta_C + \Delta_P - i\,\gamma_{31}\right) - i\,\Omega_C^2} \tag{B.1}$$

so that the atomic linear polarisation responsible (See equations (1.42) and (1.45) is given by

$$P^{(L)} = \frac{2\mathfrak{N}\left|\mu_{21}\right|\left(\Delta_C + \Delta_P - i\,\gamma_{31}\right)\Omega_P}{4\left(\Delta_P - i\,\gamma_{21}\right)\left(\Delta_C + \Delta_P - i\,\gamma_{31}\right) - \Omega_C^2} \,. \tag{B.2}$$

This can be further decomposed into linear and non-linear terms of the Rabi frequencies

$$P^{(L)} = P_l^{(L)} + P_{nl}^{(L)} \,, \tag{B.3}$$

where

$$P_l^{(L)} = \frac{\mathfrak{N}\left|\mu_{21}\right|\Omega_P}{2\left(\Delta_P - i\,\gamma_{21}\right)} \tag{B.4}$$

and

$$P_{nl}^{(L)} = \frac{\mathfrak{N}\left|\mu_{21}\right|\Omega_P}{2\left(\Delta_P - i\,\gamma_{21}\right)} \cdot \frac{\Omega_C^2}{4\left(\Delta_P - i\,\gamma_{21}\right)\left(\Delta_C + \Delta_P - i\,\gamma_{31}\right) - \Omega_C^2} \,. \tag{B.5}$$

One would observe that the non-linear term has three poles at

$$\delta_0 = i\,\gamma_{21} \,. \tag{B.6}$$

and

$$\delta_\pm = \frac{1}{2}\left[i\left(\gamma_{21} + \gamma_{31}\right) - \Delta_C \pm \sqrt{\Omega_C^2 - \left(\gamma_{31} - \gamma_{21} + i\Delta_C\right)^2}\right] \,. \tag{B.7}$$

Thus, it can be expressed as

$$P_{nl}^{(L)} = \vartheta \left(\frac{\mathfrak{A}}{\Delta_P - \delta_0} + \frac{\mathfrak{B}}{\Delta_P - \delta_+} + \frac{\mathfrak{C}}{\Delta_P - \delta_-} \right) , \tag{B.8}$$

where

$$\mathfrak{A} = -4\left(\delta_+ - \delta_-\right) , \quad \mathfrak{B} = -4\left(\delta_- - \delta_0\right) , \quad \mathfrak{C} = 4\left(\delta_+ - \delta_0\right) , \quad \vartheta = \frac{\mathfrak{N}\left|\mu_{21}\right|\Omega_P}{2\left(\delta_+ - \delta_-\right)} .$$

This is simply the superposition of three resonances for $\Delta_C = 0$. However, in the weak probe regime, the sum of the linear term in equation (B.4) and the first term of the non-linear term can be neglected. Thus, the linear polarisation yields

$$P^{(L)} = \vartheta \left(\frac{\mathfrak{B}}{\Delta_P - \delta_+} + \frac{\mathfrak{C}}{\Delta_P - \delta_-} \right) . \tag{B.9}$$

For Rydberg states, $\gamma_{21} \gg \gamma_{31}$. Thus for such states, $\gamma_{21} \pm \gamma_{31} \simeq \gamma_{21}$ and taking $\Delta_C = 0$,

$$\delta_\pm \simeq \frac{1}{2}\left(i\,\gamma_{21} \pm \sqrt{\Omega_C^2 - \gamma_{21}^2} \right) , \quad \delta_- - \delta_0 \simeq -\delta_+ , \quad \delta_+ - \delta_0 \simeq -\delta_- .$$

However, one should note that generic three-level systems are being considered here.

In the strong coupling (or *secular*) limit, that is the ATS regime $\Omega_C \gg \gamma_{21} - \gamma_{31}$, then

$$\delta_\pm \simeq \frac{1}{2}\left[i\,\left(\gamma_{21} + \gamma_{31}\right) \pm \Omega_C \right]$$

so that

$$P^{(L)} \approx \frac{\mathfrak{N}\left|\mu_{21}\right|\Omega_P}{\Omega_C} \left[\frac{\Omega_C + i\,\left(\gamma_{21} - \gamma_{31}\right)}{\Delta_P - \frac{1}{2}\left[i\,\left(\gamma_{21} + \gamma_{31}\right) + \Omega_C \right]} + \frac{\Omega_C - i\,\left(\gamma_{21} - \gamma_{31}\right)}{\Delta_P - \frac{1}{2}\left[i\,\left(\gamma_{21} + \gamma_{31}\right) - \Omega_C \right]} \right] . \tag{B.10}$$

This is simply the sum of two well-separated Lorentzian lines, i.e. absorption resonances, having equal widths as shown in figure B.1(a). Each of the absorption resonances corresponds to an excitation pathway to the intermediate state. $\gamma_p = \gamma_{21} - \gamma_{31}$ is called the polarisation decay rate [15] and it has different values in different three-level systems. The linear probe absorption is given by the sum of the profiles, which corresponds to the constructive interference between the two resonances. As a result, the transparency at zero-detuning results from a gap between the two absorption resonances

Consider the weak coupling (or *low saturation*) limit, that is the EIT regime $\Omega_C \ll \gamma_{21} - \gamma_{31}$, then

$$\delta_+ \simeq i\,\gamma_{21} - \frac{i\,\Omega_C^2}{4\,(\gamma_{21}-\gamma_{31})}\,, \quad \delta_- \simeq i\,\gamma_{31} + \frac{i\,\Omega_C^2}{4\,(\gamma_{21}-\gamma_{31})}\,.$$

Thus, the total linear polarisation reads

$$P^{(L)} \approx \frac{\Im\,|\mu_{21}|\,\Omega_P}{\left[2\,(\gamma_{21}-\gamma_{31})^2 - \Omega_C^2\right]} \left[\frac{4\,(\gamma_{21}-\gamma_{31})^2 - \Omega_C^2}{\Delta_P - i\gamma_{21} + \frac{i\,\Omega_C^2}{4(\gamma_{21}-\gamma_{31})}} - \frac{\Omega_C^2}{\Delta_P - i\gamma_{31} - \frac{i\,\Omega_C^2}{4(\gamma_{21}-\gamma_{31})}}\right]. \tag{B.11}$$

This gives a difference between two not well-separated Lorentzian lines having unequal widths, as shown in figure B.1(b). The transparency at zero-detuning results from the destructive superposition of the two absorption resonances, which leads to a narrow dip in the total absorption profile. A breakdown of the weak coupling limit theory occurs when $\Omega_C > \gamma_{21} - \gamma_{31}$ is considered. This causes a negative transparency dip in the total absorption profile, which corresponds to an impossible negative atom number. Likewise, in the strong coupling limit theory, $\Omega_C < \gamma_{21} - \gamma_{31}$ causes the individual Lorentzian absorption profiles to have negative values.

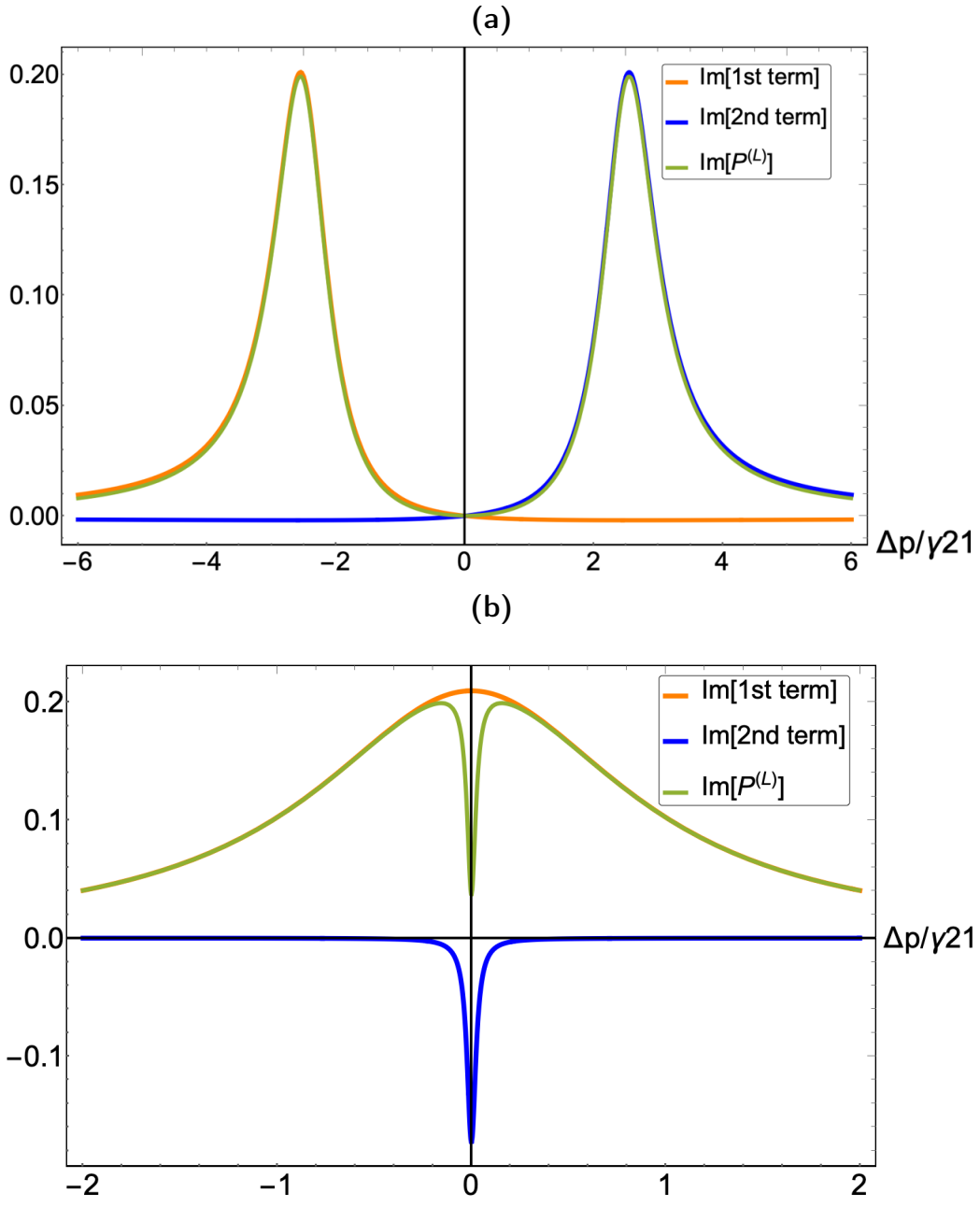

FIGURE B.1: Plots of two-photon transition absorption profiles in (for **(a)** the strong coupling regime; **(b)** the weak coupling regime) a functions of probe detuning showing the two absorption resonances and their corresponding interferences. In the plots, $\Omega_P = 0.1\gamma_{21}$, $\gamma_{31} = 0.005\gamma_{21}$ and **(a)** $\Omega_C = 5\gamma_{21}$; **(b)** $\Omega_C = 0.2\gamma_{21}$.

C Table for Clebsch-Gordan Coefficients for ^{87}Rb two-photon transitions for different configurations of the beam polarisation

Polarisation configuration	Transitions	Coefficients
σ_+ - σ_+	$\lvert 5S_{1/2}, F=2, m_F=2\rangle \rightarrow \lvert 5P_{3/2}, F'=3, m_F=3\rangle$	$\sqrt{\frac{1}{2}}$
	$\lvert 5P_{3/2}, F=3, m_F=3\rangle \rightarrow \lvert nD_{5/2}, F'=4, m_{F'}=4\rangle$	$\sqrt{\frac{2}{3}}$
σ_+ - σ_-	$\lvert 5S_{1/2}, F=2, m_F=2\rangle \rightarrow \lvert 5P_{3/2}, F'=3, m_F=3\rangle$	$\sqrt{\frac{1}{2}}$
	$\lvert 5P_{3/2}, F=3, m_F=3\rangle \rightarrow \lvert nD_{5/2}, F'=4, m_{F'}=2\rangle$	$\sqrt{\frac{1}{42}}$
σ_+ - π	$\lvert 5S_{1/2}, F=2, m_F=2\rangle \rightarrow \lvert 5P_{3/2}, F'=3, m_F=3\rangle$	$\sqrt{\frac{1}{2}}$
	$\lvert 5P_{3/2}, F=3, m_F=3\rangle \rightarrow \lvert nD_{5/2}, F'=4, m_{F'}=3\rangle$	$-\sqrt{\frac{1}{6}}$
σ_- - σ_+	$\lvert 5S_{1/2}, F=2, m_F=2\rangle \rightarrow \lvert 5P_{3/2}, F'=3, m_F=1\rangle$	$\sqrt{\frac{1}{30}}$
	$\lvert 5P_{3/2}, F=3, m_F=1\rangle \rightarrow \lvert nD_{5/2}, F'=4, m_{F'}=2\rangle$	$\sqrt{\frac{5}{14}}$
σ_- - σ_-	$\lvert 5S_{1/2}, F=2, m_F=2\rangle \rightarrow \lvert 5P_{3/2}, F'=3, m_F=1\rangle$	$\sqrt{\frac{1}{30}}$
	$\lvert 5P_{3/2}, F=3, m_F=1\rangle \rightarrow \lvert nD_{5/2}, F'=4, m_{F'}=0\rangle$	$\sqrt{\frac{1}{7}}$
σ_- - π	$\lvert 5S_{1/2}, F=2, m_F=2\rangle \rightarrow \lvert 5P_{3/2}, F'=3, m_F=1\rangle$	$\sqrt{\frac{1}{30}}$
	$\lvert 5P_{3/2}, F=3, m_F=1\rangle \rightarrow \lvert nD_{5/2}, F'=4, m_{F'}=1\rangle$	$-\sqrt{\frac{5}{14}}$
π - σ_+	$\lvert 5S_{1/2}, F=2, m_F=2\rangle \rightarrow \lvert 5P_{3/2}, F'=3, m_F=2\rangle$	$-\sqrt{\frac{1}{6}}$
	$\lvert 5P_{3/2}, F=3, m_F=2\rangle \rightarrow \lvert nD_{5/2}, F'=4, m_{F'}=3\rangle$	$\sqrt{\frac{1}{2}}$
π - σ_-	$\lvert 5S_{1/2}, F=2, m_F=2\rangle \rightarrow \lvert 5P_{3/2}, F'=3, m_F=2\rangle$	$-\sqrt{\frac{1}{6}}$
	$\lvert 5P_{3/2}, F=3, m_F=2\rangle \rightarrow \lvert nD_{5/2}, F'=4, m_{F'}=1\rangle$	$\sqrt{\frac{1}{14}}$
π - π	$\lvert 5S_{1/2}, F=2, m_F=2\rangle \rightarrow \lvert 5P_{3/2}, F'=3, m_F=2\rangle$	$-\sqrt{\frac{1}{6}}$
	$\lvert 5P_{3/2}, F=3, m_F=2\rangle \rightarrow \lvert nD_{5/2}, F'=4, m_{F'}=2\rangle$	$-\sqrt{\frac{2}{7}}$

It should be noted that:

- it is possible to have a beam polarisation coupling a certain ground hyperfine state to several upper states. However, only the ones with strongest transition strengths have been considered in the table above. For example a σ_--polarised coupling beam in a σ_+-σ_- configuration can also be restricted to the $|5\mathrm{P}_{3/2}, \mathrm{F} = 3, m_\mathrm{F} = 3\rangle \rightarrow |n\mathrm{D}_{5/2}, \mathrm{F}' = 2, m_{\mathrm{F}'} = 2\rangle$ transition with co-efficient $\sqrt{\frac{1}{105}}$. Also, a π-polarised coupling beam in a σ_+-π configuration can also be restricted to the $|5\mathrm{P}_{3/2}, \mathrm{F} = 3, m_\mathrm{F} = 3\rangle \rightarrow |n\mathrm{D}_{5/2}, \mathrm{F}' = 3, m_{\mathrm{F}'} = 3\rangle$ transition with co-efficient $\sqrt{\frac{1}{10}}$.
- the probe beam transition has already been restricted to $|5\mathrm{S}_{1/2}, \mathrm{F} = 2, m_\mathrm{F} = 2\rangle \rightarrow |5\mathrm{P}_{3/2}, \mathrm{F}' = 3, m_{\mathrm{F}'}\rangle$ via locking. The varying polarisation on just varies the values of m_F.

Bibliography

[1] D. Jaksch, J. Cirac, P. Zoller, S. Rolston, R. Cote and M. Lukin. *Fast quantum gates for neutral atoms*. Phys. Rev. Lett., 85(10), 2208, Sep. 2000.

[2] M. D. Lukin, M. Fleischhauer, R.Cote, L. Duan, D. Jaksch, J. Cirac and P. Zoller, *Dipole Blockade and Quantum Information Processing in Mesoscopic Atomic Ensembles*. Phys. Rev. Lett. 87(3), 037901, June 2001.

[3] I. E. Protsenko, G. Reymond, N. Schlosser and P. Grangier, *Operation of quantum phase gate using neutral atoms in microscopic dipole trap*. Phys. Rev. A. 65, 052301, Apr. 2002.

[4] T. Wilk, A. Gaëtan, C. Evellin, J. Wolters, Y. Miroshnychenko, P. Grangier, and A. Browaeys. *Entanglement of Two Individual Neutral Atoms Using Rydberg Blockade*. Phys. Rev. Lett. 104(1), 010502, Jan. 2010.

[5] L. Isenhower, E. Urban, X. Zhang, A. Gill, T. Henage, T. Johnson, T. Walker and M. Saffman. *Demonstration of a Neutral Atom Controlled-NOT Quantum Gate*. Phys. Rev. Lett. 104(1), 010503, Jan. 2010.

[6] K. M. Maller, M. T. Lichtman, T. Xia, Y. Sun, M. J. Piotrowicz, A. W. Carr, L. Isenhower and M. Saffman. *Rydberg-blockade controlled-not gate and entanglement in a two-dimensional array of neutral-atom qubits*. Phys. Rev. A 92(2), 022336, Aug. 2015.

[7] Y. Wang, A. Kumar, T.-Y. Wu and D. S. Weiss. *Single-qubit gates based on targeted phase shifts in a 3D neutral atom array*. *Science* 352(6293), 1562-1565, June 2016.

[8] M. Cozzini, T. Calarco, A. Recati and P. Zoller, *Fast Rydberg gates without dipole blockade via quantum control*. Opt. Comms. 264(2), 375-384, Aug. 2006.

[9] E. Brion, L. H. Pedersen and K. Mølmer, *Implementing a neutral atom Rydberg gate without populating the Rydberg state*. J. Phys. B: At. Mol. Opt. Phys. 40(9), S159-S166, April 2007.

[10] E. Brion, K. Mølmer, and M. Saffman, *Quantum Computing with Collective Ensembles of Multilevel Systems*. Phys. Rev. Lett. 99, 260501, Dec. 2007.

[11] M. Saffman and K. Mølmer, *Scaling the neutral-atom Rydberg gate quantum computer by collective encoding in holmium atoms*. Phys. Rev. A 78(1), 012336, July 2008.

[12] T. Amthor. *Interaction-Induced Dynamics in Ultracold Rydberg Gases – Mechanical Effects and Coherent Processes*. Ph.D. thesis, Fakultät für Mathematik und Physik, Albert-Ludwigs-Universität Freiburg, Sept. 2008.

[13] K. J. Boller, A. Imamoglu, and S. E. Harris. *Observation of electromagnetically induced transparency*. Phys. Rev. Lett. 66(20), 2593-2596, May 1991.

[14] X. Lu, X. Miao, J. Bai, L. Pei, M. Wang, Y. Gao, L. Wu, P. Fu, R. Wang and Z. Zuo. *Transition from Autler-Townes splitting to electromagnetically induced transparency based on the dynamics of decaying dressed states*. J. Phys. B: At. Mol. Opt. Phys 48(5), 055003, Feb. 2015.

[15] T. Y. Abi-Salloum. *EIT and AT: Two Similar but Distinct Phenomena in Two Categories of Three-Level Atomic Systems*. arXiv:1002.2148v1 [quant-ph], Feb. 2010.

[16] K. Bergmann, H. Theuer and B. W. Shore. *Coherent population transfer among quantum states of atoms and molecules*. Rev. Mod. Phys. 70(3), 1003 , July 1998.

[17] E. Arimondo. *Coherent population trapping in laser spectroscopy*. E. Wolf editor, Progress in Optics, Elsevier Science, Amsterdam, 35, 257-354, 1996.

[18] E. Cerboneschi1, F. Renzoni and E. Arimondo, *Quantum interference and slow light propagation in cold samples of open three-level atoms*. J. Opt. B: Quantum Semiclass. Opt. 4(4) S267-S272, July 2002.

[19] L. V. Hau, S. E. Harris, Z. Dutton and C. H. Behroozi. *Light speed reduction to 17 metres per second in an ultracold atomic gas*. Letters to Nature, 397, 594-598, Feb. 1999.

[20] Z. Dutton, N. S. Ginsberg, C. Slowe and L. V. Hau. *The art of taming light: ultra-slow and stopped light*. Europhysics News, Volume 35, Number 2, Pages 33-39, April 2004.

[21] N. B. Phillips, A. V. Gorshkov and I. Novikova. *Optimal light storage in atomic vapor*. Phys. Rev. A Volume 78, 023801, Aug. 2008.

[22] R. Santra, E. Arimondo, T. Ido, C. H. Greene and J. Ye. *High-Accuracy Optical Clock via Three-Level Coherence in Neutral Bosonic ^{88}Sr*. Phys. Rev. Lett. 94(17), 173002, May 2005.

[23] B. Olmos and I. Lesanovsky. *Collective photon emission from symmetric states created with Rydberg atoms on a ring lattice*. Phys. Rev. A 82(6), 063404, Dec. 2010.

[24] I. Friedler, D. Petrosyan, M. Fleischhauer and G. Kurizki. *Long-range interactions and entanglement of slow single-photon pulses*. Phys. Rev. A 72(4), 043803, Oct. 2005.

[25] H. Weimer, M. Müller, I. Lesanovsky, P. Zoller and H. P. Büchler . *A Rydberg quantum simulator*. Nature Physics 6, 382-388, Mar. 2010.

[26] D. Møller, L. B. Madsen and K. Mølmer, *Quantum Gates and Multiparticle Entanglement by Rydberg Excitation Blockade and Adiabatic Passage*. Phys. Rev. Lett. 100(17), 170504, April 2008.

[27] K. Singer, M. Reetz-Lamour, T. Amthor, L. G. Marcassa and Matthias Weidemüller, *Suppression of Excitation and Spectral Broadening Induced by Interactions in a Cold Gas of Rydberg Atoms*. Phys. Rev. Lett. 93(16), 163001, Oct. 2004.

[28] D. Tong, S. M. Farooqi, J. Stanojevic, S. Krishnan, Y.P. Zhang, R. Côté, E.E. Eyler, and P.L. Gould. *Local Blockade of Rydberg Excitation in an Ultracold Gas*. Phys. Rev. Lett. 93(6), 063001, Aug. 2004.

[29] T. Vogt, M. Viteau, J. Zhao, A. Chotia, D. Comparat and P. Pillet. *Dipole Blockade at Förster Resonances in High Resolution Laser Excitation of Rydberg States of Cesium Atoms*. Phys. Rev. Lett. 97(8), 083003, Aug. 2006.

[30] T. Vogt, M. Viteau, A. Chotia, J. Zhao, D. Comparat and P. Pillet. *Electric-Field Induced Dipole Blockade with Rydberg Atoms*. Phys. Rev. Lett. 99(7), 073002, Aug. 2007.

[31] T. Cubel Liebisch, A. Reinhard, P. R. Berman and G. Raithel. *Atom Counting Statistics in Ensembles of Interacting Rydberg Atoms*. Phys. Rev. Lett. 95(25), 253002, Dec. 2005.

[32] C. Ates, T. Pohl, T. Pattard and J. M. Rost, *Strong interaction effects on the atom counting statistics of ultracold Rydberg gases*. J. Phys. B: At. Mol. Opt. Phys. 39 L233, May 2006.

[33] D. Tong, S. M. Farooqi, J. Stanojevic, S. Krishnan, Y. P.Zhang, R. Côté, E. E. Eyler, and P. L. Gould. *Local Blockade of Rydberg Excitation in an Ultracold Gas*. Phys. Rev. Lett. 93(6), 063001, Aug. 2004.

[34] R. Löw, H. Weimer, J. Nipper, J. B. Balewski, B. Butscher, H. P. Büchler and T. Pfau. *An experimental and theoretical guide to strongly interacting Rydberg gases*. J. Phys. B: At. Mol. Opt. Phys. 45, 113001, May 2012.

[35] F. Robicheaux and J. V. Hernández. *Many-body wave function in a dipole blockade configuration*. Phys. Rev. A 72(6), 063403, Dec. 2005.

[36] S. Sevinçli, C. Ates, T. Pohl, H. Schempp, C. S. Hofmann, G. Günter, T. Amthor, M Weidemüller, J. D. Pritchard, D. Maxwell, A. Gauguet, K. J. Weatherill, M. P. A. Jones and C. S. Adams. *Quantum interference in interacting three-level Rydberg gases: coherent population trapping and electromagnetically induced transparency*. J. Phys. B: At. Mol. Opt. Phys. 44(18), 184018, Sep. 2011.

[37] C. Ates, S. Sevinçl, and T. Pohl. *Electromagnetically Induced Transparency in strongly interacting Rydberg Gases*. Phys. Rev. A 83(4), 041802(R), April 2011.

[38] R. Heidemann, U. Raitzsch, V. Bendkowsky, B. Butscher, R. Löw, L. Santos and T. Pfau. *Evidence for Coherent Collective Rydberg Excitation in the Strong Blockade Regime*. Phys. Rev. Lett. 99(19), 163601, Oct. 2007.

[39] Y. O. Dudin, L. Li, F. Bariani, and A. Kuzmich, *Observation of coherent many-body Rabi oscillations*. Nature Physics Vol. 8, 790-794, Nov. 2012.

[40] T. Johnson, E. Urban, T. Henage, L. Isenhower, D. Yavuz, T. Walker and M. Saffman, *Rabi oscillations between ground and Rydberg states with dipole-dipole atomic interactions*. Phys. Rev. Lett. 100(11), 113003, Mar. 2008.

[41] G. Askaryan. *Effect of the field gradient of an intense electromagnetic beam on electrons and atoms*. Technical Report, AD-A-233047/0/XAB; FTD-ID(RS)T–1379-90, Jan. 1991.

[42] A. Ashkin. *Acceleration and trapping of particles by radiation pressure*. Phys. Rev. Lett. 24(4), 156-159, Jan. 1970.

[43] C. antori, P. Tamarat, P. Neumann, J. Wrachtrup, D. Fattal, R. G. Beausoleil, J. Rabeau, P. Olivero, A. D. Greentree, S. Prawer, F. Jelezko, and P. Hemmer. *Coherent Population Trapping of Single Spins in Diamond under Optical Excitation*. Phys. Rev. Lett. 97(24), 247401, Dec. 2006.

[44] L. Thévenaz. *Slow and fast light in optical fibres*. Nat. Phot. 2, 474-481, Aug. 2008.

[45] X. Xu, B. Sun, P. R. Berman, D. G. Steel, A. S. Bracker, Dan Gammon and L. J. Sham. *Coherent population trapping of an electron spin in a single negatively charged quantum dot*. Nat. Phys. 4, 692-695, Aug. 2008.

[46] S. Weis, R. Riviére, S. Deléglise, E. Gavartin, O. Arcizet, A. Schliesser and T. J. Kippenberg. *Optomechanically Induced Transparency*. *Science* 330(6010), 1520-1523, Dec. 2010.

[47] A. Ghosh, K. Islam, D. Bhattacharyya and A. Bandyopadhyay. *Revisiting the four-level inverted-Y system under both Doppler-free and Doppler-broadened conditions: an analytical approach*. J. Phys. B: At. Mol. Opt. Phys. 49, 195401, Sep. 2016.

[48] J. O. Weatherall. *Quantum Control of Linear Susceptibility in five level Atoms via dressed interacting ground states, with a focus on group velocity control*. PhD Thesis, Faculty of the Stevens Institute of Technology, May 2009.

[49] H. P. Breuer and F. Petruccione. *The theory of Open Quantum Systems*. Oxford University Press, ISBN 0 19 852063 8, 2002.

[50] A. O. Odufowora. *Phonon Squeezing Through Effective Photon-Phonon Interaction*. Master Thesis, University of Trieste, Italy, 2016.

[51] M. Saffman. *Quantum computing with atomic qubits and Rydberg interactions: progress and challenges* . J. Phys. B: At. Mol. Opt. Phys. 49, Oct. 2016.

[52] S. Kuhr, W. Alt, D. Schrader, I. Dotsenko, Y. Miroshnychenko, A. Rauschenbeutel and D. Meschede, *Analysis of dephasing mechanisms in a standing-wave dipole trap*. Phys. Rev. A 72(2), 023406, Aug. 2005.

[53] V. Gorini, A. Kossakowski and E. Sudarshan. *Completely positive dynamical semigroups of N-level systems. American Institute of Physics*. Journal of Mathematical Physics, Volume 17, Issue 5, May 1976.

[54] G. Lindblad. *On the generators of quantum dynamical semigroups*. Communications in Mathematical Physics, Volume 48, Issue 2, pages 119-130, DOI: 10.1007/BF01608499, June 1976.

[55] P. Meystre and M. Sargent, *Elements of Quantum Optics*. Springer-Verlag, Berlin, 4th edition, ISBN: 3540742093, 2007.

[56] K. Fujii. *Introduction to the Rotating Wave Approximation (RWA): Two Coherent Oscillations*. arXiv:1301.3585v3 [quant-ph], May 2014.

[57] J. Pritchard. *Cooperative Optical Non-linearity in a blockaded Rydberg Ensemble*. PhD thesis, Department of Physics, Durham University, May 2011.

[58] W. W. Erickson. *Electromagnetically Induced Transparency*. Thesis, The Division of Mathematics and Natural Sciences, Reed College, May 2012.

[59] M. V. Pack, R. M. Camacho and J. C. Howell, *Electromagnetically induced transparency line shapes for large probe fields and optically thick media*. Phys. Rev. A 76, 013801, July 2007.

[60] R. S. Bennink, *Frequency conversion of optical signals using coherently prepared media*. PhD thesis, University of Rochester, Institute of Optics, Rochester, 2004.

[61] M. O. Scully and M. S. Zubairy, *Quantum Optics*. Cambridge University Press, Cambridge, ISBN: 0524235953, Sep. 1997.

[62] J. D. Jackson, *Classical Electrodynamics*. John Wiley and Sons, Hoboken, 3rd edition, ISBN: 9780471309321, 1999.

[63] R. W. Boyd, *Nonlinear Optics*. Academic Press, 3rd edition, ISBN: 148328823, Oct. 2007.

[64] S. Wielandy and A. L. Gaeta, *Investigation of electromagnetically induced transparency in the strong probe regime*. Phys. Rev. A 58(3), 2500, Sep. 1998.

[65] S. Harris, J. Field and A. Imamoglu. *Nonlinear optical processes using electromagnetically induced transparency*. Phys. Rev. Lett., Volume 64, Issue10, Page 1107, Mar. 1990.

[66] S. Harris, *Electromagnetically Induced Transparency*. Physics Today, Volume 50, Number 7, Pages 36-42 1997.

[67] G. Alzetta, A. Gozzini, L. Moi, and G. Orriols, *An experimental method for the observation of R.F. transitions and laser beat resonances in oriented Na vapour*. Il Nuovo Cimento B, 36:5-20, Nov. 1976.

[68] E. Arimondo and G. Orriols, *Nonabsorbing Atomic Coherences by Coherent Two-Photon transitions in a Three-Level Optical Pumping*. Lettere Al Nuovo Cimento Volume 17, Number 10, Pages 333-334, Nov. 1976.

[69] E. Arimondo, *V Coherent Population Trapping in Laser Spectroscopy*. Progress in Optics, Volume 35, Pages 257-354, 1996.

[70] S. H. Autler and C. H. Townes. *Stark Effect in Rapidly Varying Fields*. Phys. Rev. 100(2), 703-722, Oct. 1955.

[71] U. Fano. *Effects of Configuration Interaction on Intensities and Phase Shifts*. Phys. Rev. 124(6), 1866, Dec. 1961.

[72] P. M. Anisimov, J. P. Dowling, and B. C. Sanders. *Objectively Discerning Autler-Townes Splitting from Electromagnetically Induced Transparency*. Phys. Rev. Lett. 107(16), 163604, October 2011.

[73] T. Y. Abi-Salloum. *Interference Between Competing Pathways in the Interaction of Three-Level Ladder Atoms and Radiation*. Journal of Modern Optics 57(14-15), 1366-1376, Apr. 2010.

[74] M. Fleischhauer. *Electromagnetically induced transparency and coherent-state preparation in optically thick media*. Optics Express 4(2), 107-112, Jan. 1999.

[75] M. Fleischhauer, A. Imamoglu and J. Marangos. *Electromagnetically induced transparency: Optics in coherent media*. Rev. Mod. Phys., 77(2), 633, July 2005.

[76] L. Hao, Y. Jiao, Y. Xue, X. Han, S. Bai, J. Zhao and G. Raithel, *Transition from electromagnetically induced transparency to Autler-Townes splitting in cold cesium atoms* . New J. Phys., 20, 073024, July 2018.

[77] S. Khan, M. P. Kumar, V. Bharti and V. Natarajan. *Coherent population trapping (CPT) versus electromagnetically induced transparency (EIT)*. European Physical Journal D, 71(38), Feb. 2017.

[78] H. Y. Ling, Y. Li, and M. Xiao. *Coherent population trapping and electromagnetically induced transparency in multi-Zeeman-sublevel atoms*. Phys. Rev. A 53(2), 1014, Feb. 1996.

[79] S. Brandt, A. Nagel, R. Wynands and D. Meschede. *Buffer-gas-induced linewidth reduction of coherent dark resonances to below* 50 *Hz*. Phys. Rev. A 56(2), R1063(R), Aug. 1997.

[80] J. Oreg, F. T. Hioe and J. H. Eberly. *Adiabatic following in multilevel systems*. Phys. Rev. A 29(2), 690, Feb. 1984.

[81] C. Mansell and S. Bergamini. *A cold-atoms based processor for deterministic quantum computation with one qubit in intractably large Hilbert spaces*. New J. Phys. 16, 053045, May 2014.

[82] I. Beterov, M. Saffman, E. Yakshina, D. Tretyakov, V. Entin, G. Hamzina and I. Ryabtsev, *Simulated quantum process tomography of quantum gates with Rydberg superatoms*. J. Phys. B: At. Mol. Opt. Phys. 49(11), May 2016.

[83] R. Stebbings and F. Dunning (Editors). *Rydberg States of Atoms and Molecules*. Cambridge University Press, Apr. 1983.

[84] H. Held, J. Schlichter and H. Walther. *Quantum chaos in Rydberg atoms*. Lecture Notes in Physics, Volume 503, Springer, Berlin, Heidelberg, 1998.

[85] H. Weimer. *Quantum many-body physics with strongly interacting Rydberg atoms*. PhD Thesis, Institute for Theoretical Physics, University of Stuttgart, 2010.

[86] J. Olmsted III, *Excitation of Nitrogen Triplet States by Electron Impact*. Radiation Research 31(2), 191-200, June 1967.

[87] M. Haugh, T. G. Slanger and K. D. Bayes, *Electronic Excitation Accompanying Charge Exchange*. J. Chem. Phys. 44(2), 837, 1966.

[88] S. A. Saakyan, V. A. Sautenkov, E. V. Vilshanskaya, B. B. Zelener and B. V. Zelener, *Two-photon excitation of ultracold atoms to Rydberg states*. J. Phys.: Conf. Ser. 653 012123, 2015.

[89] J. Deiglmayr, M. Reetz-Lamour, T. Amthor, S. Westermann, A. L. de Oliveira and M.Weidemüller, *Coherent excitation of Rydberg atoms in an ultracold gas*. Opt. Commun. 264(5), 293–298, Aug. 2006.

[90] B. A. Bushaw, W. Nörtershäuser, G. W. F. Drake, and H.-J. Kluge, *Ionization energy of ^{6,7}Li determined by triple-resonance laser spectroscopy*. Phys. Rev. A 75, 052503, May 2007.

[91] A. Kowalczyk. *Manipulation and Control of Ultracold Rubidium Atoms*. PhD thesis, Open University, Milton Keynes, United Kingdom, 2012.

[92] C. Mansell, *Cold Atoms for Deterministic Quantum Computation with One Qubit*. PhD thesis, Open University, Milton Keynes, 2014.

[93] T. F. Gallagher, *Rydberg atoms*. Cambridge University Press, ISBN: 0521385318, 1994.

[94] C. Avigliano. *Towards deterministic preparation of single Rydberg atoms and applications to quantum information processing*. PhD Thesis, Universite Pierre et Marie Curie, Paris VI, France, 2014.

[95] M. Copley-May, *Microscopic Optical Trapping of Ultracold Neutral Atoms for Applications in Quantum Information*. PhD Thesis, Open University, Milton Keynes, United Kingdom, May 2018

[96] A. Browaeys and T. Lahaye, *Interacting Cold Rydberg Atoms: a Toy Many-Body System*. Seminaire Poincare, Volume XVII, Pages 125-144, 2013.

[97] W. Li, I. Mourachko, M. W. Noel and T. F. Gallagher, *Millimeter-wave spectroscopy of cold Rb Rydberg atoms in a magneto-optical trap: Quantum defects of the ns, np, and nd series*. Phys. Rev. A 67(5), 052502, May 2003.

[98] W. Li, P. J. Tanner and T. F. Gallagher. *Dipole-Dipole Excitation and Ionization in an Ultracold Gas of Rydberg Atoms*. Phys. Rev. Lett. 94(17), 173001, May 2005.

[99] L. G. D'yachkov and P. M. Pankratov. *On the use of the semiclassical approximation for the calculation of oscillator strengths and photoionization cross sections*. J. Phys. B: At. Mol. Opt. Phys. 27(3), 461-472, 1994.

[100] T. Amthor, M. Reetz-Lamour, S. Westermann, J. Denskat and M. Weidemüller, *Mechanical Effect of van der Waals Interactions Observed in Real Time in an Ultracold Rydberg Gas*. Phys. Rev. Lett. 98(2), 023004, Jan. 2007.

[101] I. I. Beterov and M. Saffman. *Rydberg blockade, Förster resonances, and quantum state measurements with different atomic species*. Phys. Rev. A 92(4), 042710, Oct. 2015.

[102] E. Urban, T. A. Johnson, T. Henage, L. Isenhower, D. D. Yavuz, T. G. Walker and M. Saffman, *Observation of Rydberg blockade between two atoms*. Solid State Communications, Highlights in Condensed Matter Physics and Materials Science, Nature Physics 5, 110-114, Feb. 2009.

[103] M. Weidemüller, *Rydberg atoms: There can be only one*. Matthias Nature Physics 5, 91-92, Feb. 2009.

[104] K. Modi, H. Cable, M. Williamson, and V. Vedral, *Quantum Correlations in Mixed-State Metrology*. Phys. Rev. X 1(2), 021022, Dec. 2011.

[105] K. Krzyzanowska, M. Copley-May, R. Romain, C. MacCormick and S. Bergamini. *Quantum-enhanced protocols with mixed states using cold atoms in dipole traps*. IOP Conf. Series: Journal of Physics: Conf. Series, 793, 012015, Jan. 2017.

[106] C. MacCormick, S. Bergamini, C. Mansell, H. Cable and K. Modi, *Supraclassical measurement using single-atom control of an atomic ensemble*. Phys. Rev. A 93, 023805, Feb. 2016.

[107] I. Bouchoule and K. Mølmer, *Spin squeezing of atoms by the dipole interaction in virtually excited Rydberg states*. Phys. Rev. A 65(4), 041803(R), April 2002.

[108] G. Santarelli, Ph. Laurent, P. Lemonde, A. Clairon, A. G. Mann, S. Chang, A. N. Luiten and C. Salomon, *Quantum Projection Noise in an Atomic Fountain: A High Stability Cesium Frequency Standard*. Phys. Rev. Lett. 82(23), 4619, June 1999.

[109] D. J. Wineland, J. J. Bollinger, W. M. Itano and D. J. Heinzen, *Squeezed atomic states and projection noise in spectroscopy*. Phys. Rev. A 50(1), July 1994.

[110] M. Ebert, A. Gill, M.Gibbons, X. Zhang, M. Saffman and T. G. Walker, *Atomic Fock State Preparation Using Rydberg Blockade*. Phys. Rev. Lett. 112, 043602, Jan. 2014.

[111] M. Saffman and T. G. Walker, *Creating single-atom and single-photon sources from entangled atomic ensembles*. Phys. Rev. A 66, 065403, Dec. 2002.

[112] A. Gaëtan, Y. Miroshnychenko, T. Wilk, A. Chotia, M. Viteau, D. Comparat, P. Pillet, A. Browaeys and P. Grangier. *Observation of collective excitation of two individual atoms in the Rydberg blockade regimes*. Nat. Phys. 5, 115-118, Jan. 2009.

[113] M. Piotrowicz. *Ultracold Rydberg Atoms*. PhD thesis, Open University, Milton Keynes, United Kingdom 2010.

[114] A. K. Ekert, *Quantum cryptography based on Bell's theorem*. Phys. Rev. Lett. 67(6), 661, Aug. 1991.

[115] M. Manko and V. Manko. *Entanglement and other quantum correlations of a single qudit state as a resource for quantum technologies*. ArXiv:1409.4221v1 [quant-ph], Sep. 2014.

[116] M. P. A. Jones, J. Beugnon, A. Gaëtan, J. Zhang, G. Messin, A. Browaeys and P. Grangier. *Fast quantum state control of a single trapped neutral atom*. Phys. Rev. A 75(4), 040301(R), April 2007.

[117] J. Beugnon, C. Tuchendler, H. Marion, A. Gaëtan, Y. Miroshnychenko, Y. R. P. Sortais, A. M. Lance, M. P. A. Jones, G. Messin, A. Browaeys and P. Grangier. *Two-dimensional transport and transfer of a single atomic qubit in optical tweezers*. Nature Physics 3, 696-699, Aug. 2007.

[118] T. Pellizzari, S. Gardiner, J. Cirac and P. Zoller. *Decoherence, Continuous Observation, and Quantum Computing: A Cavity QED Model*. Phys. Rev. Lett., Volume 75, Issue 21, Page 3788, Nov. 1995.

[119] G. Brennen, C. Caves, P. Jessen and I. Deutsch. *Quantum Logic Gates in Optical Lattices*. Phys. Rev. Lett. 82(5), 1060, Feb. 1999.

[120] D. Jaksch, H. Briegel, J. , C. Gardiner and P. Zoller. *Entanglement of Atoms via Cold Controlled Collisions*. Phys. Rev. Lett. 82(9), 1975, Mar. 1999.

[121] M. Lukin and P. Hemmer. *Quantum Entanglement via Optical Control of Atom-Atom Interactions*. Phys. Rev. Lett. 84(13), 2818, Mar. 2000.

[122] M. Müller, I. Lesanovsky, H. Weimer, H. Büchler and P. Zoller. *Mesoscopic Rydberg Gate Based on Electromagnetically Induced Transparency*. Phys. Rev. Lett. 102(17), 170502, April 2009.

[123] E. Knill and R. Laflamme. *On the Power of One Bit of Quantum Information*. Phys. Rev. Lett., 81(25), 5672, Dec. 1998

[124] A. Datta, A. Shaji, and C. Caves. *Quantum Discord and the Power of One Qubit*. Phys. Rev. Lett., 100(5), 050502, Feb. 2008.

[125] A. Datta, S. Flammia and C. Caves. *Entanglement and the Power of One Qubit*. Phys. Rev. A 72(4), 042316, Oct. 2005.

[126] C.-S. Yu, J. Zhang and H. Fan. *Quantum dissonance is rejected in an overlap measurement scheme*. Phys. Rev. A 86(5), 052317, Nov. 2012.

[127] R. Dorner, S. R. Clark, L. Heaney, R. Fazio, J. Goold and V. Vedral. *Extracting Quantum Work Statistics and Fluctuation Theorems by Single-Qubit Interferometry*. Phys. Rev. Lett. 110(23), 230601, June 2013.

[128] L. Mazzola, G. De Chiara and M. Paternostro. *Measuring the Characteristic Function of the Work Distribution*. Phys. Rev. Lett. 110(23), 230602, June 2013.

[129] D. Poulin, R. Laflamme, G. J. Milburn and J. P. Paz. *Testing integrability with a single bit of quantum information*. Phys. Rev. A 68(2), 022302, Aug. 2003.

[130] D. Poulin, P. R. Blume-Kohout, R. Laflamme and H. Ollivier. *Exponential Speedup with a Single Bit of Quantum Information: Measuring the Average Fidelity Decay*. Phys. Rev. Lett. 92(17), 177906, April 2004.

[131] S.P. Jordan and P. Wocjan. *Estimating Jones and HOMFLY polynomials with one clean qubit*. Quantum Inf. Comput. 9(3-4), 0264-0289, 2009.

[132] B. Lanyon, M. Barbieri, M. Almeida and A. White. *Experimental Quantum Computing without Entanglement*. Phys. Rev. Lett., 101(20), 200501, Nov. 2008.

[133] G. Passante, O. Moussa, C. Ryan and R. Laflamme. *Experimental Approximation of the Jones Polynomial with One Quantum Bit*. Phys. Rev. Lett. 103(20), 250501, Dec. 2009.

[134] P. W. Shor and S. P. Jordan. *Estimating Jones Polynomials is a Complete Problem for One Clean Qubit*. Quantum Information and Computation 8, 681 , Feb. 2008.

[135] W. R. Anderson, J. R. Veale and T. F. Gallagher. *Resonant Dipole-Dipole Energy Transfer in a Nearly Frozen Rydberg Gas*. Phys. Rev. Lett. 80(2), 249, Jan. 1998.

[136] S. Bergamini, B. Darquié, M. Jones, L. Jacubowiez, A. Browaeys and P. Grangier. *Holographic generation of microtrap arrays for single atoms by use of a programmable phase modulator*. Journal of the Optical Society of America B 21(11), 1889-1894, Feb. 2004.

[137] I. Beterov, M. Saffman, E. Yakshina, V. Zhukov, D. Tretyakov, V. Entin, I. Ryabtsev, C. Mansell, C. MacCormick, S. Bergamini and M. Fedoruk, *Quantum gates in mesoscopic atomic ensembles based on adiabatic passage and Rydberg blockade*. Phys. Rev. A 88(1), 010303, July 2013.

[138] D. McCarron, S. King and S. Cornish. *Modulation transfer spectroscopy in atomic rubidium*. Measurement Science and Technology 19(10), Aug. 2008.

[139] R. Abel, A. Mohapatra, M. Bason, J. Pritchard, K. Weatherill, U. Raitzsch and C. Adams. *Laser frequency stabilization to excited state transitions using electromagnetically induced transparency in a cascade system*. Appl. Phys. Lett., 94, 071107, Jan. 2009.

[140] *DL 100 Grating Stabilized Diode Laser Head Manual*. Toptica Photonics, Mar. 2006.

[141] B. Danielle, *First observation of Rydberg blockade in a frozen gas of divalent atoms*. PhD thesis, Department of Physics, Durham University, Durham, United Kingdom, Aug. 2014.

[142] D. J. McCarron, I. G. Hughes, P. Tierney and S. L. Cornish, *A heated vapor cell unit for dichroic atomic vapor laser lock in atomic rubidium*. Rev. Sci. Instrum., 78(9), Sep. 2007.

[143] C. Wieman and T. W. Hänsch, *Doppler-free laser polarization spectroscopy*. Phys. Rev. Lett. 36(12), 1170, May 1976.

[144] G. C. Bjorklund, *Frequency-modulation spectroscopy: a new method for measuring weak absorptions and dispersions*. Optics Letters 5(1), 15-17, Jan. 1980.

[145] J. H. Shirley, *Modulation transfer processes in optical heterodyne saturation spectroscopy*. Optics Letters 7(11), 537-539, Nov. 1982.

[146] R. K. Raj, D. Bloch, J. J. Snyder, G. Camy and M. Ducloy, *High-frequency optically heterodyned saturation spectroscopy via resonant degenerate four-wave mixing*. Phys. Rev. Lett. 44(19), 1251, May 1980.

[147] (a) *TA/DL-SHG 110 Frequency Doubled High Power Laser System Manual*. Toptica Photonics, Aug. 2005.
(b) *TA 100 Tapered Amplifier System Manual*. Toptica Photonics, Aug. 2007.

[148] G. D. Boyd and D. A. Kleinman. *Parametric Interaction of Focused Gaussian Light Beams*. Journal of Applied Physics 39(8), 3597, 1968.

[149] M. D. Lukin. *Colloquium: Trapping and manipulating photon states in atomic ensembles*. Rev. Mod. Phys. 75(2), 457, April 2003.

[150] A. V. Gorshkov, A. André, M. Fleischhauer, A. S. Sørensen, and M. D. Lukin. *Universal Approach to Optimal Photon Storage in Atomic Media*. Phys. Rev. Lett. 98(12), 123601, Mar. 2007.

[151] M. J. Piotrowicz, C. MacCormick, A. Kowalczyk, S. Bergamini, I. I Beterov and E. A. Yakshina. *Measurement of the electric dipole moments for transitions to rubidium Rydberg states via Autler-Townes splitting*. New J. Phys 13, 093012, Sep. 2011.

[152] D. Steck, a.) *Rubidium 87 D Line Data*.
b.) *Rubidium 85 D Line Data*.
Theoretical Division, MS B285, Los Alamos National Laboratory Los Alamos, NM 87545, Sep. 2001.

[153] D. M. Brink and G. R. Satchler. *Angular Momentum*. Oxford University Press, Mar. 1994.

[154] B. V. Numerov. *A method of extrapolation of perturbations*. MNRAS, 84, 592-601, June 1924.

[155] E. A. Donleya, T. P. Heavner, F. Levib, M. O. Tataw and S. R. Jefferts. *Double-pass acousto-optic modulator system*. Rev. Sci. Instrum. 76, 063112 June 2005.

[156] C. Henry. *Theory of the linewidth of semiconductor lasers*. IEEE Journal of Quantum Electronics, 18(2), 259-264, Feb. 1982.

[157] H. Ludvigsen, M. Tossavainen and M. Kaivola. *Laser linewidth measurements using self-homodyne detection with short delay*. Optics Communications 155 180-186, Oct. 1998.

[158] L.D. Turner, K.P. Weber, C.J. Hawthorn and R.E. Scholten. *Frequency noise characterisation of narrow linewidth diode lasers*. Optics Communications 201 391-397, Jan. 2002.

[159] R. Daschner. *Addressable Rubidium vapor cells for optical and electrical read-out of Rydberg excitations*. PhD Thesis, Physics Institute, University of Stuttgart, 2015.

[160] A. C. H. Yu, A. H. Steinman and R. S. C. Cobbold. *Transit-Time Broadening in Pulsed Doppler Ultrasound: A Generalized Amplitude Modulation Models*. IEEE Transactions on Ultrasonics, Ferroelectrics, and Frequency Control, 53(3), 530-541, Mar. 2006.

[161] C. Ates, T. Pohl, T. Pattard and J. M. Rost. *Many-body theory of excitation dynamics in an ultracold Rydberg gas*. Phys. Rev. A 76(1), 013413, July 2007.

[162] C. Ates, T. Pohl, T. Pattard and J. M. Rost. *Antiblockade in Rydberg excitation of an ultracold lattice gas*. Phys. Rev. Lett. 98(2), 023002, Jan. 2007.

[163] T. Laycock, B. Olmos and I. Lesanovsky. *Creation of collective many-body states and single photons from two-dimensional Rydberg lattice gases*. J. Phys. B: At. Mol. Opt. Phys. 44(18), 184017, Sep. 2011.

[164] R. Grimm, M. Weidemüller, Y. B. Ovchinnikov. *Optical Dipole Traps for Neutral Atoms*. Advances In Atomic, Molecular, and Optical Physics 42, 95-170, 2000.

[165] Y. O. Dudin and A. Kuzmich. *Strongly Interacting Rydberg Excitations of a Cold Atomic Gas*. *Science* 336(6083), 887-889, May 2012.

[166] K. Krzyzanowska *Development of a cold atoms platform for a DQC*1 *implementation*. PhD thesis, Open University, Milton Keynes, United Kingdom, Dec. 2017.

[167] T. W. Hänsch and A. L. Schawlow, *Cooling of gases by laser radiation*. Opt. Commun. 13(1), 68-69, Jan. 1975.

[168] P. Zeeman, *The Effect of Magnetisation on the Nature of Light Emitted by a Substance*. Nature 55, 347, Feb. 1897.

[169] P. D. Lett, W. D. Phillips, R. N. Watts, C. I. Westbrook and H. J. Metcalf, *Observation of Atoms Laser Cooled below the Doppler Limit*. Phys. Rev. Lett. 61(2), 169, July 1988.

[170] J. Dalibard and C. Cohen-Tannoudji, *Laser cooling below the Doppler limit by polarization gradients: simple theoretical models*. JOSA B 6(11), 2023-2045, June 1989.

[171] P. J. Ungar, D. S. Weiss, E. Riis and S. Chu, *Optical molasses and multilevel atoms: theory*. JOSA B 6(11), 2058-2071, June 1989.

[172] D. S. Weiss, E. Riis, Y. Shevy, P. J. Ungar and S. Chu, *Optical molasses and multilevel atoms: experiment*. JOSA B 6(11), 2072-2083, June 1989.

[173] D. Haubrich, H. Schadwinkel, F. Strauch, B. Ueberholz, R. Wynands and D. Meschede. *Observation of individual neutral atoms in magnetic and magneto-optical traps*. EPL (Europhysics Letters), 34(9), June 1996.

[174] T. Arpornthip, C. A. Sackett and K. J. Hughes. *Vacuum-pressure measurement using a magneto-optical trap*. Phys. Rev. A 85(3), 033420, Mar. 2012.

[175] G. L. Gattobigio1, T. Pohl, G. Labeyrie1 and R. Kaiser. *Scaling laws for large magneto-optical traps*. The Royal Swedish Academy of Sciences, Physica Scripta, 81(2), Feb. 2010.

[176] C. G. Townsend, N. H. Edwards, C. J. Cooper, K. P. Zetie, C. J. Foot, A. M. Steane, P. Szriftgiser, H. Perrin and J. Dalibard. *Phase-space density in the magneto-optical trap*. Phys. Rev. A 52(2), 1423, Aug. 1995.

[177] W. Ketterle, K. B. Davis, M. A. Joffe, A. Martin, and D. E. Pritchard. *High densities of cold atoms in a dark spontaneous-force optical trap*. Phys. Rev. Lett. 70(15), 2253, Apr. 19935.

[178] W. Petrich, M. H. Anderson, J. R. Ensher and E. A. Cornell. *Behavior of atoms in a compressed magneto-optical trap*. J. Opt. Soc. Am. B, 11(8), 1332-1335, Aug. 1994.

[179] *https://www.thorlabs.de/newgrouppage9.cfm?objectgroup$_i d = 149$.*

[180] N. Schlosser, G. Reymond, I. Protsenko and P. Grangier. *Sub-poissonian loading of single atoms in a microscopic dipole trap*. Letters to Nature, 411, 1024-1027, June 2001.

[181] L. Béguin. *Measurement of the van der Waals interaction between two Rydberg atoms*. PhD thesis, l'Institut d'Optique Graduate School, Dec. 2013.

[182] T. Brzozowski, M. Maczynska, M. Zawada, J. Zachorowski and W. Gawlik. *Time-of-flight measurement of the temperature of cold atoms for short trap-probe beam distances*. J. Opt. B: Quantum Semiclass. Opt.,4, 62-66, Jan. 2002.

[183] G. Birkl and J. Fortágh. *Micro traps for quantum information processing and precision force sensing*. Laser & Photon., 1(1), 12-23, Feb. 2007.

[184] M. Köhl, H. Moritz, T. Stöferle, K. Günter and T. Esslinger, *Fermionic Atoms in a Three Dimensional Optical Lattice: Observing Fermi Surfaces, Dynamics, and Interactions*. Phys. Rev. Lett. 94(4), 080403, March 2005.

[185] M. Anderlini, P. J. Lee, B. L. Brown, J. Sebby-Strabley, W. D. Phillips and J. V. Porto, *Controlled exchange interaction between pairs of neutral atoms in an optical lattice*. Nature 448, 452-456, July 2007.

[186] M. Saffman, T. Walker and K. Mølmer, *Quantum information with Rydberg atoms*. Rev. Mod. Phys. 82(3), 2313, Aug 2010.

[187] A. J. Daley, M. M. Boyd, J. Ye and P. Zoller, *Quantum Computing with Alkaline-Earth-Metal Atoms*. Phys. Rev. Lett. 101(17), 170504, Oct. 2008.

[188] P Anisimov and O Kocharovskaya. *Decaying-dressed-state analysis of a coherently driven three-level Λ system*. Journal of Modern Optics 55(19-20), 3159-3171, Dec. 2010.